Planets of young stars: The TLS-Tautenburg radial velocity survey

Dissertation
zur Erlangung des akademischen Grades
Dr. rer. nat.

vorgelegt dem Rat der Physikalisch-Astronomischen Fakultät
der Friedrich-Schiller-Universität Jena

von Massimiliano Esposito

geboren am 28. Oktober 1973 in Torre del Greco (Italien)

Gutachter

1. Prof. Dr. Artie P. Hatzes (Jena Universität)

2. Prof. Dr. M. Capaccioli (Napoli Universität)

3. Prof. Dr. G. Scarpetta (Salerno Universität)

Tag der letzten Rigorosumsprüfung: 09.01.2009

Tag der offentlichen Verteidigung: 28.04.2009

Zusammenfassung

Kapitel 1: Seit gerade einmal fünfzehn Jahren erweist sich die Suche nach extrasolaren Planeten als ein fruchtbares Feld der beobachtenden Astronomie. Die Spekulationen über deren Existenz jedoch dauern schon viel länger an. Im Folgenden werde ich einen Überblick über die wissenschaftlichen Meilensteine geben bis hin zu der modernen Ansicht zur Stellung des Menschen im Universum.

Der Nachweis eines fernen Planeten oder gar eines Planetensystems ist eine äußerst anspruchsvolle Aufgabe und man hat sich hierzu bereits viele verschiedene Techniken ersonnen. Im zweiten Abschnitt werde ich auf die wichtigsten Beobachtungsmethoden eingehen, die zu Grunde liegenden Konzepte erläutern und die Vor- als auch Nachteile aufweisen. Zu jeder Technik werde ich auch die Hauptresultate auf dem heutigen Stand aufführen.

Seitdem der erste extrasolare Planet um einen sonnenähnlichen Stern entdeckt wurde, sind viele Beobachtungsfeldzüge unternommen worden und dank der Radialgeschwindigkeitsmethode kennt man heute knapp 300 solcher fernen Welten. Im dritten Abschnitt werde ich die wesentlichen Eigenschaften dieser Planeten als auch die ihrer Muttersterne aufführen, welche sich in den statistischen Studien abzeichnen.

Kapitel 2: Eine der essenziellen Motivationen für die Untersuchungen auf dem Gebiet der extrasolaren Planeten ist der Wunsch zu verstehen, wie sich Planetensysteme formieren und sich entwickeln, was uns dazu bringt unser eigenes Sonnensystem in einem größeren Zusammenhang zu sehen. Da man davon ausgeht, dass der Prozess der Planetenentstehung alsbald nach der Bildung des Muttersterns beginnt, werde ich in Abschnitt 1 zunächst kurz das derzeitig akzeptierte Modell zur Sternentstehung in Erinnerung rufen, welche im Folgenden zur Entstehung der zirkumstellaren Scheiben führt, die als Geburtsstätte von Planeten gelten.

Die theoretischen Untersuchungen zur Planetenentstehung haben eine lange Geschichte, wobei sie ursprünglich vor allem dazu ausgeführt wurden, die Entstehung und Konfiguration unseres Sonnensystems zu erklären. In Abschnitt 2 werde ich einen Überblick über die Theorie zum “solaren Nebel” geben. Da es aber keinen Grund gibt, hier zu sehr ins Detail zu gehen, werde ich eher einen schematischen Einstieg zur Planetenentstehung gemäß dieser Theorie geben. Insbesondere werde ich an dieser Stelle Betonung auf die physikalischen Grundlagen zur Entwicklung eines Systems geben und werde die theoretischen Werkzeuge präsentieren – die numerischen als auch die analytischen, die zur Verfügung stehen, das System zu modellieren.

Die Feststellung, dass Exoplaneten Eigenschaften zeigen, die sehr verschieden von denen der hiesigen Planeten des Sonnensystems sind – hier insbesondere die hohen Exzentrizitäten von jupiterähnlichen Planeten auf kurzperiodischen Orbits – hat dazu geführt, dass die Theorien zur Planetenentstehung überarbeitet werden mussten. Neuere Studien bedienen sich nun der Planetenmigration auf Grund von Wechselwirkungen zwischen

den planetaren Körpern und der Gasscheibe oder zwischen den Planeten selbst, um die beobachteten Eigenschaften erklären zu können. Abschnitt 3 widme ich der Schilderung dieser neuen theoretischer Ansätze.

Kapitel 3: In diesem Kapitel wird die wissenschaftliche Motivation dieser Arbeit aufgezeigt. Die meisten Vorgänge, von denen die endgültige orbitale Konfiguration eines Planetensystems und die physikalischen Eigenschaften seiner Planeten abhängen, finden in der frühen Phase der Entwicklung statt, d.h. noch während sich die Planeten in der protoplanetaren Scheibe bilden und in den rund 100 Millionen Jahren ihrer Existenz. Aus diesem Grunde vermag eine Charakterisierung der beobachteten Eigenschaften von Planeten Aufschluss über die Entstehung von Planeten geben.

Es gibt zahlreiche Möglichkeiten, Beobachtungsdaten mit Theorien zur Planetenentstehung und -evolution abzugleichen und letztere somit weiter zu verfeinern und offene Fragen zu klären. Ist z.B. das Fehlen von sehr massereichen Planeten auf kurzperiodischen Orbits um alte Sterne auch eine Eigenschaft von jungen Sternen? Die Antwort auf diese Frage wird uns auch Auskunft über die Rolle von Planetenmigration und -evaporation (Kapitel 1) geben. Man nimmt an, dass gravitative Wechselwirkungen zwischen Planeten zu hohen Exzentrizitäten der Planetenbahnen führt. Sollte diese Annahme der Wahrheit entsprechen, hätte das zur Folge, dass junge Planeten durchschnittlich Orbits geringerer Exzentrizität haben. Da die interplanetaren Wechselwirkungen auch dazu führen können, dass Objekte aus einem System katapultiert werden, sollten jüngere Systeme auch durchschnittlich mehr Planeten haben. Eine zusätzliche interessante Eigenschaft von jungen Planeten entspringt der Tatsache, dass sie intrinsisch heller sind als ältere. Sie stellen also die optimalen Ziele für einen direkten Nachweis dar (Abschnitt 3).

In Abschnitt 4 werden die Probleme vorgestellt, die mit den Studien der Radialgeschwindigkeitsmethode bei jungen und damit (magnetisch) aktiven Sternen einhergehen. An dieser Stelle werden die wichtigsten Phänomene, die trügerische Variationen in der Radialgeschwindigkeit hervorrufen können, und die üblichen Methoden zur Bestimmung stellarer Aktivität analysiert. Resultate vorangegangener Beobachtungskampagnen sollen hier auch erwähnt sein.

Kapitel 4: In diesem Kapitel wird das Reservoir an Sternen vorgestellt, das dieser Arbeit zu Grunde liegt. Die Bestimmung des Alters der Sterne ist hierbei durchaus eine schwierige Aufgabe. Die am häufigsten angewandten Methoden zur Diagnose stellaren Alters werden in Abschnitt 1 vorgestellt. Diese Methoden wurden genutzt um Sterne mit einem Alter zwischen 30 und 200 Myr zu identifizieren.

Insgesamt wurden 43 Sterne auf ihre Radialgeschwindigkeiten hin überwacht. Diese Zahl stellt einen Kompromiss zwischen einer statistisch signifikanten Anzahl von Systemen auf der einen und der benötigten Anzahl von Spektren pro Objekt auf der anderen Seite dar. Darüber hinaus wurde eine umfassende Literatur- und Archivrecherche unternommen, um jede möglicherweise nützliche Information zu dem vorliegenden Sample zu verwerten (Abschnitte 2 und 3).

Kapitel 5: Die Beobachtungen wurden mit dem 2-Meter-Teleskop TLS-Tautenburg und dem an ihm montierten hochauflösenden Coudé Echelle Spektrographen durchgeführt (Abschnitt 1). Der damit abgedeckte Wellenlängenbereich erstreckt sich von 4.700 nach 7.400 Åbei einer inversen spektralen Auflösung von R=67.000.

Alles in allem wurden ∼2000 Spektren in der Zeit zwischen 2001 und 2006 aufgenommen. Die Belichtungszeiten lagen zwischen 5 und 30 Minuten – je nach Helligkeit des Objektes. Das Signal-zu-Rausch-Verhältnis (S/N) pro spektralem Bin lag in der

Größenordnung von 10 (Abschnitt 2).

Die Datenreduktion wurde mit der Software IRAF (Image Reduction and Analysis Facility) durchgeführt. Dabei wurden die Pakete noao.imred.ccdred und noao.imred.echelle benutzt (Abschnitt 3).

Kapitel 6: Das Tautenburger Teleskop ist in der Lage hochauflösende Messungen zur Radialgeschwindigkeit unter Nutzung der Jodzelle vorzunehmen. Die Methode besteht darin, dem beobachteten Sternenspektrum eine große Anzahl eng beieinander liegender Absorptionslinien zu überlagern, welche sowohl eine synchrone, akkurate Referenz zur Justierung der Wellenlänge als auch die Erstellung eines instrumentenspezifischen Profils ermöglichen. Die Jodzelle und die Software RADIAL, welche dazu benutzt wurde, die Radialgeschwindigkeiten zu bestimmen, werden in Abschnitt 1 vorgestellt.

Eine Analyse der Fehler bei den Messungen der Radialgeschwindigkeit wird vorgenommen und es wird erklärt, wie diese von relevanten Parametern des Sterns, wie z.B. der Helligkeit und der Rotationsgeschwindigkeit, abhängen. Für die meisten beobachteten Sterne werden Fehler in der Größenordnung von $\sim$10 m s^{-1} erreicht.

Kapitel 7: Eines der Resultate der Radialgeschwindigkeitsüberwachung ist die Entdeckung von 7 spektroskopischen Binärsystemen. 4 von ihnen waren vor diesen Untersuchungen nicht als Binärsysteme bekannt und von dreien wurden die dynamischen Parameter bestimmt (Abschnitt 1).

Bei den restlichen 36 Sternen dient eine generelle Analyse der Radialgeschwindigkeitsvariabilität als Demonstration des Potenzials dieser Methode bei Anwendung auf junge Sterne (Abschnitt 2). Das Vorhandensein von Variationen als Signatur von möglichen Begleitern der Primärkomponente wurde untersucht unter Zuhilfenahme von Periodogrammen (Abschnitt 3). Zusätzlich wurden zeitaufgelöste, photometrische Daten untersucht in Hinblick auf die Bestätigung oder Ablehnung der Annahme eines planetaren Begleiters. Insbesondere standen für alle Sterne bis auf einen Daten vom Satelliten Hypparchos zur Verfügung (Abschnitt 4).

Für zwei interessante Objekte wurde eine detailliertere Studie vorgenommen. HD41593 zeigt Variationen mit einer Periode von P$\sim$4 Tagen, was kompatibel mit der Anwesenheit eines Planeten mit einer Mindestmasse von $M_p \sin i$=0.16 M$_J$ auf einem exzentrischen Orbit mit e=0.25 ist. In Anbetracht der relativ hohen Anzahl von statistischen Ausreißern kann HD41593 z.Z. nurmehr als Kandidat für einen von einem Exoplaneten umrundeten Stern gelten (Abschnitt 5). Der Fall von HD171488 zeigt deutlich wie die Aktivität die Messungen zur Radialgeschwindigkeit beeinflussen kann. Hier wurde ein periodisches Signal mit P$\sim$1.3 d nachgewiesen, welches allerdings mit der stellaren Rotationsperiode übereinstimmt wie aus photometrischen Untersuchungen und solchen zum Dopplereffekt bekannt ist (Abschnitt 6).

Obwohl kein eindeutiger Nachweis eines Exoplaneten erreicht werden konnte, so erlauben die gewonnenen Datensätze jedoch die Auferlegung einer stringenten oberen Grenze für die Existenz von Planeten um die untersuchten Sterne. Zu diesem Zwecke wurde eine Reihe von Monte-Carlo-Simulationen zur Studie der von Orbitperiode und Planetenmasse aufgespannten Ebene im Bereich zwischen P=0.7-800 d und $M_p \sin i$=0.05-30 M$_J$ durchgeführt. Aus ihnen folgt z.B, dass wir für 77% der Sterne in unserem Repertoire mit 99%-iger Wahrscheinlichkeit einen Planeten mit P=10 d und $M_p \sin i$=1 M$_J$ ausschließen können und mit gleicher Wahrscheinlichkeit auch keinen Planeten mit P=300 d und $M_p \sin i$=3 M$_J$ um 66% unserer Sterne finden.

Kapitel 8: In diesem Kapitel werden die Hauptresultate der vorliegenden Arbeit aufgearbeitet. Im Zuge der Auswertung der Kampagne konnte gezeigt werden, dass die auf

Messungen der Radialgeschwindigkeit beruhende Methode zum Nachweis von Exoplaneten auch erfolgreich auf die Untersuchung junger Sterne angewendet werden kann – trotz deren erhöhter Aktivität.

Das Fehlen von Planeten um die hier untersuchten Sterne ist statistisch kompatibel mit dem häufigen Auftreten von Planeten um alte sonnenähnliche Sterne, welches auf $\sim$7 % ($\sim$1 % für Heiße Jupiter) geschätzt wird. Das Resultat widerspricht jedoch der verbreiteten Annahme, dass junge Sterne eine weitaus größere Population von sehr massereichen Planeten auf engen Bahnen haben könnten als alte Sterne.

Abstract

Chapter 1: The quest for extra-solar planets has turned into an active field of observational astronomy only in the last fifteen years. However the existence of other worlds has been matter of speculation and debate since long before. Thus I will begin this introductory chapter by quickly running through the scientific milestones which have led to the modern vision of the mankind's place in the Universe.

The detection of a planet, or a planetary system, orbiting a star is a challenging task. Different techniques have been devised to achieve this goal. In Section 2 I will review the most important observational methods by explaining their working concepts and pointing out merits and drawbacks. For each case I will also report the major results obtained up to now.

Since the first extrasolar planet orbiting a solar-like star was discovered, the observational campaigns multiplied, and, thanks especially to radial velocity (RV) surveys, today almost 300 exoplanets are known. Section 3 will discuss the main properties of these planets as well as of their host stars, that have emerged from statistical studies.

Chapter 2: One of the main drivers of the exoplanets field of research is the will to understand how planetary systems form and evolve, and therefore to put our own Solar system in context. Since the process of planet formation is believed to take place right after the host star has formed, I will first very shortly recall in Section 1 the current view of stellar formation which also lead to the formation of a circumstellar protoplanetary disk.

The theoretical studies on planet formation have a long history and understandably they have mostly attempted to account for the formation of the Solar system and to explain its present configuration. In Section 2 I will review the "Solar Nebula Theory". There is no pretension to give an exhaustive treatment of the subject. I will rather introduce schematically the main phenomena which leaded to the formation of the Solar system according to the Solar Nebula theory. In particular, I put the accent on the basic physics necessary to describe the system evolution and present the theoretical tools, analytical and numerical, that are at hand to model the system.

The discovery that exoplanets show different properties from solar planet, mainly the highly eccentric orbits and the existence of Jupiter-like planets on short-period orbits, has led to revise the planet formation theories. New studies call for mechanisms, like planet migration due to interaction with the gas disk or planet-planet gravitational scattering, in order to explain the observed exoplanet properties. In Section 3 those new theoretical developments will be depicted.

Chapter 3: In this chapter the scientific motivation of the thesis will be presented. Most of the phenomena that shape the orbital configuration of planetary systems and the physical properties of planets occur in the early evolutionary phases, that is while planets are still forming in the protoplanetary disk and right afterward in the first few

hundred million years of their life. Therefore the observational characterization of a sample of planets of young stars can provide with valuable information to a better comprehension of the planetary systems formation.

There are in particular many observational tests that can help constraining open issues in the current theories of planet formation and evolution. Is the lack of very massive planets on short period orbits observed in old stars also a feature of young stars? The answer to this question will tell us about the role played by mechanisms like orbital migration in the disk and planet evaporation (Section 1). Extrasolar planets show often highly eccentric orbits. It is believed that planet-planet gravitational scattering is the mechanism able to bring planets on eccentric orbits. If this is true, young planets should have on average less eccentric orbits. In addition, since scattering can also lead to planet ejections, the frequence of multiple systems should be larger for young stars (Section 2). An additional interesting property of young planets is that they are intrinsically brighter than old planets. Young planets are therefore optimal targets to attempt direct detection (Section 3).

In Section 4 the problems inherent to the measuring of precise RV for young, and therefore active, stars will be discussed. The more important phenomena able to produce spourious RV variations and the commonly used diagnostics of stellar activity will be analysed. Results from previous RV-surveys will also be reported.

Chapter 4: The sample of young stars that have been studied in this thesis will be introduced in this chapter. The assessment of the age of stars is not a trivial task; the most used diagnostics of stellar age are discussed in Section 1. These diagnostics have been used to select stars whose age is confidently in the range 30-300 Myr.

In total 43 young stars have been RV-monitored. This number is a trade-off between the will to have a statistically significant sample and the need to collect a number of spectra sufficient to detect a planet RV-signature and estimate the orbital parameters. An extensive search for literature and archives data has been done to collect all possibly useful information on the sample (Sections 2 and 3).

Chapter 5: The observational campaign has been performed with the TLS-Tautenburg 2m telescope equipped with an high resolution Coudé Echelle Spectrograph (Section 1). With the adopted setup, the spectral range from 4700 to 7400 Åis covered with a resolving power of R=67000.

A total of ∼2000 spectra have been taken, spanning the period from 2001 to 2006. Depending on the stellar brightness, exposure times between 5 and 30 minutes have been used; typical S/N per spectral bin of a few tens are so obtained (Section 2).

The data reduction has been performed using the IRAF software (Image Reduction and Analysis Facility). The preliminary work is done with the noao.imred.ccdred IRAF package; the actual echelle spectra reduction is performed with a set of specific tasks implemented in the noao.imred.echelle package (Section 3).

Chapter 6: High precision RV measurements are achieved with the Tautenburg telescope by means of the iodine-cell technique. It consists of superimposing to the stellar spectrum a large number of narrow absorption lines which provide both a simultaneous very accurate wavelength reference frame and a specification of the instrumental profile. The iodine-cell technique and RADIAL, the software used to determine the radial velocities, are described in Section 1.

An analysis of the errors on the RV measurements and how they depend on the relevant stellar parameters (magnitude, rotational velocity) is performed. For most of the surveyed stars, errors of ∼10 m s^{-1} are achieved.

Chapter 7: One of the results of the RV monitoring has been the finding of 7 spectroscopic binaries. 4 of these objects were unknown as binaries before the RV survey and for 3 of them the spectroscopic orbital parameters have been derived (Section 1).

For the remaining 36 stars, a preliminar general analysis of the RV variability serves to demonstrate that the detection of planets, by use of the RV technique, is practicable also for young stars (Section 2). The existence of periodic RV variations, as a signature of possible orbiting companions, has been investigated by calculating periodograms (Section 3). In addition, as a way to support or discard the presence of a planet, photometric time-series have been checked. In particular, for all the star in the sample but one, Hypparcos satellite photometric data were available (Section 4).

The examinations of two interesting objects are reported in detail. HD41593 shows RV variations with period P$\sim$4 days compatible with the presence of a planet of minimum mass $M_p \sin i$=0.16 M_J on an eccentric orbit (e=0.25). However, given the relatively high numbers of RV outliers, HD41593 can presently only be considered as a candidate planet host star (Section 5). The case of HD171488 shows well how activity can affect RV measurements. A periodic signal with P$\sim$1.3 days is found, but this is known to be the stellar rotational period from photometric surveys as well as Doppler imaging (Section 6).

Although no evident planet detections have been achieved, the RV data sets allow to put stringent upper limits to the existence of planets orbiting the surveyed stars. For this purpose a series of Monte Carlo simulations have been performed, exploring the planet period-mass plane in the ranges P=0.7-800 days and $M_p \sin i$=0.05-30 M_J. As a result, we can exclude, for example, a planet with P=10 days and $M_p \sin i$=1 M_J for 77% of the stars in the sample, to a 99% confidence level, and a planet with P=300 days and $M_p \sin i$=3 M_J for 66%.

Chapter 8: The main conclusions that can be drawn from the thesis work are discussed in this chapter. The survey has demonstrated that the RV technique for the detection of extrasolar planets can be succesfully applied also to young stars, in spite of their enhanced level of activity.

The non-detection of planets around the surveyed sample is statistically compatible with the frequency of planets around old solar type stars, which is estimated to be $\sim$7 % ($\sim$1 % for hot Jupiters). This result goes against the ventilated idea that young stars could have a much larger population of very massive close-in planets than old stars.

Contents

Chapter 1

Extra-solar planets

1.1 Introduction

The search for planets orbiting stars other then our own Sun is a branch of astronomy that has undergone an impressive development in the last fifteen years and that promises to be protagonist on the science stage for the decades to go. The reason for such an interest crosses the boundaries of astronomy addressing fundamental questions that accompany the human kind since ever: What is our *position* in the Universe, and are we alone?

In every civilization people meet the need to have a representation of the surrounding world, that is to create a cosmological model. For instance, the Babylonians believed the Earth to be a big circular plane surrounded by a river beyond which lies an impassable mountain barrier, with the whole thing resting on a cosmic sea. No human may cross the river surrounding the Earth. The mountains support the vault of heaven, which is made of a very strong metal. There is a tunnel in the northern mountains that opens to the outer space and which also connects two doors, one in the East and one in the West. The Sun comes out through the eastern door, travels below the metallic heaven and then exits through the western door; he spends the nights in the tunnel. Aristotle described his cosmological model in *On the Heavens*, the most influential treatise of its kind as it was accepted for almost two millennia. The idea that all bodies, by their very nature, have a natural way of moving is central to Aristotelian cosmology. Some bodies naturally move in straight lines, others naturally stay still. But there is yet another natural movement: the circular motion. Since to each motion there must correspond a substance, there ought to be some things that naturally move in circles. Aristotle then states that such things are the heavenly bodies which are made of a more exalted and perfect substance than all earthly objects. Since the stars and planets are made of this exalted substance and then move in circles, it is also natural, according to Aristotle, for these objects to be spheres too. The cosmos is then made of a central earth (which he accepted as spherical) surrounded by the moon, sun and stars all moving in circles around it. This conglomerate he called "*the world*".

Nowadays we use to confine those beliefs in the province of mithology, religion or philosophy. Since they have no empirical fundaments at all or intermix the observation of natural phenomena with metaphysical concepts, the modern scientists have little use for them in the effort to understand the Universe.

A milestone in the road to the current conception of the Universe is represented by

the "Copernican revolution". Copernicus in his *De revolutionibus orbium coelestium* (1543) dismantled the mankind's belief to be the centre of the Universe, downgrading the Earth to just one of the planets orbiting the central Sun. Giordano Bruno, though he was a philosopher rather than a scientist, embraced the Copernicus's ideas and took them even further. In the *De l'infinito Universo et mondi* (1584) he claimed that the Universe is infinite in size and filled with stars which are nothing but other suns, each surrounded by planets. Bruno paid the highest price for the affection to his beliefs and his books were placed upon the Index by the Inquisition, nevertheless his ideas outlasted.

About one century later Isaac Newton approved for printing the *Philosophae Naturalis Principia Mathematica* (1687), where he enunciated the "universal" law of gravitation. Following the Newton's ideas, Immanuel Kant laid out the Nebular Hypothesis (*Allgemeine Naturgeschichte*, 1755), and deduced that the Solar System formed from a large cloud of gas. Pierre-Simon Laplace indipendently presented a similar theory in the *Exposition du système du monde* (1796). The Kant-Laplace hypothesis of coupled star and planet formation seemed reasonable, along with its inplication that planetary systems may be as abundant as the stars themselves (see Figure 1.1, middle right).

During the nineteenth century the debate on the plurality of worlds went on. William Whewell published in 1853 *Of a plurality of Worlds: An Essay* , the most influential antipluralist treatise of the century. On the other hand, also enthusiastic supporters of ubiquitous life in the Universe, like Camille Flammarion (*Pluralitè des mondes*, 1862) and Richard A. Proctors (*Other Worlds Than Ours*, 1870), found many disciples. Although all these authors professed a merely scientific approach to the matter, in fact they often turned to teleological or methaphysical arguments to give strength to their conclusions. Indeed, at the beginning of the twentieth century, still Alfred R. Wallace wrote: *Our position in the material universe* (see Figure 1.1, bottom left) *is special and probably unique, and ... it is such as to lend support to the view, held by many great thinkers and writers today, that the supreme end and purpose was the production and development of the living soul in the perishable body of man* (from *Man's place in the Universe*, 1903).

The next important steps toward the modern view of the Universe occurred around the 1920s. In 1918 Harlow Shapley reported [169], based on his study of the distribution of globular clusters of stars, that our solar system was located at the periphery of the Milky Way, which by itself became larger than the Wallace's Universe. In 1926 Edwin P. Hubble showed [83] that many other galaxies exist outside our own, further increasing the size of the known Universe. The most diffused opinion since then is well expressed in the Harold Spencer Jones's words: *We see the Earth as a small planet, one member of a family of planets revolving round the Sun; the Sun, in turn, is an average star situated somewhat far out from the centre of a vast system, in which the stars are numbered by many thousands of millions; there are many millions of such systems, more or less similar to each other, peopling space to the farthest limits to which modern exploration has reached. ... Can it be that throughout the vast deeps nowhere but on our own little Earth is life to be found? ... it would seem inherently improbable that our small Earth can be the only home of life.* (from *Life on other Worlds*, 1940).

Peter van de Kamp began in 1938 a long-term program to search for low mass companions of nearby stars, by means of accurate astrometric measurements. The telescope to be used for this program was the Sproul Observatory's 24-inch refractor.

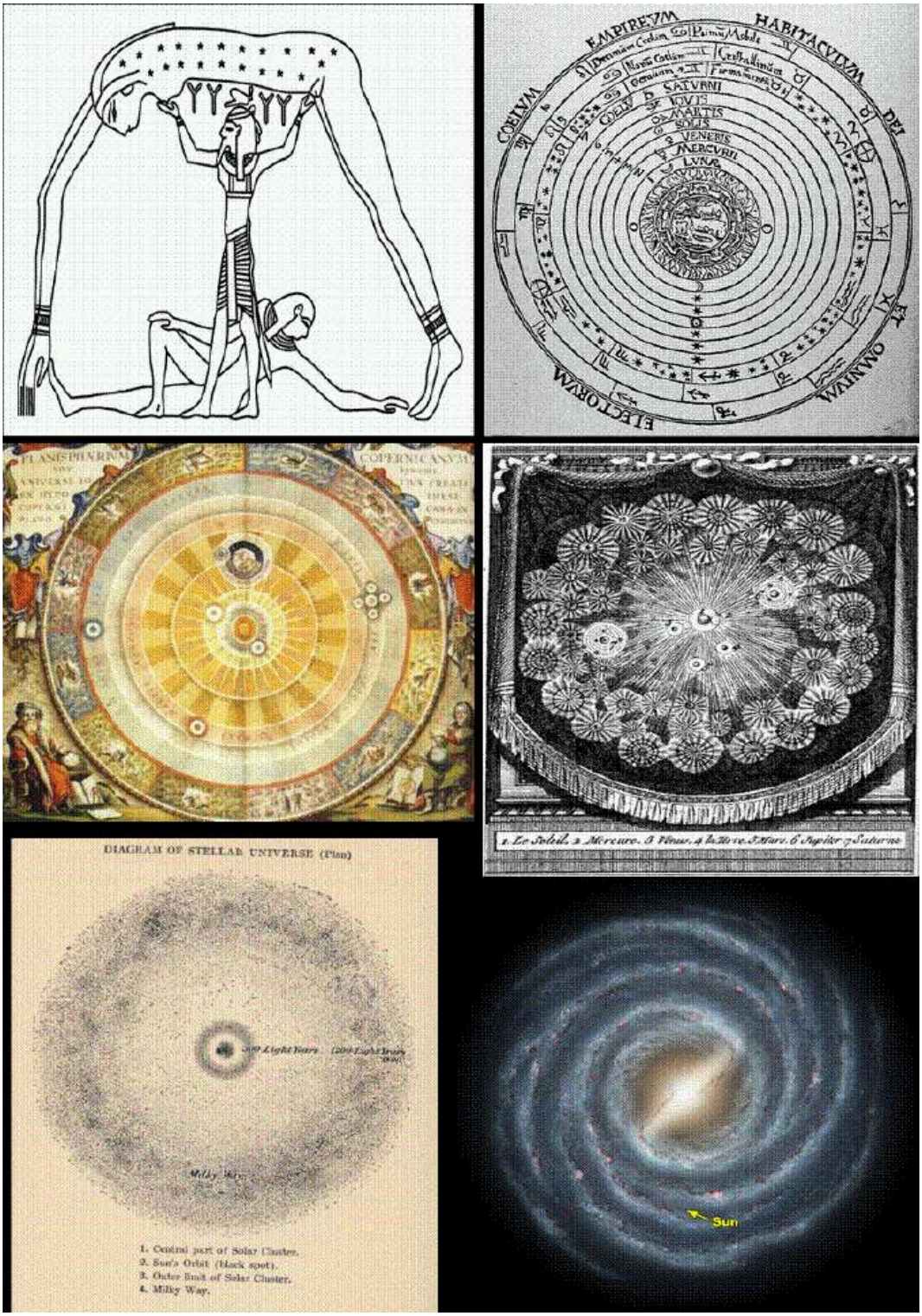

Figure 1.1: **Top left:** Egyptian Cosmology. Shu, the god of the air, upholds Nut, the sky-goddess, while Geb, the earth-god, reclines under Nut. **Top right:** The Christian Aristotelian cosmos, engraving from Peter Apian's *Cosmographia*, 1524. **Middle left:** The Copernican System, from Andrea Cellarius's *Harmonia Macrocosmica*, 1661. **Middle right:** Frontispiece to the 1784 London edition of *Entretiens sur la pluralité des mondes* from Bernard Le Bovier de Fontenelle, 1686. **Bottom left:** Diagram of the stellar Universe according to Alfred Russel Wallace, *Man's place in the Universe*, 1903. **Bottom right:** Schematic representation showing the position of the Sun in the Milky Way, one of the billion galaxies populating the Universe, on the basis of the XX century cosmology.

1.2 Detection techniques

This section is devoted to concisely reviewing the techniques that have been exploited by now to achieve the detection of exoplanets. The merits and limitations intrinsic to the different methods will be discussed and the major observational results reported.

1.2.1 Direct imaging

Imaging of an exoplanet generally refers to the finding of a faint point source image in the proximity of the parent star. This is perhaps the most intuitive method to discover a planet and it offers many advantages. In principle it could bring to the detection of a multiple planetary system with a single image and, by measuring the absolute magnitude in different bands, allow to estimate the surface temperature and the size of the planet. If the stellar parallax is known, the projected planet-star distance can also be determined. Moreover, a monitoring spanning over the orbital revolution time-scale would lead to the knowledge of the orbital parameters (eccentricity, inclination) as well as the mass of the planet.

Direct imaging, however, presents challenging technical problems to be solved. An example can well illustrate the case. The Jupiter to Sun luminosity ratio is $L_J/L_\odot \sim 10^{-9}$ and a Sun-Jupiter system at a distance of 10 pc would be seen at a maximum angular separation of 0.5". Therefore, even under ideal sky seeing conditions, the planet light would be immersed in the stellar photon noise.

Efforts have been directed to both improve the spatial resolution of ground-based telescopes and lower the star to planet luminosity contrast. Adaptive optics (AO) systems [7] are presently able to correct for the image blurring caused by the atmospheric turbulence pushing the telescope angular resolution almost to the diffraction limit. Remarkable examples are the NACO system installed at the VLT 8m telescopes [160], ALTAIR at the Gemini North 8m telescope [176] and NGS at the Keck 10m telescopes [191]. Coronographic masks placed on the focal plane are effectively used to reduce the light coming from the central star [110]. To diminish further on the brightness ratio, observations are usually carried out in infrared wavelengths where the planet thermal radiation peaks. Additionally, higher dynamic range images can be obtained by summing up many single exposure frames. Nakajima et al. [135] list the performances of all the existing AO systems; the dynamic range of the better system, NACO+SDI (Simultaneous Differential Imaging), is ΔH=11.2 at 0.5" which is still far away from the ΔH=22.5 needed for the Sun+Jupiter system at 10 pc.

A few surveys have been done, and others are ongoing, to image sub-stellar companions. In order to increase the detection probability, mainly young nearby stars have been targeted. In fact, according to theoretical calculations [30], a 1 Myr old planet is up to 10^3 times brighter than when it is 1 Gyr old.

Neuhäuser et al. [137] report of a companion of the young ($\leq$2 Myr) classical T Tauri star GQ Lup at 140$\pm$50 pc (see Fig. 1.2). GQ Lup B is located 0.7" west of GQ Lup A, corresponding to a projected physical separation of 100$\pm$35 AU. Using different evolutionary theoretical models, the GQ Lup B mass lies between 1 and 42 Jupiter masses. Chauvin et al. [38] have discovered a planet orbiting the brown dwarf 2MASSWJ1207334-393254, member of the 8 Myr old TW Hydrae Association. They claim the mass of that planet to be 5 M_J or less. Indeed, these two discoveries have made clear which are at the moment the main limitations inherent to the the direct imaging

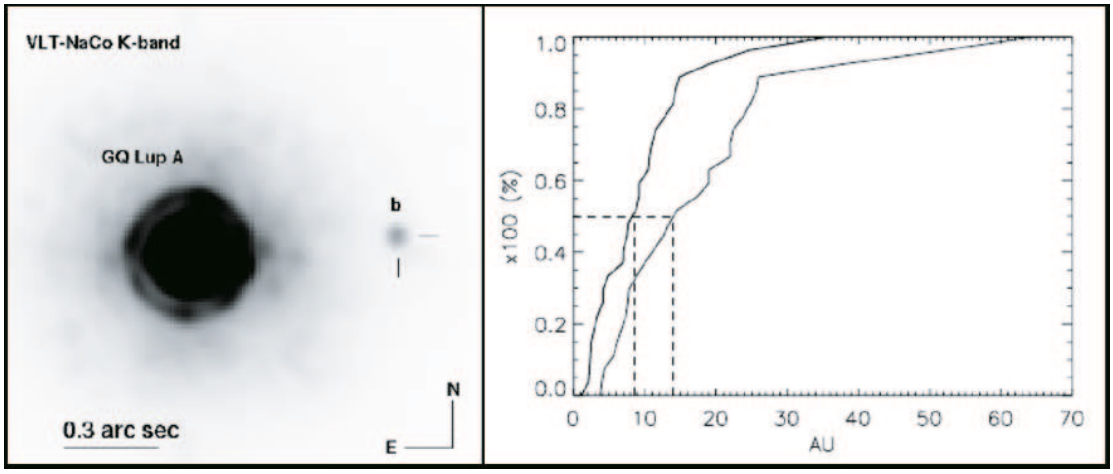

Figure 1.2: **Left:** Adaptive-optics image of GQ Lup and its 6 mag fainter planet candidate companion. (From Neuhäuser et al. 2005 [137]). **Right:** Cumulative distribution function of the detection limit as a function of the planet orbital separation for a sample of 28 nearby young stars. This distribution implies that in 50% of the cases (median value) there are no $5M_J$ planets at distances larger than 14 AU and no $10M_J$ planets at distances larger than 8.5 AU. In 100% of the cases, these values increase to 36 and 65 AU, respectively. (From Masciadri et al. 2005 [115]).

technique. Detections are possible only for companion with large orbital semi-major axis and with correspondingly very long orbital periods. This circumstance makes practically impossible to determine the orbital parameters and calculate a dynamical mass for the companion. By now masses can only be estimated relying on theoretical evolutionary tracks which are very uncertain and essentially untested.

However, apart from those two detections, surveys have called attention to the short-age of sub-stellar companions on wide orbits. McCarthy & Zuckerman [121] monitored, with the Keck telescope, 102 nearby G, K and M stars with a typical age of 300 Myr. They report a frequency of 1±1% for brown dwarfs companions (masses between 12 and 75 M_J) at 75 to 300 AU. For a subsample of 42 stars observations were sensible enough to detect exoplanets in the mass range 5-12 M_J at 75 to 300 AU, but no planet was found. Masciadri et al. [115], using NACO at VLT, observed 28 nearby K and M stars ∼10-200 Myr old. Although they have better sensitivity compared with previous studies (see Fig. 1.2) they did not find any planet.

1.2.2 Astrometry

The motion of a planet around a star causes the star to undergo a reflex motion about the star-planet barycentre. This results in the periodic perturbation of stellar observables thus offering the opportunity for indirect detections of planets.

The path of a star around the star-planet barycentre appears projected on the plane of the sky as an ellipse with angular semi-major axis β (in arcsec) given by:

$$\beta = k\frac{M_p}{M_*}\frac{a}{d} \tag{1.1}$$

where M_p and M_* are tle planet and star mass respectively in common units, a is the semi-major orbital axis in AU and d is the stellar distance in pc. The factor k can vary between $\sqrt{1-e^2}$ and 1 depending on the orbital spatial orientation, where e is the orbital eccentricity.

Jupiter orbiting the Sun viewed from a distance of 10 pc would produce an astrometric signature only ∼0.5 milliarcsec (mas) in amplitude. Atmospheric turbulences make extremely difficult to achieve such a precision with ground-based observations. Attempts have been made from the space to confirm planets detected with the radial velocity method. The Hipparcos satellite, which provided 1 mas accuracy, failed to detect any planet, only serving to derive loose upper limits to their masses ([151], [119], [211]). Benedict et al. [18] used the Hubble Space Telescope with the fine guidance sensor to observe Gliese 876, a 0.3 $M_\odot$ star at 4.7 pc, known from radial velocity measurements to have a planet with period P=61 days. Properly scheduling the observations near the companion peri- and apastron, after subtracting the proper motion (1174.2±5.4 mas yr^{-1}) and the parallax (214.6±0.2 mas) contribution to the stellar motion, they have found a residual perturbation with an amplitude of 0.25±0.06 mas. From that they can estimate the orbital inclination angle i=84°±6° and the planet mass M_p=1.9±0.5M_J.

1.2.3 Radial velocities (RV)

The radial velocity variations that a planet induces on the parent star are described by the following set of equations:

$$RV(t) = \gamma + K\left(\cos\left(\omega + \nu(t)\right) + e\cos\omega \right) \tag{1.2}$$

$$K = \left(\frac{2\pi G}{P}\right)^{1/3} \frac{M_p \sin i}{(M_p + M_*)^{2/3}} \; \frac{1}{(1-e^2)^{1/2}} \tag{1.3}$$

$$\tan\left(\frac{\nu(t)}{2}\right) = \left(\frac{1+e}{1-e}\right)^{1/2} \tan\left(\frac{E(t)}{2}\right) \quad ; \quad \frac{2\pi}{P}(t-\tau_0) = E - e\sin E \tag{1.4}$$

In the Eq. (1.2) γ is the radial velocity of the star-planet barycentre; K is the semi-amplitude of the RV variations; ω is the longitude of periastron; ν, the true anomaly, encompasses the time dependence; and e is the orbital eccentricity. Eq. (1.3) points out the way K depends on the orbital period P, the planet mass M_p, the stellar mass M_*, the orbital inclination i and the eccentricity. The two equations in (1.4) render explicit how ν changes with time. The first one expresses the relation between ν and the eccentric anomaly E. The second one, known as the Kepler equation, is a transcendent equation. In it, τ_0 represents the epoch of passage to periastron.

Determining the RV orbital solution thus gives access to the planet orbital period and eccentricity. The presence of the $\sin i$ factor in Eq. (1.3) means that orbital systems seen face on (i=0) result in no RV perturbation and that $M_p \sin i$, rather than M_p, can be measured only providing a lower limit to the planet mass. The determination of $M_p \sin i$ also requires an indipendent evaluation of M_*.

The RV method is also suitable for the detection of multiple planetary systems and, as far as the planet-planet gravitational interaction is negligible, the RV curve can be modeled simply adding up the contribution from each planet (see Fig. 1.3).

Using again our solar system as a benchmark, the effect of Jupiter is about K=12.5 m s^{-1} with a period of 11.9 yr, while the Earth is about 0.1 m s^{-1}. Presently RV

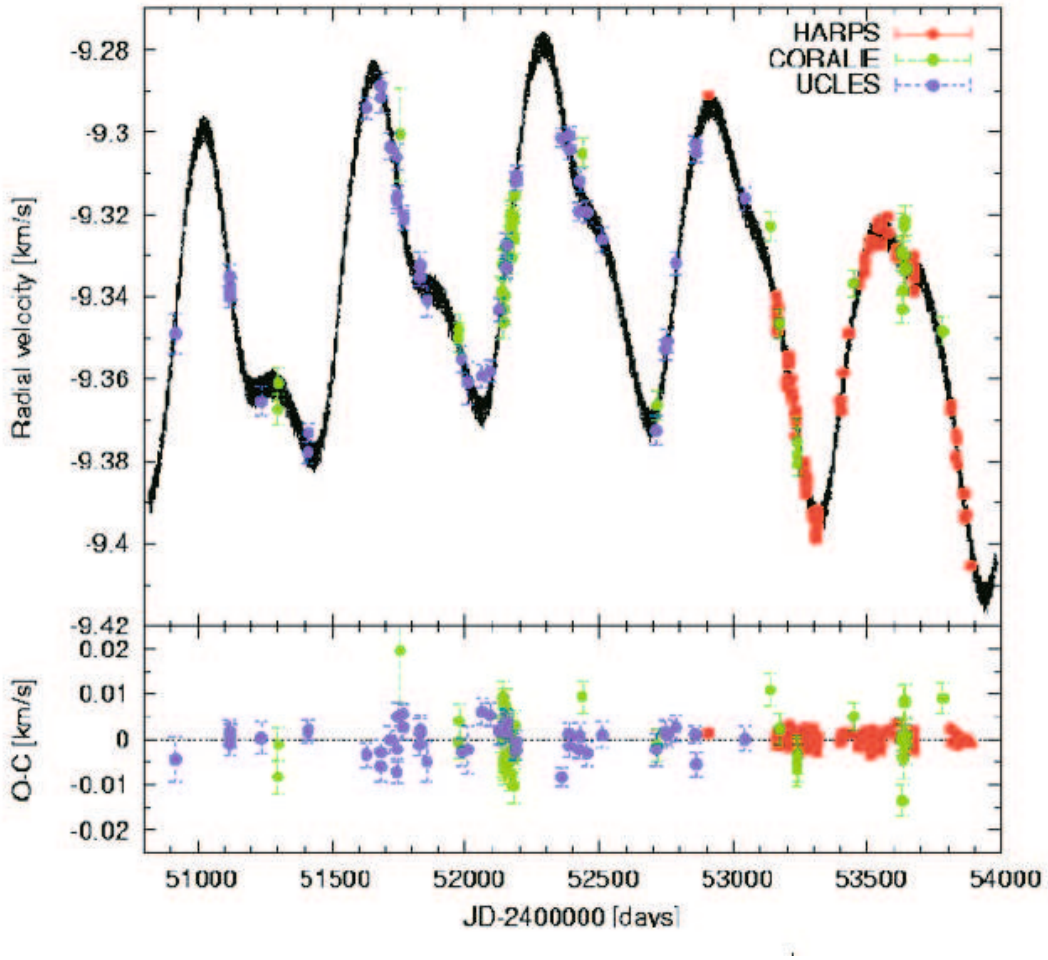

Figure 1.3: RV data set and best-fit curve of the star μ Arae. This is one of the two stars known to be orbited by 4 planets. The very precise RV measurements taken with HARPS allowed to confirm the presence of a forth planet and to obtain a full solution with fixed orbital parameters. (From Pepe et al. [149]).

measurements with precision down to $\sim$1m s^{-1} are achieved and, in fact, almost all the planets known up to now have been detected by means of the RV technique.

The possibility to measure radial velocities relies on the Doppler effect. Stellar RV are obtained estimating the small, systematic change in wavelength of the many absorption lines that make up the star's spectrum. Therefore, in order to reach a few m s^{-1} precision, a very accurate wavelength calibration of the spectra is mandatory (this topic will be examined in detail in Chap 6). Although the RV amplitude is indipendent of the distance to the star, the need for high resolution and high signal-to-noise spectra favors the detection of planets around bright and nearby stars.

Since the discovery of the first exoplanet orbiting a solar type star was announced in 1995 [118], the number of RV-detected planets has being steadily increasing and it recently surpassed 200. Several observational campaigns have been carried out and many others are on-going. ELODIE, a fiber-fed echelle spectrograph with resolving power of R=42000 and 3906$-$6811 Å spectral coverage [13], has been in operation since 1993 at the OHP 1.93m telescope. Some 330 stars have been monitored; they were selected according to the following criteria: visual magnitude $m_V \leq 7.65$, declination $\delta \geq 0$, projected stellar rotational velocity $v \sin i \leq$ 4 km s^{-1}, spectral type from F8 to M0 [150]. A total of 9000 measurements have been performed with average errors of $\sim$8 m s^{-1}, leading to the detection of about 25 exoplanets. CORALIE is an updated version of ELODIE mounted at the 1.2m Swiss Euler Telescope at La Silla ESO, Chile since 1998. CORALIE is monitoring a sample of about 1600 stars in the southern emisphere selected with the same criteria as ELODIE. CORALIE has succeded to detect almost 40 new exoplanets up to now.

More than 100 planets are the yield of the California & Carnegie Planet Search. This international collaboration uses the HIRES spectrograph [196] at the 10m Keck telescope [31], the Hamilton Echelle spectrograph at the Shane 3m Lick telescope [195] and the UCLES spectrograph on the 4m Anglo-Australian telescope at Siding Spring Observatory [43]. Using an I_2 gas absorption cell as the reference velocity metric, RV accuracy of 3$-$10 m s^{-1} have been achieved [111]. The target stars of this multisite survey were about 1000 nearby (d$\lesssim$100 pc), low-mass (0.7 M$_\odot \lesssim$ M$_* \lesssim$ 1.5 M$_\odot$), bright ($5 \lesssim m_V \lesssim 9$), old (2 Gyr $\lesssim$ Age $\lesssim$ 10 Gyr), slowly rotating ($v \sin i \lesssim$5 kms^{-1}) stars [190].

There are many other observational facilities used to attempt the detection of exoplanets measuring high precision radial velocities. Following is a list comprising the principal ones:

- **AFOE** (Advanced Fiber-Optic Echelle) spectrograph at the 60 inches of the Whipple Observatory (from 2005 moved to the 100 inches Hooker Telescope at the Mt. Wilson Observatory);

- **Cross-Dispersed Echelle Spectrometer** at the 2.7m Harlan J. Smith Telescope;

- **Coudé Echelle Spectrograph** at the 2m Alfred-Jensch-Teleskop of the TLS Tautenburg Observatory (see Chapter 5);

- **CES** (Coudé Echelle Spectrograph) at the ESO La Silla 3.6m telescope, now replaced with HARPS;

- **HARPS** (High Accuracy Radial velocity Planetary Search) at the ESO La Silla 3.6m telescope. HARPS, which became available to the astronomical community

in October 2003, is at the present time the most accurate instrument for RV measurements achieving a $\sim$1 m s^{-1} precision;

- **HRS** (High Resolution Spectrograph) at the 10m Hobby-Eberly Telescope;

- **MIKE** (Magellan Inamori Kyocera Echelle) spectrograph at the 6.5m Clay Magellanic telescope.

- **Sandiford Cassegrain Echelle Spectrometer** at the 2.1m Otto Struve telescope;

- **SOPHIE** is a cross-dispersed echelle spectrograph that since August 2006 has replaced ELODIE on the OHP 1.93m telescope;

- **SARG** (Spettrografo Alta Risoluzione Galileo) at the 3.6m TNG telescope;

- **UVES** (Ultraviolet and Visual Echelle Spectrograph) at the VLT UT2 telescope.

1.2.4 Timing

The stellar wobble induced by a companion causes changes in thelight travel time across the orbit. The great accuracy attainable for time interval measurements would make possible the detection of very low mass planets, if only a timing reference on which to base such measurements were available. Unfortunately, there is only few types of stellar sources known where this method is viable, i.e. pulsars and white dwarfs

Pulsars are rapidly spinning neutron stars that emit narrow beams of radio emission parallel to their magnetic dipole axis, seen as pulses at the object spin frequency due to a misalignement of the magnetic and spin axes. Millisecond pulsars are extremely accurate frequency standards, with periods changing only through a tiny spin-down at a rate $\sim 10^{-19}$ s s^{-1} [11].

The first extra-solar planetary system discovered was found around the 6.2 ms pulsar PSR1257+12 (d$\sim$500 pc) with two companions having masses of 4.3 and 3.9 $M_\oplus$ and periods of 66.5419 and 98.2114 days respectively [207]. Although a number of alternative ways of producing the observed timing residuals were examined, the planetary hypotheses received a compelling confirmation when the foreseen mutual gravitational perturbations between the two planets were observed as microsecond variations of the arrival times of radio pulses [95]. Further analysis revealed the existence of a third planet with a mass as low as 0.020 $M_\oplus$ on a P=25.262 days orbit.

With the exception of PSR B1257+12, no planetary companion have emerged from the precise timing of 48 Galactic millisecond pulsars, [108] suggesting that these systems have to be rare.

A subset of white dwarf stars, namely hDAV (hot DA Variable) stars, exhibit variability with extreme amplitude and frequency stability. Well monitored hDAVs show a drift rate less than a few times 10^{-15} for the most stable modes [133] . Mullally et al. [133] surveyed some 30 targets but as of now no planet orbiting a white dwarf has been confirmed.

The timing technique has been successfully applied to detect recently a $M \sin i$=3.2 M_J planet orbiting the extreme horizontal branch star V391 Peg, at a separation of 1.7 AU, with a period of 3.2 yr [172].

1.2.5 Transits

A further possibility to detect a planet is by measuring the brightness attenuation that occurs when by chance the planet transits across the stellar disk. The geometric probability of a transit, for a circular orbit, is

$$p = \frac{2}{\pi} \arcsin\left(\frac{R_* + R_P}{a}\right) \tag{1.5}$$

where R_* and R_P are the star and planet radii respectively and a is the semi-major orbital axis. For instance, for a Sun-Jupiter system it is p=6×10^{-4}, while for the close-in planet orbiting the star HD209458 p=0.08 . Transits of planets on wide orbits are not only rare but even more difficult to observe since the fractional duration of the transit is $\Delta t/P \propto p$.

The luminosity drop produced by a planet on the line of sight of the star is

$$\frac{\Delta L}{L_*} \simeq \left(\frac{R_P}{R_*}\right)^2 \tag{1.6}$$

In fact, the effect depends on the local surface brightness of the star, which decreases moving outwards from the center of stellar disk, due to the limb darkening [165]. Values of $\Delta L/L_*$ for the Earth and Jupiter transiting the Sun are 8.4×10^{-5} and 1.1×10^{-2} respectively.

Radial velocity surveys of dwarf stars have revealed the unexpected existence of a class of extrasolar massive planets with orbital separations of $a \lesssim 0.1$ AU. Such planets, having a $\sim$10% probability to transit their parent stars, raised the attention for photometric monitoring of large stellar samples. If both radial velocities and transits are observed, the orbital inclination uncertainty can be solved providing with a precise estimation of the planet mass. Moreover, if the stellar radius is known, the planet radius can also be evaluated, which in turn allows to calculate the average density and the surface gravity of the planet. Thus first constraints on structural and atmosphere models for low mass objects can be assessed.

The first transiting planet was discovered in 1999 around the star HD209458 [36], already known to have a planet from RV measurements (see Fig. 1.4). The commonly adopted strategy for detecting planetary transits consists in observing regions of the sky with high stellar surface density using telescopes with large fields of view. As a result of the photometric monitoring of hundreds of thousands of stars, 14 transiting planets are presently known.

Observations at infrared wavelengths may detect the secondary eclipse as the planet passes behind the star. Two of such detections have been recently achieved by means of Spitzer Space Telescope photometric time series for HD209458b [40] and TrES-1 [35]. These detections leaded to the first estimation of effective temperature and albedo for a planet.

The COROT satellite, which was succesfully launched on december 2006, will allow the detection of a conspicuous number of transiting planets [5]. The relative photometric precision achievable by COROT from the space is of the order of 10^{-4} , far better than ground-based observations. Such a precision will make affordable the detection of smaller planets down to the Earth radius. Observing continously the same field for 5 months (at least 6 fields will be monitored during the mission life time), with COROT planets with period up to $\sim$50 days could be discovered [26]. More than 60000 stars, with V magnitude between 12 and 15.5, will be surveyed.

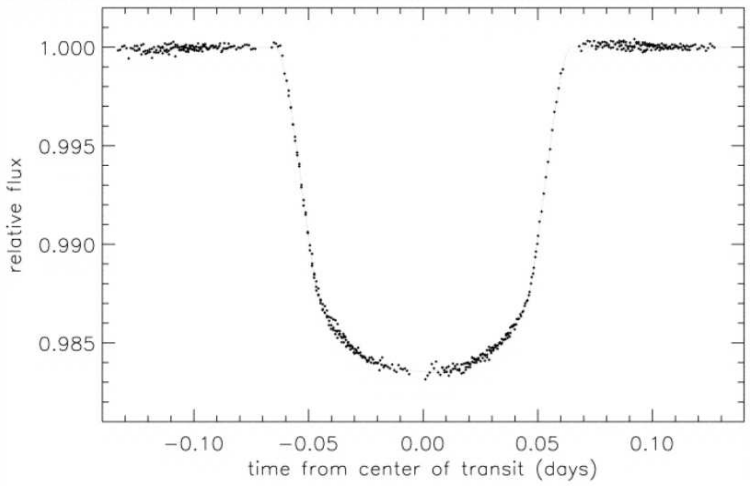

Figure 1.4: Phase-folded (P=3.52474 days) light curve of the transit of the planet of HD 209458. Observations were made with STIS spectrograph on the Hubble Space Telescope achieving a photometric relative precision of $\sim 1.1 \times 10^{-4}$. (From Brown et al. 2001 [29]).

1.2.6 Microlensing

Gravitational lensing is the focusing of light rays from a distant source due to a massive object, the lens, intervening on the line of sight. Microlensing refers to the intensity amplification of the source image as a result of the focusing of many unresolved micro-images.

Relative motion between the source, the lens and the observer leads to a brightening and subsequent dimming of the image, whose magnification factor A and time-scale t_m depend on the particular geometry of the lens-source system. For stellar sources and lenses in the Galactic bulge and halo, typical values are A=10 and t_m=40 days.

If the lens star is orbited by a planet, the light curve shows a caracteristic feature (see Fig. 1.5). The microlensing method has the sensitivity to detect planets with masses down to 1 $M_\oplus$ and less. However it has also many drawbacks. Microlensing events are rare; stars in the Galactic bulge have a probability of $\sim 10^{-6}$ to be lensed at any time [140]. Specific systems cannot be selected for study and furthermore the lens star is often too faint for follow-up observations aimed to better characterize the system. Analysis of the light curve gives access only to the planet to star mass ratio and the projected angular separation and, due to the many parameters needed to model the curve, the best-fit solution is not always unique.

Up to now four exoplanets have been announced, all of them initially detected by the OGLE survey (Optical Gravitational Lensing Experiment) [188]. Follow-up observations were then carried out by networks of telescopes like PLANET (Probing Lensing Anaomalies NETwork) [46] .

Fig 1.5 shows the light curve for OGLE-2005-BLG-390, a M-type star with a mass of 0.22 $M_\odot$ located at a distance of about 6500 pc. OGLE-2005-BLG-390b, with a mass of 5.5 $M_\oplus$, is up to now the lightest planet known to orbit a main-sequence star [16].

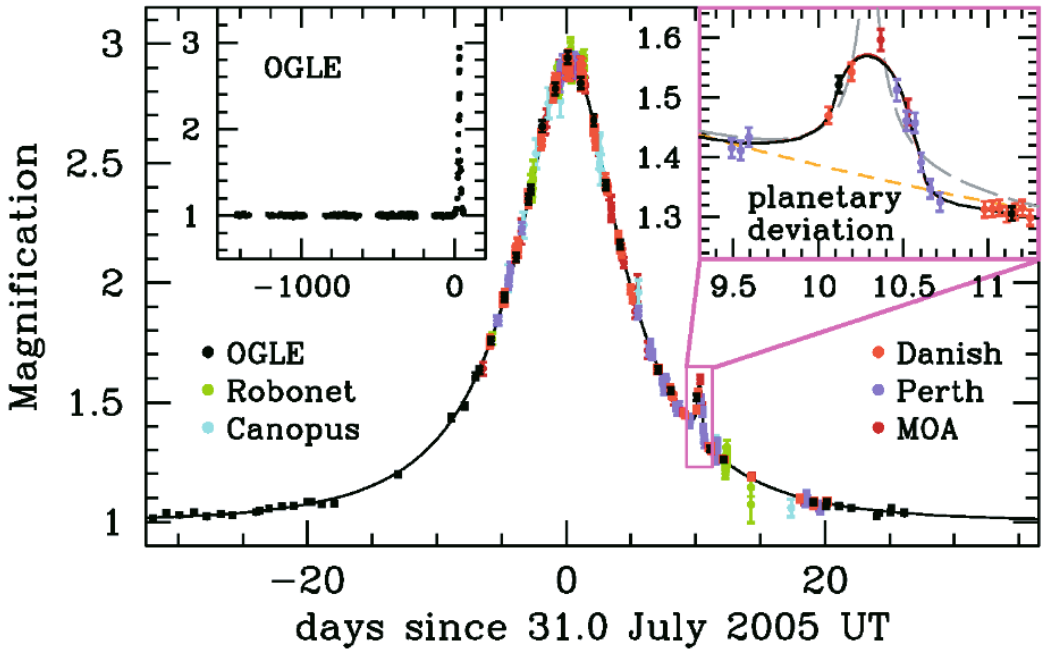

Figure 1.5: The observed light curve of the OGLE-2005-BLG-390 microlensing event and best fit model plotted as a function of time. The top left inset shows the OGLE light curve extending over the previous 4 years, whereas the top right one shows a zoom of the planetary deviation, covering a time interval of 1.5 days. The solid curve is the best lens model with a planet-to-star mass ratio of q=7.6±0.7×10^{-5}, and a projected separation d=1.610±0.008 R_E (where R_E is the Einstein ring radius). The dashed grey curve is the best binary source model that is rejected by the data, while the dashed orange line is the best single lens model. (From Beaulieu et al. [16]).

1.3 Observational properties

[1]

The discovery of now more than 200 planets makes it possible to establish statistical properties for extrasolar planetary systems. However one has to pay attention to the way observational biases can affect the derived characteristics of the planet population.

A main issue is the fact that almost all the planets have been detected by means of the RV method. In fact, in order to fully exploit the potentiality of the method [164], all the major RV survey focused on solar-like stars, i.e. old, main-sequence, G and K spectral type, dwarf stars. The mass distribution for the stars known to host planets (Fig. 1.6), as well as the stellar spectral type distribution (Fig. 1.7), reflect this circumstance.

The frequency of stars hosting planetary systems is a fundamental issue to address [102]. However, since different surveys probed different regions in the star+planet space of parameters (masses, period, orbital separation, etc), by now only partial results have been achieved. Marcy et al. [112] find that the fraction of F, G, K stars harboring giant planets with 1 M_J < M < 13 M_J within 5 AU is at least 88/1330 = 6.6%. This is no doubt a lower limit, as planets between 3-5 AU are not efficiently detected due to the limited duration (6-8 years) of the Doppler survey. Endl et al. [50], after surveying a sample of 90 M dwarfs, estimate an upper limit of 1.27% to the frequency of close-in (a <1 AU) jovian planets around M dwarfs. Albrow et al. [6] searched for signatures of planets in 43 microlensing events. As they found no anomalies in the light curves, they infer that less than one-third of the ∼0.3 $M_\odot$ stars that typically comprise the lens population have Jupiter mass companions with semi-major axes in the range of 1.5 AU <a< 4 AU. Transit surveys have been able to put upper limits to the frequency of very short period planets. For instance, Gould et al. [65] (OGLE-III transit surveys toward the Galactic bulge and Carina) report a total of 3 planets detected in the 1-3 day period range among 2062 stars probed, and 2 planets detected among 618 stars probed in the 3-5 day range (for planet radii uniformly distributed over $1<r/r_J<1.25$). Recently, Johnson et al. [87] pointed out a positive correlation between stellar mass and the occurrence rate of Jovian planets ($M_P sin(i)$>0.8 M_J) within 2.5 AU. They estimate percentages of 1.8±1.0% for $M_*<0.7M_\odot$, 4.2±0.7% for $0.7<M_*<1.3M_\odot$ and 8.9±2.9% for $1.3<M_*<1.9M_\odot$.

Spectroscopic studies have demonstrated that stars with extrasolar planets tend to have higher metallicity than stars without detected planets. Fischer & Valenti [54] determined the metallicity ([Fe/H]) for the 1040 FGK-type stars of the Keck, Lick and AAT planet search program. From there, they selected a uniform subsample of 850 stars (see Fig. 1.8) and found that the probability $\wp$ for a star to have a giant planet can be well fit with a power law in the range -0.5<[Fe/H]<0.5:

$$\wp(planet) = 0.03 \times 10^{2.0[Fe/H]} \tag{1.7}$$

Santos et al. [163] previously performed a similar analysis on the CORALIE sample finding qualitatively similar results.

The sample of known extrasolar planets shows a striking variety of physical and orbital characteristics. In contrast to what is observed in the solar system, Jupiter-mass planets have been found orbiting their parent stars with periods down to P=1.2 days

[1] Most of the data reported in this section have been extracted from "The Extrasolar Planets Encyclopaedia" website (http://exoplanet.eu) which is an extensive and continuously updated source of information on the exoplanet topic.

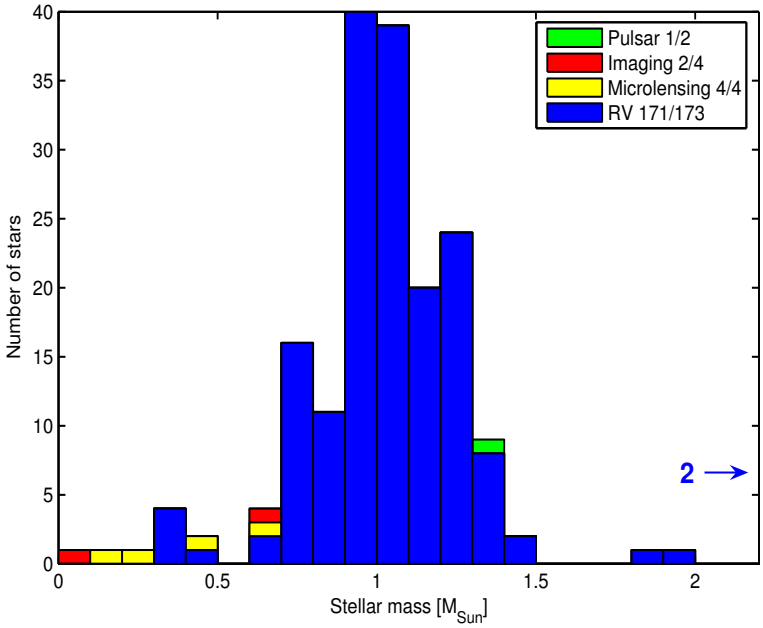

Figure 1.6: Histogram of the masses of the stars hosting one or more planets. The distribution peaks around m=1 $M_{\odot}$ in consequence of the criteria adopted for the selection of stellar samples in the main RV surveys. The legenda reports, for the different detection methods, the fraction of stars for which the stellar mass is known. Two stars fall beyond the plotted mass range.

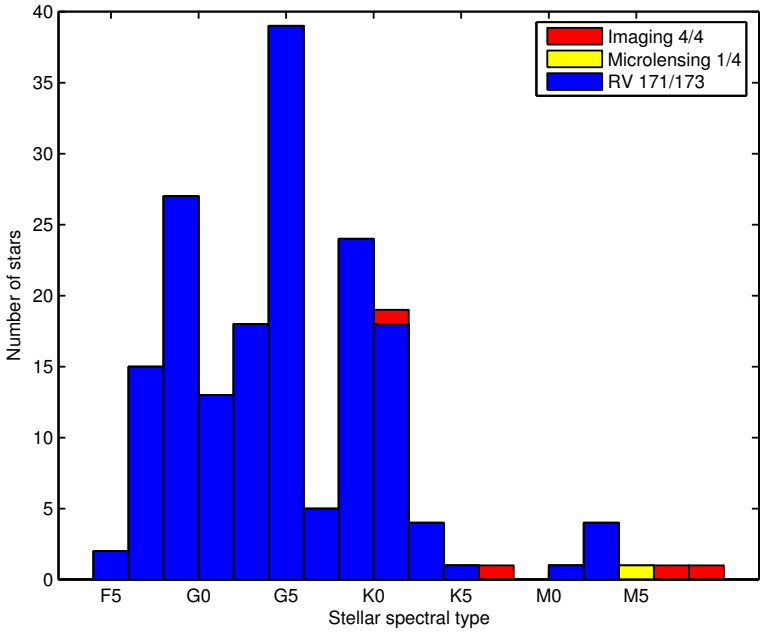

Figure 1.7: Histogram of the spectral type of the stars with planets. G and K type stars have spectra with many more absorption lines than earlier type stars, therefore they are optimal targets for RV surveys. M type stars are difficult because they are faint and show molecular absorption bands.

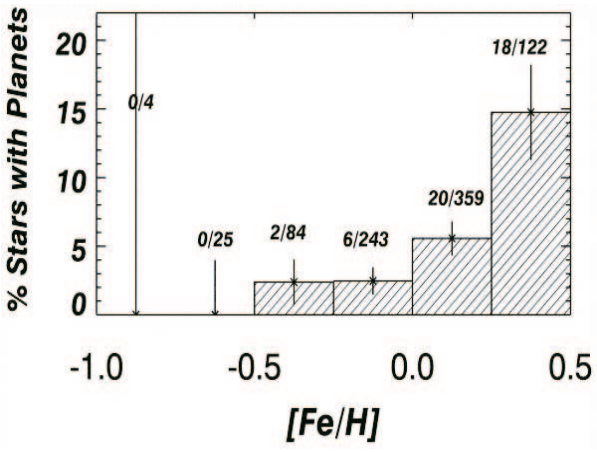

Figure 1.8: The percentage of stars with detected planets rises with iron abundance. In all, a subset of 850 stars were grouped according to metallicity. This subset of stars had at least 10 RV measurements over 4 yr, providing uniform detectability for the presence of planets with velocity amplitudes greater than 30 m s^{-1} and orbital period less than 4 yr. 13 stars have [Fe/H]<-1.0, and no planets have been found around these stars. (from Fischer & Valenti [54].)

and semi-major axes down to a=0.017 AU. For comparison, Mercury has P=88 days and a=0.387 AU. Most of the known planets have quite eccentric orbits, the record being held by HD80606b with e=0.927; the most eccentric planet in the solar system is Mercury[2] with e=0.206. In the rest of this section the main properties emerging from the orbital parameters distributions will be discussed.

Fig 1.9 shows the planet masses as a function of their orbital periods. The sharp drop of planets beyond $P\sim$3000 days reflects the current limit of RV data spanning, thus it is not a genuine observational feature. Remarkably, even though the RV method favors the detection of massive planets, the number ($\sim$130) of planets with $m<2M_J$ is larger than that ($\sim$80) with $2M_J<m<20M_J$. The fact that only minimum masses are measured with the RV technique does not chamge this result. Another noteworthy aspect is that massive planets ($m>2M_J$) tend to lie on wider orbits; only 13 out of 77 have a period $P<$100 days (7 out of 70 if we exclude planets orbiting stars in double systems).

Fig. 1.10 displays how the known planets spread on the eccentricity-period plane. The distribution presents a loose upper envelope such that the maximum eccentricity rises as the period gets larger. In particular, in the very short period regime ($P\lesssim$3 days), almost all the planets have circular orbits. Halbwachs et al. [71] studied a possible dependence of eccentricity on planet mass but do not find any clear correlation. Similarly they conclude that stellar metallicity is not related with the eccentricity. Halbwachs et al. [71] also compare the period-eccentricity diagram for planet-star systems and star-star systems, showing that planets have less eccentric orbits than binary stars and that the bias against detection of orbits with large eccentricities cannot explain this result.

[2]According to a recent IAU Resolution, Pluto (e=0.248) has no longer to be considered as a planet.

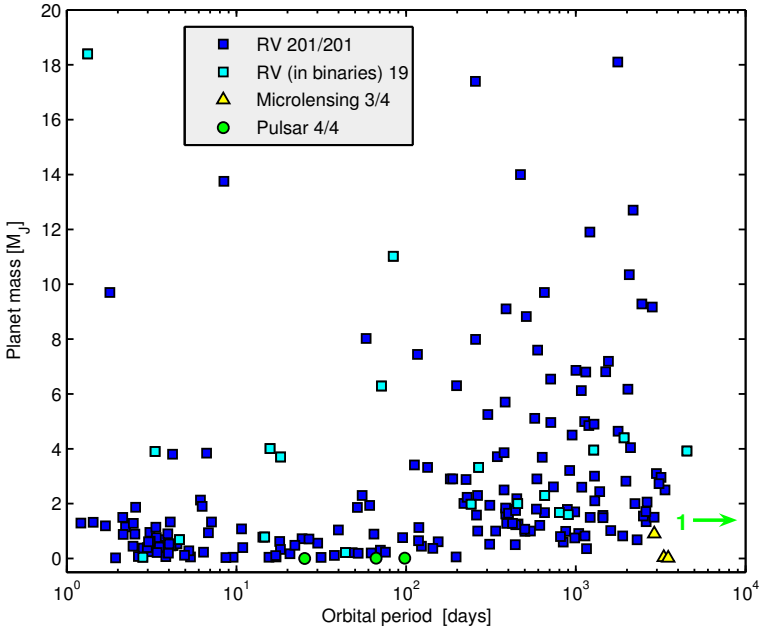

Figure 1.9: Period-mass diagram for the extrasolar planets discovered up to now. For the RV-detected planets minimum mass values are indeed displayed. It is remarkable the shortage of high mass and short period planets that are easiest to find with RV surveys.

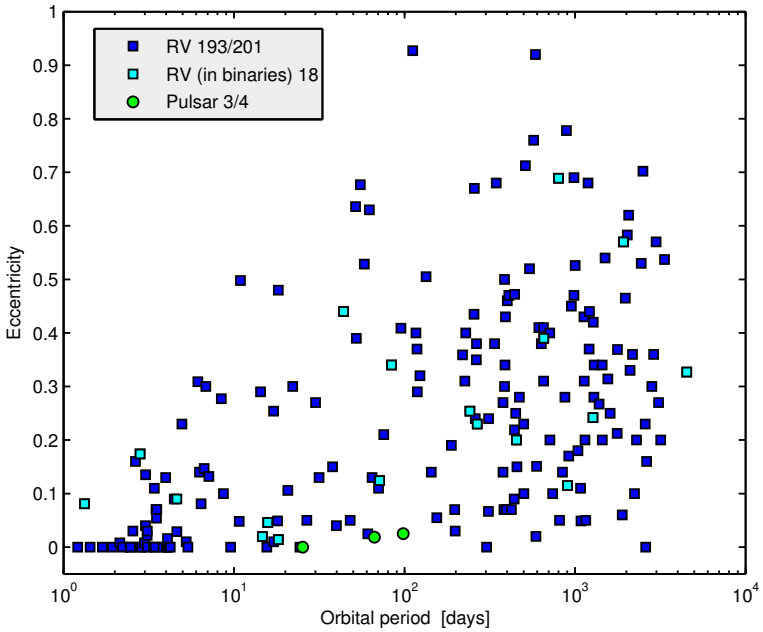

Figure 1.10: Exoplanets eccentricity-period diagram. In contrast to what is seen in our solar system, planets with high eccentricity are common. Very short period planets, however, have circular orbits.

Chapter 2

Formation and evolution of planetary systems

The formation of planetary systems is closely related to the formation of the host star. Therefore, Section 2.1 will first briefly recall the steps of stellar formation leading to a central compact object surrounded by a disk of dust and gas.

The protoplanetary disk is the environment where planet formation takes place. Kant and Laplace first attempted to give scientific form to the idea that planets form out of a disk. While a number of alternative theories have been proposed [208], the disk hypothesis is now generally accepted, being able to explain much of the observational features of our solar system. In fact, in the course of the twentieth century, many authors contributed to develop a thorough theory of planet formation which is known as the "Solar Nebula Theory" (Section 2.2).

The discovery of extrasolar planets forced to revise the standard model. In particular, the existence of close-in jupiter-mass planets was unexpected and several mechanisms causing planets to migrate inward have been invoked (Section 2.3).

2.1 Stellar formation

Stars form by collapse and fragmentation of interstellar clouds of gas and dust grains [170]. Clouds have a typical linear size of 10−100 pc and masses in the range of 10^4−10^6 $M_\odot$. Density perturbations may cause the gravitational binding energy of a certain region of the cloud to exceed its termal energy, in which case the region begins to contract (Jeans instability criterion). Magnetic fields also play a role in slowing the early phases of the cloud collapse [131]. The increased average density then causes smaller fractions of the cloud to become gravitationally bound and the cloud itself undergoes a hierarchical fragmentation process.

Gas cores eventually form that are the actual stellar birthplaces. The frequency of binaries and multiple systems is high [47], [3]. Unfortunately much of the theoretical work to model late stages of star formation has considered only single stars. Star formation can be better understood if the formation of stars in clusters is simulated [15].

The conservation of angular momentum for a collapsing core, even with a modest initial rotation, will lead to a flattened system. The central part of this system, which is not sustained by the centrifugal force, will contract to form an overdense object: the

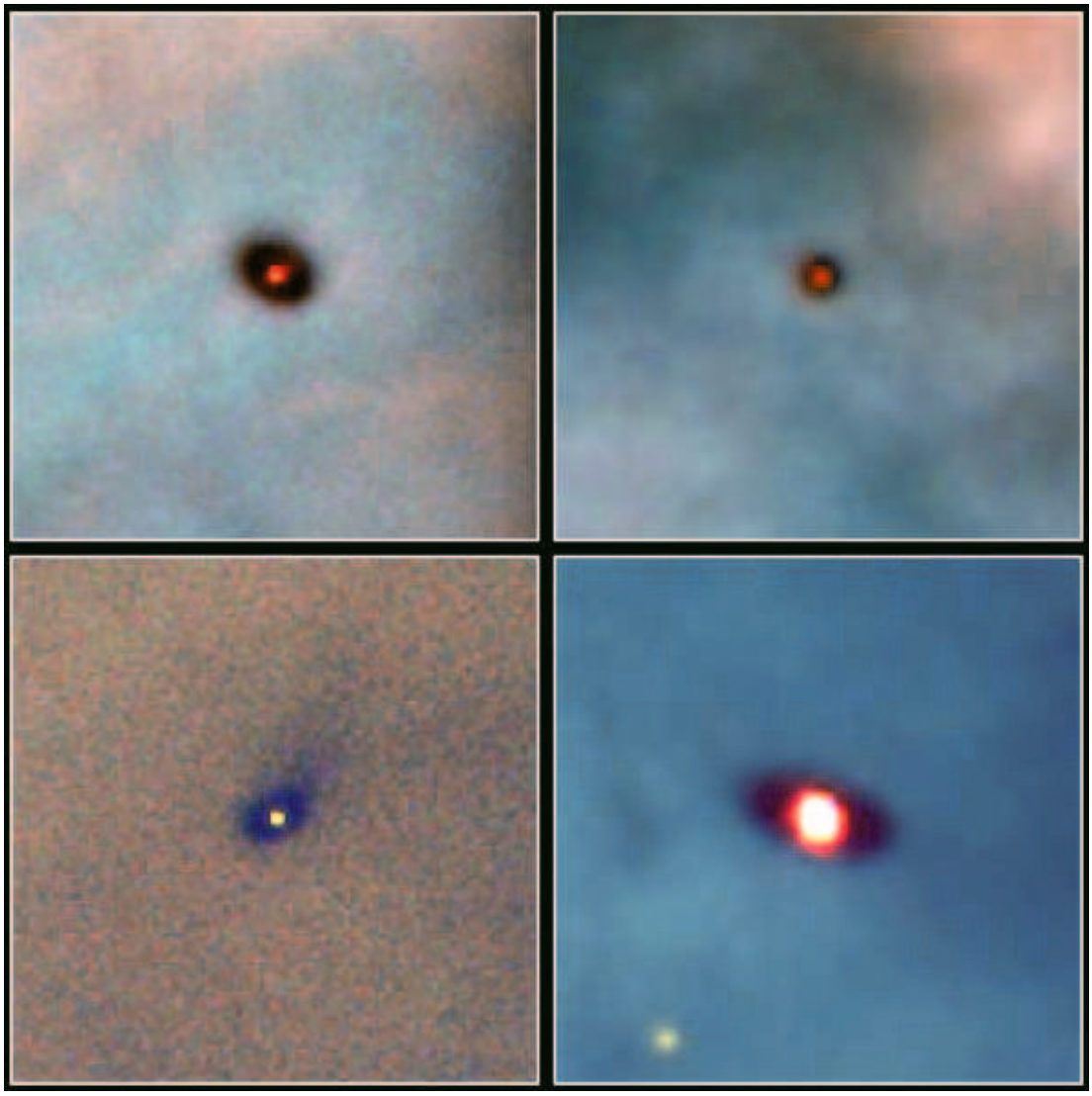

Figure 2.1: Hubble Space Telescope images of four protoplanetary disks around young (∼1 Myr) low-mass (0.3−1.5 $M_\odot$) stars in the Orion Nebula, at a distance of about 450 pc. Images are created combining three different narrow-filter exposures: blue represents the [O III] radiation (λ=5007 Å), green the Hα radiation (λ=6563 Å), red the [N II] radiation (λ=6583 Å). Each panel covers 4.1×4.1 arcsec, corresponding to ∼1850 AU. The dark disks are silhouetted against the bright backdrop of the hot gas of the Orion Nebula. (From McCaughrean & O'Dell 1996 [122]).

protostar. The protostar will then accrete material from the surrounding disk while its internal temperature will increase up to the value necessary to trigger hydrogen burning. The timescale of the star forming process is $\sim 10^7$ yr. Low mass stars then take 10^7--10^8 yr to reach the main sequence. Fig 2.1 shows some examples of young stars still surrounded by a protoplanetary disk.

2.2 The "Solar Nebula Theory"

The Solar Nebula Theory aims to describe the formation of the Solar System and its following evolution up to the present day. The "Nebula" is the protoplanetary disk that surrounded the young Sun right after its formation. The Nebula contained a mixture of gas (primarily H_2 molecules along with H and He atoms and simple molecules such as CO, CO_2, N_2, CH_4 and H_2O) and dust grains of $0.05-100$ μm (condensed atoms of Si, O, C with outer coatings of H_2O and CO_2) [90].

A critical problem is to fix the nebula initial conditions, in particular its total mass and density distribution. A lower boundary on the mass of the protoplanetary disk can be estimated as follows: Imagine that the material in each planet was augmented with volatiles to solar composition and spread out over an annulus ranging halfway to the orbits of its two neighbors. The resulting disk would have a mass of $0.01-0.02$ $M_\odot$ and a surface density which decreases with distance from the Sun as $\sim r^{-3/2}$ [198]; this is usually referred to as the "minimum-mass" solar nebula. While it is reasonable to assume a solar composition for the protoplanetary disk, current models suggest that the amount of condensed matter was initially several times larger than the minimum-mass value, with most of the excess material having resided in the outer parts of the Solar System [104]. On the other hand an upper limit of ~ 0.3 $M_\odot$ to the initial mass of the disk exists, beyond that the disk would have been gravitationally instable [171].

The process of planetary growth can be schematically divided in three distinct stages:

- From dust (~ 10 μm) to planetesimals (~ 1 km)
- From planetesimals to terrestrial planets
- Formation of giant gaseous planets by core accretion

In fact, it is unlikely that planet formation proceeds in a pure sequential way as layed out above. Rather, those processes are significantly overlapped in time and also affect each other. However, it is very difficult to establish a single overall theory capable to describe the planet growth through at least 12 orders of magnitude in spatial scale. Therefore, it is useful to consider different size regimes in which the interation between the solid component and the gas is qualitatively distinct.

2.2.1 Formation of solid planetesimals

As we mentioned before the protoplanetary disk contains dust grains. For a disk of solar composition, the first abundant condensates are silicates and iron compounds; in a carbon-rich gas instead, carbides would condense first. At lower temperatures, characteristic of the outer region of our planetary system, large quantity of water and other ices can condense [14]. The place where this transition occurres is referred to as the "ice-line".

Growth of solid particles then proceeds primarily by mutual collisions. The mechanical and chemical processes involved in grain agglomeration are still being investigated [22]. Laboratory studies and numerical models imply that loosely packed structures are formed. However, most primitive meteorites contain chondrules, which are compact glassy objects ~ 1 mm in size. It is believed that chondrules underwent a rapid heating and cooling before being incorporated into larger bodies [130].

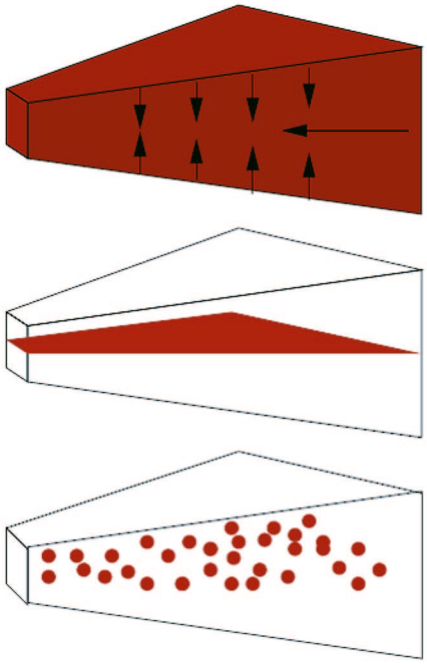

Figure 2.2: Schematic illustration of the mechanism for planetesimal formation. Dust settles to the midplane of the protoplanetary disk. The less turbulent is the nebula, the more thin will be the dust layer, speeding up the process of planetesimal formation. (From Armitage 2007 [8]).

The motions of small grains in a protoplanetary disk are strongly coupled to gas [2], which rotates at a sub-keplerian rate because the gas pressure contributes to balance the gravity. The vertical component of the star's gravity causes dust to sediment out towards the midplane of the disk. The settling speed v_z of a grain of density ρ and radius R, located at a distance z from the midplane of the disk, in a gas of density ρ_g with sound speed c, is [199]

$$v_z = -\Omega^2 z \frac{R\rho}{\rho_g c} \tag{2.1}$$

where Ω is the orbital angular frequency. Equation 2.1 yields sedimentation times for 1 μm grains of $\sim 10^6$ years. However, collisional growth of grains during their descent to the midplane shortens sedimentation times by several orders of magnitude, and differential settling velocities increase the collision rates between particles of differing sizes.

Once meter-size bodies form, they have increasingly weak coupling to the gas and consequently circle the star at Keplerian rate. The gaseous component of the disk, however, is partially supported against stellar gravity by a pressur gradient in the radial direction dP/dr. The "effective gravity" felt by the gas is

$$g_{\text{eff}} = -\frac{GM_*}{r^2} - \frac{1}{\rho_g}\frac{dP}{dr} \tag{2.2}$$

where M_* is the mass of the star. For estimated protoplanetary disk parameters, the gas rotates $\sim$0.5% slower than the Keplerian speed [200]. Thus, large particles encounter a headwind, which removes part of their angular momentum and causes them to spiral inward towards the star. Drift rates depend on the body size and peaks to $\sim 10^6$ km/yr for $\sim$1 m large objects. Thus, the material that survives to form planets must complete the transition from centimeter-size to kilometer-size rather quickly, unless it is confined to a thin dust-dominated subdisk in which it is the gas to be dragged along.

Two alternative theories describe the growth through this size range. If the nebula is quiescent, i.e its motion is laminar, the particles settle into a thin layer where the

dust density exceeds the gas density. Such a thin disk would be gravitationally instable leading to the rapid formation of ∼1 km large planetesimals [64]. In a turbulent disk, however, growth continues via simple 2-body collisions. One possibility to make this process fast enough is that small fractions of the grains grow into small solid planetesimals via fortuitous circumstances (e.g. being located at temporary nodes in the turbulent flow [48]) and that these planetesimals subsequently sweep up many times their mass in small particles (see Figure 2.2.

Although zeroth-order questions remain regarding the mechanism for planetesimal growth, most models predict that the formation timescale of kilometer-sized bodies is dominated by the dust setting time (10^4−10^5 years).

2.2.2 From planetesimal to terrestrial planets

Once planetesimals have formed, further interaction between the solid and gaseous components of the disk is limited until bodies with sizes $> 10^3$ km form that are large enough to have a gravitational coupling to the gas. Therefore, further growth to form protoplanets or planetary embryos is a well-posed N-body problem in which gravity provides the dominant physics. Being well-posed is not the same as easy − if the Earth formed from 5 km radius planetesimals then $N{\sim}10^9$. The usual approach is therefore a combination of statistical and N-body methods.

For sufficiently small bodies, the effects of gravity can be ignored for the purposes of determining whether they will physically collide. A massive planet, on the other hand, can gravitationally focus other bodies toward it, and, as a result, has a collision cross section that is much larger than its geometrical cross section. To evaluate the magnitude of this *gravitational focusing*, consider two bodies of mass m, moving on a trajectory with impact parameter b. The relative velocity at infinity is σ. At closest approach, the bodies have separation R_c and velocity V_{max}. Equating energy in the initial (widely separated) and final (closest approach) states we have,

$$\frac{1}{4}m\sigma^2 = mV_{max}^2 - \frac{Gm^2}{R_c} \tag{2.3}$$

Noting that there is no radial component to the velocity at the point of closest approach, angular momentum conservation gives $V_{max} = (1/2)(b/R_c)\sigma$. If the sum of the physical radii of the bodies is R_s, then for $R_c < R_s$ there will be a physical collision, while larger R_c will result in a harmless flyby. Stresses caused by tidal forces during close encounters between planetesimals might also fragment bodies, but Sridhar & Tremaine [174] show this is a very rare event. The largest value of the impact parameter that will lead to a physical collision is thus,

$$b^2 = R_s^2 + \frac{4GmR_s}{\sigma^2} = R_s^2\left(1 + \frac{v_{esc}^2}{\sigma^2}\right) \tag{2.4}$$

where $v_{esc}^2 = 4Gm/R_s$ is the escape velocity from the point of contact. The cross section for collisions is then,

$$\Gamma = \pi R_s^2\left(1 + \frac{v_{esc}^2}{\sigma^2}\right) \tag{2.5}$$

where the term in brackets represents the enhancement to the physical cross section due to gravitational focusing F_g. Clearly a planet growing in a "cold" planetesimal disk for

which $\sigma \ll v_{esc}$ will grow much more rapidly as a consequence of gravitational focusing. Therefore, determining the velocity dispersion of bodies of different masses during the planet formation process is extremely important.

The ratio between σ and v_{esc} also enters into the likely outcome of collisions. When two bodies collide, there are *three possible outcomes*: 1) The kinetic energy of the collision may break up one or both of the bodies, creating a number of unbound fragments. This is described as a disruptive or shattering collision. 2) The two bodies may bounce off each other elastically, and remain unbound. 3) Enough energy may be dissipated in the collision that the two bodies become gravitationally bound, and accrete (with or without fragmentation, which can occur followed by accretion if the fragments are themselves bound).

Determining the precise boundary between these outcomes as a function of impactor size and velocity is not easy, because the intrinsic strength of planetesimals and larger bodies is not well known [19]. For a rough estimate, however, we can note that for a head-on collision between two bodies, the collision velocity is $v_c = (\sigma^2 + v_{esc}^2)^{1/2}$. If the coefficient of restitution (measuring how elastic the collision is) is ϵ, then for rebound velocities $\epsilon v_c < v_{esc}$, we expect that the bodies will be bound − accretion will result irrespective of whether the initial impact fragments the bodies. Conversely, if $\epsilon v_c > v_{esc}$, the bodies will be unbound − no accretion will result and one or more of the objects may have shattered, depending on the tensile strength of the bodies. The boundary between these outcomes occurs for a coefficient of restitution

$$\epsilon = \left(1 + \frac{\sigma^2}{v_{esc}^2}\right)^{-1/2} \tag{2.6}$$

Inspection of this equation shows that if $\sigma \ll v_{esc}$, then accretion is likely unless ϵ is very close to unity, whereas fragmentation requires $v_{esc} \ll \sigma$. In the early history of the Solar System, before massive planets formed that were able to stir up the population of small bodies, conditions must have been more favorable for accretion rather than disruption.

A more subtle distinction that nevertheless plays a crucial role in planet formation is whether encounters between bodies can be described via 2-body dynamics − in which only the gravity of the two objects themselves matters − or whether the tidal influence of the Sun also needs to be considered (3-body dynamics) [62]. We consider a 3-body system consisting of a large body (a "planet") with mass M_p, a small body of negligible mass (described as a test particle), and the Sun, and define the *Hill radius* r_H as the radius within which the gravity of the planet dominates. Roughly, this is obtained by equating the angular velocity for an orbit at distance r_H from the planet with the angular velocity of the planet around the star. We find

$$r_H = \left(\frac{M_p}{3M_*}\right)^{1/3} a \tag{2.7}$$

where the factor 3 is included for consistency with more detailed derivations. If we define a characteristic velocity at the Hill radius $v_H \equiv (GM_p/r_H)^{1/2}$, then for $\sigma > v_H$ 2-body dynamics describes collisions quite well. This regime is called *dispersion dominated*. Conversely, for $\sigma < v_H$, 3-body effects are important. This regime is called *shear dominated*. When $\sigma < v_H$ and we are shear dominated, the collision rate is reduced compared to expectations based on 2-body dynamics.

We now proceed to derive an estimate for how fast a planet will grow due to accretion of planetesimals. We assume that the growing body, of mass M, radius R_s, and surface

escape speed v_{esc} is embedded within a swarm of planetesimals with local surface density Σ_p, velocity dispersion σ, and scale height h_p. The volume density of the planetesimal swarm is $\rho_{sw} = \Sigma_p/2h_p$. Then if 3-body effects can be ignored, the large body grows at a rate

$$\frac{dM}{dt} = \rho_{sw}\sigma\pi R_s^2 \left(1 + \frac{v_{esc}^2}{\sigma^2}\right) \sim \frac{1}{2}\Sigma_p \Omega \pi R_s^2 F_g \tag{2.8}$$

where we assumed that $h_p \sim \sigma/\Omega$ [105] We note that the velocities of the planetesimals enter only via the gravitational focusing term, which can however be very large. The rate of mass growth scales linearly with Σ_p – we expect faster growth in disks that have more mass in planetesimals (due to a higher gas mass and/or a higher ratio of solids to gas). Other things being equal, growth will be slower at large radii, due to lower Σ_p and smaller Ω. Complexity arises because as a planet grows, it starts to influence both the velocity dispersion and, eventually, the surface density of the planetesimal swarm in its vicinity. Two simple solutions of the growth equation give an idea of the possibilities present in more sophisticated models. First, assume that the gravitational focusing term F_g is constant. In this regime $dM/dt \propto R_s^2 \propto M^{2/3}$ which has solution $R_s \propto t$. If we assume the fiducial values Σ_p=10 g cm^{-2} at the orbital radius of Jupiter and ρ_{planet}=3 gcm^{-3}, then $dR_s/dt \simeq 0.2\ F_g$ cm yr^{-1}. This initial growth rate is slow, which implies that to form the cores of the giant planets in a reasonable time, large gravitational focusing factors are needed. For example, to reach 1000 km in 10^5 yr, we require $F_g \sim 5000$. Since empirically F_g must be large, a second useful limit to consider is the case where $F_g \gg 1$. If we assume that σ is constant (i.e. consider the regime where the growing planet has not yet managed to dominate the dynamical excitation of the planetesimal swarm), then $F_g \simeq v_{esc}^2/\sigma^2 \propto M/R_s$. The growth equation becomes $dM/dt \propto MR_s$ which has solutions such that $M \to \infty$ in a finite time, allowing much more rapid growth.

As noted above, rapid growth requires that σ remains low – i.e. that the planetesimals remain on roughly circular orbits. This means that there is a finite supply of planetesimals that have orbits that pass close enough to a growing planet to collide – once these have all been consumed, growth is bound to slow. The mass at which this slow-down occurs is described as the *isolation mass*, M_{iso}. To estimate the isolation mass, we note that a planet grows by accreting planetesimals within a "feeding zone". The size of the feeding zone Δa_{max} is set by the maximum distance over which the planets gravity is able to perturb planetesimal orbits sufficiently to allow collisions, so it will scale with the Hill radius. Writing $\Delta a_{max} = Cr_H$ with C a constant of order unity, we have that the mass of planetesimals within the feeding zone is

$$2\pi a \cdot 2\Delta a_{max} \cdot \Sigma_p \propto M^{1/3} \tag{2.9}$$

Note the 1/3 power of the planet mass, which arises from the mass dependence of the Hill radius. As a planet grows, its feeding zone expands, but the mass of new planetesimals within the expanded feeding zone rises more slowly than linearly. We thus obtain the isolation mass by setting the planet mass equal to the mass of the planetesimals in the feeding zone of the original disk, which gives

$$M_{iso} = \frac{8}{\sqrt{3}}\pi^{3/2} C^{3/2} M_*^{-1/2} \Sigma_p^{3/2} a^3 \tag{2.10}$$

Evaluating this expression in the terrestrial planet region, taking a=1 AU, Σ_p=10 gcm^{-2}, M_*=$M_\odot$ and C=$2\sqrt{3}$ [105], we obtain $M_{iso} \simeq 0.07 M_\oplus$. Repeating the estimate for the

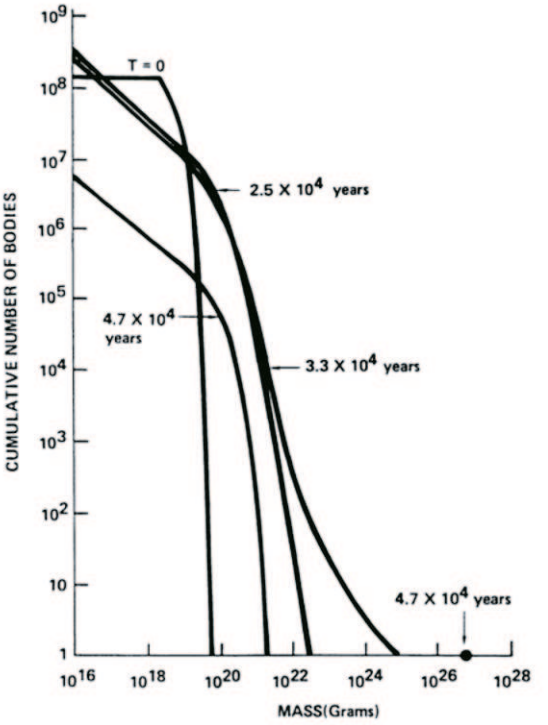

Figure 2.3: The evolution of the mass distribution of a swarm of planetesimals distributed between 0.99 and 1.01 AU using the velocity evolution equations of Stewart & Wetherill 1988 [175]. This simulation includes fragmentation, a reduction of gravitational perturbations of runaway bodies from the uncorrelated encounter approximation, and the 3-body gravitational enhancement in accretion cross-sections for low velocity bodies. Note the rapid runaway growth of the largest bodies, with the most massive planetary embryo becoming detached from the remainder of the swarm. (From Wetherill & Stewart 1989 [202]).

conditions appropriate to the formation of Jupiters core, using Σ_p=10 gcm^{-2} as adopted by Pollack et al. [156], gives $M_{iso} \simeq 9M_{\oplus}$. This estimate is comparable to, or larger than, the current best determinations for the mass of the Jovian core [70]. Full isolation may or may not be relevant to the formation of Jupiter, depending upon the adopted disk model.

One might legitimately question whether the assumption that the mass distribution of growing bodies can be neatly divided into two groups − planetesimals and growing planetary embryos − is any good. The quantitative approach to describe the evolution of an arbitrary size distribution is based on the *coagulation equation*. This allows us to drop the two groups approximation though at the expense of an enormous increase in complexity. To write the coagulation equation in its simplest form, assume that the masses of bodies are integral multiples of some small mass m_1. At time t there are n_k bodies of mass $m_k = km_1$. The coagulation equation in discrete form is

$$\frac{dn_k}{dt} = \frac{1}{2}\sum_{i+j=k} A_{ij} n_i n_j - n_k \sum_{i=1}^{\infty} A_k n_i \qquad (2.11)$$

where A_{ij} is the rate of mergers between bodies of mass m_i and m_j. The first term on the right-hand side of the equation describes the increase in the number of bodies of mass m_k due to collisions of all possible pairs of bodies which masses m_i and m_j sum to m_k. The second term describes the decrease due to bodies of mass m_k being incorporated into even larger bodies. The possibility of fragmentation is neglected here. In this formulation of the planetary growth problem, all of the physics − such as gravitational focusing − enters via the rate cofficients A_{ij}. Equation (2.11), or variants of it, has been used extensively to study planet formation [84], [89]. Only very simple cases exist for which an analytic solution is known while, for realistic cases, only numerical solutions have been found. They fall in two classes: Solutions that exhibit *orderly growth*, in which

the mass distribution evolves smoothly with time toward higher mean masses; Solutions that show *runaway growth*. In this case the mass distribution develops a power-law tail toward high masses − physically this corresponds to one or a handful of bodies growing rapidly at the expense of all the others.

Looking at equation 2.8, we note that the rate coefficient is expected to scale as $A \propto R_s^2 \propto m^{2/3}$ in the regime where gravitational focusing is unimportant, and $A \propto R_s^2 v_{esc}^2 \propto m^{4/3}$ where gravitational focusing is dominant. We expect that the initial growth of planetesimals will occur in the orderly regime, while runaway growth may occur once the largest bodies are massive enough for gravitational focusing to become significant (see Fig. 2.3).

The estimated value for the isolation mass at 1 AU, M_{iso}=0.07$M_\oplus$, implies that the formation of terrestrial planets requires a further step. The initially relatively isolated planetary embryos, left over by the runaway oligarchic growth, are perturbed onto crossing orbits due to influence of the already formed external giant planets and mutual secular resonances [34]. The final assembly of the terrestrial planets takes around 100 Myr, with the predicted configuration varying depending upon the assumed surface density of planetesimals and the existence or not of giant planets [93], [99]. One of the final impacts on the Earth is widely considered to have given rise to the ejection of enough mass into orbit to subsequently form the Moon.

2.2.3 The formation of giant gaseous planets by core accretion

[1]

Atmospheric gases surround many of the smaller planets and moons in the Solar System, amounting to far less than 1% of the mass of each body. These atmospheres consist primarily of high-Z elements. The most abundant gas in the atmospheres of the four massive planets is H_2; the next common is He. Hydrogen and helium make up ∼10% of the mass of Uranus and Neptune, and a majority of the mass of Jupiter and Saturn. Because hydrogen and helium cannot condense under solar nebula conditions, they must have been accreted in gaseous form by the giant planets. They must thus have become gravitationally bound to the solid core of the giant planets prior to the dispersal of the gaseous component of the Solar Nebula. This provides an upper bound on the timescale for the accretion of the giant planets. Dispersal rates of protoplanetary disk are difficult to estimate, but both observations of young stars [17] and theoretical calculations [148] suggest lifetimes of 10^6 to 3×10^7 years. However recent observations by the Spitzer satellite show that the outer part of the disk can survive much longer [126]

The main stages in the formation of a gas giant via core accretion are as follows. A core of rock and/or ice forms via the same mechanisms that we have previously outlined for terrestrial planet formation. Initially, there is either no atmosphere at all (because the potential is too shallow to hold on to a bound atmosphere), or any gas is dynamically insignificant. However, as the core grows, eventually it becomes massive enough to hold on to a significant envelope. At first, the envelope is able to maintain hydrostatic equilibrium. The core continues to grow via accretion of planetesimals, and the gravitational potential energy liberated as these planetesimals rain down on the core provides the main source of luminosity. This growth continues until the core reaches a

[1] An alternative theory exists to explain the formation of gaseous giant planets: the *gravitational instability* model, based on the idea that a massive protoplanetary disk might collapse directly to form massive planets [27].

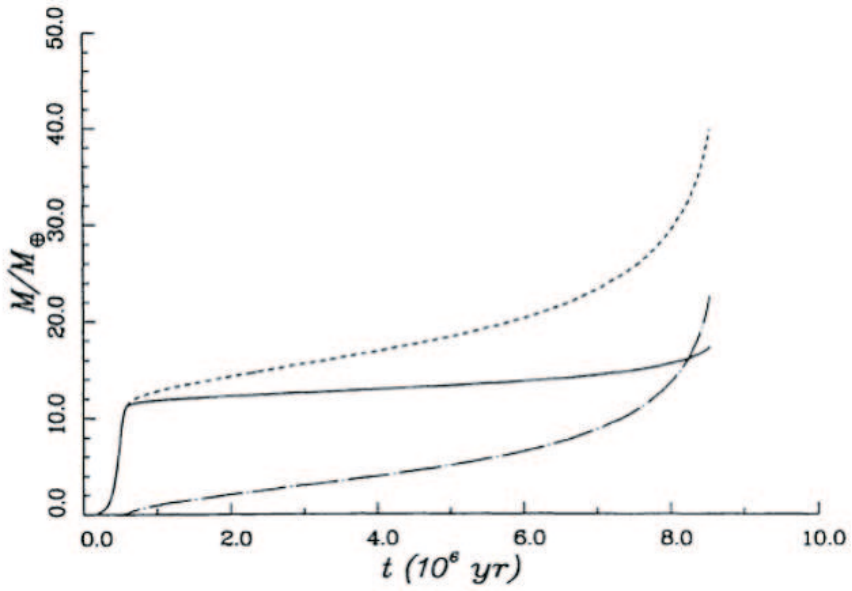

Figure 2.4: Mass of a growing planet (dashed curve) as a function of time, according to a model of Pollack et al. [155]. The mass of the solid component is given by the solid curve, whereas the dot-dashed curve represents the gas mass. The solid core grows rapidly by runaway accretion in the first million years. The rate of solid body accumulation decreases once the planet has accreted nearly all of the condensed material within its gravitational reach. The envelope accumulates gradually, with its settling rate determined by its ability to radiate away the energy of accretion. Eventually, the planet becomes sufficiently cool and massive for gas to be accreted rapidly. The substantial increase in the planet total mass that results from this accretion of gas expands its feeding zone into regions undepleted of solid planetesimals by previous accretion, causing an increase also in the accumulation rate of solids. (From Pollack et al. [155]).

critical mass. Once the critical mass is reached, the envelope can no longer be maintained in hydrostatic equilibrium. The envelope contracts on its own Kelvin-Helmholtz time scale, and a phase of rapid gas accretion occurs. This process continues until (a) the planet becomes massive enough to open up a gap in the protoplanetary disk, thereby slowing down the rate of gas supply, or (b) the gas disk itself is dispersed.

Mizuno [128] used numerical models to demonstrate the existence of a maximum core mass, and showed that it depends only weakly on the local properties of the gas within the protoplanetary disk. The gas mass equals the mass of the solid core when the total mass of the planet is 20-50 $M_\oplus$ [24], [155]. The principal factors accounting for this range are the accretion rate of planetesimals, which supplies energy to the atmosphere, and the magnitude of the opacity of the upper region of the atmosphere, which regulates how effective is the radiative release of that energy (see Fig. 2.4).

While the broad outlines of how core accretion works are well established, further work is needed to delineate under what circumstances (i.e. for what values of the surface density, disk lifetime, migration rates and envelope opacity) it results in successful formation of a massive planet.

2.3 Orbital evolution

The Solar Nebula theory accounts for the present mass and configuration (semi-major axis, eccentricity) of the solar system planets. The observed properties of extra-solar planetary systems, in particular the presence of a population of "hot Jupiters" orbiting the parent stars with period P<10 days as well as the frequent occurence of eccentric orbits, were unexpected in the framework of the Solar Nebula theory. Recent studies called upon different mechanisms leading to post-formation planet orbital evolution, in order to explain the characteristics of extra-solar planets.

Two mechanisms received mainly consideration: (i) Interaction between planets and the gaseous protoplanetary disk. This leads to orbital migration as a consequence of angular momentum exchange between the planet and the gas disk, and can be important for both terrestrial-mass planets and gas giants while the gas disk is still present. (ii) Interaction within an initially unstable system of two or more massive planets. There is no guarantee that the architecture of a newly formed planetary system will be stable over the long run. Instabilities can lead to planet-planet scattering, which usually results in the ejection of the lower mass planets, leaving the survivors on eccentric orbits, both closer and farther to the star.

2.3.1 Gas disk migration

The most detailed calculations of the rate of angular momentum exchange between a planet and a gas disk are based on summing up the torques exerted at discrete *resonances* within the disk. This calculation was introduced in the planetary context in a paper by Goldreich & Tremaine [63]. Here I want to summarize the conditions for resonances to exist, and discuss the effect of the torques on the planet and on the disk in the limits of high and low planet masses.

We consider a planet orbiting a star on a circular orbit with angular frequency Ω_p. A *corotation resonance* exists for radii in the disk where the angular frequency $\Omega = \Omega_p$; *Lindblad resonances* exist when $m\,(\Omega - \Omega_p) = \Omega$, where m is an integer [21]. If we approximate the angular velocity of gas in the disk by the Keplerian angular velocity, the Lindblad resonances are located at

$$r_L = \left(1 \pm \frac{1}{m}\right)^{2/3} r_p \tag{2.12}$$

where r_p is the planet orbital radius. For an orbiting test particle, the resonances are locations where the planet can cause a strong perturbation to the motion. For a gas disk, angular momentum exchange between the planet and the gas disk occurs at resonant locations. The sense of the exchange is that the planet gains angular momentum from the gas disk at the interior Lindblad resonances ($r_L < r_p$), this tends to drive the planet outward. Conversely, the planet loses angular momentum from the gas disk at exterior Lindblad resonances ($r_L > r_p$) and tends to move inward.

The flux of angular momentum exchanged at each Lindblad resonance can be written as

$$T_{LR}(m) \propto \Sigma M_p^2 f_c(\xi) \tag{2.13}$$

where Σ is the gas density and M_p the planet mass. The factor $f_c(\xi)$ is the *torque cutoff function* [10], which encodes the fact that resonances very close to the planet contribute little to the net torque. The torque cutoff function peaks at a radial location $r \simeq r_p \pm h$,

where h is the disk scale height. This result implies that a three-dimensional treatment is necessary for the dominant resonances if the planet is completely embedded within a gas disk, as is the case for low mass planets. Angular momentum trasfer T_{CR} at the corotation resonance needs also to be considered for three-dimensional disks whenever there is gas present close to the planet's location [183].

Type I migration

For low mass planets (generically $M_p \sim M_\oplus$, though the exact mass depends upon the disk properties) the angular momentum flux injected into the disk as a consequence of the planet-disk interaction is negligible when compared to the viscous transport of angular momentum. As a result, the gas surface density profile $\Sigma(r)$ remains approximately unperturbed, gas is present at the location of each of the resonances, and the net torque on the planet is obtained by summing up the torque exerted at each resonance. Changes to the planets orbit as a result of this net torque are called "Type I migration". Actually evaluating the sum is not easy, however invariably it is found that the Lindblad resonances exterior to the planet are more powerful than the interior ones, so that the net torque due to Lindblad resonances leads to inward migration. The torque at corotation is of comparable magnitude to the net Lindblad torque, but does not reverse the sense of migration. Tanaka, Takeuchi & Ward [183] compute the net torque on a planet in a three-dimensional but isothermal gas disk, including the effect of both Lindblad and corotation resonances. For a disk in which $\Sigma(r) \propto r^{-\gamma}$ they obtain a migration time scale

$$\tau_I \equiv -\frac{r_p}{\dot{r}_p} = (2.7 + 1.1\gamma)^{-1} \frac{M_*}{M_p} \frac{M_*}{\Sigma_p r_p^2} \left(\frac{c_s}{r_p \Omega_p} \right)^2 \Omega_p^{-1} \tag{2.14}$$

where Σ_p, c_s and Ω_p are respectively the gas surface density, gas sound speed, and angular velocity at the location of a planet orbiting at distance r_p from a star of mass M_*. Type I migration is therefore most rapid for the largest body for which the assumption that the gas disk remains unaffected by the planet is still valid. The timescale also becomes shorter for cooler disk and larger local disk mass (see Fig. 2.5).

The Type I migration timescale thus can be significantly shorter than the disk lifetime, resulting in a survival problem for proto-Jovian mass planet cores. The resolution of this problem possibly comes from the releasing of the oversimplifying hypothesis that the disk is laminar. More realistically, angular momentum transport itself derives from turbulence, which is accompanied by a spatially and temporally varying pattern of density fluctuations in the protoplanetary disk. These fluctuations will exert random torques on planets of any mass embedded within the disk. If we assume that the random torques are uncorrelated with the presence of a planet, then the random torques (linearly scaling with planet mass) will dominate over the usual Type I torque (scaling as M_p^2) for sufficiently low masses. The turbulence will then act to drive a random walk in the semi-major axis of low mass planets [98], [136].

Type II migration

For sufficiently large planet masses, the angular momentum flux from the planet locally dominates the viscous flux. As a consequence, gas is repelled from high m resonances. The surface density drops near $r = r_p$, forming a *gap*, an annular region in which the surface density is smaller than its unperturbed value.

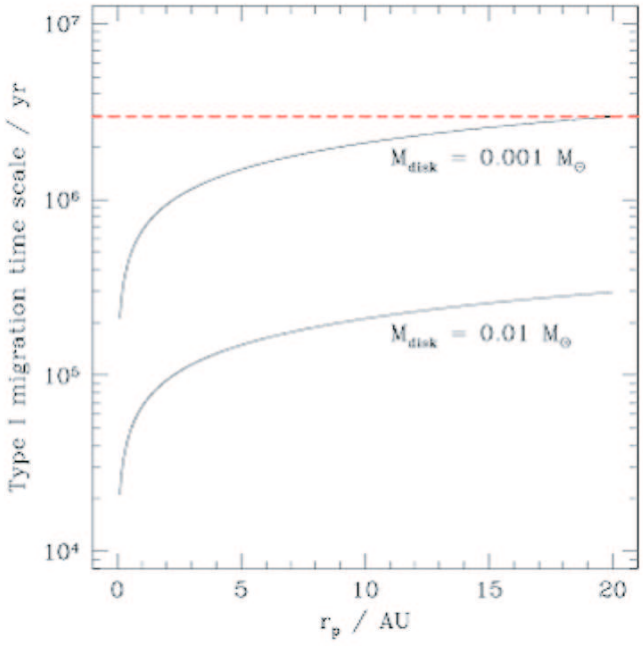

Figure 2.5: The inward Type I migration time scale for a $5M_\oplus$ core as a function of orbital radius, calculated using the three-dimensional isothermal disk formula of Tanaka, Takeuchi & Ward 2002 [183]. The lower curve assumes a disk with $\Sigma \propto r^{-1}$, h/r = 0.05, and a total mass of 0.01 $M_\odot$ within 30 AU. The upper curve shows the migration time scale in a similar disk with a mass of only 0.001 $M_\odot$ −the absolute minimum needed to form a Jupiter mass planet. The red dashed line illustrates a typical estimate for the lifetime of the gas disk. (From Armitage 2007 [8]).

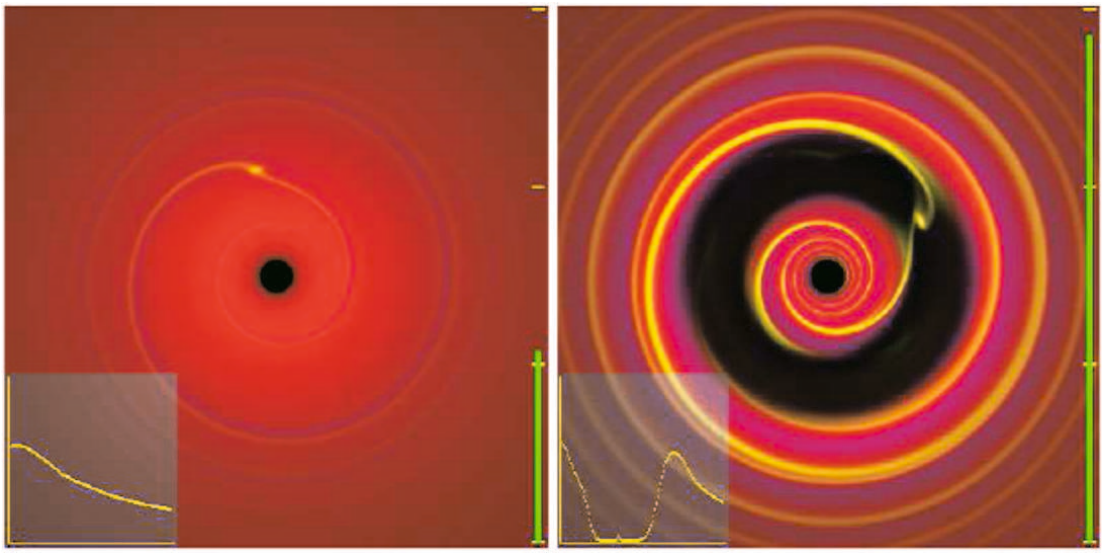

Figure 2.6: An illustration of the interaction between a planet on a fixed circular orbit with a laminar (non-turbulent) protoplanetary disk, computed from a two-dimensional hydrodynamic simulation with a locally isothermal equation of state and a constant kinematic viscosity. In the left-hand panel showing the regime of Type I migration, a relatively low mass planet excites a noticeable wave in the disk gas but does not significantly perturb the azimuthally averaged surface density profile (shown as the inset graph). In contrast, a 10 M_J planet (right-hand panel) clears an annular gap in the disk, within which the surface density is a small fraction of its unperturbed value. As the disk evolves over a viscous time scale, the planet is predicted to track the motion of the gas (either inward or outward) while remaining within the gap. This is Type II migration. (From Armitage & Rice 2005 [9]).

Two conditions are necessary for gap formation. First, the Hill sphere of the planet needs to be comparable to the thickness of the gas disk, $r_H \gtrsim h$, which requires a mass ratio $q \equiv M_p/M_* \gtrsim 3(h/r_p)^3$. This condition is satisfied, assuming typical protoplanetary disk parameters, for $q{\sim}4{\times}10^{-4}$, i.e. for planet masses somewhere between that of Saturn and Jupiter. Second, we require that the tidal torques must be able to remove gas from the gap region faster than viscosity can fill the gap back in [142]. Takeuchi et al. [182] estimate the time scale for viscous diffusion to close a gap of width Δr, t_{close}, and the time scale to open a gap at the m-th Lindblad resonance, t_{open}. Setting $t_{open}{=}t_{close}$,

$$\frac{1}{m^2 q^2 \Sigma_p}\left(\frac{\Delta r}{r_p}\right)^2 = \frac{(\Delta r)^2}{\nu} \tag{2.15}$$

and taking the value of m where the torque cutoff function peaks, $m = r_p\Omega_p/c_s$, they calculate, for typical disk parameters, $q \sim 10^{-4}$.

Once a planet becomes massive enough to open a gap, it exchanges angular momentum with the gas disk according to the Type II migration mechanism. Provided that the local disk mass exceeds the planet mass, i.e. that $\pi r_p^2 \Sigma \gtrsim M_p$, and using the standard α-prescription by Shakura and Sunayev [168], the migration time scale is given by [143]

$$t_0(\mathrm{yr}) = \frac{1}{3\alpha}\left(\frac{r_p}{h}\right)^2 \Omega_p^{-1} = \frac{0.05}{\alpha}\left(\frac{r_p}{h}\right)^2 \left(\frac{r_p}{1\mathrm{AU}}\right)^{3/2} \tag{2.16}$$

If we adopt $h/r_p{=}0.1$ and consider α in the range 10^{-3}-10^{-2}, we get $t_0{\sim}10^3$ yr at $r_p{=}1$ AU ($t_0{\sim}10^4$ yr at $r_p{=}5$ AU). These timescales are anyway much shorter than the disk lifetime and the estimated planetary formation timescales. In practice, the assumption of a *disk dominated migration* often fails. Syer & Clark [181] found the Type II migration timescale can better be expressed by

$$t_{II} = t_0\left(\frac{M_p}{4\pi r_p^2 \Sigma}\right)^{\gamma} \tag{2.17}$$

where the value of γ can vary between 0 and 1 depending on the disk properties.

Many mechanisms have been invoked that would be able to stop Type II migration. Some of them call upon different planet-star interactions stopping the planet on small radii and thus explaining the observed population of hot-Jupiters. For instance tidal interaction with a rapidly rotating star would halt orbital decay [101]. A planet overflowing its Roche lobe and losing part of its mass to the central star would also halt at small radii. This is because during the transfer of mass the planet moves outward to conserve the angular momentum [186]. A further possibility is that the planet enters a cavity where the gas has been cleared off by the central star [100]. It has been suggested that migration of a giant planet could be stopped at any radius if migration and disk dissipation were concurrent [187]. If the disk dissipates while migration is taking place, then the drift timescale may increase in such a way that the planet stalls at some finite radius. Orbital migration occurring for different planets at different rates, depending on local disk parameters, can produce convergent migration and lock planets on resonant orbits. It has been suggested that for some planet masses and disk conditions, resonant trapping of planets could lead to a reversal of Type II migration [116]. A further possibility is that most planets fall indeed into the host stars and what we observe are just the survivors [85], [42].

2.3.2 Planet-planet scattering

While the gas disk is present, gas damping can potentially protect a multiple planet system against the development of crossing orbits from planet-planet gravitational interactions (at least if interactions with the gas disk actually damp eccentricity, which is somewhat uncertain). Once the gas is gone, gravity can go to work on what may be an unstable planetary system and change the orbital radii and eccentricities of the planets via gravitational scattering. This process is the most widely invoked mechanism to explain the large eccentricities of many extrasolar giant planets.

The general N-body problem of the motion of N point masses interacting under Newtonian gravity is analytically insoluble for $N > 2$. For $N=3$, an extension of the so called *circular restricted 3-body problem* [134] provides informations on the stability of two planets orbiting a star. Let us consider two planets of mass $m_2 = \mu_2 m_1$ and $m_3 = \mu_3 m_1$ where m_1 is the mass of the central star and $\mu_1, \mu_2 \ll 1$. Assuming that the planets move on circular orbits with semi-major axes a_2 and $a_3 = a_2(1 + \Delta)$, Gladman [61] shows that the system is guaranteed to be stable provided that the relative separation Δ exceeds the critical value $\Delta_c \simeq 2.40(\mu_2 + \mu_3)^{1/3}$. This analytic result leaves open the question of whether systems with $\Delta < \Delta_c$ are unstable. As an example, if we compute the critical separation for planets of the mass of Jupiter and Saturn, we obtain $\Delta_c \simeq 0.26$. The actual separation of Jupiter and Saturn in these units is $\Delta = 0.83$, so an isolated planetary system in which Jupiter and Saturn were on circular orbits would assuredly be stable for all time. For any planetary system with $N > 3$ no analytical stability criterion is known.

Many authors have performed numerical simulations of planetary orbital evolution for systems with 2, 3 or more planets. The numerical approach presents a number of challenges. The parameter space of possible initial conditions is enormous, with each scenario requiring numerous N-body integrations to map out the statistics of the various possible outcomes. Moreover, it is not always obvious that N-body integrations suffice to capture the relevant physics. Interactions with gas, or with planetesimals, may also play a role in either driving planets toward instability or in damping instabilities.

If a two-planet system is unstable, the possible outcomes of the instability can be divided into four classes: (i) The separation evolves (increases) until the system achieves a state that is stable over the long term. (ii) One planet is ejected, while the other remains bound. (iii) One planet fall into the star. (iv) The planets physically collide. The first three cases will in general lead to larger eccentricities for the survived planets. Ford, Havlickova & Rasio [55] present a comprehensive study of the dynamics of equal mass two planet systems. The planets were set up on circular orbits close to the stability boundary, and allowed to evolve under purely N-body forces until the system relaxed to a stable state. They found that the predicted fraction of collisions increases sharply for small orbital radii and/or larger planetary radii. For pairs of Jupiter mass and radius planets initially located at 5 AU, the most common outcome is two planets (65%), followed by ejections (35%) and collisions (10%). If the same pair of planets starts at 1 AU, however, collisions occur roughly 30% of the time. This conclusion is important for studies of extrasolar planet eccentricity, because collisions yield relatively low eccentricities for the merged planet. Indeed equal mass planet scattering failed to match the observed distribution of eccentricities. However, subsequent calculations that relaxed the equal mass assumption showed that two planet systems in which the planets have a realistic range of masses can yield agreement with observations [56].

Models starting with three or more planets have also been studied in some detail ([4], [114], [184], [192]) and it seems likely that (given the substantial uncertainties in the initial conditions) multiple planet models can also be constructed that match the observational data.

Overall, the eccentricities of massive extrasolar planets appear to be broadly consistent with a scattering origin. Further tests of scattering models appear quite feasible in the near-term, either from the accumulation of better statistics that can be compared with models (for example, on the eccentricity distribution as a function of radius, or on the prevalence and properties of additional planets further out), or from the discovery of additional multiple systems whose dynamics can be used to constrain the origin of planetary eccentricities. Distinguishing between different scattering scenarios may be more difficult, and may have to await until observational information as to the abundance and evolution of planets of young stars, i.e. prior to the scattering phase, will become available.

Chapter 3

Looking for planets of young stars: The scientific case

Most of what we know about extra-solar planets nowadays comes from studies of stars similar to the Sun. In order to achieve the best precision, most RV surveys conducted so far have targeted nearby, dwarf, late spectral type, old stars. This limited sample already showed a wide variety of planetary systems, which in turn triggered a number of theoretical works. As a result, it has become clear that, in order to fully understand the physics of planetary formation and evolution, it is necessary to observationally study the characteristics of planetary systems in correspondence to a much broader assortment of stellar properties.

In this respect, several different types of survey are being undertaken. For instance the presence of planets around wide visual binary stars ([42], [49]), as well as close spectroscopic binaries [94] has been investigated. Endl et al. [51] and Bonfils et al. [25] reported about RV surveys dedicated to M stars. Searches for planets around evolved G and K giant stars have also been performed ([45], [73], [127]). Many photometric surveys looked for planetary transits of stars in open clusters to establish the frequency of hot-Jupiters in large stellar samples with same known age, metallicity and distance (see for example von Braun et al. [197]). To understand the role that environmental effects play on hot-Jupiter formation and survival also globular clusters were surveyed [201]

This work, whose ultimate goal is to characterize the planets of young stars, should be seen as an additional piece (of information) to the puzzle of planetary systems theories. In this chapter the main open issues, that can be addressed studying planets of young stars, will be highlighted:Why there are close-in planets? Why orbits are often eccentric? In wich extent mechanisms like migration, planet-planet scattering, evaporation can shape the orbital configuration and physical properties of planetary systems as we see them around old stars? The problems arising from the young age of the stars that can hinder the detection of planets by means of the RV method, will also be discussed.

3.1 The shortage of close-in very massive planets

As I discussed in Section 1.3 (see also Fig. 1.9), RV surveys showed that there is a lack of massive planets ($M_p \gtrsim 2M_J$) on short period orbits ($P \lesssim 100$ days). How can this be explained? In the frame of the core accretion theory there is general consensus about the fact that massive planets can form only in the outer part of the protoplanetary

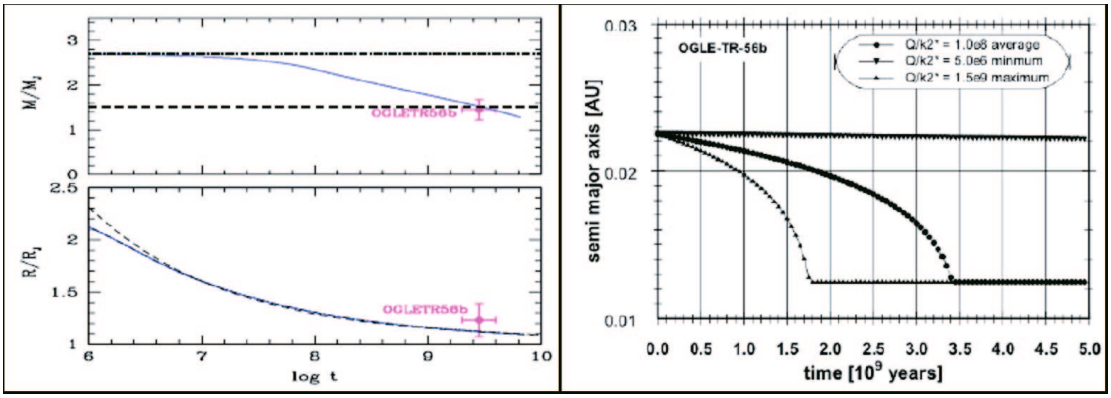

Figure 3.1: **Left:** Effect of evaporation on the radius and mass as a function of time (in years) for planets at $a = 0.023$ AU from their parent star. The solid curve is an evaporating planet with initial mass 2.7 M_J, which reaches 1.5 M_J in 3 Gyr, reproducing the properties of OGLE-TR-56b. (From Baraffe et al. [12]) **Right:** Estimated time evolution of the semi-major axis of the planet OGLE-TR-56b for different models of stellar structure. t=0 corresponds to the today's age of the star. The planet could fall into the star in the next few billion years. (From Pätzold et al. [145]).

disk, where the isolation mass M_{iso} is large enough to allow the formation of the solid core of giant gaseous planets. The absence of such giant planets closer to the star can then be explained in two different ways: (i) The Type II migration, which is believed to be responsible for the drift inward of the gaseous planets, is less effective for more massive planets (see eq. 2.17). As a consequence, it is possible that larger planets never get closer to the parent star. (ii) Giant planets are able to reach the central regions, but then they experience a significant mass loss or even fall into the star. Baraffe et al. [12] showed that a close-in planet, exposed to the strong radiation field coming from the central star, can lose by evaporation a large part of its gaseous envelope (see Fig. 3.1, left). Obsevational evidence of evaporation has been reported by Vidal-Madjar & Etangs [193] for HD209458b. Pätzold et al. [145], as a result of numerical simulations, find that a close-in planet experiences extreme tidal interactions with its host star that, if the planet orbital period is smaller than the star rotation period, lead in turn to a decrease of the orbital semi-major axis a and eventually to the planet engulfment (see Fig. 3.1, right). Remarkably, they find that da/dt is proportional to the planet mass.

It must be noticed that both the evaporation and the engulfment mechanisms are much more effective for very short period planets and it is not clear whether they could never act on planets with periods up to $P \sim$100 days. However it must also be considered that evaporation could be much more effective for young stars. In fact it has been shown that EUV radiation (100 Å$< \lambda <$ 1200 Å) is the main driver of gas escape from planetary atmospheres [33]. Since young stars have much stronger EUV fluxes than old stars, correspondingly the evaporation timescale is calculated to be roughly an order of magnitude shorter [41].

The characterization of the population of planets around young stars will allow to distinguish between the two scenarios mentioned above. Since the evaporation as well as the engulfment have a typical timescale of $\lesssim$1 Gyr, we can now be more specific about what we mean by young stars. We refer to a star as young when its age is confidently

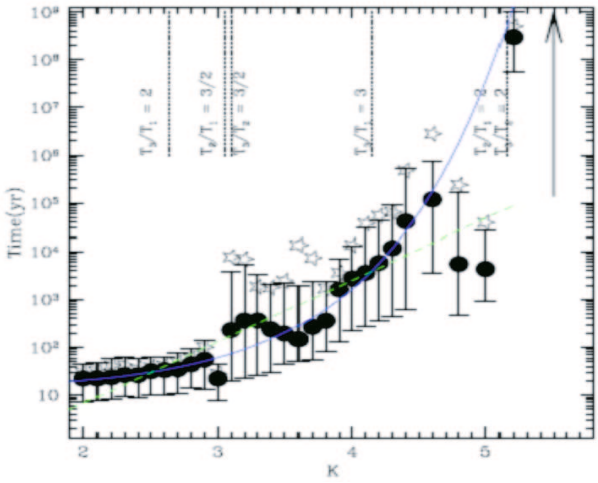

Figure 3.2: Results of simulations of orbital evolution of a system of three planets with M=1 M_J. The closer planet is placed initially at a_1=5 AU, while the two other planets are at $a_{i+1} = a_i + KR_{Hi,i+1}$, with R_H being the mutual Hill radius. The instabilty growth timescale as a function of the spacing parameter K is shown. The filled circles are the medians (the stars are the averages) of the distributions of stability timescales for the respective values of K. The bars show the ±34% range in the timescale. (From Chatterjee et al. [37]).

less than 1 Gyr. Thus, the detection of very massive planets on close-in orbits around young stars will imply that they do migrate inward. The mass and orbital distributions of these planets would then tell us about the real effectiveness of evaporation and/or engulfment. In particular already the detection of a single eclipsing hot-Jupiter around a young star would be valuable to find out wether evaporation plays a role or not. Conversely, a distribution of young planets on the mass-period diagram similar to the one for old stars would cast doubts on the idea of planet migration itself. With the migration scenario ruled out, in order to explain the existence of hot Jupiters either the core accretion theory should be revisited to allow for giant planets to form close to the parent star, or the alternative theory of gravitational instability should be invoked.

3.2 Eccentricity of young planets

The post-formation planet-planet gravitational interaction in planetary systems is considered the most plausible mechanism to account for the observed highly eccentric orbits. The timescale of this mechanism spans from tens to billions years, strongly depending on the initial conditions, i.e. the planet and star masses and especially the planet orbital separations (see Fig 3.2). Simulations show that the final orbital configuration is usually unrelated to the initial one [114]. As a consequence, the *evolved* planetary systems observed up to now can only be used in a limited extent to infer where planets formed in the disk. On the other hand, by observing young stars we could find planets for which the gravitational scattering had no time to operate yet or it is currently going on. Such planets will provide much stronger costraints on the planet formation in the disk. In particular, is gravitational scattering the only mechanism able to excite planet eccentricities? Or the disk can give birth to already eccentric planets?

A common outcome of close encounters is, according to simulations, the ejection of a planet. If this phenomenon is really frequent in newly formed planet systems, then we will find young stars to have an higher frequency of multiple systems than their old analogs.

Gravitational scattering can also lead one planet to lose most of its angular momentum and fall on a highly eccentric orbit. When such a planet, at the periastron, passes very close to the star, tidal interaction will damp its eccentricity [86]. Eventually the

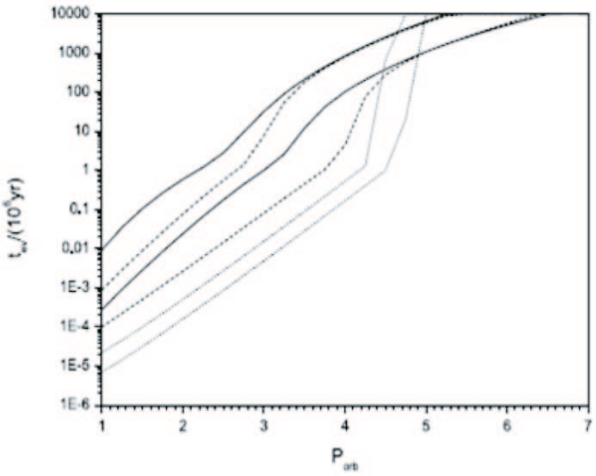

Figure 3.3: The circularization timescale t_{ev} for 1 M_J planet around a 1 $M_\odot$ star, as a function of the planet orbital period after the stage of tidal circularization, P_{orb} (in days). Different types of curves correspond to different models. (From Ivanov & Papaloizou [86]).

planet will be set on a close-in circular orbit. The actual tidal circularization timescale (see Fig. 3.3) depends on many stellar and planet factors as well as on the adopted modeling of the interaction. For instance, a 1 M_J planet on a P=3 days orbit could take from 5×10^3 to 3×10^7 yr to be circularized. I have pointed out in Section 1.3 (see Fig. 1.10) that very short period planets ($P \lesssim 3$ days) have zero eccentricity. As they all orbit around old stars they have had anyway time to be circularized and we do not know whether they were once on eccentric orbits. However, even a single detection of a very close-in young planet on an eccentric orbit would confirm the genesis by gravitational scattering of these planets. Conversely, the alternative hypothesis, that calls upon the interaction with the disk to cause planet spiraling inward on a series of quasi-circular orbits, would be seriously questioned.

3.3 Luminosity of young planets

A further interesting aspect for a search of young planets is that they are intrinsically more luminous than old planets of similar mass. In fact, both stars and planets, after they form, experience a phase of contraction during which the gravitational energy released is converted in radiative energy. However, whereas stars at some point reach a status of hydrostatical equilibrium and their luminosity levels out (i.e. stars arrive on the main-sequence track in the H-R diagram), the fate of planets is to fade indefinitely (eventually the stellar radiation will become the main source of energy leading to the thermal equilibrium). Burrows et al. [30] study the luminosity evolution of low mass stars, brown dwarfs and giant planets of solar metallicity (see Fig. 3.4). As it can be seen the planet to star luminosity contrast L_p/L_* decreases significantly when the system gets old, for instance $(L_p/L_*)_{t=100Myr} \sim 10^2\,(L_p/L_*)_{t=3Gyr}$.

Thus young stars are optimal candidates for attempting to image planets directly (see Section 1.2.1). Planets detected with the RV technique will perhaps orbit too close to the star to be spatially resolved. Nevertheless it might be well possible that other planets orbit the same star at larger semi-major axes.

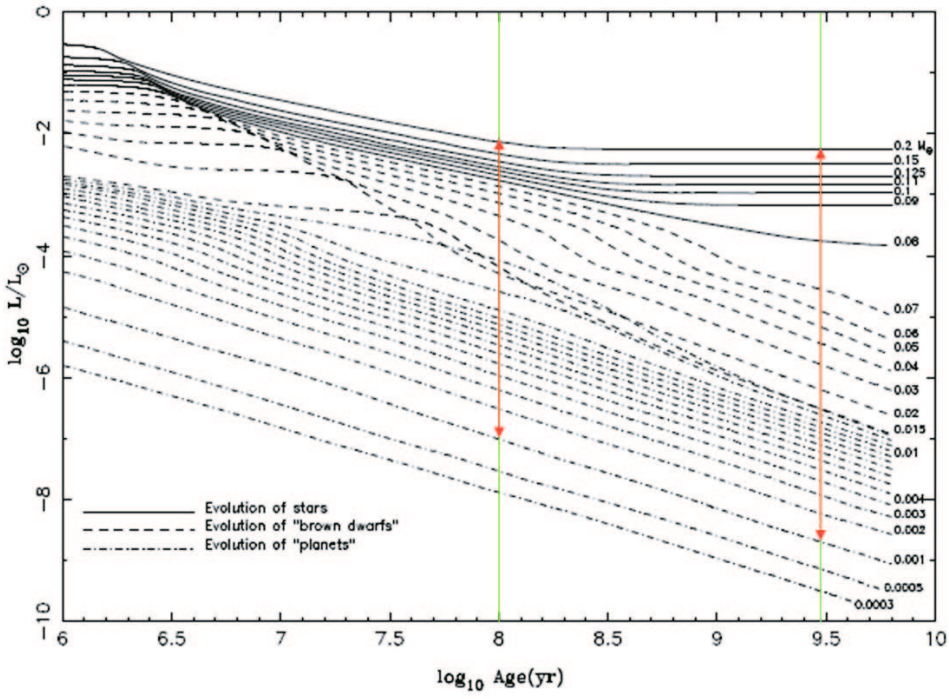

Figure 3.4: Evolution of the luminosity (in $L_{\odot}$)) of solar-metallicity M dwarfs and substellar objects vs. time (in yr) after formation. The masses (in $M_{\odot}$) label most of the curves, with the lowest three corresponding to the mass of Saturn, half the mass of Jupiter, and the mass of Jupiter. The green lines correspond to an age of 100 Myr and 3 Gyr respectively, the red arrows show the decrease in luminosity ratio for a 1 M_J planet orbiting a 0.2 $M_{\odot}$ star. (From Burrows et al. [30]).

3.4 Activity induced RV-jitter of young stars

Variations in stellar radial velocity measurements can originate not exclusively from the presence of an orbiting companion. Different mechanisms intrinsic to stars are known causing RV variations. These mechanisms can be seen as a source of noise in RV measurements that make it more difficult or impossible to detect the periodic RV signature from a planet.

Stellar RV are obtained measuring the position of photospheric absorption lines in wavelength calibrated stellar spectra. Therefore, the activity induced RV variations are due to the shift and/or shape alteration of the absorption lines. The variations of the line profiles can be outlined by the *bisector*. The bisector of an absorption line is the midpoint of the horizontal segment connecting points on the left and right sides of the profile with the same flux level. The line bisector is obtained by connecting bisector points ranging from the core toward the wings of the line (see Fig. 3.5). The amplitude of RV variations consequent to line profiles changes are often estimated by means of the *velocity span*, that is the difference between the RV measured from the bisector at two different levels (see Fig. 3.5). If RV variations are only due to an orbiting companion, the velocity span is constant (but not necessarily equal to zero). Conversely spurious RV variations will mirror in velocity span variations.

Following is a description of the major stellar phenomena able to produce RV vari-

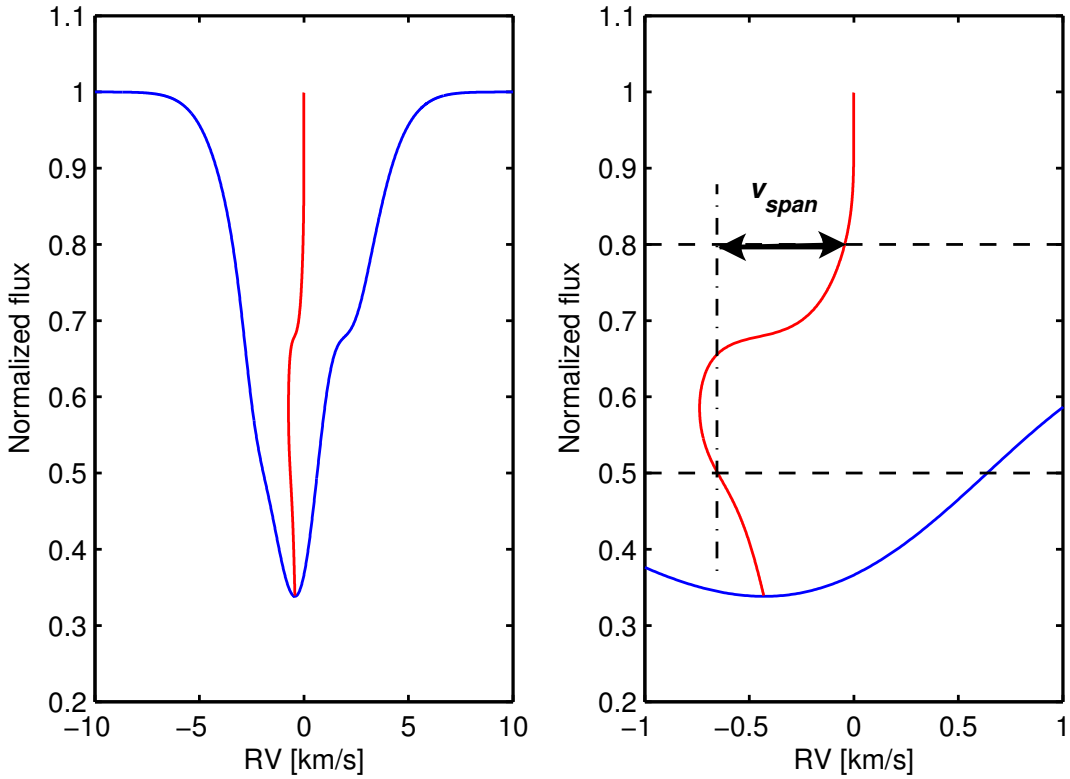

Figure 3.5: **Left:** Sketch of a spectral absorption line (blue) and its bisecor (red). **Right:** The abscissa has been expanded to better show the bisector shape. The definition of velocity span is also illustrated.

ations:

– *Stellar pulsations.*

Radial as well as non-radial pulsations modify the velocity field of stellar surfaces, therefore they can change the average (stellar disk integrated) RV. Many classes of stars are known to pulsate, showing periodicities ranging from minutes to years and RV variations from meters to kilometers in amplitude. Pulsations also cause brightness and color modulations which can be used to reveal the real nature of RV variations which, additionally, result to be wavelength dependent. While pulsations have been observed in pre-main sequence δ-Scuti stars, which are early-type intermediate-mass young stars [159], and theoretical calculations suggest that also young brown dwarfs could oscillate [141], young solar-mass stars do not show significant pulsations at the current level of radial velocity precision. In addition, the period of P-mode oscillations on the Sun are on time-scales of minutes. For young solar-like stars the periods would not be that different. Confusion with orbiting planets thus is impossible because oscillations with periods of days/months are impossible.

– *Stellar spots.*

Magnetic fields are at the basis of the appearance of spots on the stellar surfaces. Dark spots as well as bright spots (plages) are observable on the Sun disk (see Fig. 3.6). In order to understand the effect of a spot on the radial velocity let us consider a dark spot (one that emits no light at all). The observed spectrum of a star is the sum of element spectra emitted by each element surface in the stellar disk. Due to

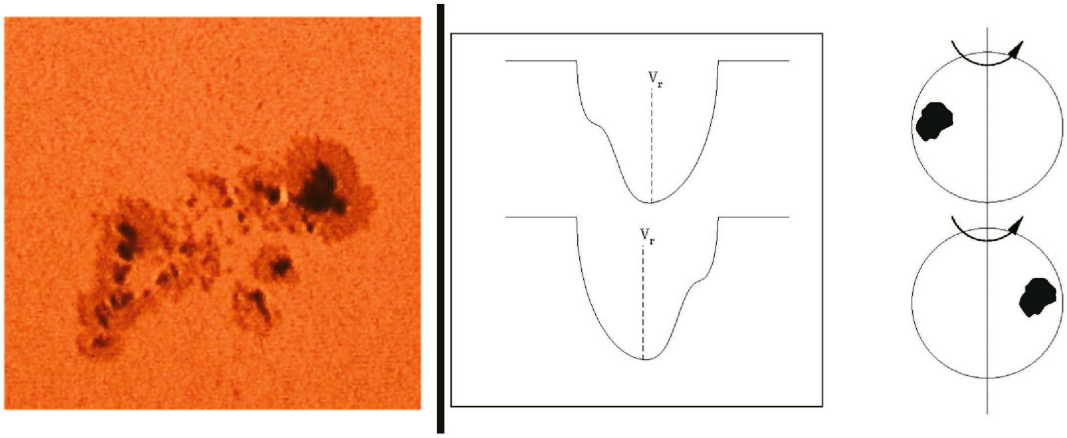

Figure 3.6: **Left:**Image of a cold spot on the Sun disk. **Right:** Illustration of the effect of a spot of a rotating star on the profile of an absorption line. (From Queloz [157]).

stellar rotation, an element surface has a radial velocity depending on its position on the stellar disk. When the dark spot is on the half of the disk approaching us, part of the blue-shifted element spectra will miss and a hump will appear on the blue wing of absorption lines causing an apparent spectral red-shift. Viceversa a dark spot on the half of the disk receding us will lead to a spectral blue-shift (see Fig. 3.6)

The presence of spots, combined with the stellar rotation, can induce periodic RV variations, liable to be erroneously interpreted as indicative of the presence of a planet. In this respect, the bisector analysis proved to be a useful diagnostic [158]. Spots also generate photometrical variations which can be used to discriminate between planets and stellar activity. In particular, periodic photometrical variability with period similar to the RV variations, will strongly suggest the intrinsically stellar nature of the latter. Additionally, spots move on the stellar surface and have a finite lifetime, therefore the RV signal they induce will change in time.

– *Variability of granulation patterns.*

Late-type stars have convective envelopes where bubbles of hot gas continously rise up to the stellar surface, cool down and sink back again. This effect is at the origin of the observed granulation on the Sun disk. The rising part of the granules is located in the center where the plasma is hotter. The outer edge of the granules is darker due to the cooler descending plasma. The existence of granulation on spatially unresolved stellar disks is inferred from the typical C-shaped bisector of the photospheric absorption lines [66]. For an inactive star , although the granulation pattern is locally in continuous evolution, the disk-integrated line profiles are constant in time because of the high number of granules. On the other hand, active stars present areas with altered granulation associated with enhanced magnetic fields. As the star rotates, these inhomogeneus areas move across the stellar disk leading to a time-variable non-axisymmetric velocity field that produces apparent changes of RV. The latitude of the active region, its relative inhomogeneity, and the stellar $v \sin i$ are all factors that affect the bisector variability and the related changes of RV.

Young stars are challenging targets for high-precision RV measurements because

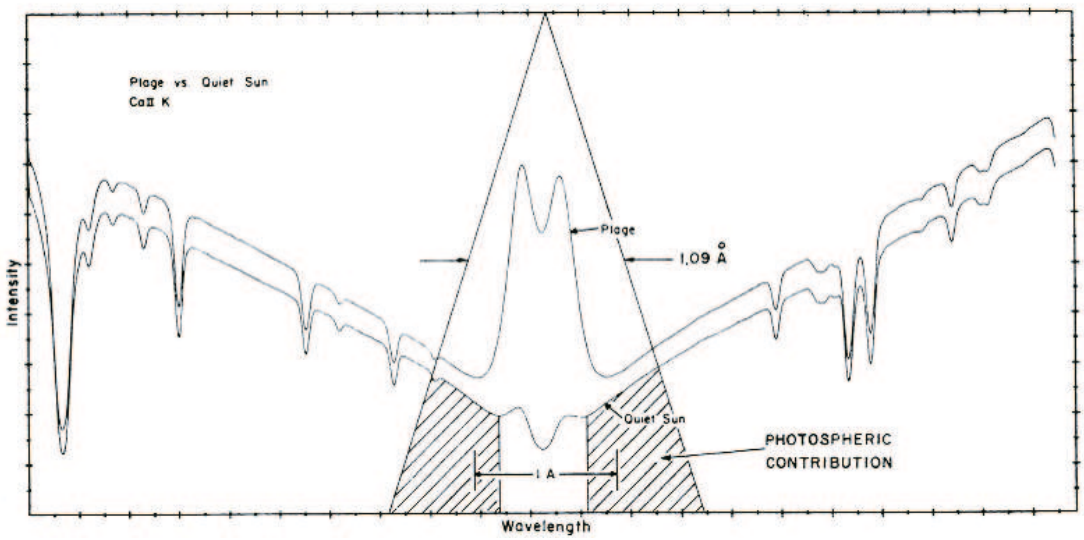

Figure 3.7: The central portion of the calcium K line from two regions of the solar surface: an area with little magnetic activity, the quiet sun, and one with strong magnetic activity, a plage. (From Hartmann et al. [72]).

of their relative larger rotational velocity and enhanced activity. A large amount of observational data have been now accumulated, showing that, statistically, stars rotate more rapidly when they are young. Both spectroscopic campaigns, able to measure the projected rotational velocity $v \sin i$, and photometric monitoring, that obtain the stellar rotational period from light curves, confirm this result [79]. A star with larger $v \sin i$ shows broader spectral lines which make it more difficult to measure precise RV. Moreover, broader lines have a higher chance to be blended, deteriorating the achievable RV precision further on.

Fast rotating stars have also higher level of activity. In fact, three ingredients combine to create magnetic activity in lower main sequence stars: convection in the external envelope, internal magnetic field, differential rotation. The role of a larger rotational velocity, thus, is to make more rapid and effective the rise of very intense magnetic lines of force that break through the star's surface and are observed as spots [144]. Young stars are expected to have numerous and larger spots together with more inhomogeneous convection patterns.

The surfaces of dwarf stars other than the Sun cannot be resolved, therefore the individual starspots cannot be seen [1]. Only the spatially averaged signal of starlight can be measured and the contribution from non-magnetic areas of the stellar surface dilutes the signal from magnetic areas. The most widely used indicator of stellar magnetic activity is the Fraunhofer H (λ3967) and K (λ3934) doublet of the calcium singly ionized (CaII). The cores of the H and K CaII lines show emission features that brighten with increasing magnetism (see Fig. 3.7) For the Sun, a low-activity star, the disk-integrated fluxes of the H and K emission cores can have relative changes on the order of 20% [203], a variability that can be easily measured.

[1] In fact Doppler imaging is a technique to reconstruct the spatial flux variations on stellar disks. However up to know it has been successfully applied only to very fast rotating stars ($v \sin i \gtrsim 40$ km s^{-1}).

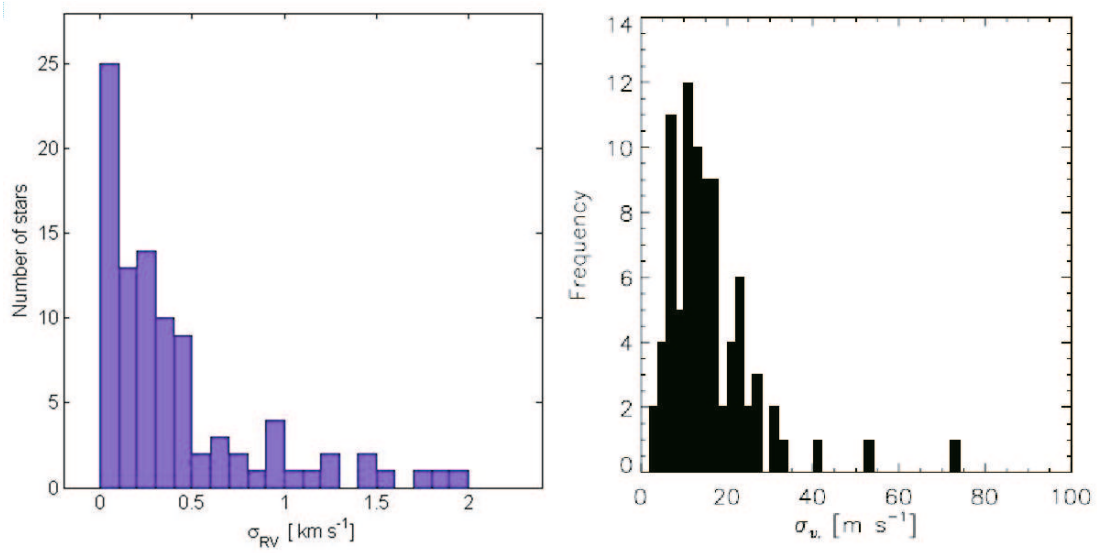

Figure 3.8: **Left:** Distribution of the scatter of RV measurements for a sample of young pre-main sequence stars (age $\lesssim$ 5 Myr) in Chamaeleon, Lupus, Scorpius Centaurus, ρ Ophiuci and Corona Australis star-forming regions. (Data from Guenther et al. [69]). **Right:** Same for a sample of stars member of the Hyades open cluster (age $\sim$ 600 Myr). (From Paulson et al. [146]).

While it is clear that an enhanced magnetic activity can lead to larger spurious RV variations, the exact amount of this RV-*jitter* is difficult to estimate on a theoretical basis. Saar & Donahue [162] first attempted to make simple models to assess the amplitude of RV perturbations. They found that for a solar-age G star, the amplitude due tue spots is $A_S \lesssim 5$ m s^{-1}, increasing to $A_S \sim$ 30-50 m s^{-1} for Hyades-age ($\sim$ 600 Myr) stars. Saar & Donahue also found that convective inhomogeneities can induce, on young F and G dwarf stars, RV perturbations with amplitude $A_C \lesssim 50$ m s^{-1}.

Interesting results come from previous RV surveys of young stars. Guenther et al. [69] report RV measurements for a sample of pre-main sequence stars belonging to several star-forming regions $\lesssim$ 5 Myr old (see Fig. 3.8). Such young stars often show an excess in the infrared emission that is indicative of the presence of a surrounding disk. Therefore, discovering planets of these stars would give interesting informations on the planet formation and the planet-disk interaction. Unfortunately, these stars display a typical RV-scatter of a few 100 m s^{-1} (in some cases up to a few km s^{-1}), making extremely challenging the detection of a planet RV signature. The situation improves significantly when member stars of the Hyades open cluster (age $\sim$ 600 Myr) are considered (see Fig. 3.8). Paulson et al. [146] surveyed a sample of 94 Hyades stars and found that most of them have a radial velocity rms less than 30 m s^{-1}, with an average of 16 m s^{-1}.

In this chapter it has been shown that the detection of planets of young stars will give an answer to many open questions about the formation and the orbital evolution of planetary system. Ideally one would like to observe planets while they are forming. However previous studies demonstrated that the RV technique is not possible for stars

with an age of $\lesssim$5 Myr due to the high level of activity they show. Therefore this study addressed stars with ages between 30 and 300 Myr; the full characterization of the surveyed sample is the main subject of the next chapter.

Chapter 4

The TLS survey of young stars: Characterization of the sample

In Chapter 3 the motivations for looking for planets of young stars have been discussed and it has been also pointed out that the age interval we are mainly interested in ranges from a few tens to a few hundreds Myrs. Locating stars of that age is not a straightforward task. Since the age of a star is not an observable, one has to rely on indirect age diagnostics. While several measurable quantities are known to be related to the age of a star, each of them has caveats; as of now a well calibrated age estimator does not exist. In Section 4.1 I will shortly describe the most used age diagnostics.

The sample was selected after a literature survey looking for objects showing one or more properties indicative of young age. The principal observational characteristics of the RV-monitored stars will be illustrated in Section 4.2. We surveyed 43 stars in total. This number is a trade-off between the will to have a statistically significant sample and the need to collect many spectra per star in order to detect with enough confidence the planet RV-signature.

In Section 4.3 brief notes on the individual stars in the sample are reported.

4.1 Age diagnostics

Very young solar-mass stars (1-5 Myrs), often referred to as T Tauri stars, have several distinct observational characteristics that make their identification relatively easy. They are observed in groups and often they are found in association with molecular clouds which provided the raw material for their assembling. T Tauri stars show large amplitude, irregular photometric variability which is ascribed to accretion events, and, compared to older stars of similar spectral type, they have an *excess* infrared emission originating from a circumstellar disk. Additionally their spectra display strong emission lines (primarily Hα) as well as characteristic lithium absorption lines.

As the time goes by, the residual gas in the cloud dissipates, circumstellar disks dissolve after possibly planets have been formed, clusters and associations disperse due to stellar differential velocities. Thus, in an influential paper in 1978, Herbig raised the question "Can Post T Tauri Stars be found?" [78]. It has been the work of the last three decades to identify and test a number of observable quantities that can be used as age diagnostics. In this respect, the ROSAT satellite, a X-ray observatory in operation from 1990 to 1999, gave a major contribution. As a result, last years have seen the discovery

of many young stellar associations as well as young field stars with estimated ages of few tens to a few hundreds Myrs.

4.1.1 Stellar kinematics

The knowledge of the three-dimensional motion of stars, together with models of the Galaxy gravitational potential, allows to trace back the positions of the stars, and recognize that stars, appearing today as indipendent field objects, were once packed in a much smaller volume and formed a stellar association. The time of maximum clustering offers a good estimate for the common age of those stars. This kinematical method requires precise measurements of stellar distances and proper motions and for this reason can be successfully applied only to nearby stars. For instance, this method has been used to evaluate an age of 11.5 Myr for the β Pictoris Moving Group [139].

Kinematical measurements cannot always be used to directly estimate stellar ages. Nonetheless, the fact that group of stars share the same spatial velocities has been used to infer their membership to the same stellar association and therefore their coevality. The common age is then evaluated on the basis of other age diagnostics [213].

4.1.2 The lithium Liλ6708 absorption line

The theory of pre-main sequence stellar evolution ([75], [74]) predicts that a star of mass $M_* \lesssim 1 M_\odot$ is fully convective during the earliest phases of its quasi-static gravitational contraction. As the radius decreases, a radiative core develops at the center, and the interface between radiative and convective zones gradually recedes toward the surface as the star approaches the main sequence. Bodenheimer [23] shows that the temperature at the bottom of the convection zone reaches sufficiently high values to destroy the lithium through mixing in the envelope only for stars in the low mass range (1.2 to 0.5 $M_\odot$). Thus, these stars, which correspond to late spectral types (G to early M), burn all the primordial lithium content during the early phases of their evolution. The presence of the lithium Liλ6708 absorption line is, therefore, used as a reliable diagnostic of young age for late-type stars [214]. However, measurements of Liλ6708 equivalent width (EW) for stars in young clusters show a significant spread for a given age and color. Speculations as to what causes the spread include rotation rate, magnetic fields, large photospheric spots, accretion, mass lost via a stellar wind. Therefore, while the presence of lithium is a clear indicatore of youth, the Liλ6708 can be used as an age estimator only in a statistical sense. It is useful in costraining the age of young coeval star associations, while it can provide only qualitative informations on individual field stars.

4.1.3 Rotation and activity

Stars spin down as they get old due to stellar wind. Therefore a high rotational velocity is a clue of youth for low-mass stars. However, as the initial spin rate extends over a wide range [79], a large rotational velocity alone is not enough to conclude that a star is young.

Different methods exist to estimate how fast stars rotate. Photometrical monitoring allows to detect periodic variability. Under the assumption that such variability is caused by spots transiting over the stellar disk, this allows a measurement of the rotational period P_{rot}. Single high resolution spectra offer the possibility to determine the stellar projected rotational velocity $v \sin i$, where i is the angle between the stellar spin axis

and the line of sight. As the $\sin i$ factor is usually unknown, there is an unsolved degeneracy between spin rate and axis inclination, in the sense that small $v \sin i$ stars are not necessarily slow rotators.

As we discussed in Section 3.4, larger rotational velocities induce an enhancement of stellar magnetic activity which manifests itself in different ways. Pizzolato et al. [152] studied a sample of 259 stars (110 main sequence field stars and 149 members of young clusters), and clearly showed the correlation between rotational period and relative X-ray luminosity ($R_X \equiv \log(L_X/L_{bol})$). For instance, the Sun has $R_X \simeq -5.5$, while young stars can have R_X up to -3. Thus, X-ray luminosity can be used as a proxy for the spin rate and, as a consequence, for age estimation. A further method relies on the emission in the core of the H and K calcium absorption lines (see Fig. 3.7). Many authors ([177], [138]) reported on CaII H & K surveys and confirmed the dependence of the emission intensity on the rotational period. The CaII H & K activity level is usually expressed by means of the R_{HK} index defined as $R_{HK} \equiv F_{HK}/\sigma T_{eff}^4$, where F_{HK} is the total flux in two narrow passbands centered on the H and K lines, or with R'_{HK} which considers only the cromospheric emission.

4.2 Characterization of the sample

In selecting the sample of stars to be surveyed with the TLS telescope (see Chapter 5), we had to take into account some constraints. First, most obviously, the $\sim 51^\circ$ Tautenburg's geographic latitude limits the observability to stars with declination $\delta \gtrsim -10^\circ$. It is a fact that the majority of the nearby young stellar associations lies in the southern sky [214], out of reach from Tautenburg. This unfortunate circumstance narrowed to some extent the choice. Columns 2 and 3 of Table 4.1 show the right ascensions and declinations of the 43 stars in our sample.

A fundamental requirement to measure radial velocities with high precision is to have high signal-to-noise (S/N) spectra. This translates into a lower limit on the brightness of the stars we can target. The Hyades and Pleiades young clusters are too far and therefore its members too faint for a RV survey with the 2m Tautenburg telescope. Figure 4.1 shows the distribution of V-band magnitudes for stars in our sample (see also column 4 in Table 4.1). Most of the stars fall in the range $6<V<8$ and all have $V<10$.

Figure 4.1 also points out that we selected mainly G and K spectral type stars. With respect to radial velocity measurements, G and K stars are the easiest objects to address because they present a larger number of absorption lines in the optical wavelength range. On the low mass end, M stars are more difficult because they are intrinsically fainter. Massive F and A stars are relatively bright but they show fewer photospheric absorption lines and tend to be faster rotators. Additionally, for early type stars the age estimation is more problematic.

In Fig. 4.2 the distribution of stellar distances is displayed (column 6 in Table 4.1). As a consequence of our magnitude limitation, all the stars are less than 50 pc away from us. Distances have been derived from the Hipparcos satellite parallaxes. The proximity of the stars has the additional advantage to make them suitable targets for prospective interferometric and/or adaptive optics coronographic observations aimed to the direct detection of planetary light.

25 out of the 43 stars surveyed by us have been identified by different authors as members of young associations. In particular, 12 stars belong to the Ursa Major (UMa)

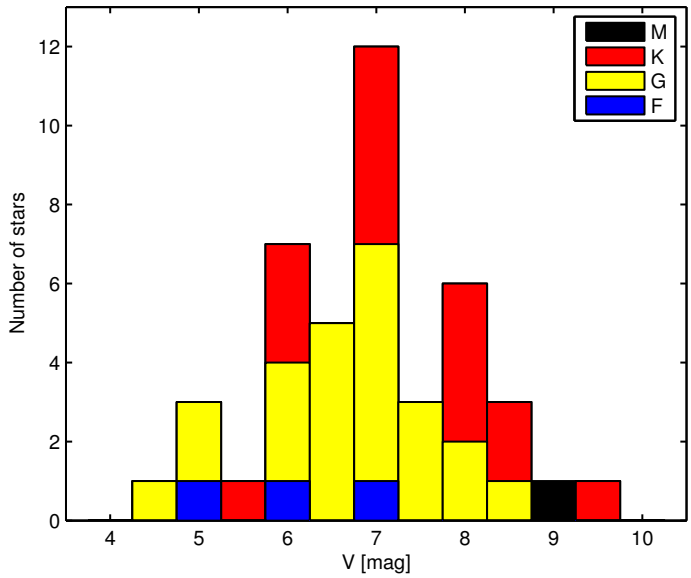

Figure 4.1: Distribution of V-band magnitudes for stars in the sample. It is also shown that mostly G and K spectral type stars have been surveyed.

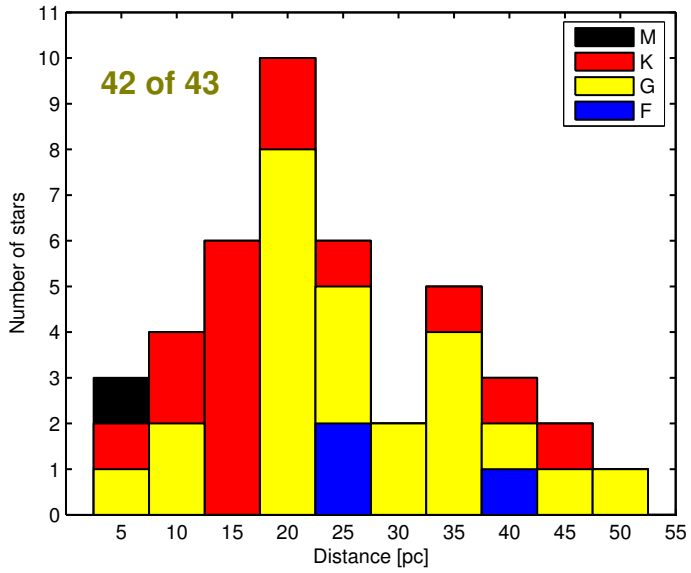

Figure 4.2: Distrubution of distances (in parsec) for 42 of the 43 stars in the sample. All distances are calculated from Hipparcos satellite parallaxes.

comoving group. Many authors agreed on a ∼300 Myr age for the UMa group (see for example Soderblom et al. [173]). However, recently King et al. [92] performed a reexamination of membership and age of the UMa group and concluded that it is probably 500±100 Myr old. 8 stars are members of the Local Association which is a widespread aggregate of young stars related to star formation in the Sco-Cen association ([28], [52]); the ages of stars within the Local Association span a range of 8-150 Myr. Additionally, we observed 1 star in the Hercules-Lyra association (∼200 Myr [107]), 1 in the Castor Moving group (∼200 Myr [129]), 1 in the AB Doradus Moving Group (∼50 Myr [212]), 1 in the Tucana/Horologium Association (∼30 Myr [213]) and 1 in the Hyades (∼600 Myr) that was brigt enough. The remaining stars have been recognized as young thanks to other age diagnostics like the presence of the lithium λ6708 absorption, the CaII H and K core emission and the enhanced X-ray luminosity.

Figure 4.3 displays the LiI λ6708 equivalent width (EW) for the TLS sample as a function of the B−V color index (respectively column 7 and 5 in Table 4.1). For each

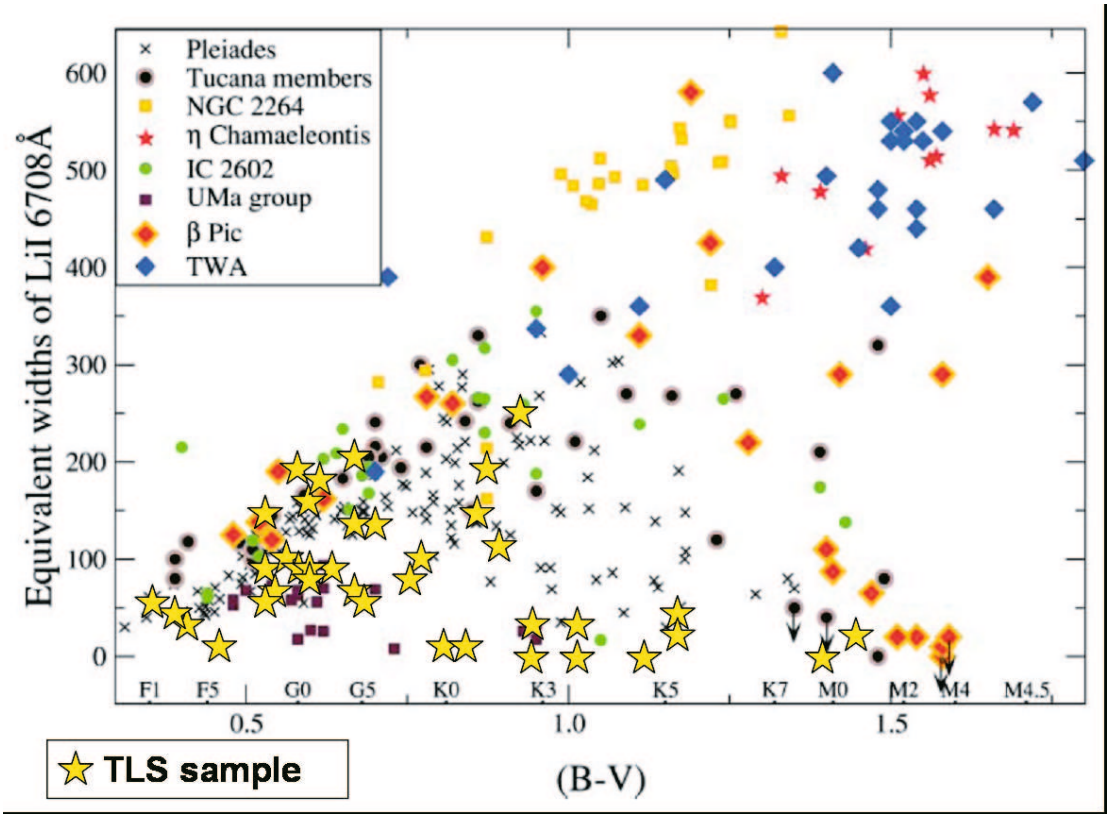

Figure 4.3: Compilation of equivalent widths of Li I 6707.76 Å, as a function of B−V, for star members of many young associations. Displayed equivalent widths are not corrected for possible contamination by Fe I 6707.44 Å. The ages of the clusters are as follows: Pleiades (∼100 Myr), Tucana (∼30 Myr), NGC 2264 (<5 Myr), η Chamaeleontis ($\lesssim$10 Myr), IC 2602 (∼30 Myr), Ursa Major (∼300 Myr), β Pictoris (12 Myr), TW Hydrae (∼10 Myr). Superimposed are the equivalent widths of stars in the TLS sample. (Modified from Zuckerman and Song(2004) [213]).

star, we compute Li EW values and errors by average and standard deviation after measuring EWs on every single spectrum. Our measurements are compared with a data collection [213] of many young stellar clusters of different ages. From Figure 4.3, it can be seen that ∼5 stars in our sample have age less than 50 Myr. There is then a numerous group (20-25 stars) with an age between the Pleiades age (∼ 100 Myr) and the Ursa Major group age (∼ 300 Myr). About 10 more stars are as old as the Ursa Major group. Eventually, we can not exclude that our sample contains a few older stars.

The examination of the X-ray luminosity can also add information about the age distribution of the surveyed stars. Unfortunately I found in literature the L_X/L_{bol} parameter only for 23 stars (Figure 4.4), though also the remaining ones are known to be bright X-ray sources.

4.3 Notes on individual stars

Here we report short notes concerning some of the stars in the sample. Remarkably many stars have been found to be part of binary or multiple systems. This circumstance must be taken into account if we want correctly interpret the results of our RV

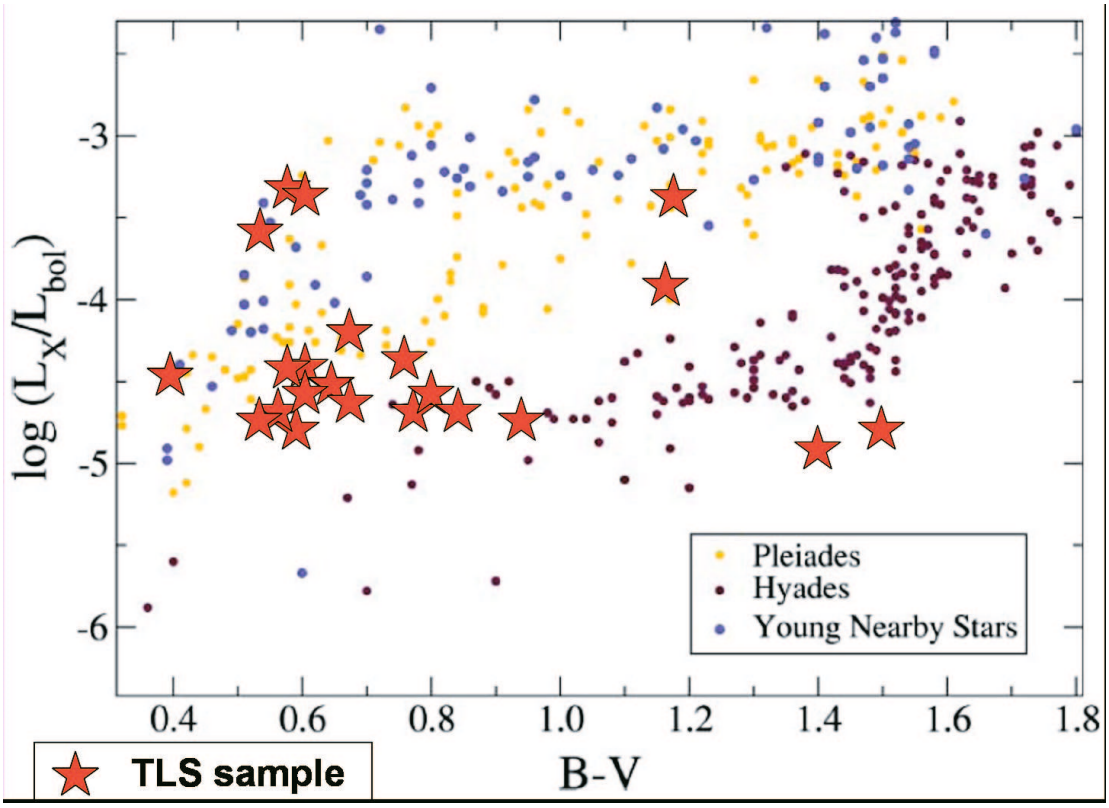

Figure 4.4: X-ray luminosity versus B−V color index of 23 TLS sample stars and, for comparison, of Hyades, Pleiades and other young nearby stars. (Modified from Zuckerman and Song(2004) [213]).

measurements.

HD5286: Horch et al. [81] found HD5286 to have a faint companion at an angular separation of ∼0.9 arcsec with Δ m = 0.91 at 503 nm.
HD17332: It is the brighter component of a visual binary. According to Zuckerman et al. [212] HD17332 is member of the AB Doradus moving group (age ∼50 Myr).
HD21845a: This G5 star has a M0 companion with magnitude V=10.5 at an angular separation of ∼8 arcsec.
V891 Tau: Paulson et al. [147] RV-monitored this star, taking 23 spectra with the MIKE spectrograph at the Magellan telescopes.
OU Gem: This is a close spectroscopic binary star with a visual companion [185].
HD77407: Visual binary with a 1.689 arcsec separation [132].
GJ355: Paulson et al. [147] RV-monitored this star, taking 23 spectra.
GJ577: Visual binary with a 5.39 arcsec separation [132].
GJ517: Paulson et al. [147] RV-monitored this star, taking 10 spectra.
HIP67422: Star with a companion at 3.6 arcsec [80]. This is most probably an old star.
Xi Boo A: Wittenmeyer et al. [205] report on the RV-monitoring of this star at McDonald Observatory with the 2.7m Harlan J. Smith Telescope.

HD171746: Visual companion at 1.7 arcsec with 0.2 magnitude difference in R band [1].
HD180617: Very faint visual companion $\Delta m_V \sim 8$ [103].
SAO70137: Member of a double system with orbital period P=23.65±2.0 yr [44].
HIP114385: This object has a visual companion that is in turn a spectroscopic binary [96].

Table 4.1: List of stars monitored during the TLS survey. We report thr following informations: (1) Star's name; (2) Right ascension; (3) Declination; (4) V magnitude; (5) B−V color index; (6) distance; (7) average LiI λ6708 equivalent width; (8) projected rotational velocity $v \sin i$; (9) photometric rotational period P_{rot}; (10) CaII H and K stellar activity indicator R'_{HK}; (11) X-ray luminosity parameter $R_X \equiv \log(L_X/L_{bol})$; (12) Young cluster membership; (13) Notes: 'y' means that additional information on the star is reported in Section 4.3.

Star	R.A. (2000) h m s	Dec. (2000) ° ' "	V [mag]	B-V [mag]	d [pc]	EW(Li) [mÅ]	$v \sin i$ [km s^{-1}]	P_{rot} [days]	$\log(R'_{HK})$	$\log(R_X)$	Assoc.	Notes
(1)	(2)	(3)	(4)	(5)	(6)	(7)	(8)	(9)	(10)	(11)	(12)	(13)
GJ5	00 06 36.784	+29 01 17.41	6.09	+0.76	13.70±0.14	82±7	4.1$^{(c)}$	6.23$^{(c)}$	-4.38$^{(c)}$	-4.38$^{(c)}$	Hercules-Lyra$^{(a)}$	n
HD3126	00 34 27.171	–06 30 14.06	6.92	+0.42	41.5±1.5	39±10	– –	– –	– –	– –	– –	n
HD5286	00 54 58.107	+23 37 42.01	5.46	+1.02	38.9±2.0	33±4	– –	– –	– –	– –	– –	y
HD7590	01 16 29.253	+42 56 21.91	6.61	+0.54	23.64±0.42	97±5	6.4$^{(c)}$	5.67$^{(c)}$	-4.46$^{(c)}$	-4.72$^{(c)}$	– –	n
HD17332A	02 47 27.42	+19 22 18.6	6.87	+0.69	32.6±2.0	142±15	– –	– –	-4.39$^{(m)}$	– –	– –	y
HD17925	02 52 32.129	–12 46 10.97	6.04	+0.87	10.381±0.083	203±7	6.2$^{(n)}$	6.85$^{(n)}$	– –	– –	Local$^{(n)}$	n
HD20630	03 19 21.696	+03 22 12.71	4.82	+0.68	9.159±0.065	52±16	4.5$^{(c)}$	9.20$^{(c)}$	-4.44$^{(c)}$	-4.65$^{(c)}$	Field	n
HD21845A	03 33 13.490	+46 15 26.54	8.29	+0.67	33.8±1.6	209±21	7$^{(b)}$	1.454$^{(d)}$	-4.0$^{(e)}$	– –	AB Dor$^{(b)}$	y
V891Tau	04 15 25.787	+06 11 58.74	6.94	+0.68	20.89±0.50	67±10	8.5$^{(f)}$	7.20$^{(g)}$	-4.417$^{(h)}$	-4.18$^{(g)}$	Ursa Major$^{(f)}$	y
V774Tau	04 15 28.801	+06 11 12.69	6.33	+0.58	21.19±0.48	87±9	4.2$^{(c)}$	Undet$^{(c)}$	-4.52$^{(c)}$	– –	Ursa Major$^{(h)}$	n
HD37394	05 41 20.336	+53 28 51.81	6.25	+0.84	12.24±0.12	11±6	4.0$^{(c)}$	10.86$^{(c)}$	-4.44$^{(c)}$	-4.74$^{(c)}$	Local	n
HD41593	06 06 40.477	+15 32 31.58	6.76	+0.81	15.45±0.22	20±9	5.0$^{(c)}$	7.97$^{(c)}$	-4.36$^{(c)}$	-4.59$^{(c)}$	Ursa Major$^{(c)}$	n
V1358Ori	06 19 08.057	–03 26 20.37	7.96	+0.54	49.8 ±2.5	147±13	47$^{(d)}$	1.150$^{(d)}$	– –	-3.629$^{(d)}$	Tuc/Hor$^{(l)}$	n
OUGem	06 26 10.249	+18 45 24.86	6.76	+0.94	14.66±0.24	NO	– –	– –	-4.299$^{(h)}$	– –	Ursa Major$^{(h)}$	y
HD63433	07 49 55.061	+27 21 47.45	6.93	+0.64	21.82±0.42	91±7	6.1$^{(c)}$	6.46$^{(c)}$	-4.34$^{(c)}$	-4.55$^{(c)}$	Ursa Major$^{(c)}$	n
HD77407	09 03 27.082	+37 50 27.52	7.10	+0.6	30.08±0.82	167±9	7.0$^{(n)}$	– –	-4.34$^{(m)}$	– –	Local$^{(n)}$	y
GJ355	09 32 25.568	–11 11 04.68	7.88	+0.92	18.34±0.33	249±8	28$^{(f)}$	1.6042$^{(o)}$	-3.37$^{(p)}$	– –	Field	y
HD97334A	11 12 32.351	+35 48 50.69	6.41	+0.61	21.72±0.42	91±8	5.6$^{(c)}$	8.25$^{(c)}$	-4.41$^{(c)}$	-4.57$^{(c)}$	Local$^{(c)}$	n
HD103095	11 52 58.769	+37 43 07.24	6.45	+0.74	9.156± 0.065	??	0.5$^{(q)}$	– –	-4.85$^{(m)}$	– –	– –	n
HD109011	12 31 18.915	+55 07 07.72	8.10	+0.94	23.7±1.8	37±9	5.5$^{(c)}$	8.81$^{(c)}$	-4.36$^{(c)}$	-4.74$^{(c)}$	Ursa Major$^{(c)}$	n
HD111456	12 48 39.464	+60 19 11.36	5.85	+0.46	24.2±1.9	17±11	35$^{(r)}$	– –	-4.38$^{(r)}$	– –	Ursa Major$^{(h)}$	n
HD115043A	13 13 37.008	+56 42 29.77	6.84	+0.60	25.69±0.44	83±9	7.5$^{(r)}$	– –	-4.476$^{(h)}$	-4.45$^{(r)}$	Ursa Major$^{(h)}$	n
GJ504	13 16 46.515	+09 25 26.96	5.19	+0.59	17.95±0.27	88±6	7.4$^{(q)}$	3.30$^{(g)}$	-4.40$^{(m)}$	-4.82$^{(g)}$	– –	n
HD116956	13 25 45.532	+56 58 13.78	8.1	+0.4	21.85±0.34	50±8	5.6$^{(c)}$	7.80$^{(c)}$	-4.15$^{(e)}$	-4.48$^{(c)}$	Local$^{(c)}$	n

continued on next page

continued from previous page

Star	R.A. (2000) h m s	Dec. (2000) ° ' "	V [mag]	B-V [mag]	d [pc]	EW(Li) [mÅ]	$v \sin i$ [km s^{-1}]	P_{rot} [days]	$\log(R'_{HK})$	$\log(R_X)$	Assoc.	Notes
(1)	(2)	(3)	(4)	(5)	(6)	(7)	(8)	(9)	(10)	(11)	(12)	(13)
GJ517	13 34 43.206	–08 20 31.33	9.37	+1.17	19.79±0.39	41±19	14$^{(f)}$	3.96$^{(g)}$	– –	-3.38$^{(g)}$	Field$^{(g)}$	y
HIP67422A	13 49 03.996	+26 58 47.68	7.04	+1.12	13.65±0.25	NO	0.3$^{(q)}$	– –	– –	– –	– –	y
EKDra	14 39 00.212	+64 17 29.96	7.54	+0.61	33.94±0.70	190±15	17.3$^{(n)}$	2.787$^{(n)}$	-4.18$^{(m)}$	– –	Local$^{(n)}$	n
GJ563.4	14 50 41.181	–15 59 50.05	5.15	+0.36	23.66±0.58	64±23	10$^{(s)}$	– –	– –	– –	Castor$^{(n)}$	n
HD130948	14 50 15.811	+23 54 42.64	5.86	+0.56	17.94±0.26	106±10	6.0$^{(c)}$	7.85$^{(c)}$	-4.45$^{(c)}$	-4.69$^{(c)}$	– –	n
XiBooA	14 51 23.379	+19 06 01.66	4.54	+0.77	6.700±0.034	109±6	4.6$^{(q)}$	6.15$^{(t)}$	-4.39$^{(h)}$	-4.72$^{(v)}$	Ursa Major$^{(z)}$	y
XiBooB	14 51 23.1	+19 06 02	6.97	+1.17	6.700±0.034	30±17	– –	11.94$^{(u)}$	-4.424$^{(u)}$	-3.95$^{(v)}$	Ursa Major$^{(z)}$	n
HD133826	15 02 58.903	+65 46 41.80	7.26	+0.54	40.14±0.89	75±10	– –	– –	– –	– –	– –	n
GJ577	15 05 49.905	+64 02 49.95	8.42	+0.68	44.3±1.3	141±10	10.6$^{(q)}$	– –	-4.35$^{(m)}$	– –	– –	y
HD135599	15 15 59.167	+00 47 46.90	7.0	+1.4	15.58±0.24	NO	4.6$^{(c)}$	5.97$^{(c)}$	-4.583$^{(h)}$	-4.94$^{(c)}$	Ursa Major$^{(c)}$	n
HIP82959	16 57 10.695	+35 17 11.53	8.10	+1.45	14.6$^{(aa)}$	20±9	– –	– –	– –	– –	– –	n
HD171488	18 34 20.103	+18 41 24.23	7.40	+0.58	37.2±1.2	193±20	37.5$^{(y)}$	1.338$^{(x)}$	-3.70$^{(e)}$	-3.313$^{(x)}$	– –	n
HD171746	18 35 53.223	+16 58 32.51	6.22	+0.53	34.2±1.8	61±10	5.0$^{(j)}$	– –	-4.459$^{(h)}$	– –	Ursa Major$^{(h)}$	y
HD180617	19 16 55.257	+05 10 08.05	9.13	+1.50	5.874±0.047	??	– –	– –	– –	-4.80$^{(k)}$	– –	y
SAO70137	20 31 07.769	+33 32 34.45	8.35	+0.86	44.7 ±2.3	156±13	8.4$^{(e)}$	– –	– –	– –	Hyades$^{(n)}$	y
GJ824	21 16 32.467	+09 23 37.77	7.95	+1.02	16.17±0.28	NO	3.7$^{(q)}$	– –	– –	– –	Local$^{(n)}$	n
HNPeg	21 44 31.330	+14 46 18.98	6.00	+0.58	18.39±0.29	97±10	9.4$^{(c)}$	4.91$^{(c)}$	-4.41$^{(c)}$	-4.46$^{(c)}$	Local $^{(c)}$	n
HD217813	23 03 04.977	+20 55 06.87	6.60	+0.61	24.28±0.51	89±8	3.1$^{(c)}$	8.05$^{(c)}$	-4.47$^{(c)}$	-4.55$^{(c)}$	– –	n
HIP114385	23 09 58.874	+47 57 33.88	7.14	+0.61	29.4±2.0	115±18	6.1$^{(w)}$	2.95$^{(w)}$	-4.52$^{(m)}$	-3.37$^{(w)}$	– –	y

(a) Lopez-Santiago et al. [107]; (b) Zuckerman et al. (2004a) [212]; (c) Gaidos et al. [59]; (d) Messina et al. [125]; (e) Stressmeier et al. [177];
(f) Paulson et al. [147]; (g) Pizzolato et al. [152]; (h) King et al. [92]; (i) Zickgraf et al. [210]; (j) Schachter et al. [167]; (k) Linsky et al. [103];
(l) Zuckerman et al.(2004b) [213]; (m) Wright et al. [209]; (n) Montes et al. [129]; (o) Messina et al.(2006) [123]; (p) Strassmeier et al.(1990) [178];
(q) Valenti et al. (2005) [190]; (r) King et al.(2005) [91]; (s) Wollf et al. [206]; (t) Plachinda et al. [153]; (u) Saar et al. [161];
(v) Hempelmann et al. [77]; (w) König et al. [96]; (x) Messina et al.(2003) [124]; (y) Marsden et al. [113]; (z) Soderblom et al. [173]; (aa) Gershberg et al. [60]

Chapter 5

The TLS survey: Facilities, observations and data reduction

All the spectroscopic data analysed in this thesis have been acquired with the TLS Tautenburg telescope and the Coudé spectrograph. In Section 5.1 the instrumental setup is described and the corresponding performances are illustrated. The survey of young stars began already in 2001 and it is still ongoing. Section 5.2 reports the log of the observations: Up to now almost 2000 spectra have been taken which required a remarkable amount of observing time. The data reduction has been performed in a uniform manner on all the spectra, using the IRAF software. Section 5.3 explains the main steps of the image processing that from raw frames lead to one-dimensional stellar spectra ready to use for measuring radial velocities and further analysis.

5.1 The telescope and the spectrograph

The TLS observatory runs a Schmidt telescope with a fork equatorial mount ('Alfred-Jensch-Teleskop', see Figure 5.1). The primary spherical mirror is 2m in diameter and has a 4m focal length. The telescope seats in a 20m diameter dome and has no pointing limitations. The dome automatically follows the telescope movements, normally 2 minutes are sufficient to point and center on the slit spectograph a new target.

The Coudé spectrograph, which is situated in a temperature stabilised room (the Coudé room) in the cellar of the observatory, is optically coupled to the telescope by means of a system of 5 flat mirrors. The light enters the spectrograph through a slit whose width can be regulated. We adopted a 0.52 mm slit width corresponding to an aperture of 1.2 arcsec on the sky; this configuration allows the spectrograph to achieve its maximum resolutive power, that is $R = 67000$.

Just before the slit, an iodine cell can be moved in and out of the optical path. The iodine cell serves to superimpose on the stellar spectrum a dense pattern of narrow absorption lines. The iodine lines provide both a highly precise wavelength scale (calibrated with a Fourier-transform spectrum) and a specification of the spectrograph instrumental profile in situ over the spectrum. This allow to measure RVs with extremely high accuracy, down to a few m s^{-1} The spectral region where iodine lines are present ranges from ∼5000 to ∼6300 Å; this part of the spectrum is almost useless for any other purpose than RV measurements.

The main light dispersing element of the spectrograph is an Echelle grating with

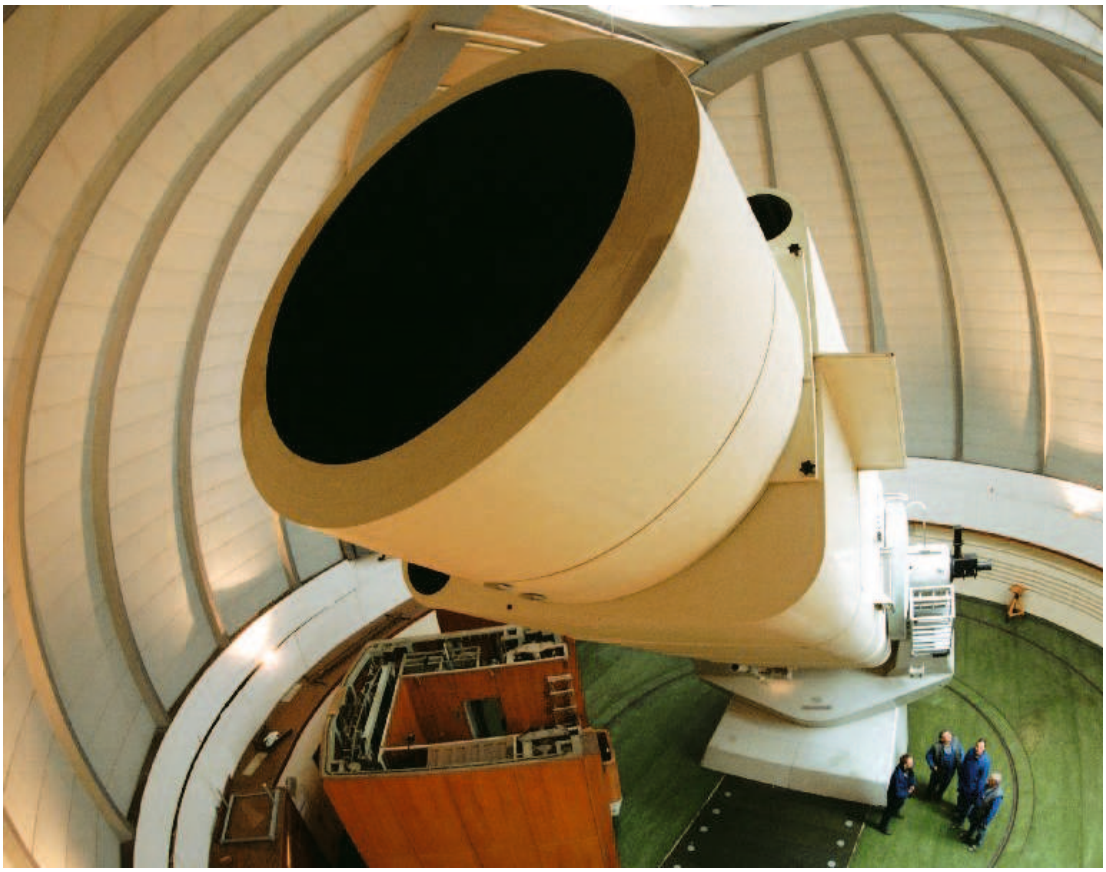

Figure 5.1: The 2m telescope ('Alfred-Jensch-Teleskop') at the TLS Observatory in Tautenburg.

31.6 grooves per millimeter. The grating has a blaze-angle of 65° and it is used in a quasi-Littrow configuration. Three grisms are available for cross-dispersing the light; with the visual grism that we always used the wavelength interval between 4700 and 7400 Å is covered, the light being distributed on 46 spectral orders (from 77 to 122).

The spectrum is finally formed by a camera onto a 2k×2k CCD chip with 15 μm square pixels. The sensitivity of the CCD is 2.6 e-/DN, and the Read-Out-Noise is 4.16 e-. Figure 5.2 shows how a typical CCD frame of an echelle stellar spectrum looks like.

The global instrumental sensitivity strongly depends on the seeing conditions, on the amount of extinction, and on the wavelength region used. The performances of the telescope+spectrograph system under typical observing conditions are illustrated in Figure 5.3. Thus, for instance, a signal to noise ratio (S/N) per spectral pixel equal to 100 is reached in one hour exposure time for a star of magitude in V of 9-9.5 with the visual grism.

Table 5.1 summarizes the main characteristics of the telescope, the spectrograph and the CCD in the configuration we adopted.

Telescope	
Latitude	50° 58' 48.4" North
Longitude	11° 42' 40.2" East
Altitude	341 m
Primary mirror	2 m
Spectrograph	
Resolving power	$R = 67000$
Spectral coverage	4700−7400 Å
CCD	
Array	2k × 2k
Pixel size	15 × 15 μm
Read-Out-Noise	4.16 e-
Sensitivity	2.6 e-/DN

Table 5.1: Technical data about the instrumental facility.

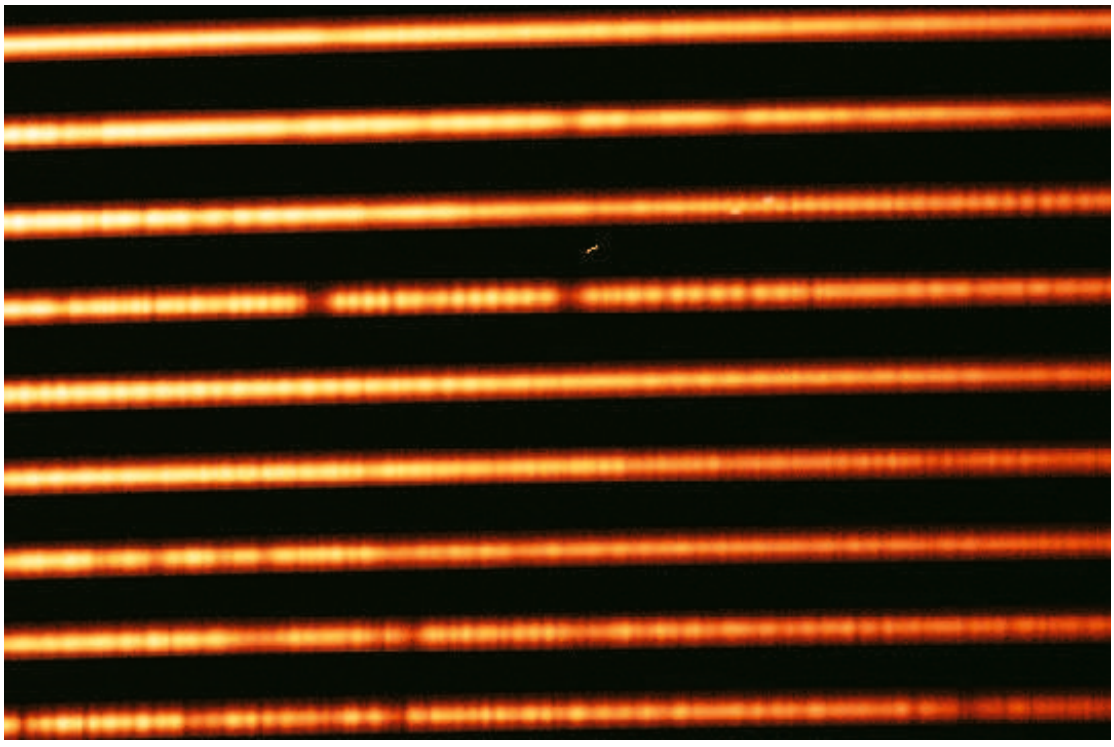

Figure 5.2: Small part of a frame of a stellar echelle spectrum. The two prominent absorbtion lines close to the center of the image are the NaI D doublet at 5890 and 5896 Å. The forest of narrow absorption lines that the iodine cell superimposes to the stellar spectrum is also clearly visible.

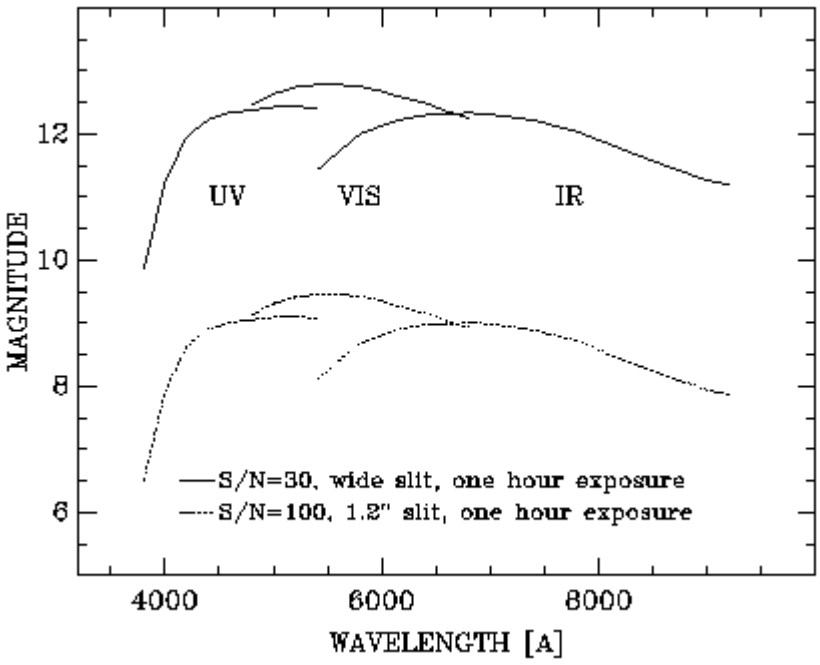

Figure 5.3: We show the limiting magnitude for two different cases (high resolution, high S/N-ratio spectra, and low resolution low S/N-ratio spectra) and for the three available grisms.

5.2 The observational campaign

First high-resolution spectra of young stars were acquired already in early 2001. As a rule, in Tautenburg two weeks a month are dedicated to spectroscopic observations. The survey of young stars shared this time with other observing programs, getting usually from 3 to 7 nights per month. Figure 5.4 shows the number of spectra that have been acquired month by month from 2001 to 2006. Beginning late 2005 new stars were included in the survey; since up to now these objects were observed only a few times, they will not be considered in this thesis. In Appendix A the heliocentric julian date (HJD) of all the spectra used for measuring radial velocities are reported. We have a total of about 1800 RV data points for the 43 objects in our sample. Most of the targets have between 20 and 50 spectra each (see Figure 5.5). Some of them appeared to be good candidates and for that reason were more intensively monitored (60 to 90 spectra).

The number of RV measurements for each star are showed in Table 5.2 together with the average exposure time. Those numbers do not include the additional spectra (one or more per target) acquired without iodine cell that served as reference. Table 5.2 also reports the average exposure times, which always are between 5 and 30 minutes. Although longer exposure times would provide higher S/N spectra, they are not recommended. In fact the number of cosmic rays hitting the CCD, which grows linearly with time, would become too high making a large fraction of the spectrum unusable for RV measurements.

5.3 Data reduction

The process of extracting informations from CCD images requires, besides science frames, additional calibration frames to be acquired. Namely:

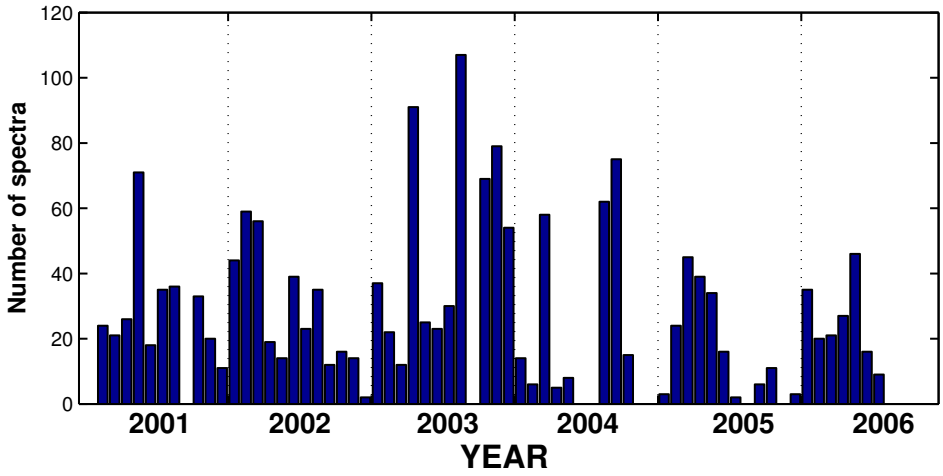

Figure 5.4: It is reported, month by month, the number of acquired spectra for targets in our sample. The campaign began in 2001 and continued regularly until 2006. Late 2005, other young stars were included to the survey which are not reported here.

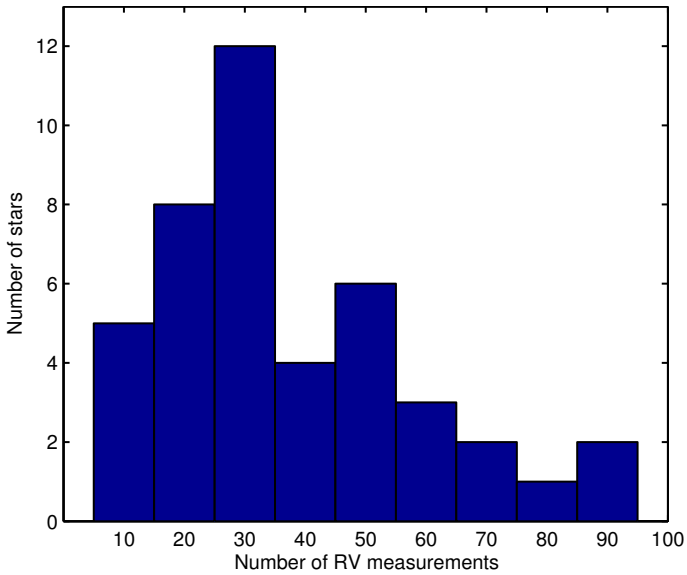

Figure 5.5: Histogram of the number of radial velocity measurements we obtained for the stars in our sample. Most of the targets have from 20 to 50 data points. Objects that during the survey turned out to be good candidates were intensively monitored and have now more than 60 RV measurements each.

Name	N_{obs}	$< t_{exp} > [s]$	Name	N_{obs}	$< t_{exp} > [s]$
GJ5	48	422	GJ504	86	465
HD3126	35	742	HD116956	34	1294
HD5286	52	392	GJ517	9	1375
HD7590	36	525	HIP67422A	15	956
HD17332A	8	1118	EKDra	73	1132
HD17925	33	508	GJ563.4	28	499
HD20630	25	365	HD130948	54	474
HD21845A	47	1229	XiBooA	54	380
V891Tau	29	601	XiBooB	16	450
V774Tau	35	455	HD133826	47	872
HD37394	21	391	GJ577	26	1223
HD41593	63	672	HD135599	12	727
V1358Ori	18	1232	HIP82959	19	1227
OUGem	13	711	HD171488	63	1174
HD63433	89	881	HD171746	33	378
HD77407	43	885	HD180617	18	1320
GJ355	20	1275	SAO70137	32	1200
HD97334A	37	488	GJ824	26	1190
HD103095	20	457	HNPeg	64	404
HD109011	33	1268	HD217813	28	469
HD111456	79	447	HIP114385	44	1004
HD115043A	71	610			

Table 5.2: Number of observations and average exposure times for the stars in our sample.

- **Bias:** These are frames with zero exposure time which serve to evaluate the slight variations of the pedestal level as a function of the position on the chip. We routinely acquire biases in groups of ten, once or twice during each observing run.

- **Flat field:** Flat field (FF) frames are obtained by illuminating uniformly the CCD chip, and are used to remove pixel to pixel gain variations. In spectroscopic applications they consist of high S/N spectra of a suitable lamp which provides smooth continuum emission. We take FFs in groups of 5−10 ($t_{exp} = 450$ s) pointing the telescope to a white screen into the dome illuminated by the lamp.

- **Comparison lamp:** In order to wavelength calibrate stellar spectra, emission lines spectra from lamps designed on purpose are normally used. In the optical wavelength range a common choice is a hollow cathode lamp containing a mixture of Thorium and Argon (ThAr lamp) which presents hundreds of narrow unblended emission lines. We take ThAr spectra at the beginning and at end of every observing night; sometime additional ThAr spectra are acquired in the middle of the night. While we use the ThAr to wavelength calibrate the full stellar spectrum, a more accurate calibration is provided by the iodine cell on the 5000−6300 Å interval used for the RV measurements.

The data reduction has been performed using the IRAF software (Image Reduction and Analysis Facility). The preliminary work is done with the noao.imred.ccdred IRAF package; the actual echelle spectra reduction is performed with a set of specific tasks

implemented in the noao.imred.echelle package. Following is a short outline of the main reduction steps resulting in stellar spectra in a suitable format for further analysis:

- **Bias subtraction:** This operation consists of two steps. First, the chip's 'overscan' region is used to estimate the average pedestal level, on science as well as calibration exposures. This value is subtracted from the frame and the overscan region is trimmed. Second, the bias exposures are averaged, the mean bias is fitted with a smooth function of the pixels coordinates and finally this function is subtracted from FF, ThAr and stellar exposures.

- **Apertures tracing:** An important point in the echelle spectra reduction is the exact location of the orders on the chip. The ideal spectrum to perform this task is one with a high S/N and a smooth continuum emission: FF exposures come in handy. Preliminarly the FF exposures are averaged to get an even higher S/N flat (FFa) where, thanks to a sigma-clipping algorithm, possible cosmic ray events are cleared away. The position and the width of the spectral orders (called apertures in IRAF) are interactively set on the central column of the frame. The IRAF routine then automatically traces the orders on both sides up to the edge of the frame, providing with the $y_n(x)$ fnctions with the index $n = 1, \ldots$,N, being N the number of orders to be extracted.

- **Flat fielding:** The flat-field image (FFb), used to correct for pixel-to-pixel gain variations, is obtained from FFa in the following way. Pixels in FFa falling outside the traced orders are fixed to the value 1. The intensity profile of each spectral order (mostly due to the blaze effect) is fitted and pixels inside the orders are divided by the fitting function leading to the normalized flat field FFb. Stellar as well as ThAr exposures are divided by FFb.

- **Order extraction:** The $y_n(x)$ functions are used to extract the orders from stellar and ThAr frames. The pixels along the width of the orders in the cross-dispersion direction can be either simply summed up or weights can be applied according to the 'optimal extraction' algorithm [82]. Before the extraction, inter-order pixels can be employed to fit and subtract background scattered light falling onto the chip.

- **Wavelength calibration:** The ThAr extracted spectra are wavelength calibrated first. This operation requires to interactively recognize a number of emission lines and assign them the proper wavelength. Based on the lines, IRAF calculates a preliminary dispersion solution $\lambda_n(x)$ and uses it to identify additional lines and calculate a refined dispersion solution. This process is iterated until no more lines can be identified. Alternatively, it is possible to make the wavelength calibration procedure fully automatic adopting as an initial guess the dispersion solution from a previous observing run. The stellar spectra then get the same dispersion solution $\lambda_n(x)$ as the ThAr spectrum that was acquired closer in time.

- **Normalization to continuum:** As a last step, stellar spectra must be, order by order, normalized to the continuum, that is the continuum is fitted by an adequate function and then the spectral order is divided by that function. The normalization is aimed to put spectra of the same star with different exposure levels to the same relative intensity scale, so that they can be more easily compared.

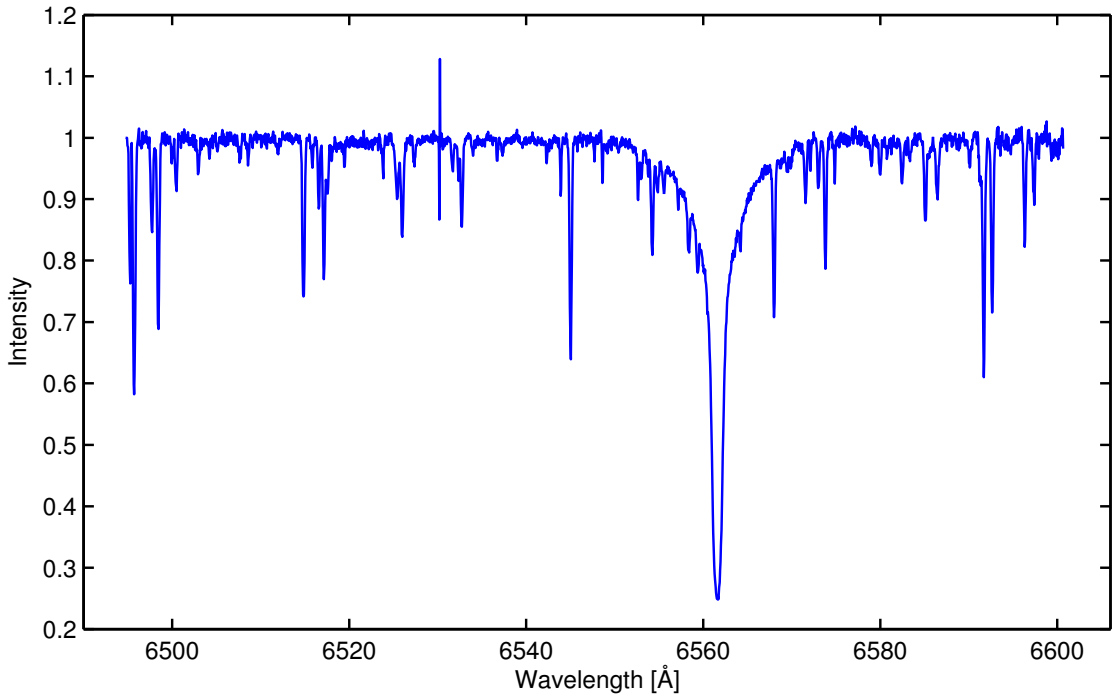

Figure 5.6: Example of an extracted, wavelength calibrated, normalized stellar spectral order.

Chapter 6

The art of measuring high-precision stellar radial velocities

For the detection of a planet like Jupiter an RV accuracy of a few m s^{-1} is required. For a long time this was considered as being impossible. However, a breakthrough of instrumental development at the end of the 20^{th} century made it possible, thus opening an entirely new field of research in astronomy. First attempts to measure RV date back to the end of nineteenth century ([194], [32]). At that time prisms were used as light dispersing elements and spectra were recorded on photographic plates; by considering single absorption lines, a RV precision of $\sim$1 km s^{-1} was often claimed, however measurements were affected by systematic errors as high as $\sim$10 km s^{-1} ([154], [58]). In the first fifty years of the twentieth century many technical improvements occurred like the introduction of diffraction gratings, the development of more sensitive photograpic films, the coming in use of more stable coudé spectrographs. Nevertheless over the sixties the typical accuracy still amounted to $\sim$1 km s^{-1} [204]. Griffin in 1969 [67] first introduced a new matching technique for measuring RV. The technique involves the use in the focal plane of the spectrograph of a special diaphragm which transmission varies along its length in a manner related to the spectrum typical of the star to be observed. The transmitted light is then focused and registered with a photomultiplier. It is expected that, scanning the spectrum, a minimum of light will be measured when the diaphragm matches the spectrum. The RV can be then measured in terms of the diaphragm matching position. Following refinements of the technique allowed Griffin to achieve RV accuracy of $\sim$0.4 km s^{-1} or better [68].

Today, almost all the planet searching RV surveys are performed employing a cross-dispersion echelle spectrograph jointly with a large format CCD, so that large S/N spectra with both high spectral resolution and broad wavelength coverage can be obtained. The Doppler information, carried by spectra acquired in this way, is a key factor to attain the few m s^{-1} precision necessary to measure the tiny RV variations that a planet induce on its host star.

An even more important factor which defines the ultimate RV precision is the wavelength calibration accuracy. Currently two different techniques are used to provide stellar spectra with a fiducial wavelength scale: the reference lamp emission spectrum technique and the iodine absorption cell technique. They both allow to reduce the sys-

tematic errors to a level of a few m s^{-1} ([31], [117]), in a regime where the dominant source of RV error, under common observing conditions, is the S/N of the spectra.

Precise RVs are measured in Tautenburg by means of the iodine cell technique. In this chapter the general method to extract RV information from a stellar spectrum with superimposed iodine absorption lines will be described . Additionally, the basic principle of RADIAL, the software package implementing the method, are discussed (Section 6.1). Section 6.2 is devoted to the analysis of the RV errors associated with spectra taken for the stars in our sample.

6.1 The iodine cell technique

Many sources of systematic errors exist which can affect the ultimate accuracy of RV measurements. A major issue is the movement of the photocenter of the stellar image at the spectrograph slit, due to atmospheric refraction, changing seeing conditions and telescope guiding errors. These movements, which can amount to a significant fraction of the slit width, convert to a $\lesssim$1 pixel displacement on the CCD corresponding to a $\sim$1 km spurious spectral shifts. Temperature fluctuations may induce variations in the relative position of the spectrograph optical components and also alter its figures. This effects not only cause spurious shifts but also affect the wavelength dispersion and the instrumental point spread function (PSF).

The usual technique to wavelength calibrate stellar spectra consists of tacking spectra of a reference thorium-argon (ThAr) lamp. The ThAr lamp provides a spectrum with a large number of narrow emission lines of known wavelength, distributed over the whole spectral range. The dispersion solution of the lamp spectrum is then directly applied to stellar spectra. However, since the light from the reference lamp traverses a path that might be slightly different from that of the stellar light, a systematic error on the wavelength calibration will be introduced. Additionally the lamp and stellar spectra are taken at different times so that occurring instrumental drifts will be not taken in account. The perfect solution would be to acquire a wavelength calibration spectrum at the same time and with the same light path as the stellar spectrum. This is the idea of the iodine absorption cell technique.

A iodine cell is a Pyrex cylindrical box with typical length and diameter of a few centimeters. It contains low pressure ($\sim$ 0.01 atm) molecular iodine (I_2) and, in operation, it is thermally stabilized. The working temperature in our case is 80 °C. The cell is placed right in front of the slit so that the stellar light has to pass trough it before entering the spectrograph. The cell superimposes to the star's apectrum a high density of absorption features. From 5000 to 6300 Å I_2 shows at least 2 features per Å with depth greater than 10%. Features are either single absorption lines or groups of intrinsically blended lines, that is they are not solvable no matter how high is the spectral resolution.

Retrieving the RV information from stellar spectra taken through a I_2 absorption cell requires a full modeling of the observation. The observed spectrum $S_{obs}(\lambda)$ is the product of the intrinsic stellar spectrum $S(\lambda)$ and the iodine cell transmission function $T_{I_2}(\lambda)$. This product has to be convolved with the one-dimensional instrumental profile IP. We have then the following formula

$$S_{obs}(\lambda) = k\,[T_{I_2}(\lambda)S(\lambda + \Delta\lambda)] * IP \tag{6.1}$$

where k is a normalization factor and $\Delta\lambda$ represents the Doppler shift we want to measure. Since the spectrograph IP can change significantly from zone to zone of the CCD, the observed spectrum has to be divided in chunks and every chunk is individually modeled.

The iodine cell transmission function T_{I_2} can be measured with high precision using a Fourier Transform Spectrometer (FTS). The resolving power of this instrument is as large as $R = 10^6$ and spectra with S/N$\sim 10^3$ can be acquired. Considering the typical resolutive power $R \lesssim 10^5$ of stellar spectrographs, the distortions introduced by the FTS IP can be neglected.

The intrinsic stellar spectrum S is somewhat more difficult to obtain. A spectrum of the star without iodine cell is taken with the same instrumental set-up as for the star+cell spectra. This spectrum can not directly serve as template S because in containts smearing from the spectrograph IP. A deconvolution of the IP is performed as follows. Observations of bright fast-rotating B-type stars are made through the iodine cell immediately before and after the stellar template acquisition. The spectrum of these B-type stars is essentially featureless so, after passing through the cell, they simply convey the I_2 absorption spectrum. By comparing the B star with iodine spectrum to the FTS iodine reference spectrum T_{I_2}, it is possible to calculate the IP [189]. This IP is then used to deconvolve the template stellar observation and obtain the "intrinsic" stellar spectrum S. S is usually calculated at an higher sampling rate than the observed spectrum S_{obs}. Within RADIAL 5 model pixels per observed pixel are considered. The transmission function T_{I_2} is interpolated and rebinned to the same sampling as S.

T_{I_2} and S are combined according to the Equation 6.1 to reproduce S_{obs}. In this best-fitting procedure a large number of parameters is set free to vary. The normalization factor and the Doppler shift $\Delta\lambda$ are only two of them. The wavelength scale has also to be modeled requirinq 2 or 3 parameters (for a linear or quadratic dispersion respectively). The ThAr wavelength calibration obtained with IRAF is used here as a start-up solution. RADIAL improves locally the wavelength calibration for every single chunk. RADIAL models the IP with 5 gaussians. That is a central gaussian and two lobes at each side of it. For the TLS spectrograph the IP is already very well reproduced if only the central gaussian is used. Figure 6.1 illustrates the modeling procedure.

RADIAL subdivides the observed spectra in N=130 chuncks of $\sim$10 Å each. The described fitting procedure is executed indipendently on all the N chunks, providing with as many independent RV measurements. In fact, it is always the case that some measurements are rejected as outliers due to either the presence of bad pixels due to cosmics in the corresponding chunk or to the improper convergence of the χ^2 minimization algorithm. Weighted mean and standard deviation of the indipendent estimations eventually supply the RV measurement with its error. It is worth noting that the iodine technique does not allow to measure absolute RV but only RV variations with reference to the template spectrum.

Stellar velocities measured from the Earth need to be transformed to a common inertial frame so that they are properly confronted. The inertial frame usually chosen is linked to the solar system barycenter (SSB) and the RV value to be added is referred to as the "barycentric correction". In order to keep the error on the barycentric correction well below 1 m s^{-1} many different effects must be taken in account [120]: the motion of the Earth around the Sun; the Earth rotation; the motion of the Moon around the Earth; gravitational perturbations from other planets; the proper motion of the observed star. RADIAL uses ephemerides for positions and velocities of the solar system bodies,

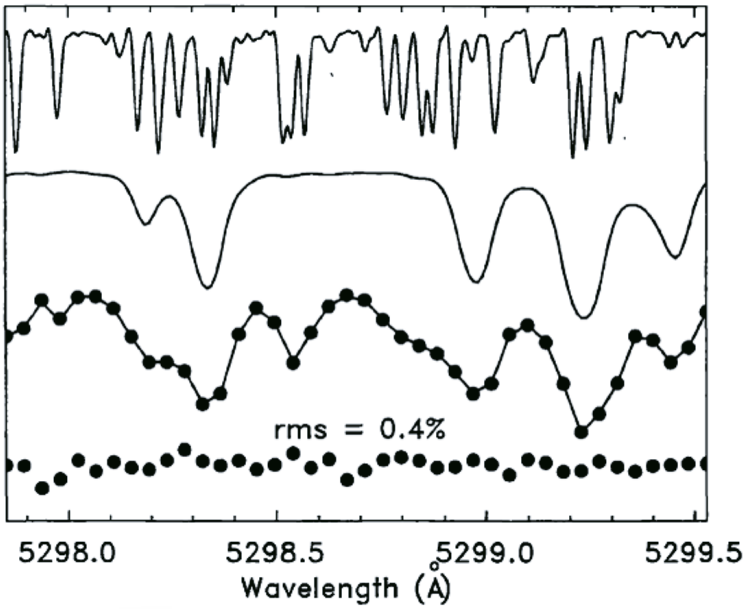

Figure 6.1: Top: The FTS iodine cell spectrum T_{I_2}. Second: An intrinsic stellar spectrum S. Third: The points represents an observed spectrum S_{obs} while the solid line is a model of the observation. Bottom: The differences between the model and the observation (the vertical scale is magnified by a factor of 10). (From Butler et al. 1996 [31]).

provided by the NASA Jet Propulsion Laboratory, in order to calculate the barycentric correction.

6.2 RV errors analysis

As described in the previous Section, RADIAL supplies RV measurements together with an "internal" estimation of the errors. It is useful to analyse how these errors correlate with the relevant stellar properties. In carrying out this analysis for the young stars in our sample, 7 objects which turned out to be binary systems (see Section 7.1) have been excluded. For each of the remaining 36 stars, the internal errors σ_{int} associated with the single RV measurements have been averaged to obtain $< \sigma_{int} >$.

Figure 6.2 shows the $< \sigma_{int} >$ versus the visual magnitude V. It can be seen that, not considering points with $< \sigma_{int} >$ larger than 50 m s^{-1}, the RV errors are basically independent on the stellar magnitude, at least up to V$\lesssim$8. Therefore for those bright stars the S/N of the spectra does not limit the ultimate RV precision. The average error for all those stars is $< \sigma_{int} > \sim$13 m s^{-1}, which is somewhat larger than expected. This circumstance has to be ascribed to the problems related to observing young stars. Figure 6.3 shows the dependence of $< \sigma_{int} >$ on the projected stellar rotational velocity $v \sin i$. The left panel displays that, for stars with $v \sin i >$10 km s^{-1}, RV measurements have systematically larger errors. The right panel zooms in the bottom left corner of the right panel, where most of the stars are located; it is evident the tendency of $< \sigma_{int} >$ to become larger for increasing values of $v \sin i$. A larger $v \sin i$ also enhances the stellar activity which in turn causes time-dependent variations of the absorption lines profiles (see Section 3.4). This fact can certainly contribute to increase the RV errors, although its effect is difficult to assess quantitatively.

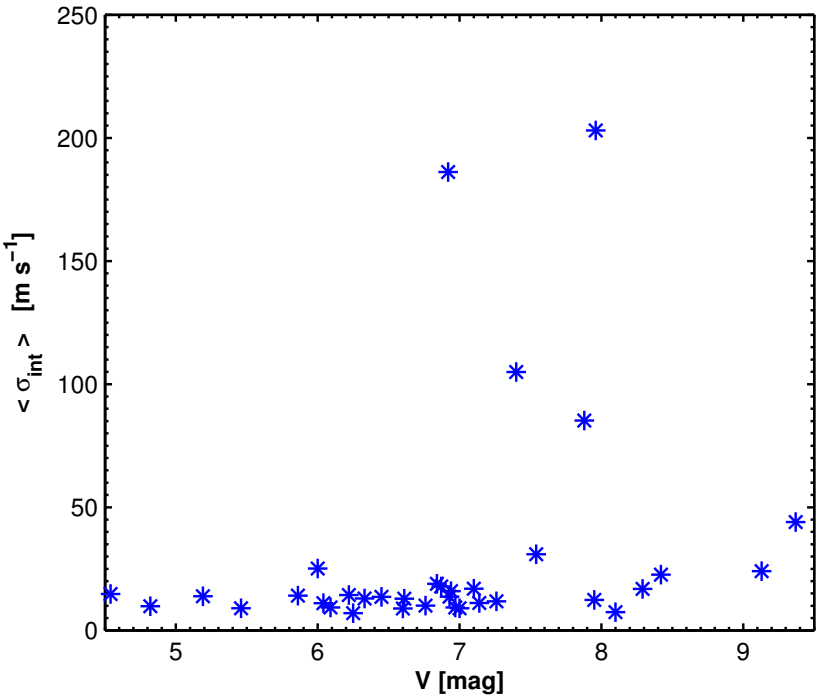

Figure 6.2: Average internal errors on the RV measurements, as estimated by RADIAL, plotted versus the visual stellar magnitude V. Up to V∼8 errors do not increase with magnitude meaning that the RV precision is not limited by the spectral S/N.

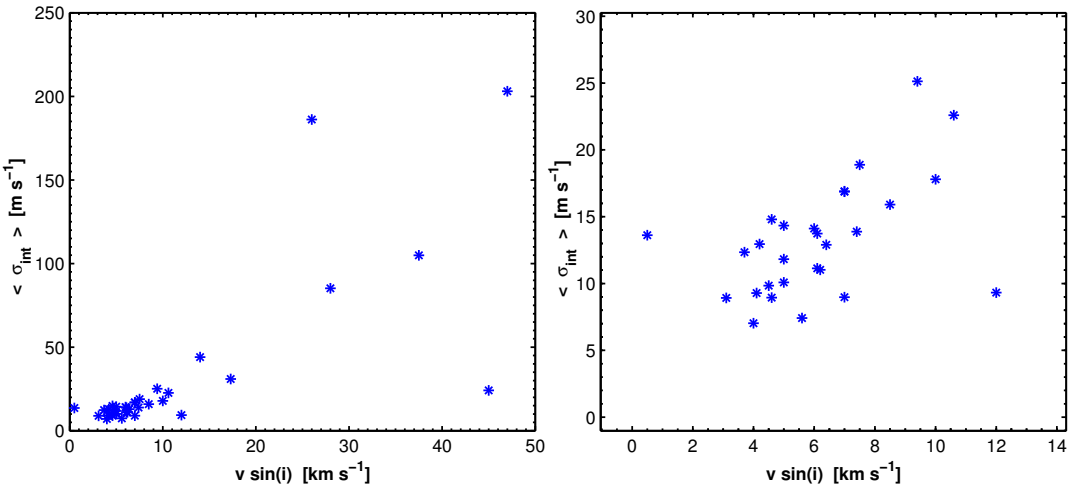

Figure 6.3: **Left:** This plot shows clearly the dependence of the RV errors on the stellar $v \sin i$. For fast rotating stars, errors are systematically larger. **Right:** A closer look to the stars with $v \sin i \lesssim 10$ km s^{-1} highlights the existence of a trend.

Chapter 7

Results

7.1 Spectroscopic binary stars

The first result obtained by the RV-survey is the detection of many spectroscopic binary stars.

HD111456: Freire Ferrero et al. [53] perform optical and near-infrared spectral synthesis of HD111456; although they find a best fit combining a F3-4V and a K5V spectrum they conclude, also on the basis of single lines analysis, that HD111456 is a single star. However, our RV measurements show clearly that this object is a single-line spectroscopic binary (SB1) with a period of $P = 1600$ days and an eccentricity of $e = 0.34$ (see Figure 7.1 and Table 7.1). Given its close distance of $d = 24.2 \pm 1.9$ pc, interferometric observations or AO imaging should be able to resolve this system.

HIP82959: The 19 RV measurements we took for this object showed it is a SB1 system. Although data do not cover a full orbital period, a credible orbital solution can be fitted to them (see Figure 7.1 and Table 7.1), with a period $P = 1394$ days and an eccentricity $e = 0.38$. Considering that the primary is a K2 star and that no signatures of the spectral lines of the secondary component are visible in the spectra, one can guess the secondary has to be a M star. This object, with a distance of 14.6 pc, is also a good target for interferometric and AO imaging.

HD109011: The amplitude of the RV variations clearly indicate that HD109011 is a binary star (Figure 7.2). However, the orbital period is so long that it is not yet possible to determine the orbital solution. Some RV measurements (HJD$\sim$2453400) depart from the general trend; the most probable explanation for this is that primary star absorption lines are distorted by the blending with secondary star lines which are, anyway, hardly seen inspecting spectra by eye. The last RV measurements, at HJD$\sim$2454100, indicate that we covered one full orbital period, however the fact they fall above the relative maximum at HJD$\sim$2452800 is interesting. This fact could be explained with the presence of a third star on a wider orbit which induce a RV trend. In this respect, it must be remarked that HD109011 is reported as an astrometric binary by Makarov & Kaplan [109].

GJ563.4: This object was first identified as a SB1 by Duquennoy & Mayor [47], based on CORAVEL RV measurements. Recently Beuzit et al. [20], using the PUEO adaptive optics system at CFHT, have imaged this double system (see Figure 7.3). They also report of additional CORAVEL RV measurements which allowed to fix the orbital

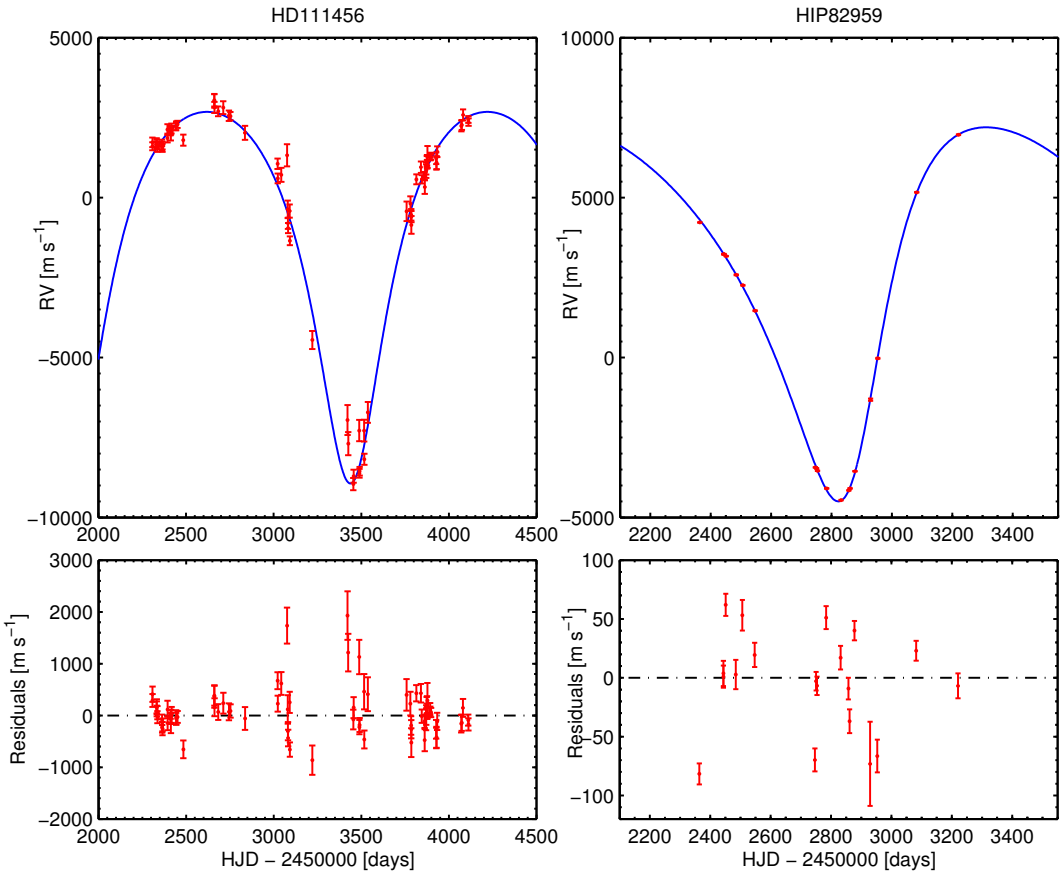

Figure 7.1: **Left:** HD111456: Our data just cover one orbital period, and we are able to fit an orbital solution. See Table 7.1 for the best-fit orbital parameters. The large RV errors are a consequence of the large $v \sin i$ of the star. Additionally it can not be excluded that the spectral lines of the faint companion contaminate the spectra making RV errors even larger. **Right:** HIP82959: Altough data do not cover a full orbital period we do attempt to determine a preliminar orbital solution (see Table 7.1). Few more spectra will help to fix the orbital parameters. The residuals appear to be significantly larger than the RV errors hovewer a periodogram analysis of the residuals has not revealed any significant signal.

	HD111456	**HIP82959**
P [days]	1600±5	1394.5±0.2
τ [HJD]	2451844±11	1490.20±0.05
K [m s^{-1}]	5807±65	5848±4
e	0.342±0.006	0.3771±0.0007
ω [°]	182.8±1.6	216.72±0.07
$a_1 \sin i$ [AU]	0.802±0.014	0.6942±0.0007
$f(m)$ [M$_\odot$]	0.0269±0.0015	(2295±8)×10^{-5}

Table 7.1: Best-fit orbital parameters for the SB1 HD111456.

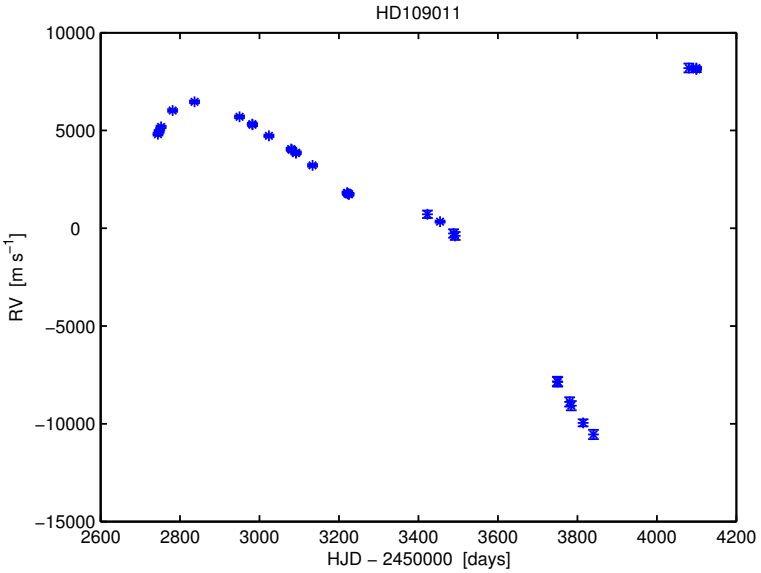

Figure 7.2: HD109011: Radial velocities plotted against heliocentric julian date. With a probable period of ∼1500 days and a peak-to-peak amplitude of ∼20 km s^{-1}, RV variations are certainly due to a companion of stellar mass.

period at P=5870 days. Our data, shown in Figure 7.3, cover only a fraction of the orbital period and confirm the nature of GJ563.4 as a SB1.

SAO70137: Docobo & Ling [44] report an astrometric orbital solution for this object (see Figure 7.4) and give a best-fit period P=23.65±2.00 yr and eccentricity e=0.34±0.10 as well as a Δm=0.1. Our spectra show asimmetric absorption lines which are the result of the blending of lines of the primary and secondary components; in fact the two components have RV differences which are never large enough to split the lines. While it is certain that the binary system has evolved in the time span of our observation, the RV linear trend we measure with RADIAL (see Figure 7.4) is not easy to interpret.

OU Gem: The analysis of the spectra of this object reveals its nature as of a double line spectroscopic binary (SB2) (see Figure 7.5). The presence of a double system of absorption lines could be deceptive for RADIAL and, as a consequence, the RV it measures are not reliable. Recently Karatas et al. [88] have reported an orbital solution for this system (K2V+K5V) with period P=6.99 days, eccentricity e=0.15 and mass ratio M_h/M_c=1.2.

HIP67422A: The orbital parameters of this double visual star are reported by Heintz [76] (P=155.75 yr, e=0.446). Strigachev & Lampens [180] observed HIP67422 in 2001 measuring a separation of 3.456" and a ΔV = 0.340 mag. Our RV measurements show irregular variations of ∼2 km s^{-1} in amplitude. The most likely interpretation for these variations is the light contamination from the secondary component changing according to the seeing conditions and the orientation of the slit relative to the binary position angle.

The possibility that some of the components of the binary systems host planets can not be excluded. Nevertheless we did not pursue any further analysis of the RV data. In fact possible light contaminations as well as incertainties in the binary orbital parameters make it particularly challenging to identify the possible planet RV signatures.

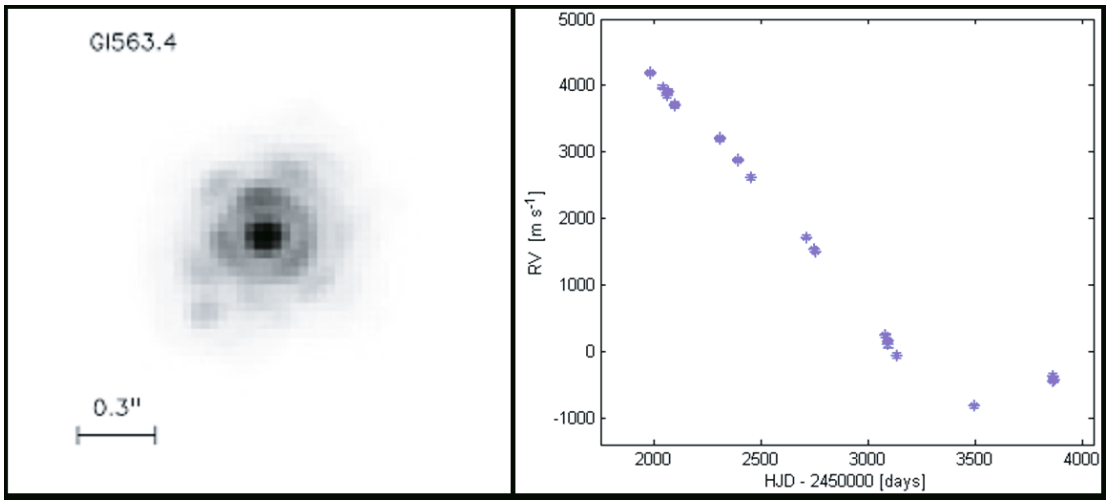

Figure 7.3: **Left:** AO imaging of GJ563.4 and its faint companion at an angular distance of 0.383" and with ΔH=3.4 (from Beuzit et al. [20]). **Right:** The Tauenburg RV measurements for GJ563.4.

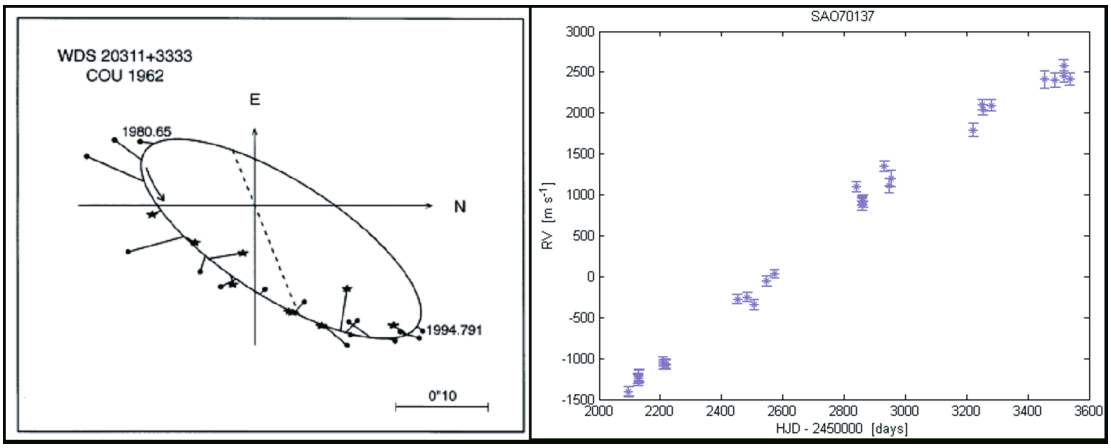

Figure 7.4: **Left:** Astrometric orbit of the double star SAO70137 (from Docobo & Ling [44]). According to this orbit the two stars were ∼0.1" apart at the epoch of the RV monitoring in Tautenburg, and we always saw them as a single star. **Right:** The RV measurements show a linear trend. Thus RADIAL is able to detect that the system is evolving, however the measurements can not be interpreted as the real RV of one of the two components.

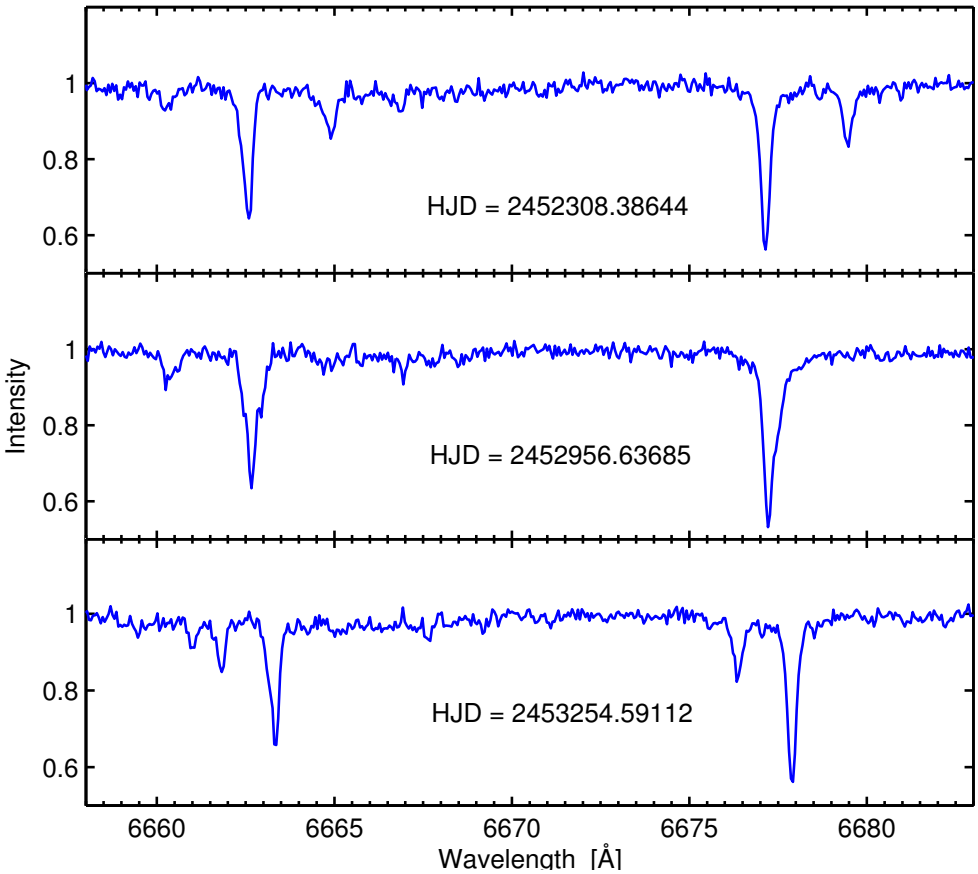

Figure 7.5: Spectra of the SB2 system OU Gem taken at three different epochs. They clearly show a double system of absorption lines moving with respect to each other.

7.2 The $v \sin i - RV_{scat}$ diagram

With the 7 binary systems left out (see Section 7.1), 36 stars remain where we can look for planets. A preliminar overall analysis of the RV data sets already gives interesting results. Figure 7.6 shows the RV scatter RV_{scat} plotted as a function of the stellar $v \sin i$. RV_{scat} is defined by the formula $RV_{scat} = \left(\sigma_{RV}^2 - < \sigma_{int} >^2\right)^{1/2}$, where σ_{RV} is the stellar RV standard deviation and $< \sigma_{int} >$ is the average RV internal error as introduced in Section 6.2. RV_{scat}, thus, is an estimate of the stellar RV jitters corrected for the $v \sin i$- $-< \sigma_{int} >$ trend (see Fig. 6.3). At this point we are also making the conservative hypothesis that no contribution to the RV variability comes from the presence of low mass companions. So as expected, there is a tendency for fast rotating stars to have a larger RV_{scat}. However, focussing our attention to the $v \sin i$<15 km s^{-1} part of the diagram, where 30 out of the 36 stars in the sample are located, we see that, for 28 stars it is RV_{scat}<80 m s^{-1} and for 23 it is RV_{scat}<50 m s^{-1}. This result demonstrates clearly that the detection of extrasolar planets of young stars by means of RV measurements is indeed possible. Figure 7.7 shows the mass-period diagram for the planets discovered up to now. Also reported are lines of equal RV semi-amplitude K (calculated for circular orbits and $M_* = 1 M_\odot$). A significant fraction of the known planets has a RV amplitude $2K \simeq$50 m s^{-1}. Such planets would be confidently detected if orbiting one of the young

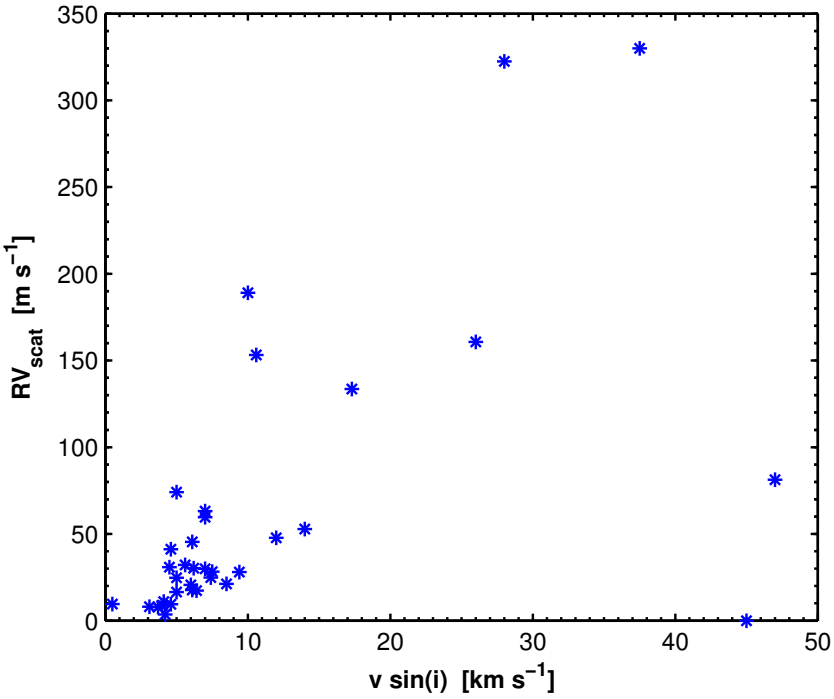

Figure 7.6: Correlation between RV_{scat} (see text for its definition) and the stellar $v \sin i$. Stars with $v \sin i$<15 km s^{-1} show a level of activity-induced RV variations which is low enough to allow the detection of the RV signature from a possible planet.

star in our sample. Schematically we divide the period-mass plane in three zones. The red zone is where the RV-detection of planets of young stars is virtually impossible, in the green zone on the contrary a planets would easily be discovered. The yellow zone represents a borderland where, depending on many factors (number of measurements, spectral S/N, etc.), a reliable detection could be achieved or not.

7.3 Periodograms analysis

The presence of a companion induces on its host star RV variations which are periodic. A powerful tool for the detection of periodic signals in unequally spaced data is the periodogram [39] [106] [166].

I calculated periodograms for each of the 36 candidate stars. Since the results turned out to be very sensitive to the presence of outliers, they have been preliminarily rejected after a visual inspection of the data sets. In no case more than two data points were rejected.

Together with the periodogram also the spectral window function is calculated. Spectral windows always show typical one day and one year peaks corresponding to the day/night cycle and target's seasonal observability. Additionally a one synodic month peak is also present as a consequence of the observing schedule in Tautenburg where usually only bright time is devoted to spectroscopy.

In order to assess the statistical significance of the peaks in the periodograms, I adopted the false alarm probability (FAP) levels as proposed by Horne & Baliunas [82]. Since there is not yet general agreement on the "correct" statistical way to calculate FAP levels [57], I also implemented the bootstrap randomization technique [97]. In this technique, the measured RV values are randomly shuffled keeping the observed times fixed and a periodogram for the shuffled data computed. The fraction of the random periodograms having power higher than the data periodogram yields the FAP that noise

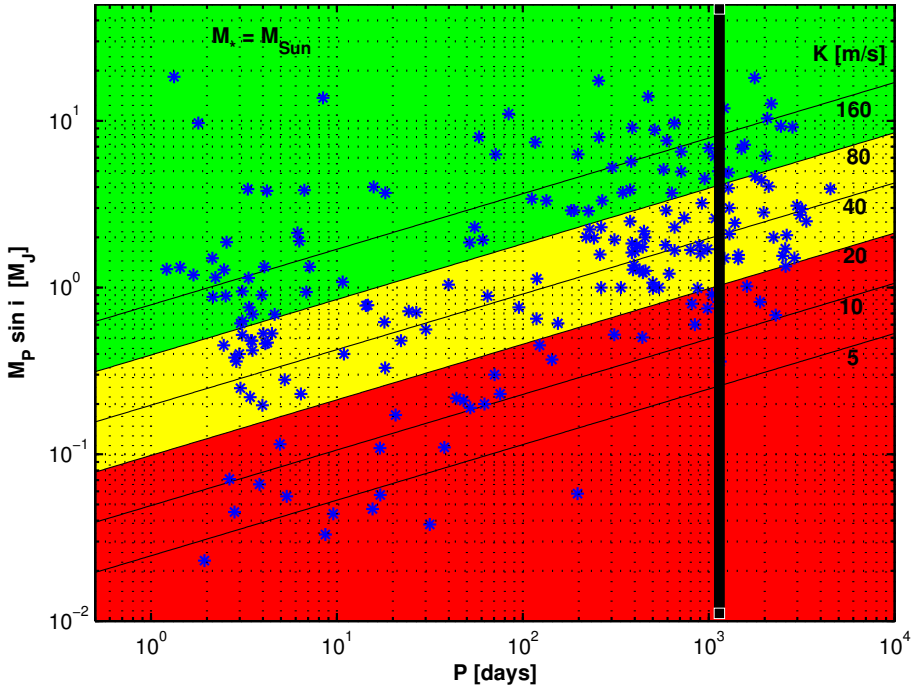

Figure 7.7: Distribution of the known planets on the minimum mass vs period diagram. Lines of constant K, the RV semi-amplitude, are also drawn (assuming circular orbits and $M_* = 1M_\odot$). The thick vertical line roughly corresponds to the time span of our RV survey.

would create the detected signal.

Figure 7.8 shows an example of Scargle and bootstrap periodograms, as well as the spectral window function, for the RV data set of GJ504, one of the best monitored stars. In the Scargle periodogram, two outstanding peaks can be noticed at f_1=0.47257 days^{-1} and f_1=0.53016 days$^{-1}\simeq f_{sw}$-f_1 , where f_{sw}=1.00273 days^{-1} is the position of the highest peak in the spectral window function. In fact the two peaks at f_1 and f_2 originate from a single periodic signal and are one the $\sim$1 day alias of the other.

The bootstrap periodogram shows the same peaks as the Scargle periodogram. A close-up of the highest peak (see Figure 7.9) serves to highlight similarities and differences between the two FAP estimation algorithms. It can be seen that the bootstrap periodogram perfectly mimics the Scargle periodogram, provided that the former is plotted on a inverse logarithmic scale. This means that the height of the Scargle periodogram peaks is indeed $\propto$-log(FAP), in qualitative agreement with the Horne & Baliunas semi-empirical formula [82]. However that formula is calibrated in such a way to greatly overvalue the FAP, that is to underestimate the significance of the Scargle periodogram peaks. For instance, considering the peak close to f=0.533 days^{-1}, while the bootstrap FAP is $\sim 10^{-4}$, the Horne & Baliunas formula gives a FAP$>10^{-2}$. Therefore, although it is a much more CPU-time expensive algorithm, I always perform the bootstrap analysis together with the normal Scargle periodogram.

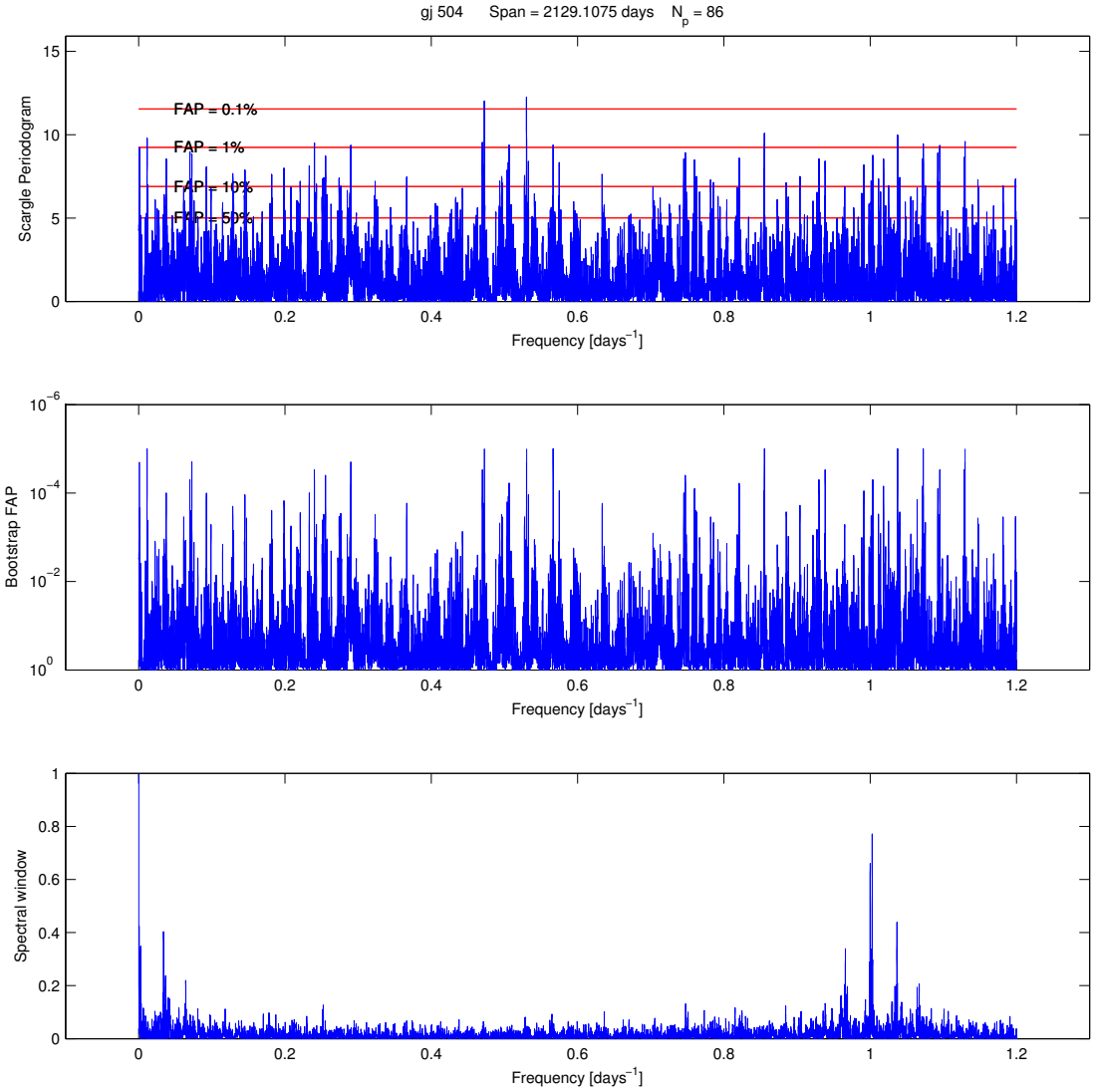

Figure 7.8: **Top:** Scargle periodogram for the RV data set of GJ504. The periodogram is calculated on the frequency interval 10^{-5}−1.2 days^{-1}, corresponding to periods ranging from ∼0.8 to 10^5 days. The horizontal red lines show different FAP levels determined according to the prescriptions by Horne & Baliunas [82]. **Middle:** FAP diagram for the same star and the same frequency range obtained by means of the bootstrap method. It can be seen that Scargle and bootstrap periodograms resemble to each other. I runned the bootstrap algorithm on 10^5 shuffled data sets, this explain why all the highest peaks "saturate" at the 10^{-5} value (the next possible value would be FAP=0 corresponding to an infinite height on the plotted inverse logarithmic scale). **Bottom:** Spectral window for the GJ504 RV data set. It can be noticed the peak at one month and the peak at one day together with its satellites. Given the x-axis scale, the one year peak is too close to zero to be clearly seen.

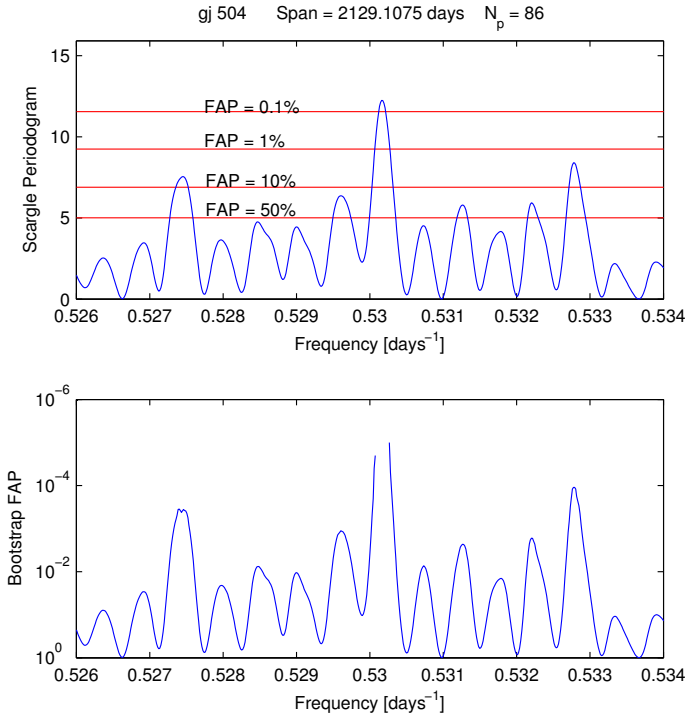

Figure 7.9: Close-up of the highest peak in the GJ504 periodogram. It allows to discern similarities and differences between the two FAP estimation algorithms. See text for more details.

7.4 Complementary analysis: photometrical variability

As I discussed in Chapter 3, periodic RV variations can be induced by activity phenomena such as the presence of spots on the stellar surface. Spots transiting the stellar disc also cause brightness variations, therefore a photometrical monitoring can help recognize and assess stellar activity. In addition, the presence of a periodic signal in photometrical time-series can be used to infer the stellar rotational period. Such studies have already been done for many of the stars in our sample and I have collected in Table 4.1 rotational period measurements from the literature.

For all the stars in the sample but one, Hipparcos satellite photometric time-series are also available. I performed the periodogram analysis of the data sets for every single star and the main results are shown in Table 7.4. Only for 20 out of 43 stars the periodograms present significant peaks. Quite surprisingly the results totally differ from what can be found in literature. In fact I find periodic variability where other authors do not find any, and viceversa. In addition, when periods are available both from the literature and my Hipparcos data analysis, they are always inconsistent. As an example the Hipparcos photometry for the star HD20630 is plotted in Figure 7.10. While I find that the Hipparcos data phase very well with a P=3.277 days period, Gaidos et al. [59] report a rotational period P=9.20 days for HD20630. I will anyway adopt the prudent policy to consider RV variations with periods close to the photometric ones as due to stellar activity rather than to a planet.

Name	N_{meas}	Hpscat [mmag]	Period [days]	Name	N_{meas}	Hpscat [mmag]	Period [days]
GJ5	98	11	11.81;3.06	GJ504	80	8	–
HD3126	72	9	–	HD116956	131	14	2.25
HD5286	92	5	–	GJ517	107	51	8.73
HD7590	97	9	1.67;1.13	HIP67422A	150	12	–
HD17332A	81	10	–	EKDra	100	27	2.34;1.42
HD17925	89	12	–	GJ563.4	83	3	–
HD20630	72	14	3.28;5.55	HD130948	149	11	–
HD21845A	92	36	2.71	XiBooA	105	13	–
V891Tau	44	11	1.86	XiBooB	–	–	–
V774Tau	43	7	1.79	HD133826	128	10	–
HD37394	141	10	–	GJ577	121	20	–
HD41593	79	15	9.33;6.69	HD135599	79	10	–
V1358Ori	98	26	1.39	HIP82959	150	18	–
OUGem	44	16	5.29;2.17	HD171488	145	31	1.69;1.20
HD63433	78	8	–	HD171746	124	12	2.96;8.03
HD77407	84	10	–	HD180617	82	17	–
GJ355	92	48	1.97	SAO70137	174	17	–
HD97334A	114	10	3.84	GJ824	89	12	1.39;4.52
HD103095	139	10	–	HNPeg	61	10	7.58
HD109011	161	15	–	HD217813	48	11	–
HD111456	142	7	–	HIP114385	202	84	1.74
HD115043A	126	11	1.87				

Table 7.2: Results of the analysis of the Hipparcos satellite photometric time-series. The first column shows the name of the stars. In the second column the number of data points are recorded. Usually one or two outliers are present that have been rejected prior to the periodogram analysis. The third column shows Hpscat, the scatter of the photometrical measurements as reported in the Hipparcos catalogue. Hpscat is a marker of the level of photometrical variability. For about half of the star in the sample, the periodograms show one or two significant peaks; the corresponding periods are reported in the fourth column.

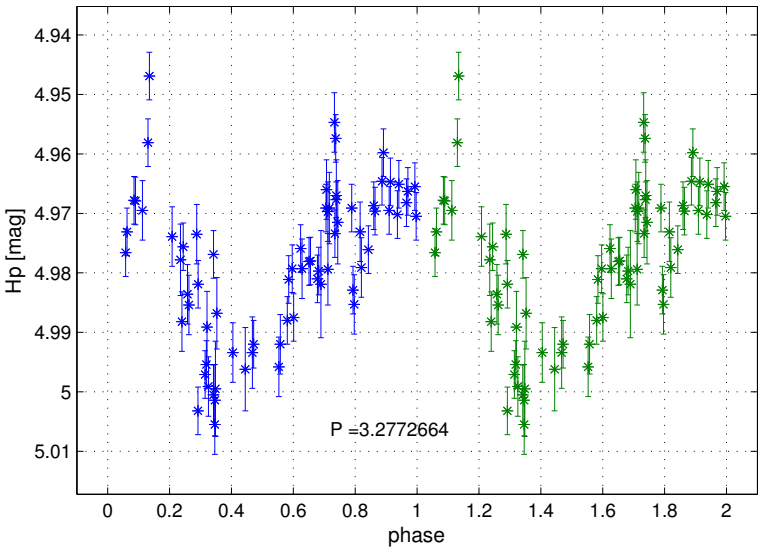

Figure 7.10: Hipparcos photometry of the star HD20630. Data are phase-folded according to the period $P = 3.277$ days, as obtained by the periodogram analysis.

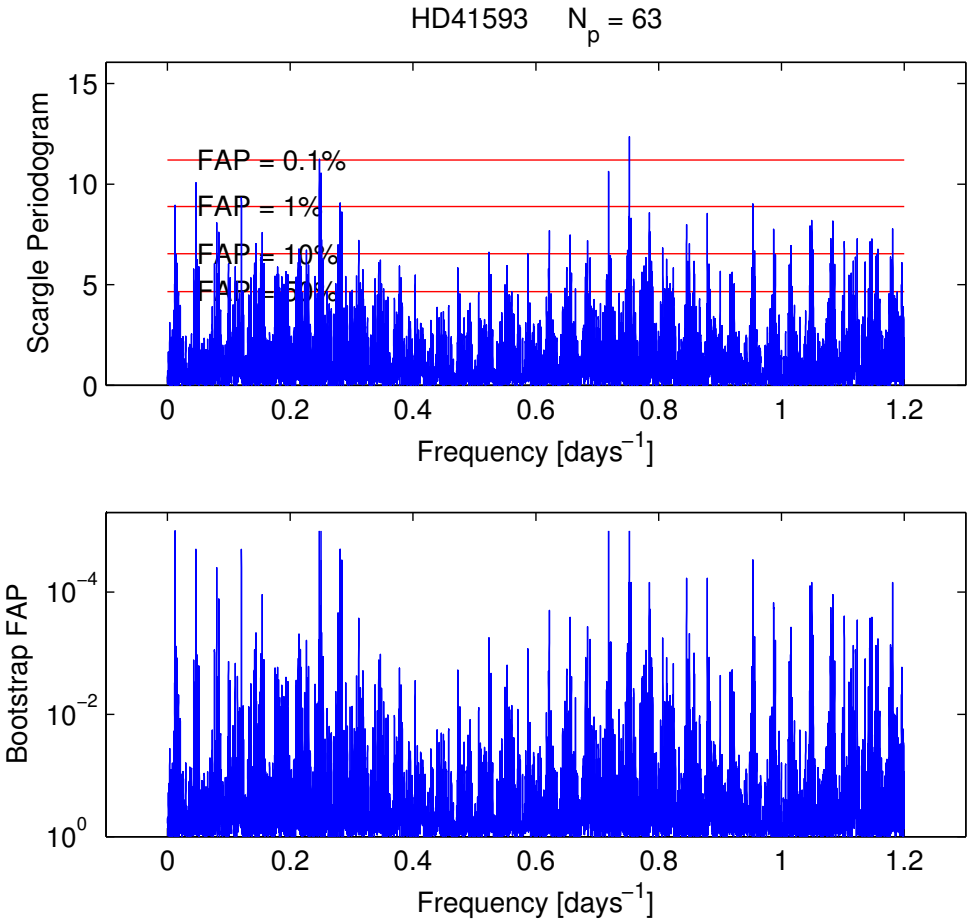

Figure 7.11: . Scargle and bootstrap periodograms for the HD41593 RV data set.

7.5 The case of HD41593

HD41593 is a K0V spectral type, magnitude V = 6.76, star with projected rotational velocity $v \sin i$ = 5.0 km s^{-1}, and it is a member of the 300-500 Myr old Ursa Major moving group.

The periodogram analysis (Fig. 7.11) of the 63 RV measurements shows two prominent peaks corresponding to periods P = 1.329 days and P = 4.038 days, which are one the 1 day alias of the other. Although the P = 1.3 days peak stands highest, after phasing the data points the RV curve for P = 4 days looks more convincing. Figure 7.12 displays the phase-folded RV measurements together with the best-fit orbital solution and the corresponding residuals. In order to obtain the best-fit solution I created a MATLAB code that implements a χ^2-mimimization algorithm and allows automatic rejection of outliers. Best-fit orbital parameters are shown in Table 7.3

At the present stage HD41593b can only be considered as a "candidate" planet. As it can be seen in Figure 7.12 as many as 16 data points out of 63 have been rejected on the basis of a 3σ clipping selection criterion. Additionally, the data points are not homogeneously distributed over all possible phases, in particular two gaps show up at phases $\phi \simeq 0.5$ and $\phi \simeq 0.7$. These facts rise doubts on the truth of the detected periodic

HD41593b	
P [days]	4.0394±0.0013
τ [HJD]	2452271.5±0.7
K [m s^{-1}]	25±7
e	0.25±0.13
ω [°]	34±59
$M_p \sin i$ [M$_{Jup}$]	0.157±0.053
a [AU]	0.046±0.031

Table 7.3: Best-fit orbital parameters for the candidate planet HD41593b.

signal. On the other hand HD41593 is known to be a variable star and the deviating RV measurements could corrrespond to isolated enhanced stellar activity episodes. The best-fit period (P=4.0394 days) is not equal to any of the photometric periods suggesting it is not related to possible rotationally modulated stellar variability.

A decisive contribution to solve the case of HD41593 could come from the bisector line analysis (see Section 3.4. A first attempt to measure the bisector on single isolated spectral lines did not succeed. In fact, given the small stellar $v \sin i$, the single lines are poorly sampled (5-7 points), and the predominant effect in the measured bisector variations turned out to be the photon noise. Both those problems could be overcome measuring the bisector of the cross-correlation function (CCF) which represents a sort of average spectral line [158]. However the CCF requires an accurate wavelength calibration all over the spectrum from which it is calculated. Unfortunately the only spectral regions usable for calculating the CCF are the ones free of iodine lines, but there the non-simultaneous Th-Ar wavelength calibration (see Section 5.3) results not to be accurate enough. A possible further attempt, which however I did not pursue , would consist of dividing out the iodine spectrum recovering the pure stellar spectrum. Such spectrum, being very well wavelength calibrated, would be suitable for the CCF calculation and the bisector analysis.

7.6 The case of HD171488

HD171488 is a G0V star with visual magnitude V=7.40. Although it is not a known member of any young stellar association, based on its lithium abundance, it has an estimated age of 30-50 Myr [179]. Given its large projected rotational velocity, $v \sin i = 39.0$ km s^{-1} [179], HD171488 is an ideal object for Doppler imaging analysis. Strassmeier et al. [179] determine a photometric rotational period P = 1.3371±0.0002 days. Assuming this period, they use 14 spectra, covering a 19 days time interval, to obtain a Doppler image of HD171488 (see Figure 7.13). They find a best-fit spin axis inclination of i = 55° and a large cool polar spot and various high-latitude cold features with a temperature contrast of 500-1600 K relative to the effective temperature. Marsden et al. [113] use 27 spectra, taken over five consecutive nights, to confirm the presence of a large polar spot extending down to almost +60° latitude. Additionally, they also account for differential rotation finding a best-fit to the observations for an equatorial rotation rate Ω_{eq}=4.786±0.013 rad (corresponding to a period P=1.313±0.004 days) and a rotational shear between the equator and the poles $d\Omega$ = 0.402±0.044 rad days^{-1} (meaning that

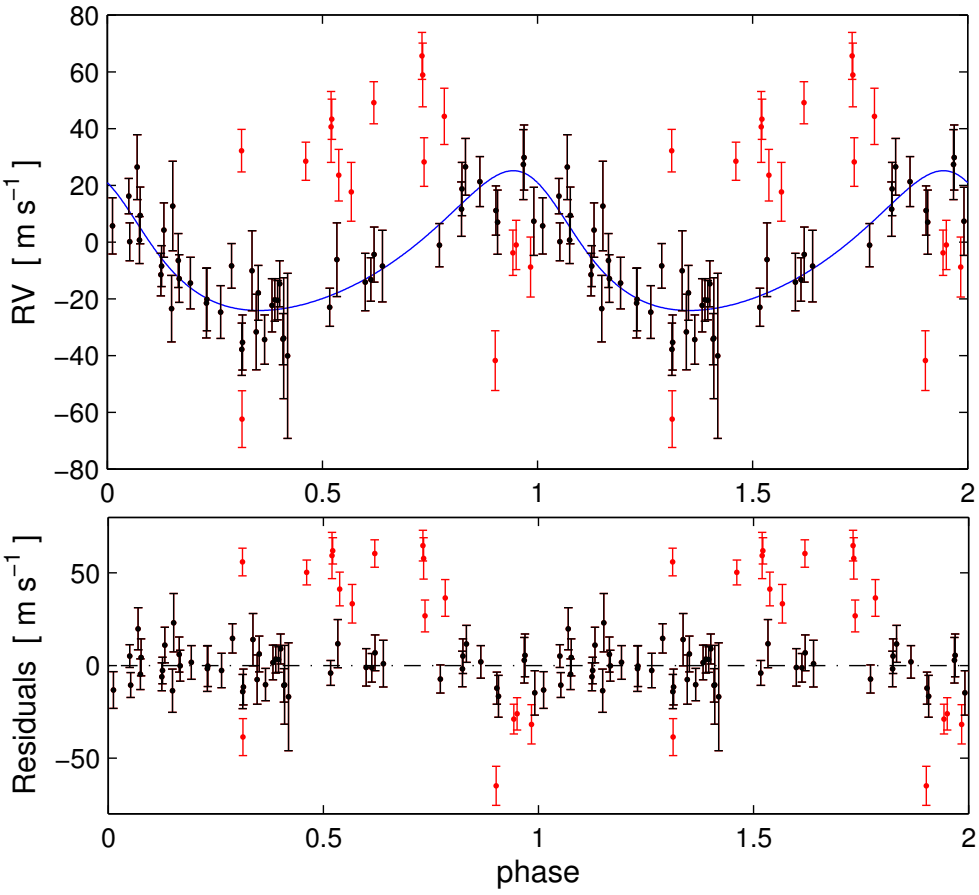

Figure 7.12: **Top:** Phase-folded RV measurements of the star HD41593. Superimposed is the best-fit orbital solution whose parameters are reported in Table 7.3. **Bottom:** RV residuals after the subtraction of the best-fit RV curve. Data points, that were rejected as outliers by the χ^2-mimimization algorithm, are displayed in red.

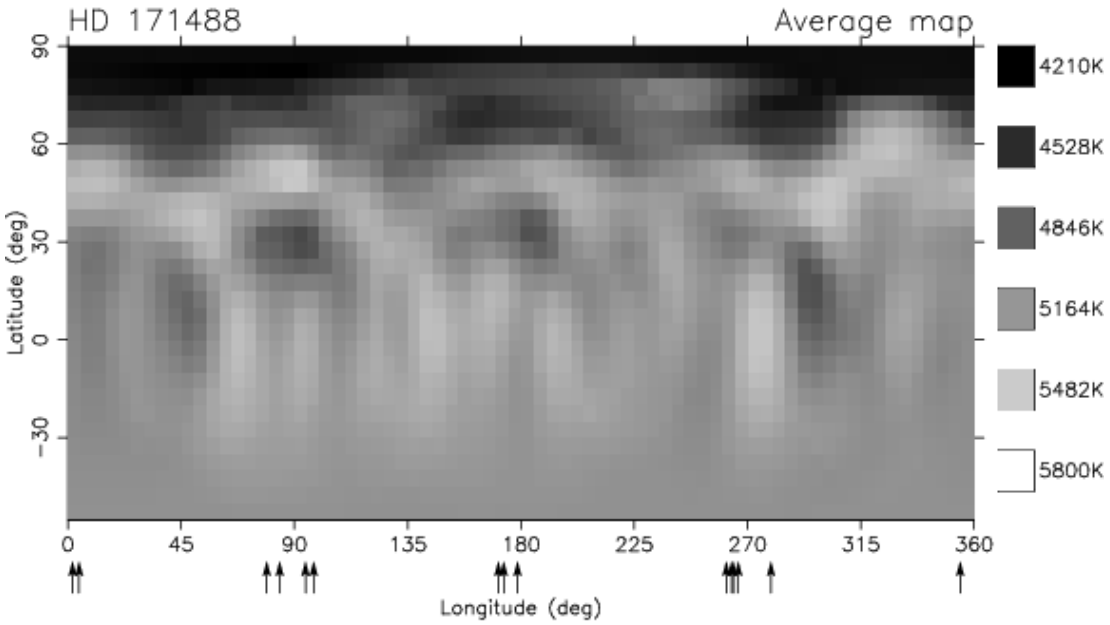

Figure 7.13: Doppler image of the star HD171488 resulting from the average of CaI6439, FeI6430, FeI6411 and FeI6393 Doppler images. The arrows below the map indicate the phase coverage of the spectra. (From Strassmeier et al. [179]).

16±2 days are needed for the equator to lap the poles).

At the TLS telescope 60 spectra of HD171488 have been taken, covering a period of almost 5 years. Quite interestingly, the periodogram of the RV data set (see Figure 7.14) shows the highest peak in correspondence of the period P=1.33698 days, which is consistent with the period determined by Strassmeier et al. [179]. Therefore, the source of periodic spectroscopic and photometric variations, whatever it is, keeps itself coherent for a time interval as large as 5 years. The RV measurements, phase-folded according to the period P=1.33698 days, are displayed in Figure 7.15. There is not a clear modulation visible in the RV variations, apart from almost systematically higher values for phases between ∼0.65 and ∼0.90. Whether this behaviour can be explained in terms of the spin axis inclination and spot distribution proposed by Strassmeier et al. [179], as shown in Figure 7.13, has still to be investigated.

7.7 Upper limits

The analysis of the RV data sets for 36 young stars leaded to the confident detection of not a single planet. This result, however negative, can provide preliminary statistical informations about the frequency of planets around young stars in the short period regime ($P \lesssim 3$ yr).

In order to estimate the detection limits inherent to our data sets or, in other words, to establish which planets (in the way of masses and periods) can be confidently excluded to be orbiting the surveyed stars, I carried out a series of Monte Carlo simulations.

The implemented algorithm is based on the LS Scargle periodogram. Therefore, it is in principle valid only for circular orbits (e=0), the only ones to produce exactly sinu-

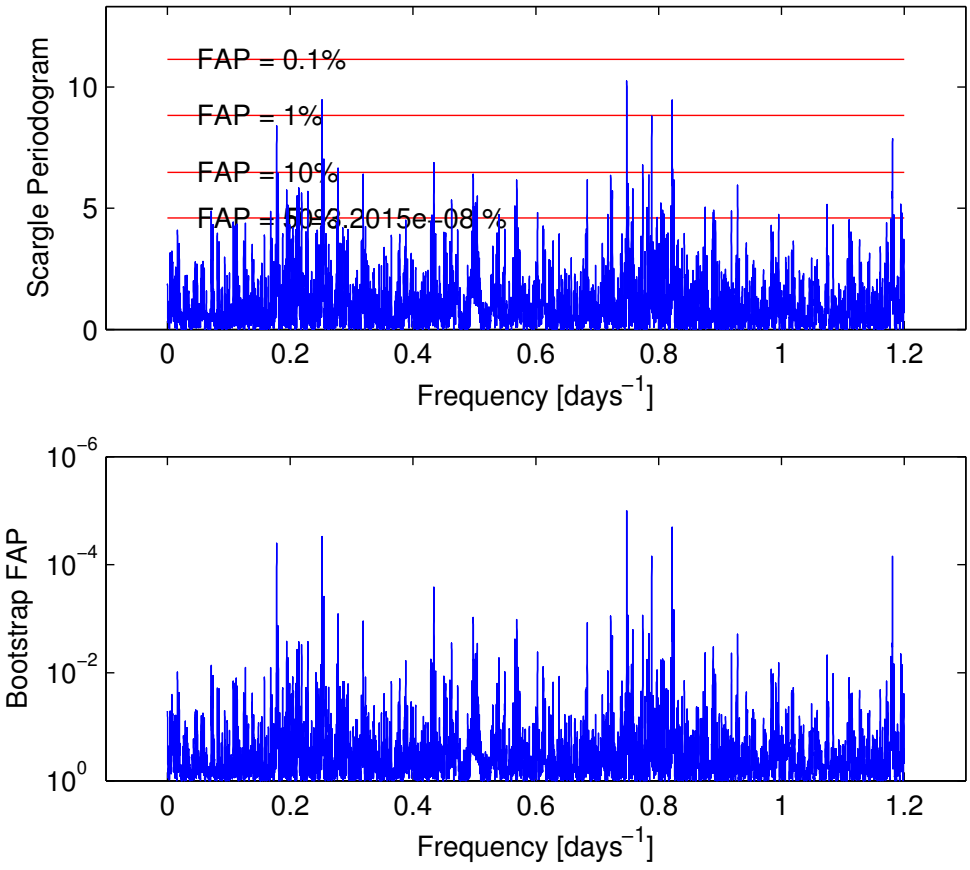

Figure 7.14: . Scargle and bootstrap periodograms for the HD171488 RV data set.

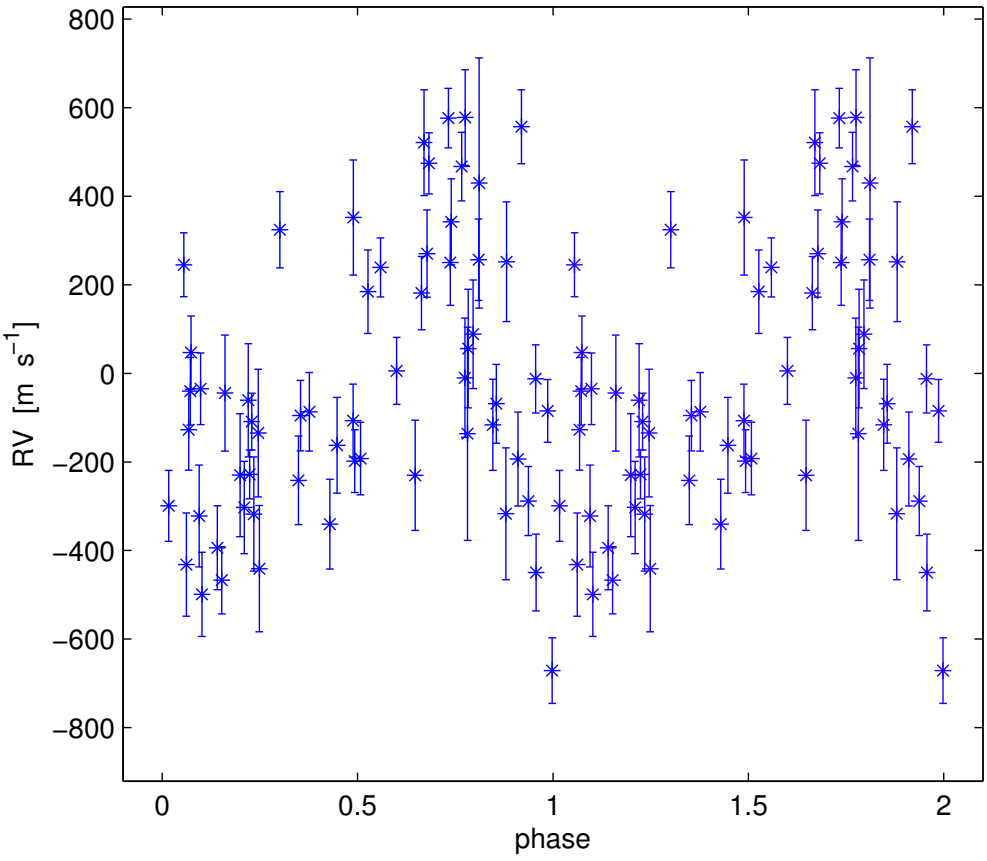

Figure 7.15: . HD171488 RV measurements phase-folded according to the period P = 1.33698 days. The zero phase has been arbitrarily chosen.

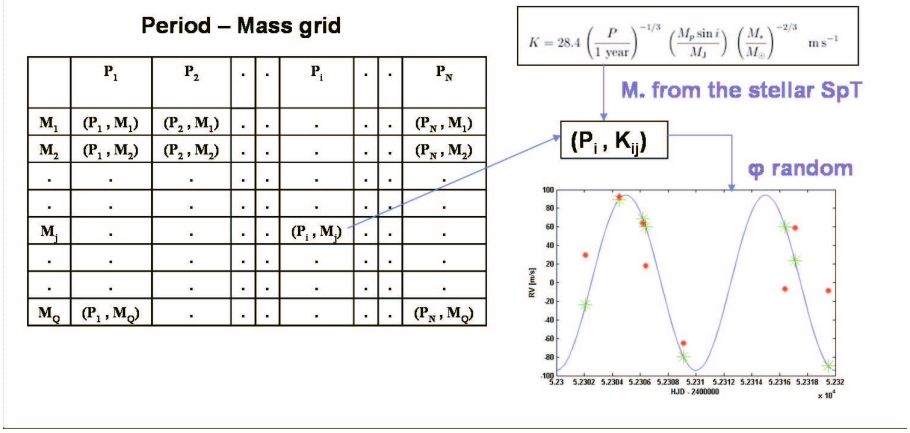

Figure 7.16: Schematical representation of the algorithm used to generate an array of simulated RV data sets. First a grid of periods P and minimum masses $M_P sin(i)$ for an hypothtetical planet is selected. For every single star, adopting a stellar mass based on its spectral type, the P-M grid is converted in a P-K grid, where K is the semi-amplitude of the RV curve for a circular orbit. For each P_i-K_{ij} point of the grid, 10000 simulated RV curves are generated varying the phase φ at random. Such curves are sampled (green asterisks in the lower right plot) in correspondence of the real julian dates of the RV measurements for the star under examination. Finally, adding gaussian noise to the RV values the simulated data sets are obtained (red points).

soidal RV variations. However, it turns out that the LS periodogram is only marginally affected as far as eccentricities $e \lesssim 0.3$ are considered.[1]

Figure 7.16 illustrates schematically how the algorithm works. To begin a grid of values is choosen for the period P and the minimum mass $M_P sin(i)$ of an hypothetical planet. In particular, for the periods, the interval P=0.7−800 days is sampled at 145 values with a constant logarithmic step. Similarly, for the masses 85 values are taken spanning the range $M_P sin(i)$=0.05−30 M_J. Using the formula reported in Fig. 7.16, the (P_i,M_j) grid can be converted in a (P_i,K_{ij}) grid. The mass of the host star M_* appears explicitly in the formula and its value is estimated according to the spectral type. Thus, to every given star a different (P_i,K_{ij}) grid is associated.

The period P_i and the RV semi-amplitud K_{ij} , together with an orbital phase ϕ choosed at random, are sufficient to define a simulated RV curve. This curve is then sampled (green asterisks in figure 7.16) in corrispondence of the julian dates of the real data set of the star under examination. Noise with a normal distribution is added (red points in figure 7.16), thus obtaining a simulated data set. The amplitude of the noise is choosed in such a way that the σ_{RV} of the simulated data matches that of the real data.

For each point in the (P_i,K_{ij}) grid, 10000 simulated data sets are created and, for each of them, the Scargle periodogram value is calculated for the period P_i. The distribution of periodogram values is finally compared with a similar distribution obtained from pure-noise data sets and with the same temporal sampling.

A detection probability is evaluated for the planet with period P_i and RV semi-amplitude K_{ij} counting the fraction of periodogram values of the signal+noise data sets

[1] According to simulations, for e=0.3, the periodogram peak height decreases by less than 10% in comparison to the e=0 height.

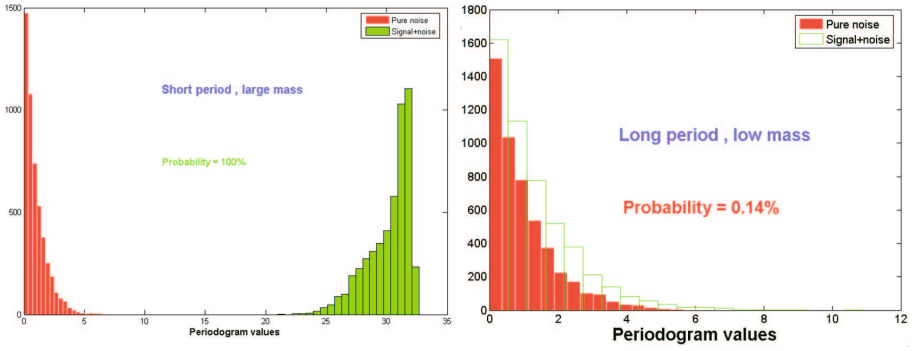

Figure 7.17: The detection probability $\wp$ of a planet of given period and minimum mass is calculated by comparing the periodogram values distribution of signal+noise RV data sets with pure noise data sets. Here two extreme cases are shown. On the left panel the case of a planet very massive and with a very short period: The signal+noise peridogram values distribution lies far apart from the pure noise distribution and correspondingly $\wp$=100% . On the right panel, for a low mass and long period planet, the two distributions are statistically indistinguishable and $\wp$=0.14%.

that are larger than all the periodogram values of the pure-noise data sets (see Figure 7.17). I adopt the probability $\wp$ calculated in this way as the level of confidence that a planet with the given mass and period would have been detected from the real data set. Or, in other words, it tells us with which level of confidence we can exclude that such a planet is really orbiting the monitored star.

The results of the Monte Carlo simulations for the 36 stars are reported in Appendix B in form of probability diagrams. As expected a key role is played by the σ_{RV} of the data sets. As a first approximation, in the $\log P - \log M_P sin(i)$ plane, iso-probability lines are straight lines stretching from lower left to upper right. For a given probability $\wp$, the 'intercept' of the corresponding straight line is proportional to σ_{RV}. Another important factor is the number of RV measurements N. For N$\lesssim$20, a number of sharp narrow vertical features begin to appear in the probability diagrams (see for example the results for HD103095 with N=20 and HD180617 with N=18). Such features mean that the detection limits get worse very rapidly in correspondence of certain periods P. As N decreases further on, the number of features increases and eventually they merge, leading to wide period intervals where the probability $\wp$ stays low no matter how large $M_P sin(i)$ is (see HD135599 with N=12, GJ517 with N=9 and HD17332a with N=8).

The simulations, thus, demonstrate the necessity to have a suitably large number of RV measurements, say N=15−20, in order to achieve, virtually for every period P, the best sensibility possible which is limited by the given σ_{RV}. Indeed, getting even larger values of N can also help by moving upward the iso-probability straight lines, however the detection limits are only a slowly increasing function of N.

The results from the simulation on the 36 stars can be summed up to provide statistical estimations of the frequency of planets orbiting young stars. Figure 7.18 shows the percentage of stars for which the presence of a planet can be excluded with a 99.9% level of confidence, as a function of the period P and the minimum mass $M_P sin(i)$. So, for instance, there is no planet with P=10 days and $M_P sin(i)$=1M$_J$ around 77% of the stars in the sample, and for P=300 days and $M_P sin(i)$=3M$_J$ a planet can be excluded for 66% of the stars.

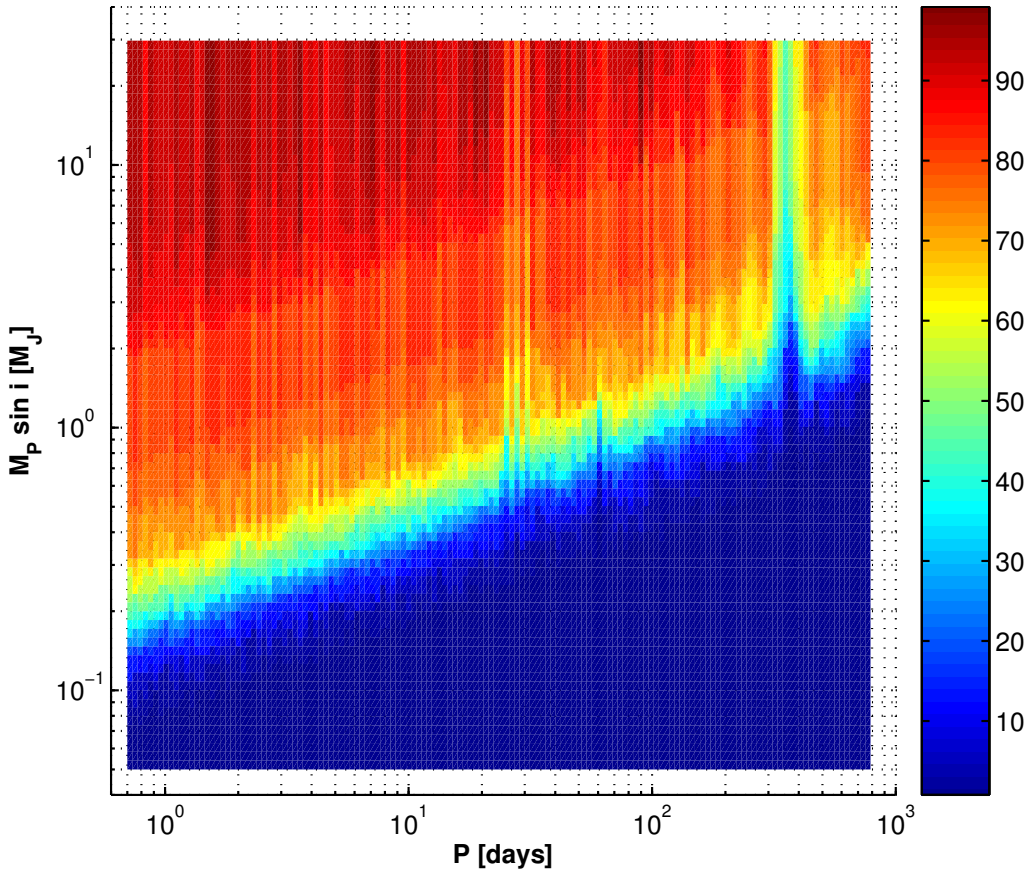

Figure 7.18: This diagram summarizes the results of the Monte Carlo simulations carried out on the RV data sets of the 36 single stars in our sample. Different colors code the percentage of stars in the sample where a planet of given period and minimum mass can be excluded at a 99.9/sensibility in correspondence of $P\sim$1 year and $P\sim$1 month, resulting from the particular data sampling.

Chapter 8

Conclusions

This thesis reports the results of an optical spectroscopic survey of a sample of 43 young, late spectral type, nearby stars aimed to the detection of extra-solar planets by means of high-precision radial velovity (RV) measurements. Observations have been carried out with the 2m Schmidt telescope and the Coudé spectrograph at the TLS Tautenburg Observatory. Stars have been monitored for almost six years (2001-2006) during which about 2000 spectra have been collected.

The discovery and characterization of the young planets population represents an important goal as it would allow to put much stronger observational constraints to the current theories of planet formation and orbital evolution. In spite of this, young stars have been systematically excluded form the main RV monitoring campaigns because it was believed that their enhanced level of magnetic activity would hinder the periodic RV signature of a planet to emerge out of the stellar RV jitters. Thus, an important result of the survey has been to assess the real level of RV-noise induced by activity in young stars. The majority of targets in our sample, which contains stars from $\sim$30 to $\sim$300 Myr old, display a RV-scatter $\lesssim$30 m s^{-1}, that is small enough to allow the detection of planets in a large portion of the mass-period diagram.

I have found 7 spectroscopic binaries in the sample, with periods ranging from a few days to several years. Indeed, in some cases the data cover only a small fraction of the orbital period. For the remaining 36 stars, periodogram analysis and RV-curve fitting have not revealed the presence of any planet at a sufficiently high level of confidence. However, thanks to the large number of RV measurements (30 to 50 for most of our targets), I have been able to well establish detection limits. For instance, I can exclude the presence of a planet, with period $P < 10$ days and minimum mass $M \sin i > 2$ M$_{Jup}$, for 80 % of the stars in our sample (95 % if we consider $M \sin i > 7$ M$_{Jup}$).

The fact I did not find any planet is statistically compatible with the frequency of planets around old solar type stars which is estimated to be $\sim$7 % ($\sim$1 % for hot Jupiters). The results of our survey, together with similar results obtained by other surveys ($\sim$80 members of the Hyades: 0 planets; $\sim$80 young stars in the southern emisphere: 1 candidate planet) seems to disprove the idea that young stars host a larger population of very massive close-in planets than old stars, which then either fall into the star or lose most of its mass by evaporation. This in turn favors the hypothesis that massive planets form in the outer protoplanetary disk and do not migrate inward.

Bibliography

[1] C. Abad, J.A. Docobo, V. Lanchares, et al. Reduction of CCD observations of visual binaries using the "Tepui" function as PSF. *A&A*, 416:811, 2004.

[2] I. Adachi, C. Hayashi, and K. Nakazawa. The gas drag effect on the elliptical motion of a solid body in the primordial solar nebula. *Prog. Theor. Phys*, 56:1756, 1976.

[3] F.C. Adams and W. Benz. Gravitational instabilties in circumstellar disks and the formation of binary companions. *ASP Conference Series*, 32:170, 1992.

[4] F.C. Adams and G. Laughlin. Migration and dynamical relaxation in crowded systems of giant planets. *Icarus*, 163:290, 2003.

[5] S. Aigrain, P. Barge, M. Deleuil, et al. The CoRoT exoplanet programme: exploring the gas-giant/terrestrial planet transition. *arXiv:astro-ph/0702062v1*, 2007.

[6] M.D. Albrow, J. An, J.P. Beaulieu, et al. Limits on the abundance of Galactic planets from 5 Years of PLANET observations. *ApJ*, 556:113, 2001.

[7] J.R.P. Angel. Ground-based imaging of extrasolar planets using adaptive optics. *Nature*, 368:203, 1994.

[8] P.J. Armitage. Lecture notes on the formation and evolution of planetary systems. *astro-ph/0701485v1*, 2007.

[9] P.J. Armitage and W.K.M. Rice. Planetary migration. *astro-ph/0507492*, 2005.

[10] P. Artymowicz. On the wave excitation and a generalized torque formula for Lindblad resonances excited by external potential. *ApJ*, 419:155, 1993.

[11] M. Bailes. Pulsar velocities. *Proceedings of IAU*, 165:213, 1996.

[12] I. Baraffe, F. Selsis, G. Chabrier, et al. The effect of evaporation on the evolution of close-in giant planets. *A&A*, 419:13, 2004.

[13] A. Baranne, D. Queloz, M. Mayor, et al. ELODIE: A spectrograph for accurate radial velocity measurements. *A&ASS*, 119:373, 1996.

[14] S.S. Barshay and J.S. Lewis. Chemistry of primitive solar material. *ARA&A*, 14:81, 1976.

[15] M.R. Bate and I.A. Bonnell. The origin of the initial mass function and its dependence on the mean Jeans mass in molecular clouds. *MNRAS*, 356:1201, 2005.

[16] J.P. Beaulieu, D.P. Bennett, P. Fouqu, et al. Discovery of a cool planet of 5.5 Earth masses through gravitational microlensing. *Nature*, 439:437, 2006.

[17] S.V.W. Beckwith and A.I. Sargent. The occurrence and properties of disks around young stars. *In: Protostars and planets III*, page 521, 1993.

[18] G.F. Benedict, B.E. McArthur, T. Forveille, et al. A mass for the extrasolar planet Gliese 876b determined from Hubble Space Telescope Fine Guidance Sensor 3 astrometry and high-precision radial velocities. *ApJ*, 581:115, 2002.

[19] W. Benz and E. Asphaug. Catastrophic disruptions revisited. *Icarus*, 142:5, 1999.

[20] J.L. Beuzit, D. Ségransan, and T. Forveille. New neighbours III. 21 new companions to nearby dwarfs, discovered with adaptive optics. *A&A*, 425:997, 2004.

[21] J. Binney and S. Tremaine. *Galactic Dynamics*. Princeton University press, 1987.

[22] J. Blum, R. Schrpler, B.J.R. Davidsson, and J.M. Trigo-Rodrguez. The physics of protoplanetesimal dust agglomerates. I. Mechanical properties and relations to primitive bodies in the Solar System. *ApJ*, 652:1768, 2006.

[23] P. Bodenheimer. Studies in stellar evolution. II. Lithium depletion during the

pre-main-sequence contraction. *ApJ*, 142:451, 1965.

[24] P. Bodenheimer and J.B. Pollack. Calculations of the accretion and evolution of giant planets. The effects of solid cores. *Icarus*, 67:391, 1986.

[25] X. Bonfils, X. Delfosse, S. Udry, et al. A radial velocity survey for planet search around M-dwarfs. *ASP Conference Proceedings*, 321:101, 2004.

[26] P. Bordé, D. Rouan, and A. Léger. Exoplanet detection capability of the COROT space mission. *A&A*, 405:1137, 2003.

[27] A.P. Boss. Giant planet formation by gravitational instability. *Science*, 276:1836, 1997.

[28] A. Brown, G.M. Harper, and T.R. Ayres. Stellar activity on young stars in the Local Association: FUSE observations of the Beta Pic and Tucana-horologium Moving Groups. In *American Astronomical Society Meeting 208*, page 208. 2006.

[29] T.M. Brown, D. Charbonneau, R.L. Gilliland, et al. Hubble Space Telescope Time-Series Photometry of the Transiting Planet of HD 209458. *ApJ*, 552:699, 2001.

[30] A. Burrows, M. Marley, W.B. Hubbard, et al. A nongray theory of extrasolar giant planets and brown dwarfs. *ApJ*, 491:856, 1997.

[31] R.P. Butler, G.W. Marcy, E. Williams, et al. Attaining Doppler precision of 3 m s^{-1}. *PASP*, 108:500, 1996.

[32] W.W. Campbell and W.H. Wright. A list of nine stars whose velocities in the line of sight are variable. *ApJ*, 12:254, 1900.

[33] J.W. Chamberlain and D.M. Hunten. *Theory of planetary atmospheres.* Orlando Academic Press, 1987.

[34] J.E. Chambers and G.W. Wetherill. Making the terrestrial planets: N-body integrations of planetary embryos in three dimensions. *Icarus*, 136:304, 1998.

[35] D. Charbonneau, L.E. Allen, S.T. Megeath, et al. Detection of thermal emission from an extrasolar planet. *ApJ*, 626:523, 2005.

[36] D. Charbonneau, T.M. Brown, D. Latham, and M. Mayor. Detection of planetary transits across a Sun-like star. *ApJ*, 529:45, 2000.

[37] S. Chatterjee, E.B. Ford, and F.A. Rasio. Dynamical outcomes of planet-planet scattering. *submitted to ApJ*, 2007.

[38] G. Chauvin, A.M. Lagrange, C. Dumas, et al. Giant planet companion to 2MASSW J1207334-393254. *A&A*, 438:25, 2005.

[39] T.J. Deeming. Fourier analysis with unequally-spaced data. *Ap&SS*, 36:137, 1975.

[40] D. Deming, S. Seager, L.J. Richardson, and J. Harrington. Infrared radiation from an extrasolar planet. *Nature*, 434:740, 2005.

[41] A. Lecavelier des Etangs. A diagram to determine the evaporation status of extrasolar planets. *A&A*, 461:1185, 2007.

[42] S. Desidera and M. Barbieri. Properties of planets in binary systems. The role of binary separation. *A&A*, 462:345, 2007.

[43] F. Diego, A. Charalambous, A.C. Fish, and D.D. Walker. Final tests and commissioning of the UCL Echelle Spectrograph. *Proceedings of SPIE*, 1235:562, 1990.

[44] J.A. Docobo and J.F. Ling. Orbits of five visual double stars. *ApJSS*, 120:41, 1999.

[45] M.P. Döellinger, L. Pasquini, A.P. Hatzes, et al. Why are G and K giants radial velocity variables? *The Messenger*, 122:39, 2005.

[46] M. Dominik, M.D. Albrow, J.P. Beaulieu, et al. The PLANET microlensing follow-up network: results and prospects for the detection of extra-solar planets. *Planetary and Space Science*, 50:299, 2002.

[47] A. Duquennoy and M. Mayor. Multiplicity among solar-type stars in the solar neighbourhood. II − Distribution of the orbital elements in an unbiased sample. *A&A*, 248:485, 1991.

[48] R.H. Durisen, K. Cai, A.C. Mejia, and M.K. Pickett. A hybrid scenario for gas giant planet formation in rings. *Icarus*, 173:417, 2005.

[49] A. Eggenberger, S. Udry, M. Mayor, et al. Detection and properties of extrasolar planets in double and multiple star systems. *ASP Conference Proceedings*, 321:93, 2004.

[50] M. Endl, W.D. Cochran, M. Kürster, et al. Exploring the frequency of close-in jovian planets around M dwarfs. *ApJ*, 649:436, 2006.

[51] M. Endl, W.D. Cochran, R.G. Tull, and P.J. MacQueen. A dedicated M dwarf planet search using the Hobby-Eberly telescope. *AJ*, 126:3099, 2003.

[52] D. Fernandez, F. Figueras, and J. Torra. Kinematic evolution of the young local associations and the Sco-Cen complex. *astro-ph/0611766*, 2006.

[53] R. Freire Ferrero, A. Frasca, E. Marilli, and S. Catalano. Magnetic activity in HD 111456, a young F56 main-sequence star. *A&A*, 413:657, 2004.

[54] D.A. Fischer and J. Valenti. The planet-metallicity correlation. *ApJ*, 622:1102, 2005.

[55] E.B. Ford, M. Havlickova, and F. Rasio. Dynamical instabilities in extrasolar planetary systems containing two giant planets. *Icarus*, 150:303, 2001.

[56] E.B. Ford, F.A. Rasio, and K. Yu. Dynamical instabilities in extrasolar planetary systems. *ASP Conference Series*, 294:181, 2003.

[57] F.A.M. Frescura, C.A. Engelbrecht, and B.S. Frank. Significance tests for periodogram peaks. *astro-ph/0706.2225*, 2007.

[58] E.B. Frost. Corrections to radial velocities of certain stars of the Orion type. *ApJ*, 31:430, 1910.

[59] E.J. Gaidos, G.W. Henry, and S.M. Henry. Spectroscopy and photometry of nearby young solar analogs. *AJ*, 120:1006, 2000.

[60] R.E. Gershberg, M.M. Katsova, M.N. Lovkaya, et al. Catalogue and bibliography of the UV Cet-type flare stars and related objects in the solar vicinity. *A&AS*, 139:555, 1999.

[61] B. Gladman. Dynamics of systems of two close planets. *Icarus*, 1993.

[62] P. Goldreich, Y. Lithwick, and R. Sari. Planet formation by coagulation: A focus on Uranus and Neptune. *ARA&A*, 42:549, 2004.

[63] P. Goldreich and S. Tremaine. The excitation of density waves at the Lindblad and corotation resonances by an external potential. *ApJ*, 233:857, 1979.

[64] P. Goldreich and W.R. Ward. The Formation of Planetesimals. *ApJ*, 183:1051, 1973.

[65] A. Gould, S. Dorsher, B.S. Gaudi, and A. Udalski. Frequency of Hot Jupiters and Very Hot Jupiters from the OGLE-III Transit Surveys toward the Galactic Bulge and Carina. *Acta Astronomica*, 56:1, 2006.

[66] D.F. Gray. *Lectures on spectral-line analysis: F, G, and K stars*. Arva: Ontario, 1988.

[67] R.F. Griffin. A photoelectric radial-velocity spectrometer. *ApJ*, 148:465, 1969.

[68] R.F. Griffin. Photoelectric radial velocities. Paper V. 69 southern HR stars. *MNRAS*, 155:449, 1972.

[69] E.W. Guenther, M. Esposito, R. Mundt, et al. Pre-main sequence spectroscopic binaries suitable for VLTI observations. *astro-ph/0702268*, 2007.

[70] T. Guillot. The interiors of giant planets: Models and outstanding questions. *Annual Review of Earth and Planetary Sciences*, 33:493, 2005.

[71] J.L. Halbwachs, M. Mayor, and S. Udry. Statistical properties of exoplanets. IV. The period-eccentricity relations of exoplanets and of binary stars. *A&A*, 431:1129, 2005.

[72] L. Hartmann, D.R. Soderblom, and R.W. Noyes. An analysis of the Vaughan-Preston survey of chromospheric emission. *ApJ*, 276:254, 1984.

[73] A.P. Hatzes, E.W. Guenther, M. Endl, et al. A giant planet around the massive giant star HD 13189. *A&A*, 437:743, 2005.

[74] C. Hayashi. Evolution of Protostars. *ARA&A*, 4:171, 1966.

[75] M. Hayashi. Pre-main-sequence stages of stars. *PASJ*, 17:177, 1965.

[76] W.D. Heintz. Orbits of 20 visual binaries. *A&ASS*, 72:543, 1988.

[77] A. Hempelmann, J.H.M.M. Schmitt, M. Schultz, et al. Coronal X-ray emission and rotation of cool main-sequence stars. *A&A*, 294:515, 1995.

[78] H.G. Herbig. Can Post-T Tauri Stars be found? In *Problems of Physics and Evolution of the Universe*, page 171. Publishing House of the Armenian Academy of Sciences, 1978.

[79] W. Herbst, J. Eislöffel, and R. Mundtand A. Scholz. The rotation of young low-mass stars and brown dwarfs. *astro-ph/0603673*, 2006.

[80] E. Horch, Z. Ninkov, W.F. van Altena, et al. Speckle observations of binary stars with the WIYN Telescope. I. Measures during 1997. *AJ*, 117:548, 1999.

[81] E.P. Horch, S.E. Robinson, R.D. Meyer, et al. Speckle observations of binary stars with the WIYN telescope. II. Relative astrometry measures during 1998-2000. *AJ*, 123:3442, 2002.

[82] K. Horne. An optimal extraction algorithm for CCD spectroscopy. *PASP*, 98:609, 1986.

[83] E.P. Hubble. Extra-galactic nebulae. *Contributions from the Mount Wilson Observatory*, 324:1, 1926.

[84] S. Inaba, H. Tanaka, K. Nakazawa, et al. High-accuracy statistical simulation of planetary accretion: II. Comparison with N-body simulation. *Icarus*, 149:235, 2001.

[85] G. Israelian, N.C. Santos, M. Mayor, and R. Rebolo. Evidence for planet engulfment by the star HD82943. *Nature*, 411:163, 2001.

[86] P. Ivanov and C. Papaloizou. Dynamic tides in rotating objects: orbital circularization of extrasolar planets for realistic planet models. *MNRAS*, in press, 2007.

[87] J.A. Johnson, R.P. Butler, G.W. Marcy, et al. A new planet around an M dwarf: Revealing a correlation between exoplanets and stellar mass. *astro-ph/07072409v1*, 2007.

[88] Y. Karatas, S. Bilir, Z. Eker, and O. Demircan. Kinematics of chromospherically active binaries and evidence of an orbital period decrease in binary evolution. *MNRAS*, 349:1069, 2004.

[89] S.J. Kenyon and J.X. Luu. Accretion in the early Kuiper belt. I. Coagulation and velocity evolution. *1998*, 115:2136, AJ.

[90] J.F. Kerridge and E. Anders. Boundary conditions for the origin of the solar system. In *Meteorites and the early solar system*, page 1149. Tucson, AZ, University of Arizona Press, 1988.

[91] J.R. King and S.C. Schuler. High-Resolution spectroscopy of Ursa Major moving group stars. *PASP*, 117:911, 2005.

[92] J.R. King, A.R. Villarreal, D.R. Soderblom, et al. Stellar kinematic groups. II. A reexamination of the membership, activity, and age of the Ursa Major Group. *AJ*, 125:1980, 2003.

[93] E. Kokubo, J. Kominami, and S. Ida. Formation of terrestrial planets from protoplanets. I. Statistics of basic dynamical properties. *ApJ*, 642:1131, 2006.

[94] M. Konacki. The radial velocity search for extrasolar planets in binary and multiple stellar systems. *Bulletin of the American Astronomical Society*, 37:1310, 2005.

[95] M. Konacki and A. Wolszczan. Masses and orbital inclinations of planets in the PSR B1257+12 system. *ApJ*, 591:147, 2003.

[96] B. König, E.W. Guenther, M. Esposito, and A. Hatzes. Spectral synthesis analysis and radial velocity study of the northern F-, G- and K-type flare stars. *MNRAS*, 365:1050, 2006.

[97] M. Kürster, J.H.M.M. Schmitt, G. Cutispoto, and K. Dennerl. ROSAT and AB Doradus: the first five years. *A&A*, 320:831, 1997.

[98] G. Laughlin, A. Steinacker, and F.C. Adams. Type I planetary migration with MHD turbulence. *ApJ*, 608:489, 2004.

[99] H.F. Levison and C. Agnor. The role of giant planets in terrestrial planet formation. *AJ*, 125:2692, 2003.

[100] D.N.C. Lin, P. Bodenheimer, and D.C. Richardson. Orbital migration of the planetary companion of 51 Pegasi to its present location. *Nature*, 380:606, 1996.

[101] D.N.C. Lin, J.C.B. Papaloizou, C. Terquem, et al. Orbital Evolution and Planet-Star Tidal Interaction. *In: Protostars and Planets IV*, page 1111, 2000.

[102] C.H. Lineweaver and D.C. Grether. What fraction of Sun-like stars have planets? *ApJ*, 598:1350, 2003.

[103] J.L. Linsky, B.E. Wood, A. Brown, et al. Stellar activity at the end of the main sequence: GHRS observations of the M8 Ve star VB 10. *ApJ*, 455:670, 1995.

[104] J.J. Lissauer. Timescales for planetary accretion and the structure of the protoplanetary disk. *Icarus*, 69:249, 1987.

[105] J.J. Lissauer. Planet formation. *ARA&A*, 31:129, 1993.

[106] N.R. Lomb. Least-squares frequency analysis of unequally spaced data. *Ap&SS*, 39:447, 1976.

[107] J. Lopez-Santiago, D. Montes, I. Crespo-Chacn, and M. J. Fernandez-Figueroa. The nearest young moving groups. *ApJ*, 643:1160, 2006.

[108] D.R. Lorimer. Binary and Millisecond Pulsars at the New Millennium. *Living Reviews in Relativity*, 4:5, 2001.

[109] V.V. Makarov and G.H. Kaplan. Statistical constraints for astrometric binaries with nonlinear motion. *AJ*, 129:2420, 2005.

[110] F. Malbet. High angular resolution coronography for adaptive optics. *A&AS*, 115:161, 1996.

[111] G.W. Marcy and R.P. Butler. Precise radial velocities with an iodine absorption cell. *1992*, 104:270, PASP.

[112] G.W. Marcy, R.P. Butler, D.A. Fischer, et al. Observed properties of exoplanets: Masses, orbits, and metallicities. *Progress of Theoretical Physics Supplement*, 158:24, 2005.

[113] S. C. Marsden, J.F. Donati, M. Semel, et al. Surface differential rotation and photospheric magnetic field of the young solar-type star HD 171488 (V889 Her). *MNRAS*, 370:468, 2006.

[114] F. Marzari and S.J. Weidenschilling. Eccentric extrasolar planets: The jumping Jupiter model. *Icarus*, 156:570, 2002.

[115] E. Masciadri, R. Mundt, T. Henning, et al. A Search for hot massive extrasolar planets around nearby young stars with the adaptive optics system NACO. *ApJ*, 625:1004, 2005.

[116] F. Masset and M.D. Snellgrove. Reversing type II migration: resonance trapping of a lighter giant protoplanet. *MNRAS*, 320:55, 2001.

[117] M. Mayor, F. Pepe, D. Queloz, et al. Setting new standards with HARPS. *The Messenger*, 114:20, 2003.

[118] M. Mayor and D. Queloz. A Jupiter-mass companion to a solar-type star. *Nature*, 378:355, 1995.

[119] T. Mazeh, S. Zucker, A. Dalla Torre, and F. van Leeuwen. Analysis of the HIPPARCOS measurements of ν Andromedae: A mass estimate of its outermost known planetary companion. *ApJ*, 522:149, 1999.

[120] C. McCarthy. *Transformation of Doppler shifts to the solar system barycenter*. PhD thesis, 1995.

[121] C. McCarthy and B. Zuckerman. The brown dwarf desert at 75-1200 AU. *AJ*, 127:2871, 2004.

[122] M.J. McCaughrean and C.R. O'Dell. Direct imaging of circumstellar disks in the Orion Nebula. *AJ*, 111:197, 1996.

[123] S. Messina, G. Cutispoto, E.F. Guinan, et al. Photometric evidence for two-temperature photospheric inhomogeneities on magnetically active K dwarf stars. *A&A*, 447:293, 2006.

[124] S. Messina, N. Pizzolato, E.F. Guinan, and M. Rodonò. Dependence of coronal X-ray emission on spot-induced brightness variations in cool main sequence stars. *A&A*, 410:671, 2003.

[125] S. Messina, M. Rodonò, and E.F. Guinan. The rotation-activity connection: Its extension to photospheric activity diagnostics. *A&A*, 366:215, 2001.

[126] M.R. Meyer, L.A. Hillenbrand, and D. Backman. The formation and evolution of planetary systems: Placing our solar system in context with Spitzer. *PASP*, 118:1690, 2006.

[127] D.S. Mitchell. *A high precision radial velocity survey of K giants*. PhD thesis, 2004.

[128] H. Mizuno. Formation of the Giant Planets. *Progress of Theoretical Physics*, 64:544, 1980.

[129] D. Montes, J. Lopez-Santiago, M.J. Fernandez-Figueroa, and M.C. Galvez. Chromospheric activity, lithium and radial velocities of single late-type stars possible members of young moving groups. *A&A*, 379:976, 2001.

[130] G.E. Morfill, E. Levy, and H. Spruit. Physical processes and conditions associated with the formation of protoplanetary disks. In *Protostars and planets III*, page 939. 1993.

[131] T.C. Mouschovias, K. Tassis, and M.W. Kunz. Observational constraints on the ages of molecular clouds and the star formation. Timescale: ambipolar-diffusion-controlled or turbulence-induced star formation? *ApJ*, 646:1003, 2006.

[132] M. Mugrauer, R. Neuhäuser, E.W. Guenther, et al. HD77407 and GJ 577: Two new young stellar binaries detected with

the Calar Alto Adaptive Optics system ALFA. *A&A*, 417:1031, 2004.

[133] F. Mullally, D.E. Winget, and S.O. Kepler. Searching for planets around pulsating white dwarf stars. *ASP Conference Series*, 352:265, 2006.

[134] C.D. Murray and S.F. Dermott. *Solar System Dynamics*. Cambridge University press, 1999.

[135] T. Nakajima, J.I. Morino, T. Tsuji, et al. A coronagraphic search for brown dwarfs and planets around nearby stars. *AN*, 326:952, 2005.

[136] R.P. Nelson. On the orbital evolution of low mass protoplanets in turbulent, magnetised disks. *A&A*, 443:1067, 2005.

[137] R. Neuhäuser, E.W. Guenther, G. Wuchterl, et al. Evidence for a co-moving sub-stellar companion of GQ Lup. *A&A*, 435:13, 2005.

[138] R.W. Noyes and L.W. Hartmann ans S.L. Baliunas. Rotation, convection, and magnetic activity in lower main-sequence stars. *ApJ*, 279:763, 1984.

[139] V.G. Ortega, R. de la Reza, E. Jilinski, and B. Bazzanella. The origin of the β Pictoris Moving Group. *ApJ*, 575:75, 2002.

[140] B. Paczynski. Gravitational microlensing by the Galactic halo. *ApJ*, 304:1, 1986.

[141] F. Palla and I. Baraffe. Pulsating young brown dwarfs. *A&A*, 432:57, 2005.

[142] J. Papaloizou and D.N.C. Lin. On the tidal interaction between protoplanets and the primordial solar nebula. I - Linear calculation of the role of angular momentum exchange. *ApJ*, 285:818, 1984.

[143] J.C.B. Papaloizou and C. Terquem. Planet formation and migration. *Rep. Prog. Phys.*, 69:119, 2006.

[144] E.N. Parker. Sunspots and the physics of magnetic flux tubes. I - The general nature of the sunspot. II - Aerodynamic drag. *ApJ*, 230:905, 1979.

[145] M. Pätzold, L. Carone, and H. Rauer. Tidal interactions of close-in extrasolar planets: The OGLE cases. *A&A*, 427:1075, 2004.

[146] D.B. Paulson, W.D. Cochran, and A.P. Hatzes. Searching for planets in the Hyades. V. Limits on planet detection in the presence of stellar activity. *AJ*, 123:3579, 2004.

[147] D.B. Paulson and S. Yelda. Differential radial velocities and stellar parameters of nearby young stars. *PASP*, 108:706, 2006.

[148] G.V. Pechernikova and A.V. Vitjazev. Thermal dissipation of gas from the protoplanetary cloud. *Adv. Space Res.*, 1:55, 1981.

[149] F. Pepe, A.C.M. Correia, M. Mayor, et al. The HARPS search for southern extra-solar planets VIII. μ Arae, a system with four planets. *A&A*, 462:769, 2007.

[150] C. Perrier, J.P. Sivan, D. Naef, et al. The ELODIE survey for northern extra-solar planets. I. Six new extra-solar planet candidates. *A&A*, 410:1039, 2003.

[151] M.A.C. Perryman, L. Lindegren, F. Arenou, et al. Hipparcos distances and mass limits for the planetary candidates: 47 Ursae Majoris, 70 Virginis, and 51 Pegasi. *A&A*, 310:21, 1996.

[152] N. Pizzolato, A. Maggio, G. Micela, et al. The stellar activity-rotation relationship revisited: Dependence of saturated and non-saturated X-ray emission regimes on stellar mass for late-type dwarfs. *A&A*, 397:147, 2003.

[153] S.I. Plachinda. Magnetic field measurements on four yellow supergiants. I. *Ap*, 48:9, 2005.

[154] J.S. Plaskett. The design of spectrographs for radial velocity determinations. *Journal of the Royal Astronomical Society of Canada*, 3:190, 1909.

[155] J.B. Pollack, O. Hubickyj, P. Bodenheimer, et al. Formation of the giant planets by concurrent solid and gas accretion. *Bulletin of the American Astronomical Society*, 25:1120, 1993.

[156] J.B. Pollack, O. Hubickyj, P. Bodenheimer, et al. Formation of the giant planets by concurrent accretion of solids and gas. *Icarus*, 124:62, 1996.

[157] D. Queloz. Indirect searches : Doppler spectroscopy and pulsar timing. *Planets outside the solar system: Theory and observations. Edited by J.-M. Mariotti and D. Alloin. Dordrecht ; Boston : Kluwer Academic Publishers,*, page 229, 1999.

[158] D. Queloz, G.W. Henry, J.P. Sivan, et al. No planet for HD 166435. *A&A*, 379:279, 2001.

[159] V. Ripepi, S. Bernabei, and M. Marconi et al. Discovery of δ Scuti pulsation in the Herbig Ae star VV Serpentis. *A&A*, 462:1023, 2007.

[160] G. Rousset, F. Lacombe, P. Puget, et al. NAOS, the first AO system of the VLT: on-sky performance. *Proceedings of the SPIE*, 4839:140, 2003.

[161] S.H. Saar and A. Brandenburg. Time evolution of the magnetic activity cycle period. II. Results for an expanded stellar sample. 524:295, ApJ.

[162] S.H. Saar and R.A. Donahue. Activity-related radial velocity variation in cool stars. *ApJ*, 485:319, 1997.

[163] N.C. Santos, G. Israelian, M. Mayor, et al. Statistical properties of exoplanets II. Metallicity, orbital parameters, and space velocities. *A&A*, 398:363, 2003.

[164] N.C. Santos, M. Mayor, D. Naef, et al. The CORALIE survey for Southern extra-solar planets. IV. Intrinsic stellar limitations to planet searches with radial-velocity techniques. *A&A*, 361:265, 2000.

[165] P. Sartoretti and J. Schneider. On the detection of satellites of extrasolar planets with the method of transits. *A&ASS*, 134:553, 1999.

[166] J.D. Scargle. Studies in astronomical time series analysis. II - Statistical aspects of spectral analysis of unevenly spaced data. *ApJ*, 263:835, 1982.

[167] J.F. Schachter, R. Remillard, S.H. Saar, et al. Optical and X-Ray characteristics of stars detected in the Einstein Slew survey. *ApJ*, 463:747, 1996.

[168] N.I. Shakura and R.A. Sunayev. Black holes in binary systems. Observational appearance. *A&A*, 24:337, 1973.

[169] H. Shapley. Globular clusters and the structure of the Galactic System. *PASP*, 30:42, 1918.

[170] F.H. Shu, F.C. Adams, and S. Lizano. Star formation in molecular clouds: Observation and theory. *ARA&A*, 25:23, 1987.

[171] F.H. Shu, S. Tremaine, F.C. Adams, and S.P. Ruden. Sling amplification and eccentric gravitational instabilities in gaseous disks. *ApJ*, 358:495, 1990.

[172] R. Silvotti, S. Schuh, R. Janulis, et al. A giant planet orbiting the 'extreme horizontal branch' star V391 Pegasi. *Nature*, 449:189, 2007.

[173] D.R. Soderblom and M. Mayor. Stellar kinematic groups. I - The Ursa Major group. *AJ*, 105:226, 1993.

[174] S. Sridhar and S. Tremaine. Tidal disruption of viscous bodies. *Icarus*, 95:86, 1992.

[175] G.R. Stewart and G.W. Wetherill. Evolution of planetesimal velocities. *Icarus*, 74:542, 1988.

[176] J.A. Stoesz, J. Veran, F.J. Rigaut, et al. Evaluation of the on-sky performance of Altair. *Proceedings of the SPIE*, 5490:67, 2004.

[177] K. Strassmeier, A. Washuettl, T. Granzer, et al. The Vienna-KPNO search for Doppler-imaging candidate stars. I. A catalog of stellar-activity indicators for 1058 late-type Hipparcos stars. *A&AS*, 142:275, 2000.

[178] K.G. Strassmeier, F.C. Fekel, B.W. Bopp, et al. Chromospheric CA II H and K and H-alpha emission in single and binary stars of spectral types F6-M2. *ApJSS*, 72:191, 1990.

[179] K.G. Strassmeier, T. Pichler, M. Weber, and T. Granzer. Doppler imaging of stellar surface structure XXI. The rapidly-rotating solar-type star HD 171488 = V889 Hercules. *A&A*, 411:595, 2003.

[180] A. Strigachev and P. Lampens. Multicolour CCD measurements of nearby visual double stars. II. *A&A*, 422:1023, 2004.

[181] D. Syer and C.J. Clarke. Satellites in discs: Regulating the accretion luminosity. *MNRAS*, 277:758, 1995.

[182] T. Takeuchi, S.M. Miyama, and D.N.C. Lin. Gap formation in protoplanetary disks. *ApJ*, 460:832, 1996.

[183] H. Tanaka, T. Takeuchi, and W.R. Ward. Three-dimensional interaction between a planet and an isothermal gaseous disk. I. Corotation and Lindblad torques and planet migration. *ApJ*, 565:1257, 2002.

[184] C. Terquem and J.C.B.Papaloizou. Dynamical relaxation and the orbits of low-mass extrasolar planets. *MNRAS*, 332:39, 2002.

[185] A. Tokovinin, S. Thomas, M. Sterzik, and S. Udry. Tertiary companions to close spectroscopic binaries. *A&A*, 450:681, 2006.

[186] D.E. Trilling, W. Benz, T. Guillot, et al. Orbital evolution and migration of giant planets: Modeling extrasolar planets. *ApJ*, 500:428, 1998.

[187] D.E. Trilling, J.I. Lunine, and W. Benz. Orbital migration and the frequency of giant planet formation. *A&A*, 394:241, 2002.

[188] A. Udalski, M. Kubiak, and M. Szymanski. Optical Gravitational Lensing Experiment. OGLE-2 the second phase of the OGLE project. *Acta Astronomica*, 47:319, 1997.

[189] J.A. Valenti, R.P Butler, and G.W. Marcy. Determining spectrometer instrumental profiles using FTS reference spectra. *PASP*, 107:966, 1995.

[190] J.A. Valenti and D.A. Fischer. Spectroscopic Properties of Cool Stars (SPOCS). I. 1040 F, G, and K Dwarfs from Keck, Lick, and AAT Planet Search Program. *ApJSS*, 159:141, 2005.

[191] M.A. van Dam, D. Le Mignant, and B.A. Macintosh. Performance of the Keck Observatory adaptive-optics system. *Applied Optics*, 43:5458, 2004.

[192] D. Veras and P.J. Armitage. Predictions for the correlation between giant and terrestrial extrasolar planets in dynamically evolved systems. *ApJ*, 645:1509, 2006.

[193] A. Vidal-Madjar and A.L.D. Etangs. "Osiris"(HD209458b), an evaporating planet. *ASP Conference Proceedings*, 321:152, 2004.

[194] H.C. Vogel. On the spectrum of α Aquilae and its velocity in the line of sight. *ApJ*, 9:1, 1899.

[195] S.S. Vogt. The Lick Observatory Hamilton Echelle Spectrograph. *PASP*, 99:1214, 1987.

[196] S.S. Vogt, S.L. Allen, B.C. Bigelow, et al. HIRES: the high-resolution echelle spectrometer on the Keck 10-m Telescope. *Proceedings of the SPIE*, 2198:362, 1994.

[197] K. von Braun, B. L. Lee, S. Seager, et al. Searching for planetary transits in galactic open clusters: EXPLORE/OC. *PASP*, 117:141, 2005.

[198] S.J. Weidenschilling. The distribution of mass in the planetary system and solar nebula. *Astrophys Sp Sci*, 51:153, 1977.

[199] S.J. Weidenschilling. Dust to planetesimals − Settling and coagulation in the solar nebula. *Icarus*, 44:172, 1980.

[200] S.J. Weidenschilling and D.R. Davis. Orbital resonances in the solar nebula − Implications for planetary accretion. *Icarus*, 62:16, 1985.

[201] D.T.F Weldrake, P.D. Sackett, and T.J. Bridges. Searching for planetary transits in globular clusters - 47 Tucanae and omega Centauri. *astro-ph/0612215*, 2006.

[202] G.W. Wetherill and G.R. Stewart. Accumulation of a swarm of small planetesimals. *Icarus*, 77:330, 1989.

[203] O.R. White and W.C. Livingston. Solar luminosity variation. III - Calcium K variation from solar minimum to maximum in cycle 21. *ApJ*, 249:798, 1981.

[204] R.E. Wilson. A new general catalogue of radial velocities. *PASP*, 63:223, 1951.

[205] R.A. Wittenmyer, M. Endl, W.D. Cochran, et al. Detection limits from the McDonald Observatory planet search program. *AJ*, 132:177, 2006.

[206] S. Wolff and T. Simon. The angular momentum of main sequence stars and its relation to stellar activity. *PASP*, 109:759, 1997.

[207] A. Wolszczan and D.A. Frail. A planetary system around the millisecond pulsar PSR1257 + 12. *Nature*, 355:145, 1992.

[208] M.M. Woolfson. The solar system - its origin and evolution. *Q. J. R. astr. Soc*, 34:1, 1993.

[209] J.T. Wright, G.W. Marcy, R.P. Butler, and S.S. Vogt. Chromospheric Ca II emission in nearby F, G, K, and M stars. *ApJSS*, 152:261, 2004.

[210] F.J. Zickgraf, J. Krautter, S. Reffert, et al. Identification of a complete sample of northern ROSAT All-Sky Survey X-ray sources. VIII. The late-type stellar component. *A&A*, 433:151, 2005.

[211] S. Zucker and T. Mazeh. Analysis of the HIPPARCOS measurements of HD 10697: A mass determination of a brown dwarf secondary. *ApJ*, 531:67, 2000.

[212] B. Zuckerman and I. Song. The AB Doradus moving group. *ApJ*, 613:65, 2004.

[213] B. Zuckerman and I. Song. Young stars near the Sun. *ARA&A*, 42:685, 2004.

[214] B. Zuckerman and I. Song. Young stars near the Sun. *ARA&A*, 42:685, 2004.

Appendix A

Tables of radial velocities

Note: The heliocentric julian date HJD* reported in the table is defined as HJD* = HJD-2400000. Radial velocities RV and their errors σ_{RV} are expressed in units of m s^{-1}.

GJ5

HJD*	RV	σ_{RV}
52096.54424	17.2	7.7
52096.54864	19.9	9.8
52124.55866	-30.3	28.6
52127.46232	-5.7	11.6
52127.46678	2.7	10.3
52132.51924	5.6	7.9
52132.52537	-1.4	8.3
52209.39985	-1.3	7.4
52209.40770	-14.9	8.2
52219.42713	-7.5	8.6
52219.43145	13.5	9.7
52247.22606	-9.1	9.7
52247.23393	1.0	9.1
52279.21944	-12.1	10.2
52334.23818	18.4	9.5
52334.24399	34.6	8.5
52483.58170	12.4	6.6
52513.57707	23.1	9.5
52548.39088	-14.7	8.8
52571.37944	17.0	8.7
52596.30697	2.5	7.6
52683.21640	-3.0	14.7
52857.50623	41.0	9.6
52859.54298	2.0	7.2
52872.47784	7.5	8.1
52874.45400	-16.7	8.5
52875.36422	1.6	12.2
52877.50377	7.4	7.6
52925.35984	-12.4	8.3
52926.38098	-10.5	8.3
52928.40292	-3.8	8.7
52930.43765	-13.6	7.6
52931.40622	-12.3	7.8
52947.28678	-29.7	9.3
52956.32072	0.5	10.9
52982.30063	5.7	13.6
52983.31827	-3.1	10.0
53222.46468	-12.2	7.3
53224.55715	-9.8	7.5
53225.49807	10.4	8.2
53250.55133	6.0	7.4
53253.45727	-1.8	7.6
53254.47483	-0.8	7.9
53272.31232	-10.9	9.5
53275.48776	-10.5	8.0
53279.37827	-17.0	8.4
53281.37336	-5.8	8.8

HD3126

HJD*	RV	σ_{RV}
52213.39316	-541.2	202.4
52213.40805	-852.4	209.9
52219.37521	171.9	154.4
52219.38653	210.8	123.7
52247.26627	21.1	158.4
52247.28115	165.5	147.0
52572.40082	168.2	187.4
52685.24639	-203.8	254.9
52859.55120	96.8	111.3
52872.48622	-75.7	179.3
52874.46233	-247.9	196.4
52877.53195	-19.0	191.8
52878.51010	135.0	217.7
52925.35365	80.6	118.2
52926.43359	104.9	89.5
52928.41131	123.2	205.4
52929.42764	73.6	127.7
52930.43025	96.8	179.2
52947.37228	-63.2	193.0
52948.28666	-618.0	350.9
52949.33968	-76.8	159.2
52952.34751	-297.8	259.0
52955.34982	144.6	177.3
52956.33494	85.1	196.4
52981.25332	49.0	254.4
52982.30931	-45.3	212.9
52983.32504	61.0	191.2
53221.53269	231.0	105.4
53222.51256	350.4	123.8
53224.56494	90.0	108.7
53250.54554	-103.8	187.6
53253.47507	76.3	226.4
53254.48268	23.0	278.8
53275.47856	76.2	157.5
53282.46754	59.9	277.5

HD5286

HJD*	RV	σ_{RV}
52127.58051	-18.2	13.6
52127.58683	-15.6	15.7
52132.53387	-34.0	16.0
52132.54214	-84.2	19.8
52209.41796	-107.5	7.5
52209.42579	-90.5	8.2
52247.24594	-71.4	8.6
52247.25392	-51.6	8.1
52279.25698	-58.6	8.4
52279.26137	-56.7	8.0
52280.33353	-60.6	8.1
52280.33994	-50.7	8.1
52333.22183	-50.7	8.5
52333.22613	-16.0	8.5
52483.58728	-9.4	8.2
52506.53151	20.8	9.1
52548.39723	63.7	7.8
52572.39108	-88.1	8.2
52574.29585	-20.1	8.2
52684.30967	-13.2	8.5
52834.49145	158.4	9.2
52857.51078	-41.0	9.1
52858.51596	2.3	8.3
52859.55771	-92.2	8.0
52872.49226	-51.1	9.3
52874.51394	36.6	11.5
52878.50212	20.9	9.4
52925.37560	48.3	8.7
52926.44086	53.6	8.0
52928.41846	-20.1	7.7
52929.43558	-14.9	7.1
52930.44258	-31.2	7.4
52931.43214	-62.6	7.6
52947.38263	5.9	8.4
52948.29399	-18.2	10.1
52949.34674	25.9	7.4
52950.48803	16.7	8.2
52950.49256	9.2	10.2
52952.37227	-7.1	9.1
52954.42581	5.6	8.5
52955.37359	7.0	7.9
52956.35717	36.0	8.1
52982.31869	102.9	8.1
52983.33369	48.4	7.9
53222.46852	61.1	8.5
53225.50890	86.9	8.1
53250.55729	1.7	7.9
53253.46147	154.4	7.9
53254.48811	121.1	8.0
53275.46803	42.2	7.7
53279.41785	41.4	7.9
53282.47362	35.2	8.4

HD7590

HJD*	RV	σ_{RV}
52833.44179	20.2	11.5
52834.48072	-10.5	9.2
52857.51473	23.8	15.2
52858.50872	5.2	11.0
52861.59398	-8.9	9.7
52872.49701	-4.5	13.3
52874.52003	-13.4	12.3
52877.55643	16.3	13.3
52878.49507	-16.8	12.7
52925.38033	34.6	10.9
52926.44730	-10.1	10.9
52928.56763	1.1	15.3
52929.45406	-17.6	10.4
52930.44792	-7.7	11.8
52931.43713	-2.7	11.0
52947.39096	-1.3	13.8
52948.29965	-13.5	15.4
52950.50044	-1.8	17.5
52950.50954	-7.3	15.1
52952.37935	31.4	12.0
52954.43615	39.0	16.2
52955.37940	35.0	12.3
52949.35246	61.0	15.1
52956.36265	-9.4	10.2
52981.28173	1.8	17.9
52982.32634	-11.3	14.0
52983.34092	0.6	11.2
53222.47269	4.0	14.6
53225.50165	-33.8	13.2
53250.56432	2.9	10.2
53253.46545	4.7	12.1
53254.49294	-41.9	11.1
53272.32040	-36.1	15.8
53275.49448	-2.4	11.5
53279.38881	-23.1	17.0
53281.55904	-5.7	9.7

HD17332a

HJD*	RV	σ_{RV}
52213.45774	97.3	14.0
52213.47261	98.1	19.4
52279.28904	248.1	19.4
52279.30041	218.0	16.6
52333.26461	-161.1	17.7
52333.27592	-124.6	14.6
52506.55914	-272.0	26.8
52548.58881	-93.7	13.9

HD17925

HJD*	RV	σ_{RV}
51951.24438	40.1	8.9
51951.25081	28.6	9.1
52209.47039	-31.1	12.5
52209.47897	-41.3	10.4
52278.31213	-30.3	13.0
52278.31716	9.8	15.3
52280.29615	70.1	11.6
52280.30075	57.3	12.1
52280.30513	66.4	9.5
52336.23868	42.4	14.4
52336.24480	49.9	12.3
52506.60919	-16.6	8.1
52509.60771	2.7	13.7
52510.60961	-5.3	10.4
52511.60943	-7.3	9.8
52513.61310	-10.2	10.1
52515.61065	37.4	13.9
52517.61338	8.5	15.8
52519.63477	2.3	8.0
52548.57768	-5.0	7.5
52925.42818	1.8	12.4
52926.45481	17.3	11.8
52928.57787	-37.5	9.3
52929.47242	-18.8	10.0

continued on next page

continued from previous page

HJD*	RV	σ_{RV}
52948.44880	-43.6	8.4
52952.42288	-9.3	12.1
52955.42758	-38.0	13.9
52956.48170	-11.5	12.2
52983.36068	-31.8	9.1
53250.57101	-31.5	9.8
53253.61377	-8.5	9.1
53254.62049	-4.2	7.5
53275.57935	-25.0	11.9
HD20630		
52515.62120	34.7	11.3
52545.55596	51.8	10.6
52545.56155	48.9	11.1
52548.50873	-19.5	9.5
52592.48654	-12.3	9.1
52596.42171	-6.7	9.2
52681.35514	25.4	11.1
52872.56331	25.3	10.4
52877.58370	-57.4	7.9
52878.55285	7.0	19.0
52925.43304	20.3	8.0
52926.48701	-15.8	8.4
52928.58456	39.4	9.7
52929.47777	-39.5	9.5
52948.44168	-36.5	7.9
52952.43077	-2.8	8.3
52955.43351	61.8	11.2
52956.48996	-31.4	9.9
52982.41731	18.4	9.7
52983.42176	-9.3	11.1
53250.57744	-33.1	9.3
53253.53540	-14.3	9.3
53254.58949	-43.0	8.5
53275.57099	-0.8	8.4
53281.59715	-11.2	7.6
HD21845a		
52213.50812	93.0	28.5
52219.45999	-117.8	13.6
52219.47479	-83.6	15.9
52278.34654	-5.3	27.3
52278.36143	7.2	29.1
52306.34174	118.2	10.5
52306.35659	104.7	13.1
52506.57649	31.9	16.1
52571.36700	105.7	14.6
52572.36103	60.4	19.0
52574.30483	68.3	25.3
52574.35469	70.1	18.3
52592.30695	-19.7	18.7
52596.29367	56.5	12.3
52628.26244	-81.0	14.7
52656.51787	-76.0	23.3
52657.28048	60.7	11.8
52661.33146	-27.4	17.2
52662.25828	-5.1	14.8
52683.41801	-13.5	19.9
52744.35826	-8.0	21.9
52750.31226	51.3	18.9
52752.31638	-71.6	15.0
52754.33420	17.8	33.5
52858.58436	60.4	16.7
52863.61664	-25.3	17.8
52877.59238	-29.6	13.1
52925.31594	-85.6	17.9
52929.48935	17.1	12.0
52931.45996	-58.8	13.3
52948.42987	-106.8	15.9
52949.41273	21.5	13.6
52956.51259	83.6	12.9
52981.32442	74.9	17.8
52982.42938	-21.6	13.4
52983.43335	-152.8	12.8
53222.49272	-27.5	20.3
53225.55357	-26.2	14.0
53224.57156	13.2	13.6
53248.53212	75.6	16.4
53250.58764	-35.1	13.5
53253.50741	-39.5	12.9
53254.50304	23.9	11.7
53281.58545	15.7	10.4
53307.55352	29.8	14.5
53454.29053	-102.6	20.2
53456.29853	-31.8	15.2
v891 Tau		
52209.50907	-13.0	11.4
52209.52043	-6.5	11.5
52213.57411	1.2	22.8
52213.58658	-6.9	20.0
52219.50078	-4.4	20.5
52308.31712	31.0	11.1
52308.32320	30.3	10.4
52332.25276	20.9	12.8
52332.25887	30.8	11.9
52336.28281	31.4	10.2
52336.29068	25.6	12.6
52363.28334	-30.2	16.0
52363.28946	8.5	18.6
52572.48714	39.6	16.9
52596.31702	-12.6	14.4
52662.35944	-2.5	12.7
52683.43897	-16.0	35.8
52872.57171	-8.2	18.2
52878.62022	69.6	26.0
52925.45979	-9.1	13.6
52931.56830	-49.0	15.2
52948.45705	-24.9	10.3
52956.52958	3.7	12.3
52982.44366	-9.6	14.7
52983.48801	-6.7	13.6
53250.60967	-18.8	16.5
53253.54925	-7.2	15.3
53254.57301	-38.4	17.1
53275.58838	-38.6	18.9
v774 Tau		
51949.33018	-20.9	7.2
51949.33523	-30.2	7.6
51983.25595	9.1	8.9
51983.26025	1.5	9.5
51983.26573	15.4	8.6
52127.60797	5.3	32.1
52213.55856	0.0	14.5
52213.56464	-11.6	16.1
52219.48848	-0.1	11.7
52219.49455	-7.0	12.5
52304.36855	10.3	13.5
52308.30182	20.4	9.7
52308.30800	6.0	9.0
52332.24226	-4.4	11.1
52332.24657	6.5	9.6
52336.31345	26.5	12.1
52336.31796	7.3	15.2
52363.27247	18.3	11.6
52363.27685	6.3	15.3
52365.29866	-3.5	32.9
52572.47511	24.0	14.2
52596.32337	-1.5	9.4
52662.35362	-4.4	11.5
52683.43252	5.4	15.1
52872.57717	-8.3	12.6
52878.62656	17.9	27.5
52925.46512	-19.6	11.0
52931.57365	-25.7	10.5
52948.46505	-6.5	8.0
52956.52397	1.8	11.8
52982.44948	-7.2	11.9
52983.49336	-8.6	10.9
53250.61614	0.4	10.0
53253.54243	-3.2	11.0
53254.56688	-16.3	9.3
HD37394		
52744.31602	14.7	5.6
52750.29564	5.8	5.8
52751.35973	2.9	7.7
52754.31768	18.9	7.6
52872.59307	-0.6	10.0
52877.60955	-11.2	7.4
52925.46838	5.4	8.2
52929.50104	-7.7	7.2
52930.54904	-13.9	6.5
52948.51122	17.0	5.6
52952.49994	-4.8	6.5
52955.53048	-8.2	6.7
52956.57087	-7.3	6.4
52982.45629	-6.8	6.1
52983.49945	-18.8	6.1
53253.55572	15.4	8.7
53254.55651	16.6	9.9
53422.37031	-7.2	5.8
53454.33787	0.4	7.7
53456.31764	-6.1	5.4
53488.34637	-4.2	6.7
HD41593		
52279.42456	27.3	12.3
52279.43099	29.8	11.5
52308.33491	-11.5	7.5
52308.34275	-8.5	7.2
52332.27114	16.2	6.2
52332.27913	0.1	6.7
52333.33233	-37.8	9.2
52333.33842	-35.4	9.7
52336.41053	0.7	8.3
52336.41665	9.4	10.0
52363.30031	65.6	8.3
52363.30643	58.9	11.2
52365.31447	-21.5	12.3
52365.32055	-20.2	11.1
52393.32779	-6.5	9.5
52393.33664	-12.9	8.4
52394.30920	-34.2	9.0
52394.31550	-33.9	21.3
52596.49565	28.5	6.7
52656.48712	-62.4	10.0
52657.31211	-23.0	6.7
52660.32668	-24.7	9.3
52661.36321	40.6	12.5
52683.46486	7.3	12.0
52712.38943	12.7	15.8
52744.37138	26.4	11.4
52750.30211	23.6	9.1
52754.32414	-6.2	13.0
52925.47398	11.1	8.7
52929.50691	-41.8	10.5
52952.52326	-14.1	10.1
52955.55783	-17.9	9.7
52956.61528	-13.2	7.7
52981.49499	-1.1	7.6
52982.46438	5.7	9.9
52983.58274	-8.4	7.9
53253.58921	4.2	9.6
53254.60478	-22.3	9.4
53420.36698	-40.1	29.1
53454.31451	11.6	9.6
53456.28857	32.2	7.5
53658.61802	-14.7	8.1
53662.63884	-20.5	6.9
53721.43075	-1.0	8.7
53749.53177	7.0	11.3
53750.50894	-23.5	11.7
53751.38427	-34.4	8.7
53751.47893	-20.4	7.5
53752.41264	-4.4	9.7
53752.48943	-8.5	12.6
53780.47271	17.7	10.4
53784.33058	43.3	7.1
53785.38688	44.3	9.9
53802.35463	-8.8	10.6
53805.39293	28.2	8.6
53814.30615	-3.8	8.0
53815.31836	-14.5	9.1
53845.31522	49.1	7.4
54080.43088	18.7	9.4
54080.46403	26.5	10.0
54080.59915	21.3	8.8
54082.49889	-10.1	14.1
54082.53818	-31.7	13.3
v1358 Ori		
51983.29746	203.5	202.2
51983.31229	162.1	198.3
52278.43520	128.8	256.4
52278.45080	188.3	243.0
52306.37780	-1.8	210.8
52306.39273	-107.8	173.3
52308.35757	91.4	167.4
52308.37432	-21.0	164.1
52363.31914	-33.1	220.9
52657.44077	-462.9	193.2
52662.34539	336.2	179.9
52684.32787	-468.0	220.4
52925.52317	25.5	189.1
52930.61129	149.4	240.1
52955.57265	179.9	213.6
52956.62636	-145.1	189.4
52982.47690	-23.3	197.3
52983.59557	-220.8	195.7
OU Gem		
52280.43660	-30300.0	34.6
52280.44442	-30158.2	34.8
52306.40647	11081.7	42.4
52306.41441	10485.6	38.4
52308.38971	-30523.4	33.2
52308.39825	-30355.4	31.2
52334.35574	12524.8	42.2
52334.36364	11954.9	44.6
52597.50303	16627.7	41.4
52684.34154	-12295.1	43.7
52956.64033	12254.4	44.0
53253.59936	11889.3	43.8
53254.59465	49013.7	43.6
HD63433		
52714.38824	-55.1	13.3
52744.38209	26.3	11.6
52747.30171	-7.8	9.3
52751.37526	44.7	8.5
52781.36731	39.8	17.2
52925.61128	34.4	21.0
52981.53654	-27.0	8.2
52982.50011	24.7	12.0
52983.61785	11.8	9.9
53134.32225	-66.5	13.3
53134.33018	-40.7	12.9
53134.35684	-21.6	19.0
53128.35727	24.4	15.4
53253.62014	34.9	21.4
53420.41308	-5.1	24.4
53422.41131	-233.4	8.8
53454.35431	-36.8	11.8
53456.32797	31.8	11.1
53489.34321	-9.6	8.2
53517.35742	14.5	18.3
53721.44171	66.1	13.2
53750.53942	31.5	12.7
53751.40933	-8.4	9.6
53751.50427	-32.4	10.0
53752.43743	-59.9	14.4
53752.51554	-38.4	13.0
53780.43904	34.0	11.6
53780.62137	43.9	16.3

continued on next page

continued from previous page

HJD*	RV	σ_{RV}
53784.55485	-18.1	10.4
53785.43649	42.0	24.0
53785.44805	13.6	8.9
53802.33392	37.0	13.8
53802.40194	21.5	9.3
53805.40669	-32.7	10.1
53814.32138	4.0	9.8
53815.33262	16.0	8.2
53840.38850	23.5	7.2
53845.32912	17.7	7.5
53846.41364	16.0	19.3
53861.33769	-10.5	17.8
53862.34682	0.1	17.9
53863.34562	9.3	16.2
54080.43744	40.6	21.4
54080.47146	26.9	21.4
54080.60638	38.9	20.8
54082.50625	-9.5	19.6
54082.54624	14.3	26.1
HD77407		
51951.63431	55.6	16.8
51951.64228	27.8	16.2
51952.47714	-15.0	17.0
51952.48498	-46.7	31.6
51979.35777	-45.6	53.6
51984.35118	11.2	48.0
51984.36473	-47.5	60.3
52005.33335	-17.9	18.2
52005.34313	-21.3	12.0
52039.39557	-45.6	10.2
52039.40689	-41.4	9.9
52043.35179	-55.1	13.1
52043.35846	-54.2	14.8
52067.36849	-40.2	11.5
52067.37984	-18.0	11.7
52209.60998	-30.5	13.1
52209.62480	-37.0	12.6
52209.67969	-17.9	18.7
52308.43405	2.2	10.6
52308.44543	-0.1	8.4
52332.31797	-10.5	10.3
52332.32931	-8.2	11.5
52334.52372	6.5	10.4
52336.43996	-13.8	16.3
52336.45156	-9.8	11.0
52362.33708	-34.7	8.8
52657.45575	3.7	10.6
52662.37728	-43.4	12.0
52684.39267	34.2	12.7
52746.33955	25.3	14.8
52747.31450	-33.7	17.1
52753.32824	-40.4	25.4
52781.39164	62.4	17.3
52981.58480	-1.9	10.1
52983.70318	25.3	10.0
53081.51843	32.1	11.2
53422.43695	-9.3	20.0
53454.39796	20.4	17.5
53456.35793	26.1	15.7
53488.33721	42.1	13.3
53489.35759	52.7	10.6
53516.38991	52.9	18.5
54080.62368	48.6	13.7
GJ355		
52008.33873	-96.4	78.8
52308.49091	-26.6	78.0
52308.50690	-33.5	67.0
52365.36397	194.1	100.9
52366.37418	-82.9	97.9
52657.54048	255.5	90.2
52662.45489	163.4	75.6
52681.45228	-197.5	74.7
52683.45498	-52.8	99.7
52684.44162	-1092.1	93.1
52746.32643	-268.8	61.0
52747.33070	306.3	80.3
52750.36594	-210.5	108.5
52983.73154	-129.5	76.7
53023.52951	501.1	79.5
53489.31833	163.7	70.9
53749.56178	-74.2	106.9
53750.55713	443.2	91.6
53814.38150	134.4	87.5
54080.63588	80.9	85.4
HD97334a		
52712.45798	15.2	15.0
52744.49513	19.5	9.0
52747.39621	23.2	6.9
52750.42271	28.1	8.9
52751.45174	28.1	7.5
52781.40426	22.1	12.9
52981.61459	36.0	10.8
52982.65411	41.5	9.7
53022.53954	-21.6	12.6
53023.48799	-37.9	10.4
53075.50912	-21.0	19.6
53076.42583	-34.4	8.3
53080.47908	-3.9	9.3
53081.40923	-3.4	8.2
53082.48681	-33.3	8.6
53133.39555	-6.2	12.2
53125.54055	-3.7	13.5
53091.51883	-6.6	22.6
53091.53433	-8.6	11.3
53092.52197	8.8	11.1
53220.34214	-6.0	13.3
53220.34644	7.6	14.3
53221.35089	19.5	20.3
53222.34288	52.4	27.0
53425.51581	-627.4	13.0
53454.50341	-246.3	10.7
53488.37397	327.9	7.7
53750.59467	-983.1	13.3
53780.55486	-765.4	11.0
53784.61353	-754.2	7.7
53786.49970	-729.6	20.4
53814.39189	-371.4	11.5
53874.50329	643.7	9.4
53877.38592	644.4	9.0
53893.41589	837.1	11.7
53894.44727	823.2	8.5
53898.43772	838.5	8.8
HD103095		
52746.45134	-11.1	7.9
52747.48225	-9.8	12.4
52750.42895	1.1	11.2
52751.45966	-14.1	11.2
52753.34873	-27.0	9.9
52781.43055	-9.2	11.7
53076.54376	-13.8	12.5
53081.41561	-5.7	13.6
53223.33841	25.2	35.5
53422.53744	5.0	12.7
53456.40592	26.4	13.4
53488.38101	-8.3	9.3
53490.47163	-7.3	8.7
53491.43819	-21.8	19.7
53515.41745	28.0	11.3
53750.60231	0.6	14.1
53751.58191	5.1	14.4
53814.39840	24.2	13.8
53840.56843	2.7	12.6
54080.65523	21.5	16.4
HD109011		
52744.53603	4809.6	70.0
52747.40600	4955.8	70.7
52752.37326	5184.8	65.4
52836.49573	6468.8	71.3
52781.44136	6024.7	67.4
52949.66169	5702.0	68.9
52981.63474	5322.0	69.2
52982.71910	5291.9	69.4
53023.56714	4724.7	60.9
53079.53277	4047.7	72.4
53081.50249	4009.6	67.5
53133.42294	3212.7	70.1
53091.46998	3840.5	69.8
53092.53123	3861.2	67.8
53220.35903	1809.8	67.9
53221.36308	1800.4	66.2
53222.35471	1761.6	71.3
53224.35623	1741.3	65.1
53225.35033	1738.6	67.9
53422.54943	716.1	191.2
53454.51212	337.0	51.3
53488.39097	-265.0	215.7
53492.40476	-391.2	202.9
53749.64504	-7831.0	239.4
53750.61898	-7858.9	244.5
53780.57837	-8882.4	241.4
53784.62884	-9072.4	238.5
53814.40842	-9952.7	182.6
53840.57895	-10548.3	236.5
54080.58232	8197.1	225.1
54099.28054	8160.1	74.1
54099.29518	8121.3	132.8
54099.30982	8193.0	54.1
HD111456		
52308.51996	1605.5	123.1
52308.52431	1727.5	148.2
52332.43210	1710.6	144.7
52332.43644	1626.4	103.9
52332.48512	1698.7	113.6
52336.49512	1543.9	115.2
52336.49943	1630.6	126.6
52363.36425	1711.6	100.1
52363.36857	1566.3	102.5
52365.51373	1627.8	123.0
52365.51803	1554.9	127.6
52394.40253	1862.7	137.4
52394.40696	2126.3	167.8
52410.50216	2049.8	107.4
52411.33933	2133.2	83.8
52414.36423	2104.1	138.3
52413.50287	1980.5	194.4
52417.33867	2158.5	154.4
52443.39772	2220.0	114.9
52443.40216	2244.2	138.7
52451.40171	2290.0	113.7
52484.56482	1796.0	171.8
52661.61134	3023.7	216.1
52661.61596	3040.6	191.8
52662.43207	2816.7	172.9
52683.60087	2696.2	153.2
52712.46543	2811.7	201.0
52744.54879	2557.6	162.7
52753.41879	2544.5	130.1
52836.53205	2025.9	220.5
53022.54541	1057.0	162.7
53023.49450	600.9	154.0
53043.49920	713.0	219.7
53076.40036	1320.4	346.3
53080.48381	-366.0	275.6
53081.41934	-802.4	177.2
53082.49132	-952.9	160.0
53091.54426	-420.4	204.5
53092.54174	-1350.2	139.3
53220.37233	-4450.4	282.9
53421.58828	-6954.4	469.9
53425.55658	-7691.5	363.5
53454.52113	-8954.9	191.2
53456.40949	-8711.0	203.0
53488.40161	-7282.9	332.2
53489.39890	-8617.2	138.6
53490.47757	-8554.1	135.6
53516.41762	-7282.8	340.3
53517.40653	-8179.4	172.4
53537.41374	-6714.8	327.4
53758.66987	-428.2	305.8
53780.59310	-187.1	228.0
53784.63916	-538.5	179.4
53785.49193	-854.5	277.8
53785.49793	-595.4	174.9
53814.36860	570.9	156.6
53840.46713	950.3	179.3
53845.36714	572.3	128.5
53861.37410	677.6	125.0
53862.38269	327.8	212.2
53870.42884	857.9	240.7
53870.46254	883.1	160.4
53873.56519	1133.9	163.6
53874.50948	1056.8	125.1
53875.38586	1169.8	162.6
53876.42461	1022.5	116.8
53877.54734	1272.3	340.6
53893.42560	1295.3	106.2
53894.45350	1254.9	88.7
53898.44373	1272.2	89.2
53927.51764	1230.2	182.2
53928.44627	1070.7	198.1
53929.48543	1093.8	204.1
53933.39533	1434.2	166.7
54070.71459	2241.2	169.3
54073.68310	2271.8	157.3
54080.66034	2583.3	174.0
54110.74679	2443.7	106.1
54111.66825	2362.7	117.6
HD115043a		
52308.53246	22.6	18.4
52308.53854	17.9	22.6

continued on next page

continued from previous page

HJD*	RV	σ_{RV}
52332.46729	35.4	15.3
52332.47511	20.6	13.8
52336.50592	-23.9	21.4
52336.51198	-13.8	21.4
52363.37657	-45.5	17.2
52363.38269	-48.2	13.6
52363.54986	-47.9	12.7
52363.55595	-30.1	13.6
52363.56208	-36.7	16.5
52365.52627	-27.6	17.2
52365.53247	-7.8	19.6
52394.41465	-11.8	29.9
52414.38064	-37.6	42.8
52443.38130	-7.6	22.4
52443.38921	0.1	19.4
52451.41095	-18.4	14.8
52657.55412	5.0	16.9
52662.43864	-41.1	35.6
52683.49438	-38.1	21.5
52683.61018	-42.8	17.3
52714.57537	-33.0	21.3
52744.55685	27.6	17.1
52750.41587	53.8	16.2
52751.40758	-5.9	12.1
52836.50842	15.5	17.0
52781.45423	-32.7	16.9
52877.32053	29.0	21.5
52982.73651	-9.3	17.1
52981.66295	-5.1	18.1
53022.55142	-22.8	17.6
53023.49971	-2.0	18.9
53043.50632	38.3	20.9
53076.55548	-37.9	17.6
53081.42580	0.5	21.9
53081.62129	-27.5	15.7
53082.49787	-29.4	14.1
53080.49122	-22.1	44.1
53091.55503	5.8	18.6
53092.54836	1.8	18.7
53220.39841	-7.0	12.8
53419.64537	52.6	24.1
53420.35304	39.5	18.7
53422.57142	-13.2	13.8
53425.63482	53.7	16.3
53431.71424	76.0	23.1
53432.55400	-3.3	25.7
53454.57578	38.5	23.8
53456.41629	56.0	14.8
53488.40984	-1.8	13.4
53488.53982	-5.5	21.2
53489.40810	6.4	11.1
53490.48509	22.4	11.3
53511.35403	16.6	13.4
53515.47550	46.7	16.9
53516.40584	32.1	13.4
53516.48253	19.4	14.0
53517.39763	20.0	17.9
53517.50094	34.8	16.8
53524.49259	-4.8	17.8
53529.55799	57.2	28.5
53537.40275	4.7	14.2
53749.65942	-13.8	20.8
53750.64864	-2.0	15.0
53785.50504	-3.8	13.6
53815.38223	19.1	17.1
53840.59181	36.7	16.5
53862.39038	-138.0	25.2
53897.53997	-3.8	16.2
54080.66712	-11.0	24.2
GJ504		
51951.57740	49.3	18.4
51951.60229	34.6	15.6
51983.43343	55.3	12.0
51983.43771	65.2	12.0
52002.50445	-14.6	18.6
52009.49899	-15.3	13.1
52009.50334	-22.3	13.8
52038.41162	71.3	12.9
52038.41606	79.7	12.1
52039.52957	-2.8	15.5
52039.53388	-14.2	14.0
52041.35929	2.4	11.8
52042.33323	24.2	14.2
52042.33751	23.5	11.1
52043.42825	-31.9	11.7
52043.43331	-20.0	12.5
52066.43040	40.8	11.5
52066.43544	50.3	14.3
52308.54640	17.5	16.4
52308.55078	33.3	13.1
52336.52119	-7.4	12.9
52336.52547	-3.3	14.0
52363.57766	-1.2	9.0
52363.58221	-16.6	8.7
52365.54580	-15.4	10.8
52365.55018	-6.9	11.0
52443.37002	-49.0	15.2
52443.37447	-27.8	19.1
52448.38246	-26.5	15.5
52448.38867	-14.6	12.8
52661.62429	-11.1	12.3
52661.63068	9.2	10.9
52683.62207	28.4	11.8
52712.47695	-3.3	21.1
52745.46922	2.0	15.4
52753.43602	38.1	16.7
52806.39837	21.4	22.5
52783.39371	28.1	14.2
52982.74101	11.6	12.5
53082.52337	-20.9	16.2
53422.58243	-18.4	12.0
53425.62791	-15.2	11.5
53454.49662	14.5	16.3
53488.42053	-21.8	14.1
53489.42086	-26.0	12.7
53516.44383	-56.6	13.8
53537.38839	11.7	12.8
53749.62144	3.3	13.5
53749.62745	-14.6	12.9
53750.63147	-30.1	16.1
53750.63765	-20.8	12.4
53751.54903	-30.3	11.0
53751.55684	-35.6	12.4
53751.66616	-28.5	11.4
53752.68996	-15.0	10.7
53780.65165	-22.7	9.5
53784.61909	-11.6	10.8
53802.56654	-14.4	10.7
53802.62067	-16.2	11.2
53840.40615	4.8	21.4
53845.46638	18.0	19.9
53846.43828	-30.5	13.1
53846.46525	-21.4	13.8
53846.48857	-31.0	11.3
53861.38671	-31.8	15.7
53862.37880	-56.3	18.6
53863.40560	-0.1	19.7
53870.47667	37.5	14.9
53873.43723	19.1	13.5
53874.50079	0.9	16.5
53876.43714	-37.3	15.2
53877.38281	31.9	14.3
53893.39602	-35.3	14.0
53894.39000	36.9	11.3
53895.39641	8.8	11.3
53896.39103	1.9	13.9
53897.38121	6.5	13.9
53898.39303	11.7	12.5
53920.37397	17.6	12.7
53921.37336	13.2	11.7
53922.37469	-22.7	14.6
53923.36921	-37.6	17.3
53925.37126	-11.5	21.9
54080.60743	17.5	13.9
54080.64357	9.3	12.3
54080.68489	20.0	12.0
HD116956		
52744.56863	-0.8	6.3
52747.47088	-33.6	4.2
52751.43303	18.5	5.2
52806.40818	9.7	8.3
52836.52202	60.5	6.6
52781.46540	43.5	5.9
53023.51068	4.8	8.4
53043.51727	-41.6	7.5
53079.54834	12.0	8.0
53080.53978	22.0	9.7
53081.43666	12.4	6.7
53081.63355	0.7	4.8
53082.51012	-43.1	5.9
53133.45706	8.5	8.9
53091.48569	-31.7	6.3
53092.55901	-21.1	7.1
53220.38691	12.6	6.8
53221.37941	29.5	7.8
53247.35255	10.9	5.8
53389.63922	1.1	7.3
53425.65000	-15.7	8.5
53456.42787	44.7	10.4
53488.42781	-7.8	6.7
53489.42764	-38.9	6.6
53491.58464	17.9	6.0
53492.42446	14.6	12.9
53516.45222	31.7	7.2
53517.41861	28.6	6.8
53537.44054	-23.9	5.4
53815.39609	10.9	9.1
53840.60442	31.3	7.0
53861.40096	-75.0	9.6
53862.40420	-91.4	9.7
54080.67756	0.9	8.8
GJ517		
52750.46404	129.7	27.8
52752.39481	-38.9	29.1
52754.40776	52.8	41.2
52784.38250	-65.0	41.1
52783.40635	-36.8	42.2
53082.54969	-79.2	55.4
53489.45008	-24.5	30.9
53861.42205	20.1	67.7
53862.42852	62.1	60.7
HIP67422a		
52308.56249	-56.5	9.0
52308.57387	11.2	7.4
52336.53399	-334.1	9.2
52336.54548	-291.3	10.1
52451.42376	422.4	8.4
52661.64840	-82.4	8.6
52683.63302	-103.0	11.9
52744.62807	-85.8	9.1
52783.42039	-1247.4	9.9
53220.40947	480.7	11.4
53432.56586	-505.7	20.3
53456.44448	142.3	11.6
53488.56746	592.9	11.1
53537.48880	587.7	11.8
53861.43547	393.1	12.3
EK Dra		
51983.51853	167.1	46.4
51983.52805	172.2	32.9
51983.55604	173.7	34.3
52003.50314	-94.0	35.9
52039.54301	-40.3	22.3
52039.55801	-46.0	21.1
52040.44789	-204.1	35.4
52040.45569	-163.5	29.3
52066.44205	340.2	30.8
52066.44986	349.2	33.3
52093.41991	-41.3	50.7
52094.38466	-96.7	24.6
52094.39616	-79.9	23.3
52100.44836	-2.0	29.9
52100.47065	-38.0	31.2
52129.37773	-65.4	32.4
52129.38915	-69.4	34.1
52132.38064	5.4	53.5
52132.39040	13.3	42.3
52132.40265	66.5	47.8
52308.58854	-189.1	27.0
52308.60346	-197.9	24.0
52334.29656	-47.0	31.4
52334.31139	0.5	30.1
52362.29338	-188.7	22.5
52363.47213	46.0	18.6
52363.48701	51.8	24.2
52363.50186	50.1	24.6
52365.43852	-60.6	22.9
52365.46042	-26.8	21.8
52366.52759	-137.5	27.8
52412.45669	65.5	45.7
52412.47156	-37.9	38.7
52440.36673	108.4	24.4
52440.38158	54.8	20.9
52476.53426	243.0	28.3
52478.49442	20.3	20.9
52483.35505	77.4	19.3
52484.36768	295.2	20.3
52506.39009	122.4	26.2
52507.42862	-24.7	35.0
52513.36602	-199.3	32.8
52516.35553	-214.5	65.4
52661.66899	239.5	32.0
52683.67384	-98.1	40.1
52744.63841	254.0	27.8
52752.59869	59.7	22.6
52753.55073	-125.8	22.4
52784.45287	20.0	23.5
52802.43189	35.2	37.7
52806.43186	-184	27.2
52807.41772	-72.1	21.9
52827.52221	-50.0	65.0
52877.33273	-40.1	22.7
52878.34005	30.0	23.4
52931.28658	-81.6	24.2
52953.21961	-15.3	33.5
53023.44145	63.7	29.9
53079.56378	188.3	48.2
53081.46159	6.9	22.0
53225.36714	70.5	22.1
53456.45286	-47.9	58.2
53488.45167	-248.1	23.9
53489.46266	-100.5	20.4
53490.49657	188.7	25.0
53492.44283	-248.4	65.4
53516.42916	-129.6	21.6
53517.47022	-105.6	17.6
53537.47001	88.8	24.2
53538.53920	41.8	34.0
53541.47724	-45.9	23.4
53840.62210	-16.4	22.6
53843.62883	191.6	32.9
GJ563		
51983.60808	4193.9	31.2
51983.61419	4182.9	30.8
52039.46287	3976.9	24.8
52039.46895	3977.6	28.2
52060.42142	3898.4	31.8
52060.42754	3888.5	27.1
52060.43363	3854.5	35.8
52066.38139	3902.5	25.0
52066.38746	3916.2	25.3
52095.36974	3711.2	38.6
52095.37600	3690.3	39.1
52308.69317	3208.8	29.0

continued on next page

continued from previous page

HJD*	RV	σ_{RV}
52308.69930	3188.3	26.9
52393.49282	2883.9	29.4
52393.50065	2872.4	30.5
52451.37348	2616.1	45.0
52712.56643	1721.6	33.5
52746.52069	1538.2	28.7
52753.52057	1503.6	27.8
53080.59041	241.5	35.1
53133.44362	-61.2	33.2
53091.57877	160.0	33.1
53092.58036	110.9	58.4
53454.59734	6582.9	2309.9
53492.48012	-815.5	29.5
53861.51064	-360.2	37.4
53862.45443	-437.7	31.7
53863.46637	-419.7	37.6
HD130948		
51951.64791	3.4	15.9
51951.65292	-5.0	16.7
52039.47491	-69.0	10.2
52039.48102	-56.7	11.6
52042.43089	3.4	9.5
52042.43594	2.7	9.9
52043.33615	17.6	12.3
52043.34117	28.1	14.9
52043.53727	15.7	12.3
52043.54229	36.8	12.9
52308.61600	3.9	14.9
52308.62212	9.5	12.5
52336.55416	16.2	12.1
52336.56024	29.0	46.4
52363.58999	-6.0	10.7
52363.59619	-4.0	12.2
52444.39073	5.9	16.9
52444.39516	-1.3	14.2
52448.39997	-0.2	11.2
52448.40619	10.5	12.8
52451.36324	2.1	10.1
52452.37831	-2.3	14.7
52477.35803	23.3	14.0
52483.33384	-14.8	14.1
52483.39851	1.2	12.1
52484.35723	-11.0	14.1
52506.32091	3.9	14.6
52507.34045	-5.4	13.3
52657.57798	54.3	14.3
52684.56769	-12.8	12.0
52712.55673	29.9	20.7
52746.44463	33.9	11.9
52747.48958	8.2	11.1
52752.40774	-14.7	11.7
52753.56731	12.9	10.1
52784.46864	22.6	15.0
52806.42337	38.8	14.2
52833.41320	11.9	15.3
52783.43198	-5.3	12.9
53080.58058	-36.5	11.6
53081.47705	-39.2	12.7
53220.42092	-1.8	14.8
53432.53403	31.5	11.7
53454.56758	-21.6	25.4
53456.51035	8.8	11.5
53488.46655	-10.5	16.1
53491.56430	-16.8	12.2
53515.44664	5.9	12.5
53517.46191	-20.1	11.0
53524.48966	20.5	17.8
53751.58676	3.7	14.2
53802.65188	1.6	13.0
53861.50089	-11.4	18.7
53862.44406	-80.4	12.6
Xi Boo a		
51951.56518	-79.8	12.5
51951.56950	-56.5	11.5
52002.51149	-52.8	10.2
52002.51622	-69.7	9.4
52003.54164	-34.8	7.2
52003.54593	-38.3	7.6
52039.51906	-25.5	7.0
52039.52336	-22.6	6.8
52040.41114	-60.6	7.5
52040.41545	-59.1	7.4
52041.51271	-27.2	7.6
52041.51701	-34.7	7.7
52042.45185	-46.0	7.3
52042.45616	-43.2	6.4
52043.51255	-77.1	9.3
52043.52116	-65.4	7.6
52060.46702	-41.5	9.8
52060.47859	51.9	123.3
52060.47259	-41.4	29.4
52066.50865	-114.5	94.0
52066.51415	-56.2	83.1
52090.39578	-31.1	7.6
52090.40014	-36.1	10.1
52092.45352	-45.0	11.9
52092.45786	-45.3	11.6
52100.39319	-23.6	13.8
52100.40115	-24.4	10.4
52308.63092	-14.9	8.2
52308.63543	-9.6	9.4
52366.60324	-17.2	6.9
52366.61081	-11.0	6.8
52410.44714	-21.8	9.3
52410.45149	-15.7	9.4
52451.38005	1.9	8.0
52712.57610	8.0	12.7
52746.47499	-15.3	9.4
52753.44335	-4.3	8.4
52831.41896	28.6	9.8
52831.42389	22.6	8.4
52783.37057	3.7	12.4
53080.59896	17.4	8.2
53081.48678	23.8	9.1
53220.42784	52.7	11.2
53419.68948	63.1	8.8
53422.59007	44.0	11.3
53425.66575	48.6	8.7
53430.69819	67.5	17.4
53431.57521	59.2	8.0
53432.52693	46.9	8.7
53454.48157	36.9	11.4
53456.51748	77.6	9.2
53488.47360	23.9	9.4
53489.47745	34.6	8.8
53492.46005	16.0	11.7
Xi Boo b		
52308.64218	-14.1	11.1
52308.65051	-64.1	12.1
52410.45703	57.0	7.6
52410.46164	39.7	8.6
52451.38481	3.9	8.5
52746.47984	55.4	7.8
52753.44987	59.6	6.4
52783.37675	30.4	12.3
53080.60761	-61.8	9.9
53081.49131	14.2	8.0
53220.43234	-114.9	11.7
53454.48862	27.8	12.0
53456.52367	11.8	8.5
53488.47800	-9.3	9.5
53489.48296	-13.9	6.9
53492.46982	-20.3	8.3
HD133826		
51951.70008	-5.7	22.1
51951.70651	0.4	25.1
52002.56613	7.4	13.9
52002.57446	8.0	10.9
52002.56613	7.5	13.9
52002.57446	8.0	10.9
52040.46674	-4.4	9.9
52040.47458	-4.3	8.9
52041.55687	5.6	12.3
52041.56468	22.9	13.5
52042.51055	10.3	10.4
52042.51838	21.9	8.9
52043.54667	13.3	12.3
52043.55448	3.3	11.3
52066.48396	10.5	11.6
52066.49543	7.7	13.0
52129.40296	-0.1	12.0
52132.43826	23.8	11.2
52132.44962	14.2	12.9
52209.27794	-8.1	13.5
52209.28927	11.6	16.0
52365.55821	19.3	10.8
52365.56957	12.9	12.3
52442.39254	2.3	7.8
52442.40389	17.2	9.3
52450.42191	-0.9	15.4
52450.43355	2.5	13.1
52451.39107	8.7	9.7
52484.40935	21.0	8.3
52506.35272	11.4	11.5
52657.62861	-26.4	11.7
52745.61100	2.4	9.9
52750.58101	6.1	8.7
52804.44326	-11.2	12.8
52831.43608	-4.5	11.2
52861.32980	-0.6	8.2
52863.39034	13.6	9.4
52783.58272	-33.5	13.0
52877.35636	-1.1	9.0
52929.28109	-28.3	13.2
53081.54836	-2.5	9.5
53220.44607	7.4	7.6
53251.32026	-13.6	9.6
53454.60583	-11.0	12.1
53456.56281	4.2	9.3
53861.51603	-32.4	13.3
53862.46194	-101.8	14.6
GJ577		
52753.53584	8.7	20.6
52754.41912	-92.3	28.1
52802.44824	-157.8	19.3
52831.45000	13.8	17.4
52859.36321	6.4	21.0
52861.35249	-67.6	17.2
52863.40684	69.6	19.6
52781.48109	-45.1	32.4
52783.44189	49.5	28.5
52877.38775	-66.1	17.8
52929.26527	48.5	21.3
52953.23508	-80.5	23.9
52956.23086	157.0	29.9
53081.58353	-52.0	14.8
53082.63765	-44.8	19.9
53220.46029	-94.1	15.6
53251.36510	5.2	22.3
53454.62099	30.5	35.4
53456.53307	88.3	27.4
53488.48481	-133.0	20.1
53489.49171	24.4	20.2
53516.46885	658.6	25.7
53537.50287	-131.8	20.3
53538.52319	-11.9	29.8
53541.46170	-145.4	15.8
53861.52962	-36.7	23.3
HD135599		
52746.49558	-5.4	6.8
52750.59777	6.5	8.4
52753.52791	-2.3	7.9
52807.45351	8.4	10.2
52861.34187	2.2	10.5
53081.60196	-25.3	6.3
53224.34570	-7.7	6.4
53456.54939	15.8	9.3
53488.53313	-1.9	6.4
53515.46735	3.7	8.4
53861.54640	22.4	14.7
53863.47588	-16.0	12.1
HIP82959		
52363.66560	4223.9	8.9
52443.45159	3229.0	9.4
52443.46655	3231.5	10.7
52451.44051	3169.5	9.4
52484.46915	2584.6	12.4
52506.41052	2259.5	13.0
52547.33972	1464.1	10.3
52746.54223	-3435.2	9.7
52750.60747	-3465.5	7.9
52753.59530	-3539.5	7.8
52831.49645	-4459.2	10.0
52857.35625	-4153.5	9.2
52861.38590	-4091.3	10.1
52783.55376	-4089.6	9.8
52877.40572	-3555.9	8.2
52929.29471	-1318.0	35.8
52953.26697	-23.6	13.9
53081.65022	5164.2	8.4
53220.47862	6966.0	10.6
HD171488		
52096.47964	-116.2	103.0
52096.49098	-68.7	88.8
52102.48416	653.7	116.0
52102.54300	820.3	191.1
52102.55785	911.4	120.9
52129.45125	-192.3	81.7
52132.48210	-10.0	134.8
52132.49345	56.1	134.1
52209.30506	-317.6	128.7
52209.31995	-134.8	144.2
52444.48938	-393.7	94.7
52444.50435	-467.1	75.8
52451.45854	-95.4	79.6
52476.51976	-34.9	80.9
52477.37383	250.1	96.6
52483.37965	-108.9	64.0
52484.39155	-84.8	71.0
52506.37544	-340.6	101.3
52509.52035	-136.3	240.8
52511.44435	-60.8	127.7
52513.35196	-230.2	124.3
52516.33641	-317.0	149.1
52547.32183	245.3	72.0
52597.21992	-86.6	88.7
52746.55723	47.1	82.6
52747.54087	256.6	91.9
52750.55996	-127.3	91.3
52752.51017	184.5	94.4
52753.47590	-441.0	142.4
52753.60956	-241.6	99.9
52754.60688	-322.0	114.9
52802.50366	557.0	83.6
52830.43552	429.8	282.4
52830.52904	252.1	135.2
52833.38456	-299.2	79.9
52834.38682	467.1	77.4
52835.50112	5.8	75.6
52840.44985	324.4	86.2
52857.34374	-288.3	78.0
52858.40706	576.3	67.3
52859.42361	-198.1	71.0
52860.40075	-228.1	55.1
52861.43613	-671.1	74.1
52863.42891	-106.9	82.5
52783.46273	270.3	98.5
52872.41549	-302.9	104.2
52874.35881	181.3	82.9
52875.40683	-162.4	108.0

continued on next page

continued from previous page

HJD*	RV	σ_{RV}
52877.42454	-449.4	86.7
52953.24976	521.0	119.5
52955.29385	-229.8	139.0
52956.24507	-193.4	106.1
53220.49676	239.2	66.8
53251.41310	474.4	69.0
53253.31071	-499.2	95.1
53456.61062	-44.5	130.9
53488.57955	-40.2	76.4
53489.54709	88.3	122.7
53516.50078	-12.4	76.9
53517.54905	342.3	97.0
53861.58401	-432.0	116.6
53862.53777	577.8	107.9
53863.49220	351.9	129.7
HD171746		
52483.49132	18.3	13.3
52506.45189	11.1	12.9
52597.25665	-186.1	15.9
52746.62082	80.1	11.2
52752.62109	-24.8	15.0
52804.48074	64.6	19.5
52831.50987	85.6	11.5
52857.33374	58.1	12.9
52859.44963	23.0	14.7
52860.42566	49.0	11.0
52874.37147	10.0	11.3
52952.23241	-92.5	11.9
52953.27844	-62.8	19.3
52983.22253	-38.2	18.1
53076.68884	-111.5	14.9
53081.67158	-47.9	12.0
53092.61687	-60.8	17.8
53122.52820	-85.7	18.8
53122.53565	-114.1	22.6
53220.52421	18.1	14.9
53222.43356	72.8	12.2
53223.39184	37.5	11.5
53225.39119	48.1	10.4
53247.33139	76.2	9.2
53250.39242	62.2	11.1
53251.43822	27.7	12.3
53252.41201	164.1	13.5
53253.32067	71.4	11.8
53454.65709	-83.9	26.6
53456.58343	-17.2	15.8
53488.60976	-4.4	10.2
53489.55898	-99.7	17.4
53492.61654	-26.3	11.7
HD180617		
52752.54107	25.3	30.5
52784.50226	3.1	23.1
52804.49116	-6.6	26.4
52831.52122	-10.9	19.6
52857.46050	-1.6	25.5
52859.46047	29.4	19.6
52860.46937	30.0	20.5
52783.50320	-31.5	27.0
52874.38281	-3.9	20.6
52877.44150	-20.6	20.7
52925.29073	-0.1	19.6
52952.25589	-24.6	41.0
53220.53576	-6.0	20.6
53224.44416	-10.3	18.8
53250.41434	6.8	23.3
53253.34809	15.0	18.7
53862.58167	-30.7	29.5
53863.56908	17.3	28.4
SAO70137		
52096.50668	-1404.8	66.8
52096.52209	-1400.0	58.8
52127.47910	-1262.9	66.6
52127.49401	-1241.3	61.0
52129.47888	-1207.9	72.7
52129.49377	-1216.8	71.5
52209.35285	-1073.4	59.1
52209.36893	-1037.8	54.4
52217.29889	-1062.8	54.3
52217.31375	-1075.0	52.4
52451.51201	-273.4	55.6
52483.50287	-247.3	53.7
52506.46490	-340.7	65.7
52547.37567	-54.4	60.0
52572.31544	34.3	51.0
52839.47635	1102.9	58.8
52858.38463	929.1	58.8
52859.35038	885.2	78.5
52860.52110	917.1	64.7
52862.45313	924.4	75.7
52931.32039	1353.9	62.7
52947.31504	1117.0	86.7
52952.30495	1199.8	104.5
53222.42339	1795.4	83.8
53251.51762	2109.1	62.8
53253.37674	2045.1	62.7
53280.35492	2097.1	63.6
53454.64406	2413.0	104.3
53489.60360	2404.2	88.5
53516.57953	2576.3	80.6
53517.56230	2448.5	72.2
53537.55022	2419.6	75.0
GJ824		
52210.38098	15.7	12.6
52210.39592	-36.0	25.0
52213.35722	25.7	15.6
52213.37214	-7.5	14.2
52451.53134	19.6	11.2
52483.52023	-10.2	10.9
52506.49158	2.3	9.4
52547.39316	-2.3	11.0
52572.33971	4.6	11.4
52596.33630	15.3	11.4
52860.45404	14.3	9.2
52861.48013	7.6	13.4
53220.55246	-9.2	9.7
53222.44534	3.2	9.9
53224.46087	-17.8	9.1
53225.45444	-14.7	9.6
53247.42213	4.2	12.3
53248.51979	-3.6	10.0
53250.43205	6.5	9.3
53251.45124	-27.6	8.1
53252.42516	-13.9	8.9
53253.39369	-6.9	8.0
53279.25530	10.3	11.6
53280.34132	4.3	9.8
53281.38373	-0.2	16.9
53282.35841	15.5	32.5
HN Peg		
52039.60201	-4.7	20.1
52040.59155	20.6	20.0
52040.59584	-10.9	18.8
52041.58183	42.6	19.6
52041.58684	54.8	19.7
52042.57263	-48.0	21.4
52042.57766	-56.2	21.1
52043.57573	-6.5	22.9
52043.58214	7.5	19.1
52090.50010	-15.3	25.6
52090.51761	29.7	31.1
52090.52253	-29.2	24.6
52094.54468	-10.2	17.8
52094.54902	-0.2	16.4
52096.53558	-27.9	15.5
52096.54047	-13.0	18.0
52127.45443	-25.6	21.0
52129.50880	83.4	21.5
52129.51665	95.1	19.8
52247.20713	55.4	34.4
52247.21326	56.7	33.4
52132.50650	18.3	17.6
52132.50765	52.9	20.9
52213.33613	-48.3	27.4
52213.34419	-41.9	23.8
52217.32767	-35.3	42.3
52217.33196	-16.3	75.6
52219.31973	5.1	25.5
52219.32756	-4.6	24.0
52247.20713	55.4	34.4
52247.21326	56.7	33.4
52444.51397	27.0	30.9
52444.52135	-5.2	18.9
52444.52928	0.6	21.8
52484.48425	-30.2	18.3
52506.47896	-20.6	25.9
52572.32900	-7.3	22.2
52596.32596	-21.6	24.7
52747.60992	46.9	24.1
52804.51559	81.0	25.8
52807.52448	6.8	23.8
52834.46896	-3.1	18.4
52857.48608	-53.8	22.9
52859.51791	-40.2	15.6
52860.50039	82.1	19.0
52861.49012	-7.1	18.8
52862.42552	-13.0	21.1
52874.41089	-25.7	27.7
52926.30176	4.4	34.6
52949.31796	15.3	25.3
52981.23969	-45.8	47.8
52983.25774	-9.1	36.2
53221.46753	16.1	22.0
53224.47038	-6.9	17.6
53251.53091	0.5	21.0
53252.44045	-46.7	21.2
53253.40378	-71.3	21.1
53254.40478	-31.1	29.6
53393.22192	-16.5	27.9
53454.66881	-16.4	40.1
53517.58790	-16.9	20.6
53542.56547	-32.4	23.0
53569.56901	-10.4	23.7
HD217813		
52804.51978	15.0	12.0
52807.52847	19.6	11.2
52833.52651	6.3	9.6
52857.49061	-3.4	10.2
52857.55827	-13.2	10.3
52859.52256	-8.4	7.1
52860.55548	-4.0	8.0
52861.49519	0.4	7.2
52862.43042	-5.6	7.8
52872.46003	-6.3	8.3
52874.43637	2.8	6.5
52877.49883	-14.6	8.4
52925.34055	12.3	9.9
52926.34027	-4.3	10.4
52929.41932	6.6	8.9
52931.34969	-13.6	6.8
52949.32504	-16.8	13.0
52949.39048	-7.4	12.7
52956.31308	-23.4	11.7
52983.29638	-11.3	9.8
53220.56278	-4.6	8.2
53222.52284	9.0	8.7
53224.47499	5.9	6.9
53251.54275	30.1	7.6
53252.44665	3.9	6.4
53253.40954	3.3	5.9
53254.41063	7.8	6.2
53280.49600	12.3	10.1
HIP114385		
52210.41538	-16.8	9.8
52219.34366	-26.0	10.3
52219.35849	-25.3	8.5
52484.49295	-10.9	8.8
52506.50951	-14.8	7.7
52548.36872	5.7	7.8
52596.35394	15.5	7.3
52655.22439	-1.7	18.1
52656.22959	-23.5	12.5
52657.25433	-10.0	11.5
52659.28467	-46.0	43.7
52660.27829	23.7	14.7
52661.23944	13.6	19.8
52662.24078	-21.8	10.9
52684.26556	28.8	11.8
52804.52822	-4.4	12.3
52831.53376	9.6	9.9
52834.54780	14.3	6.7
52857.49758	-29.7	8.7
52858.43480	27.9	8.0
52859.52995	24.5	7.3
52860.56247	42.5	8.5
52863.49223	-23.1	8.8
52862.43770	-8.2	8.7
52874.44408	0.6	8.7
52877.51779	10.8	9.6
52925.33006	-24.3	9.4
52926.35196	12.4	8.1
52931.36382	-45.4	8.7
52947.30187	16.5	15.6
52948.25526	-11.6	11.0
52981.34708	-1.8	13.0
52983.30813	-8.6	11.5
53022.26423	4.7	11.0
53122.55668	-3.5	17.7
53222.45568	37.4	9.1
53224.50035	26.7	8.9
53225.46473	0.7	9.7
53252.45512	-2.6	8.7
53253.41735	-5.2	8.4
53254.41791	29.0	8.5
53393.23705	10.7	12.6
53517.57369	-17.0	10.5
53569.57602	-3.1	7.3

Appendix B

Detection limits

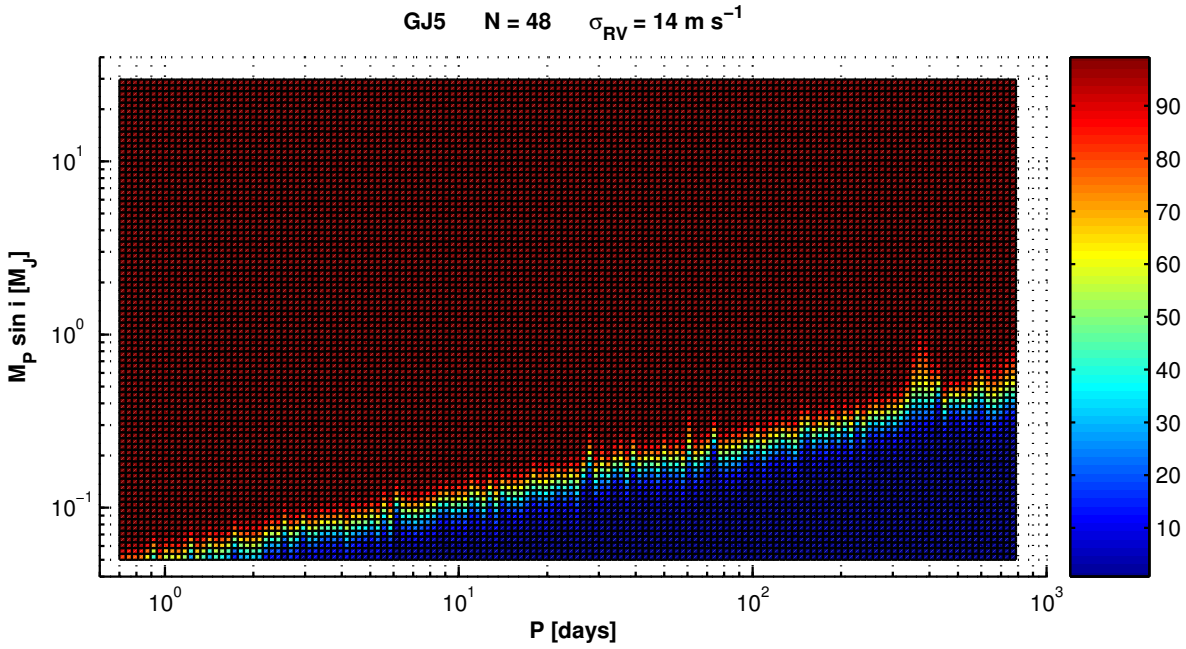

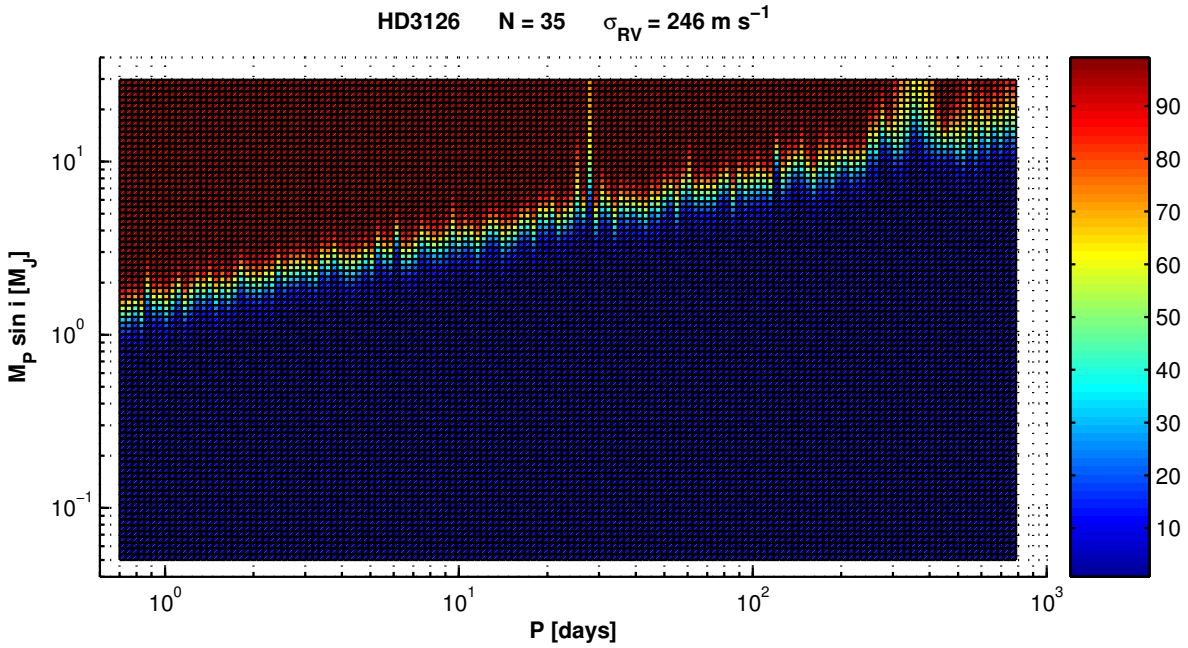
HD3126 N = 35 σRV = 246 m s−1
MP sin i [MJ]
P [days]
10
20
30
40
50
60
70
80
90

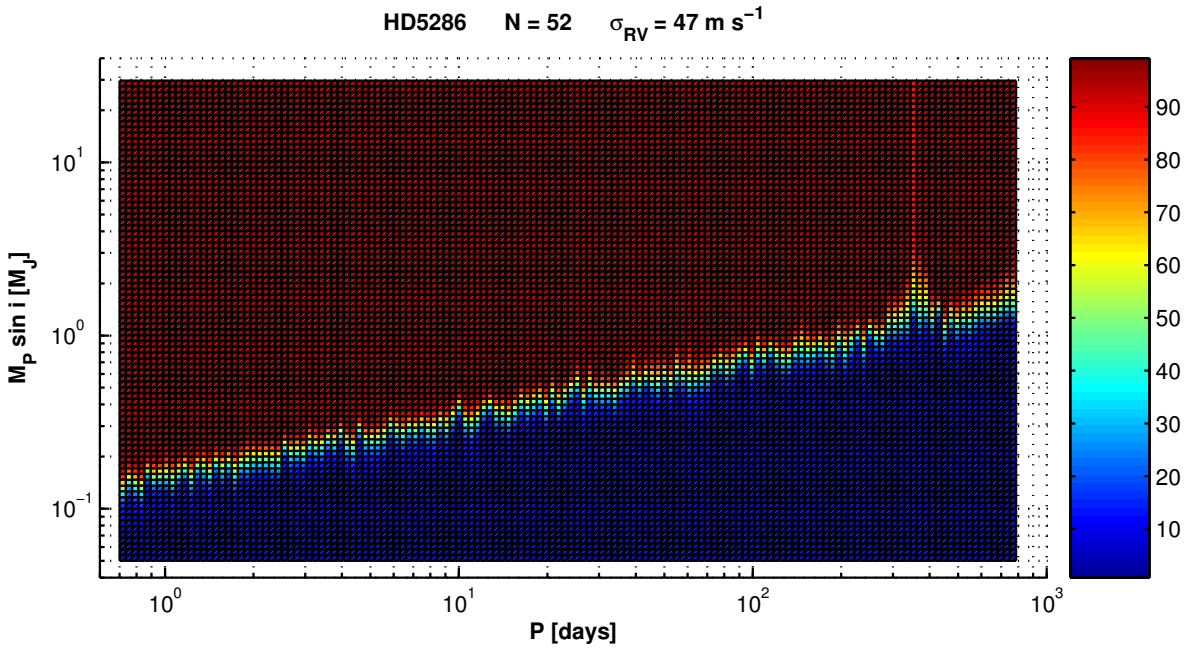
HD5286 N = 52 σRV = 47 m s−1
MP sin i [MJ]
P [days]
10
20
30
40
50
60
70
80
90

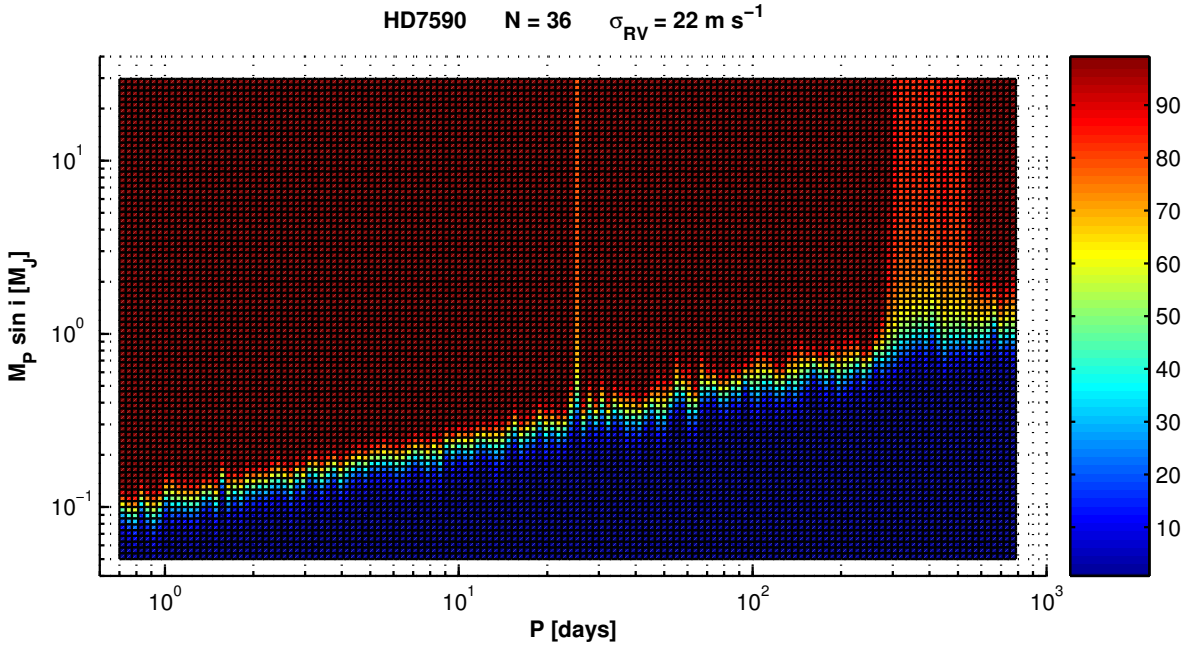
HD7590 N = 36 σRV = 22 m s−1
MP sin i [MJ]
P [days]
10^0
10^1
10^2
10^3
10^−1
10^0
10^1
90
80
70
60
50
40
30
20
10

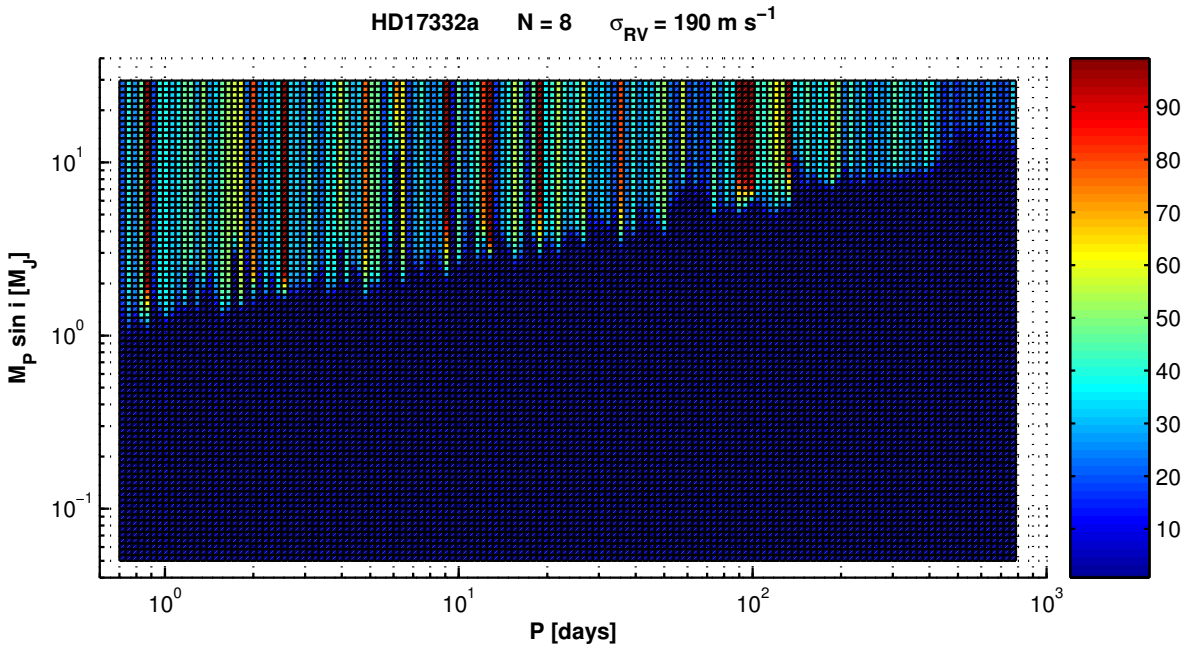
HD17332a N = 8 σRV = 190 m s−1
MP sin i [MJ]
P [days]
10^0
10^1
10^2
10^3
10^−1
10^0
10^1
90
80
70
60
50
40
30
20
10

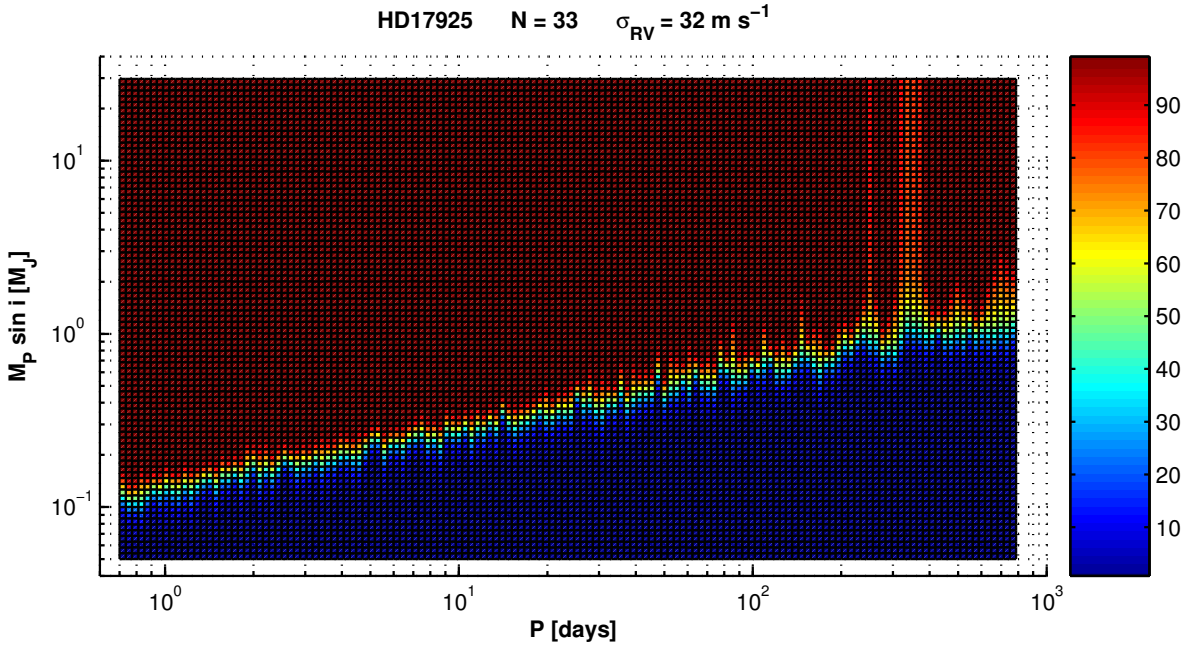
HD17925 N = 33 σRV = 32 m s−1
MP sin i [MJ]
P [days]
10
20
30
40
50
60
70
80
90

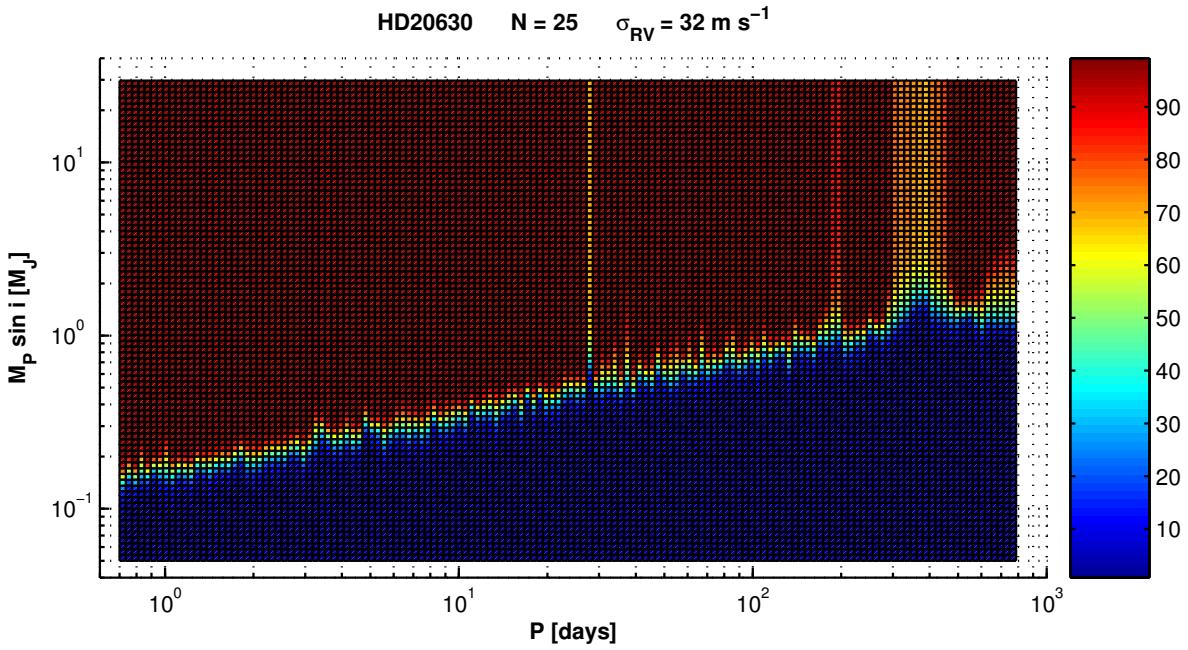
HD20630 N = 25 σRV = 32 m s−1
MP sin i [MJ]
P [days]
10
20
30
40
50
60
70
80
90

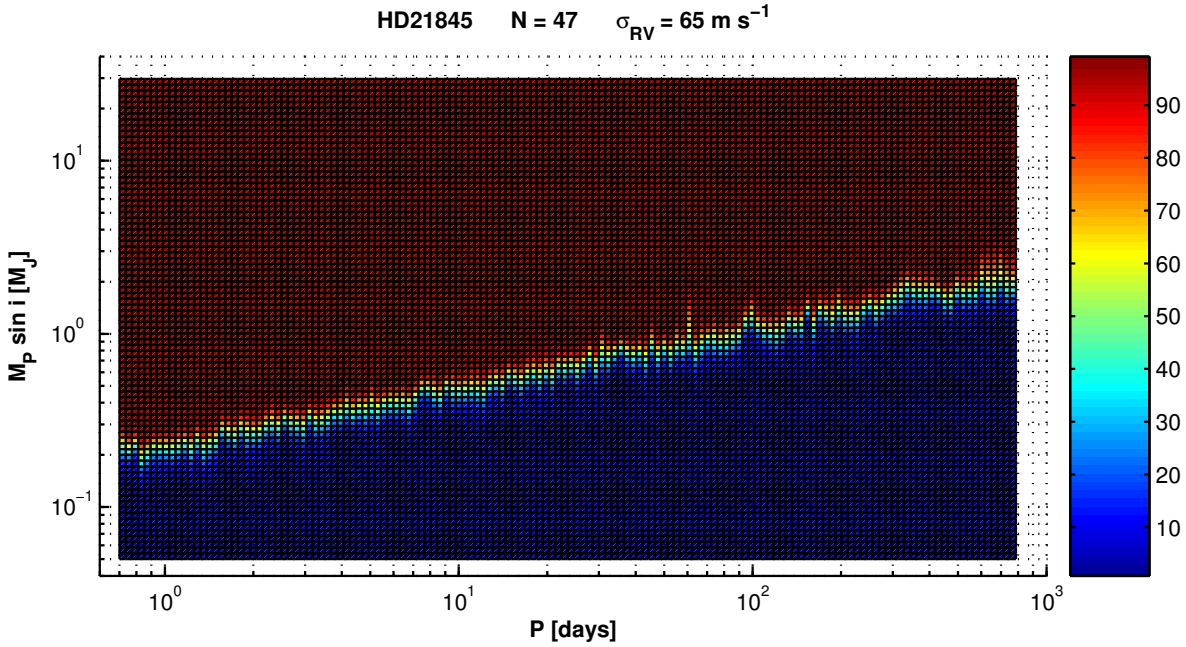
HD21845 N = 47 σRV = 65 m s−1
MP sin i [MJ]
P [days]
10^0
10^1
10^2
10^3
10^−1
10^0
10^1
90
80
70
60
50
40
30
20
10

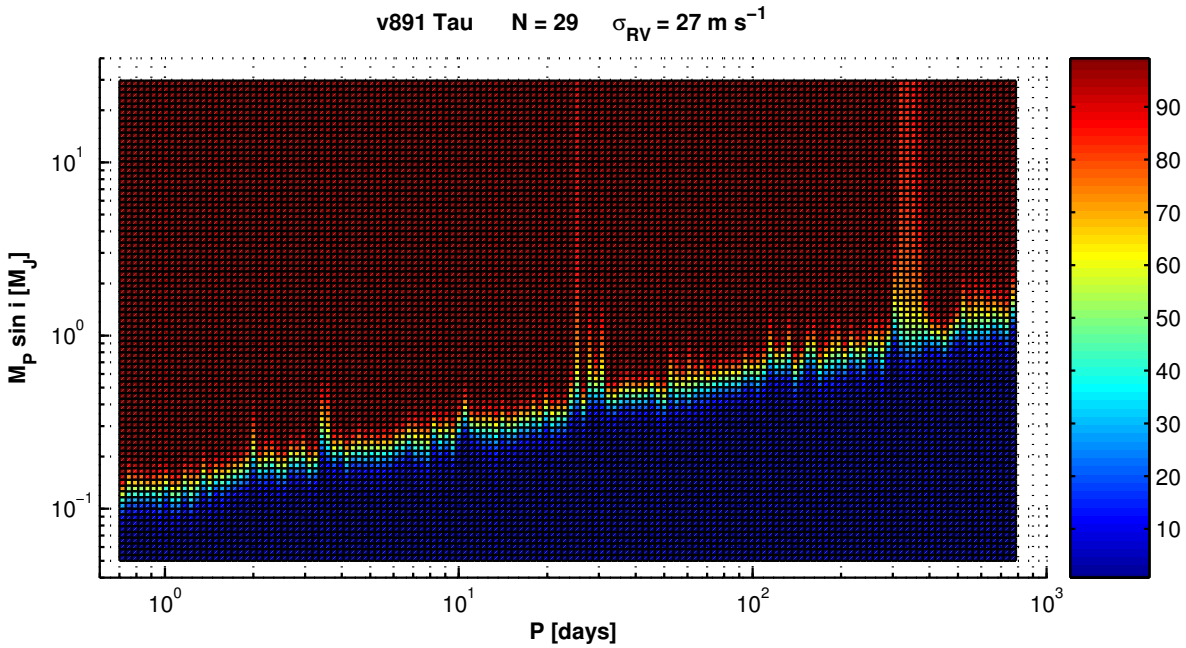
v891 Tau N = 29 σRV = 27 m s−1
MP sin i [MJ]
P [days]
10^0
10^1
10^2
10^3
10^−1
10^0
10^1
90
80
70
60
50
40
30
20
10

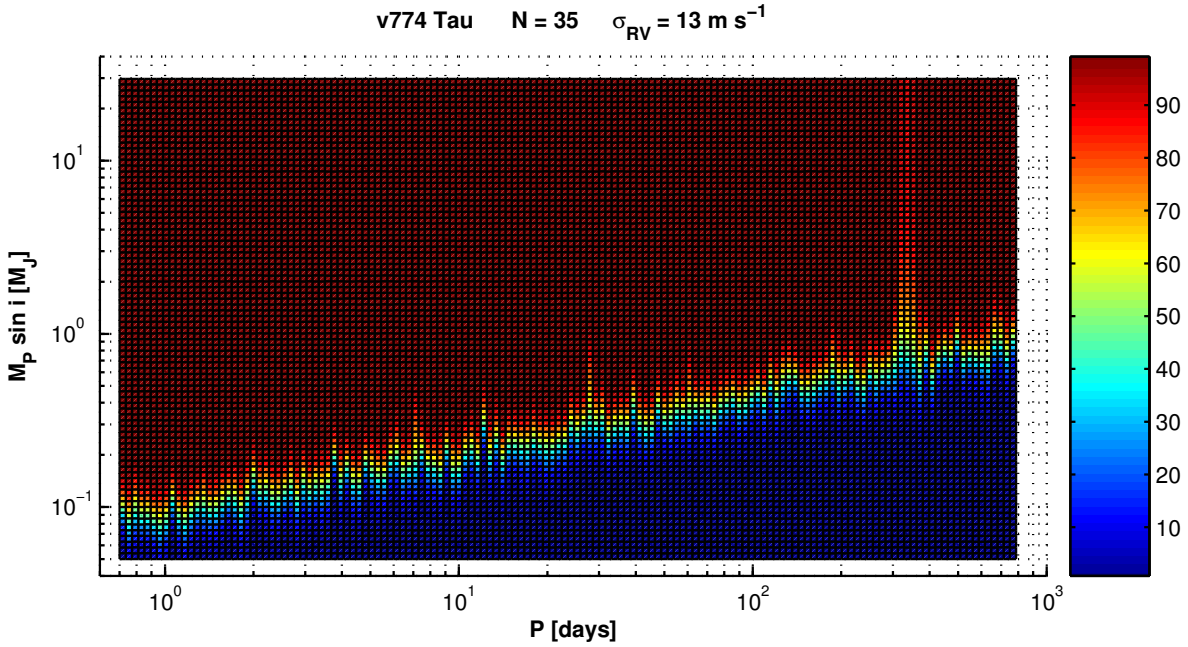
v774 Tau N = 35 σRV = 13 m s−1
MP sin i [MJ]
P [days]
10
20
30
40
50
60
70
80
90

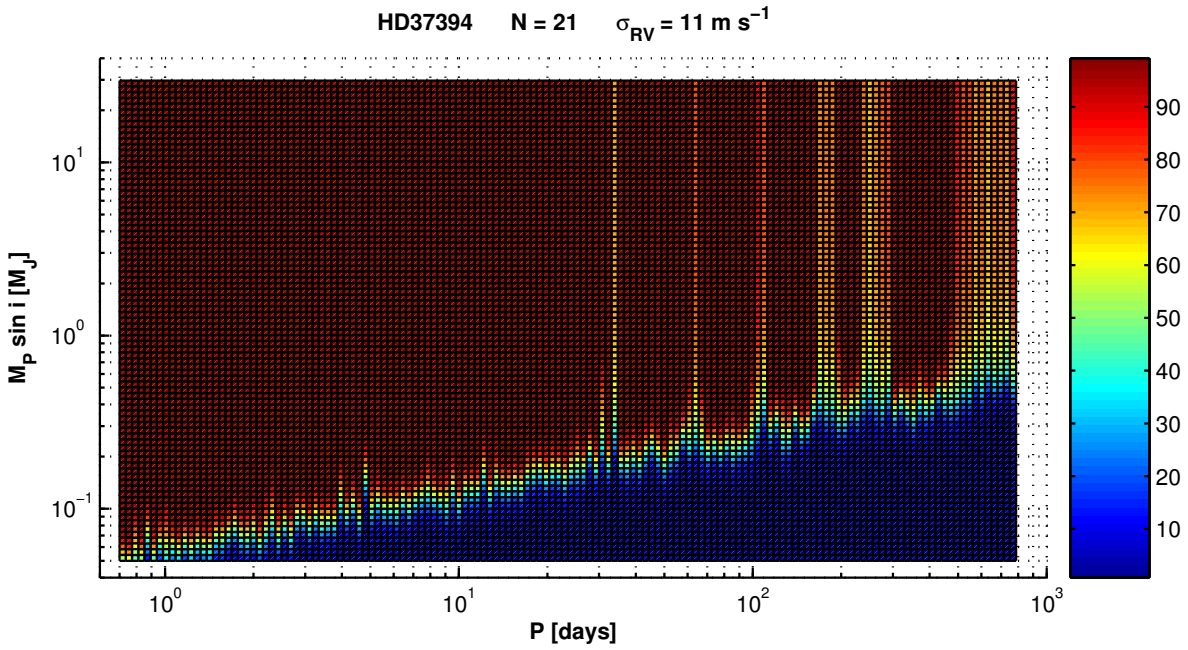
HD37394 N = 21 σRV = 11 m s−1
MP sin i [MJ]
P [days]
10
20
30
40
50
60
70
80
90

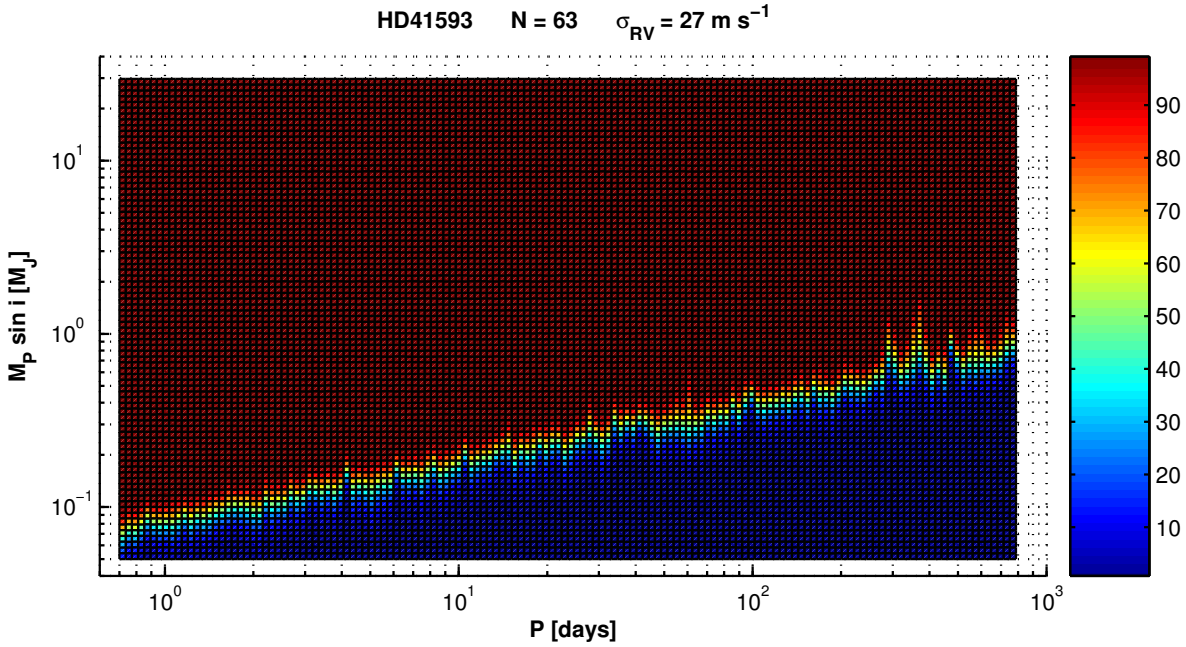
HD41593 N = 63 σRV = 27 m s−1
MP sin i [MJ]
P [days]
10^1
10^0
10^−1
10^0
10^1
10^2
10^3
90
80
70
60
50
40
30
20
10

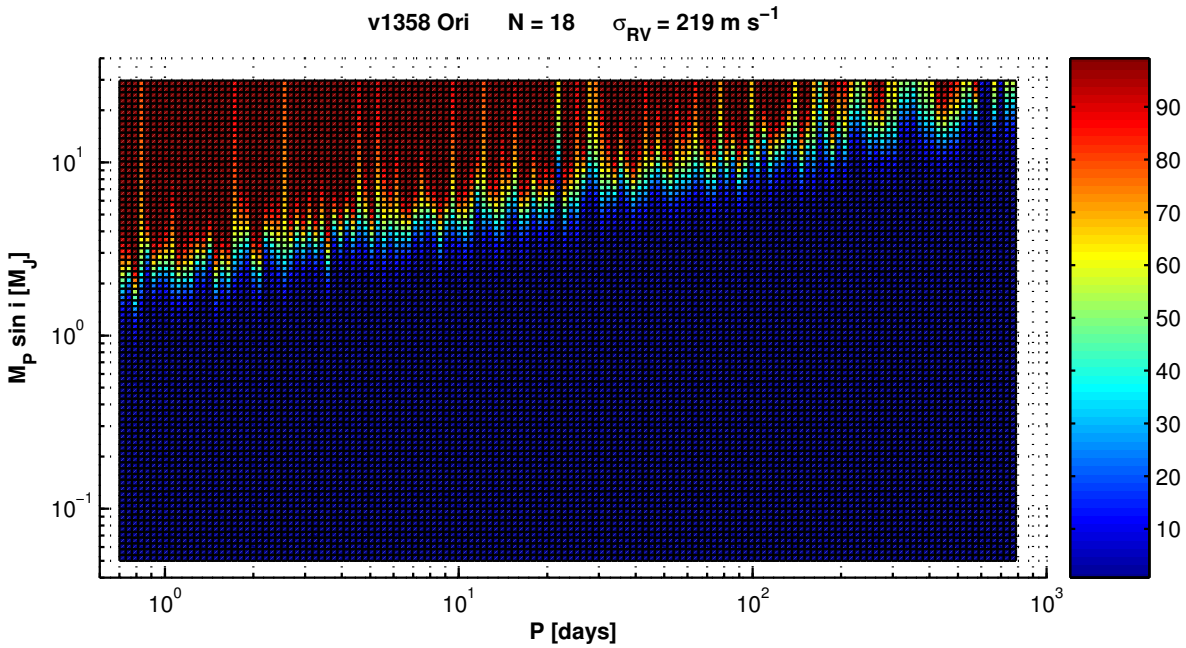
v1358 Ori N = 18 σRV = 219 m s−1
MP sin i [MJ]
P [days]
10^1
10^0
10^−1
10^0
10^1
10^2
10^3
90
80
70
60
50
40
30
20
10

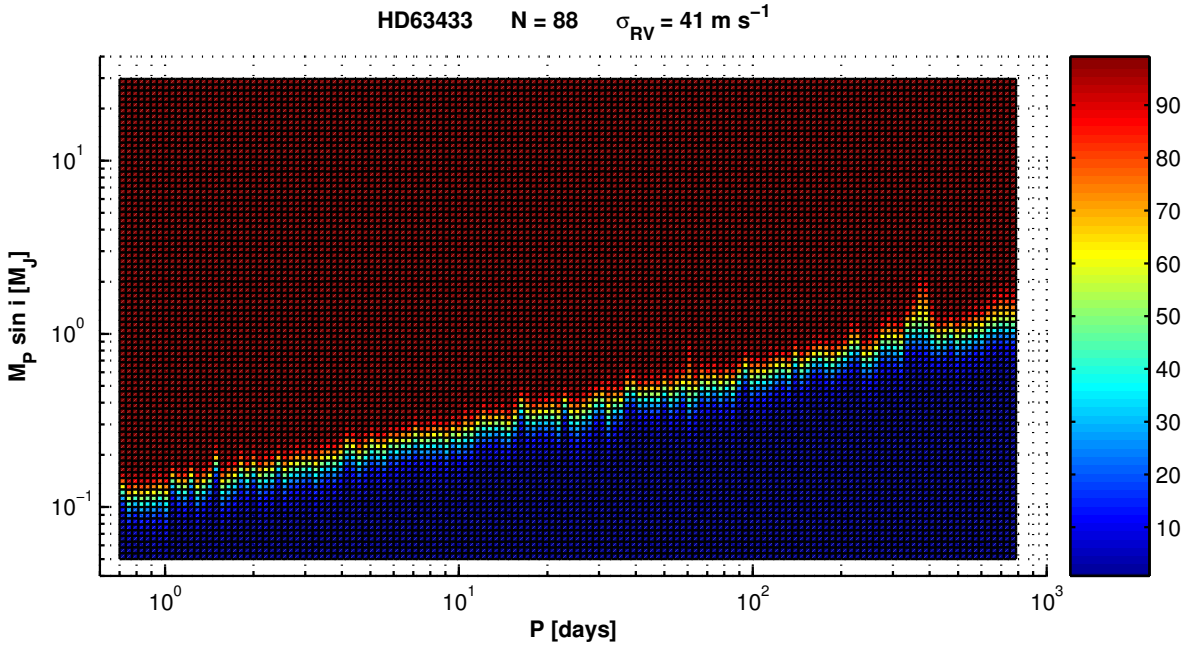
HD63433 N = 88 σRV = 41 m s−1
MP sin i [MJ]
P [days]
10
20
30
40
50
60
70
80
90

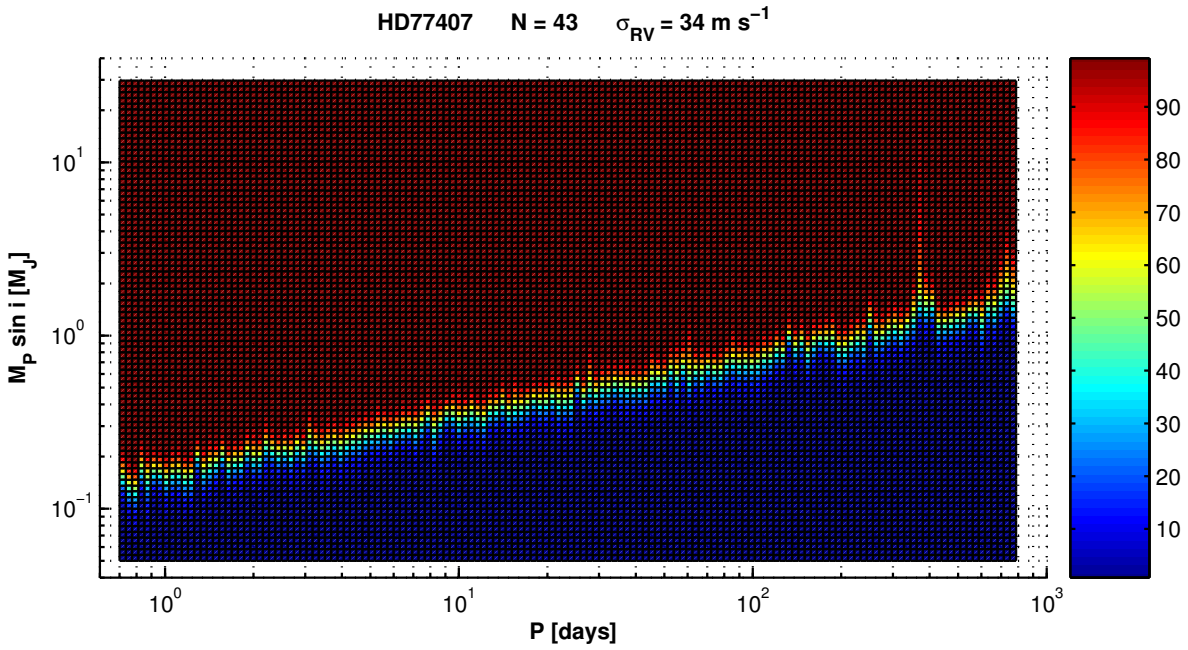
HD77407 N = 43 σRV = 34 m s−1
MP sin i [MJ]
P [days]
10
20
30
40
50
60
70
80
90

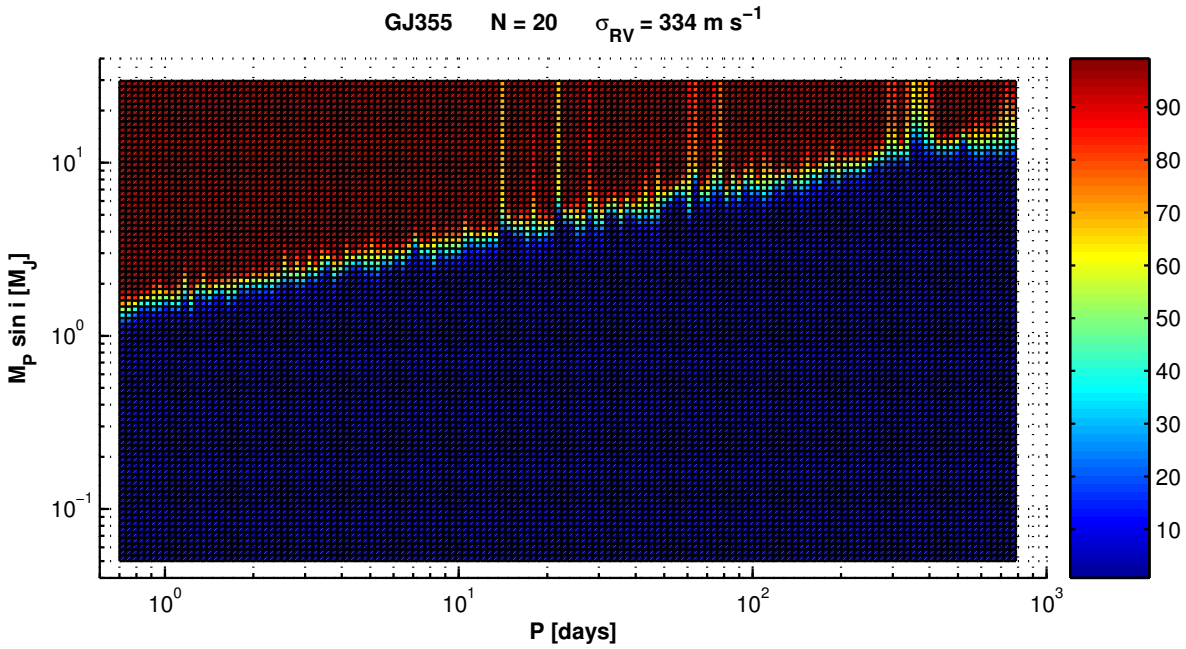
GJ355 N = 20 σRV = 334 m s−1
MP sin i [MJ]
P [days]
10
80
70
60
50
40
30
20
10

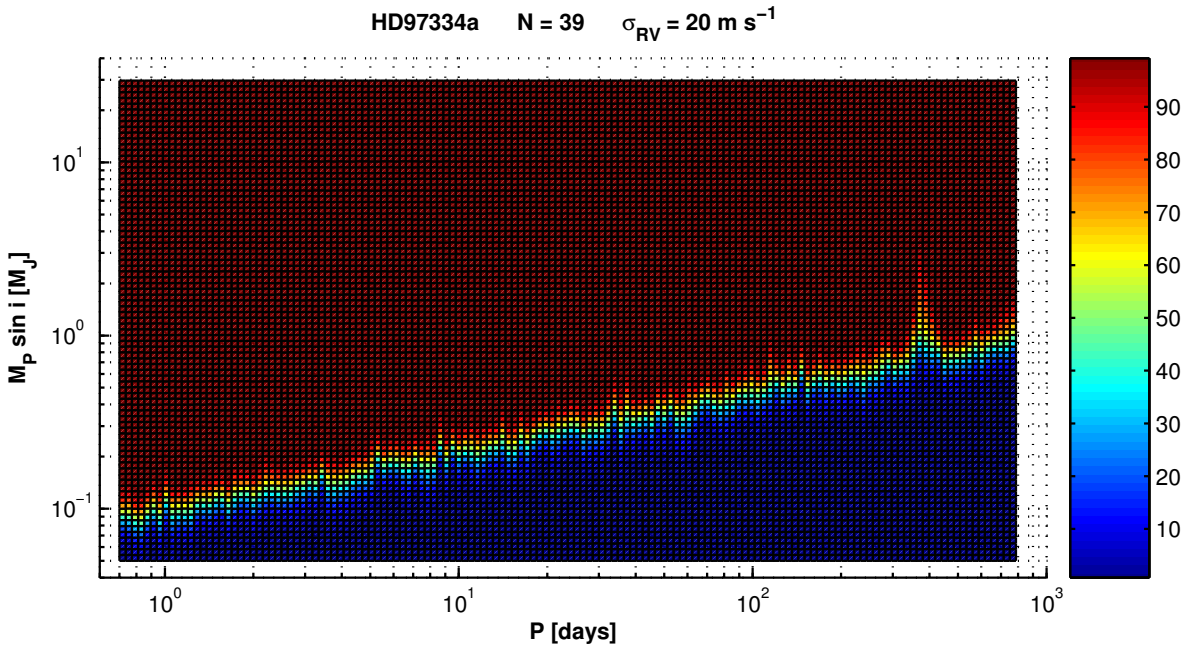
HD97334a N = 39 σRV = 20 m s−1
MP sin i [MJ]
P [days]
90
80
70
60
50
40
30
20
10

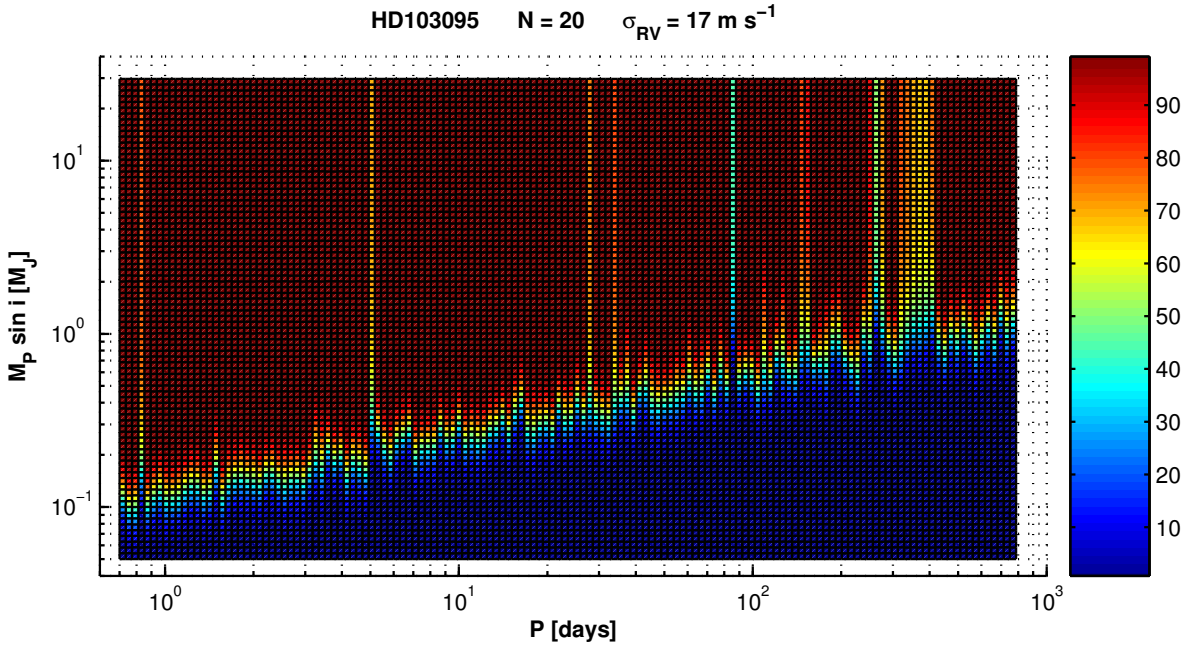
HD103095 N = 20 σRV = 17 m s−1
MP sin i [MJ]
P [days]
10
20
30
40
50
60
70
80
90

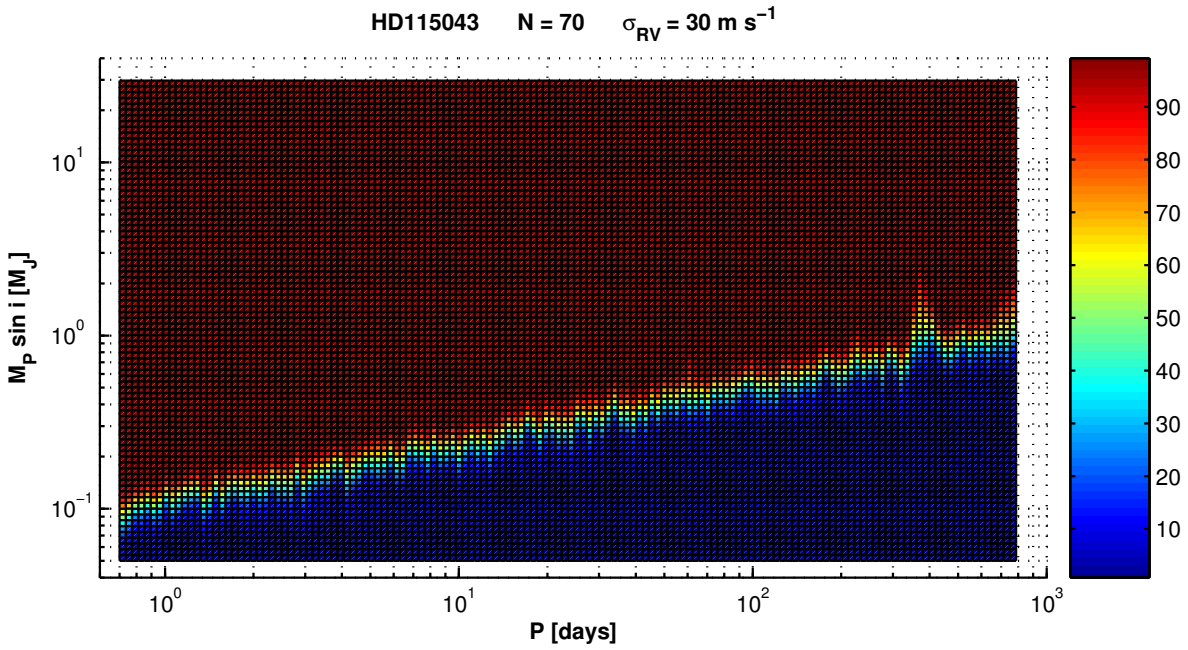
HD115043 N = 70 σRV = 30 m s−1
MP sin i [MJ]
P [days]
10
20
30
40
50
60
70
80
90

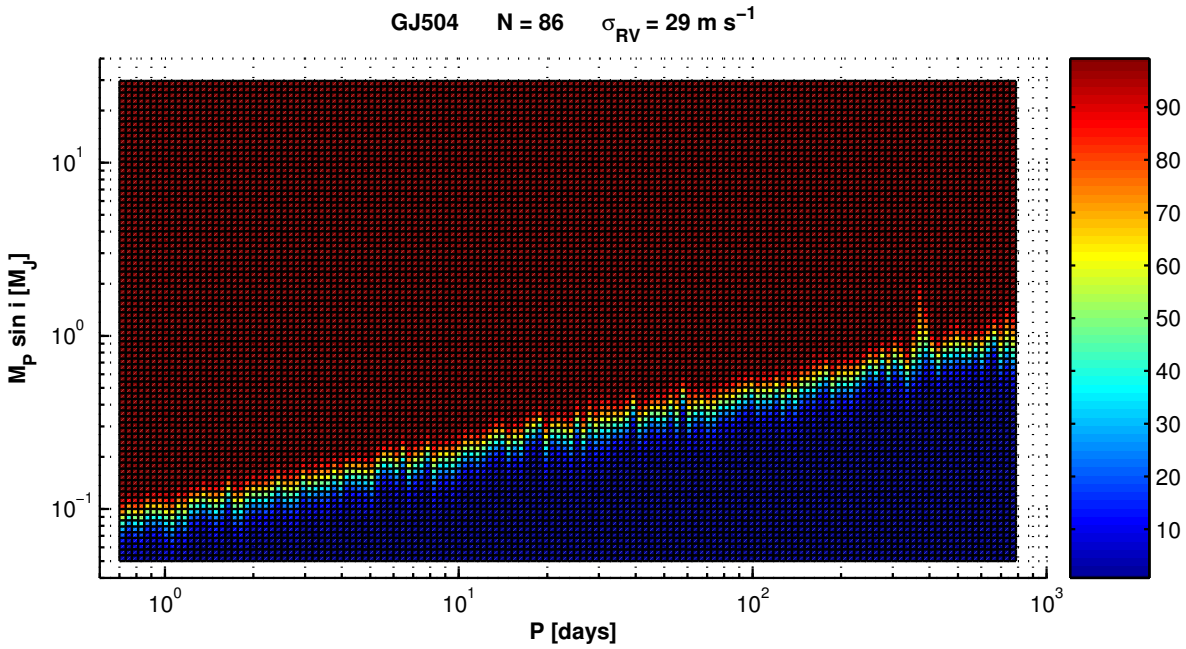
GJ504 N = 86 σRV = 29 m s−1
MP sin i [MJ]
P [days]
10^0
10^1
10^2
10^3
10^−1
10^0
10^1
90
80
70
60
50
40
30
20
10

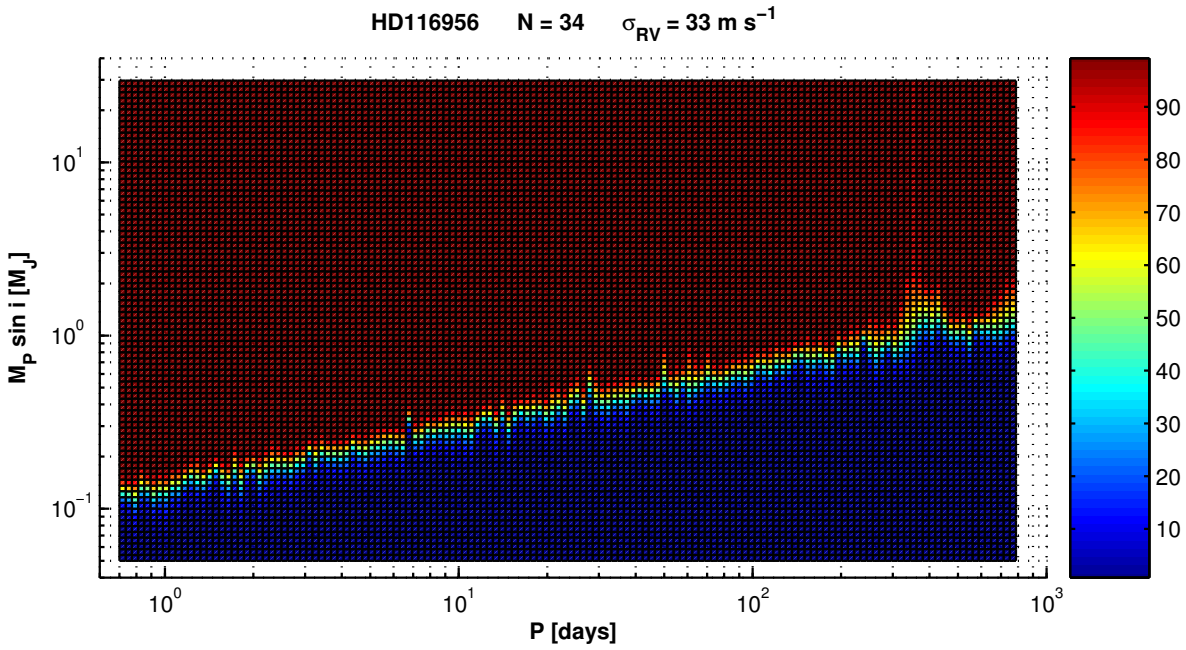
HD116956 N = 34 σRV = 33 m s−1
MP sin i [MJ]
P [days]
10^0
10^1
10^2
10^3
10^−1
10^0
10^1
90
80
70
60
50
40
30
20
10

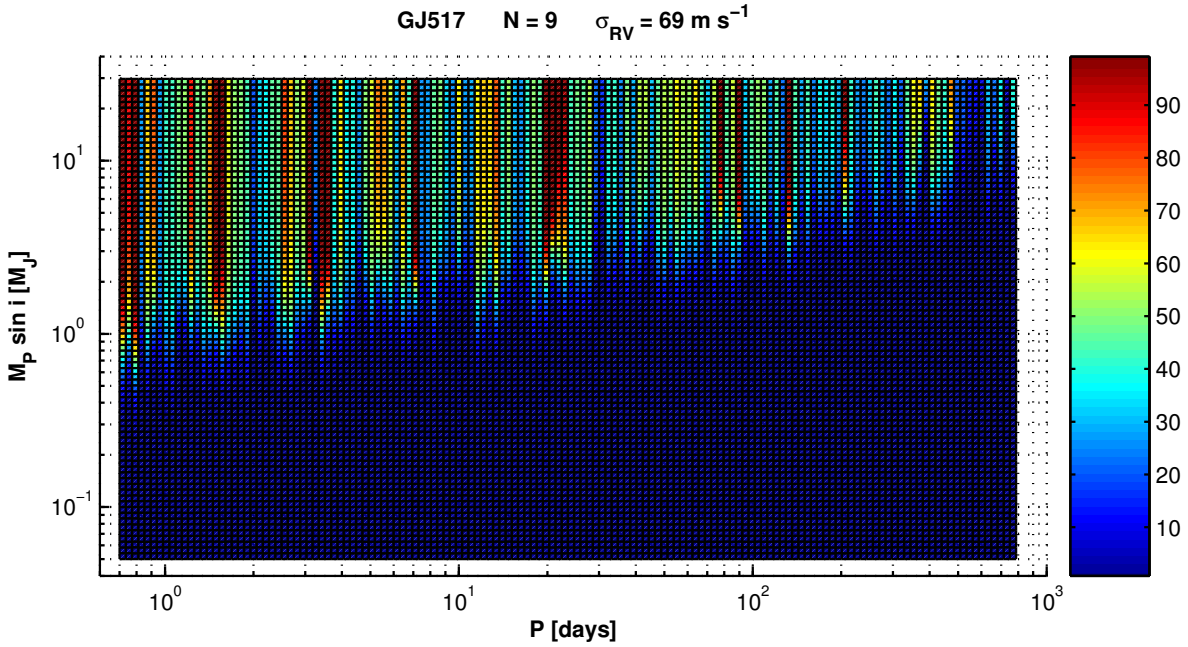
GJ517 N = 9 σRV = 69 m s−1
MP sin i [MJ]
P [days]
10
20
30
40
50
60
70
80
90

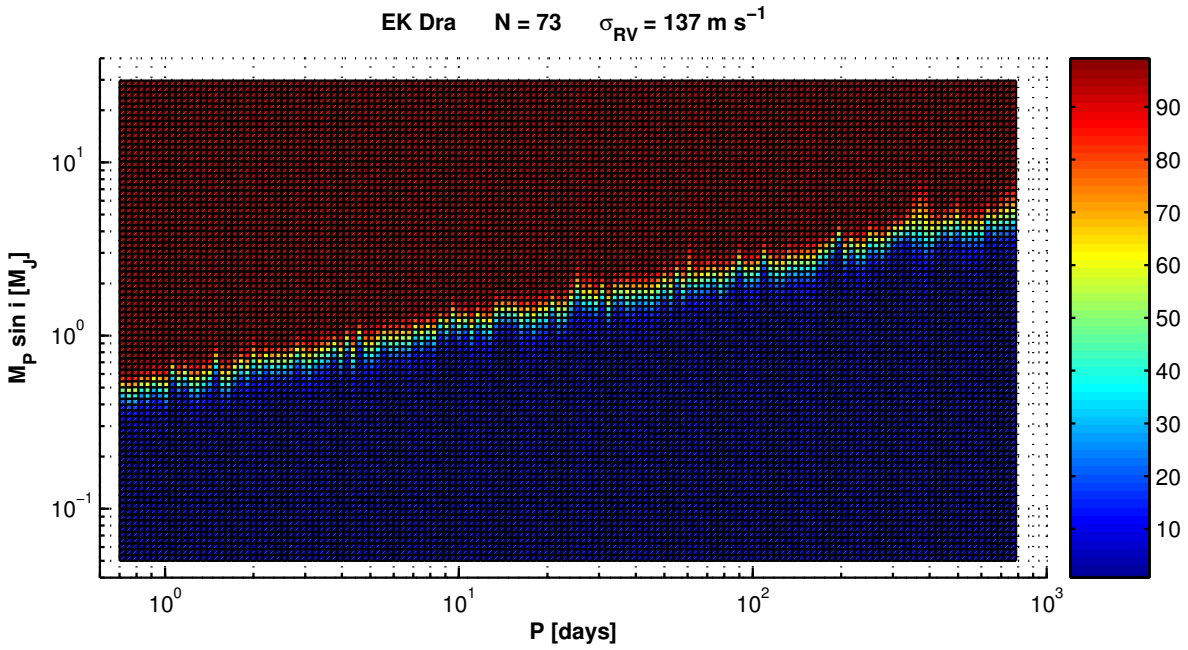
EK Dra N = 73 σRV = 137 m s−1
MP sin i [MJ]
P [days]
10
20
30
40
50
60
70
80
90

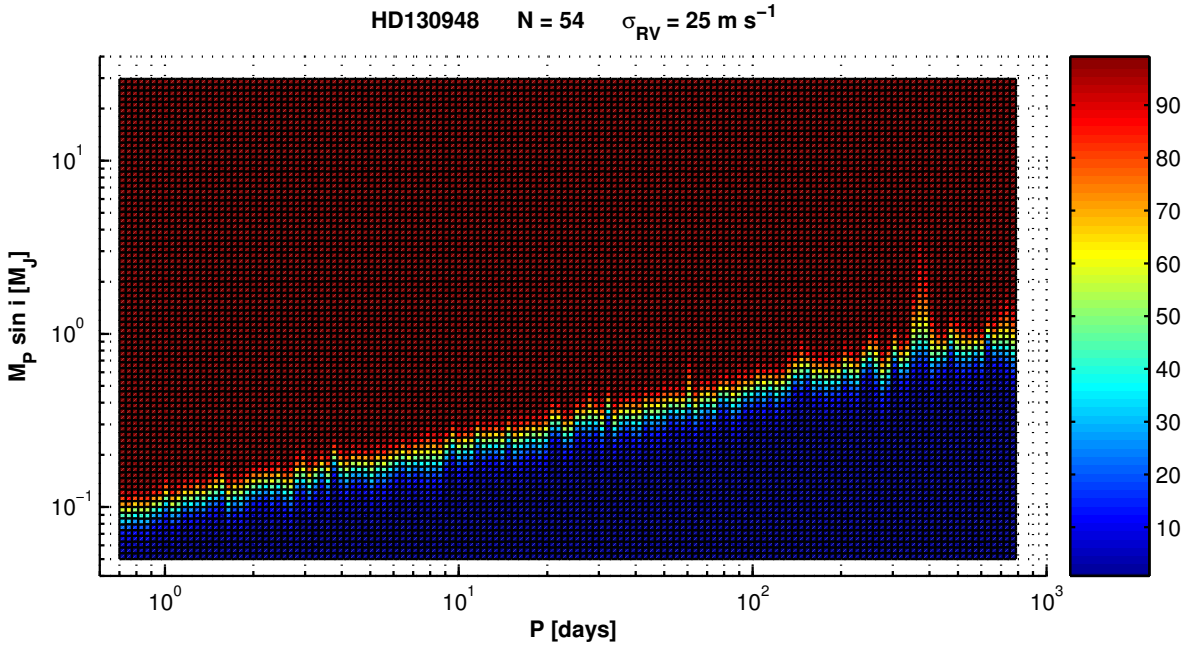
HD130948 N = 54 σRV = 25 m s−1
MP sin i [MJ]
P [days]
10^1
10^0
10^−1
10^0
10^1
10^2
10^3
90
80
70
60
50
40
30
20
10

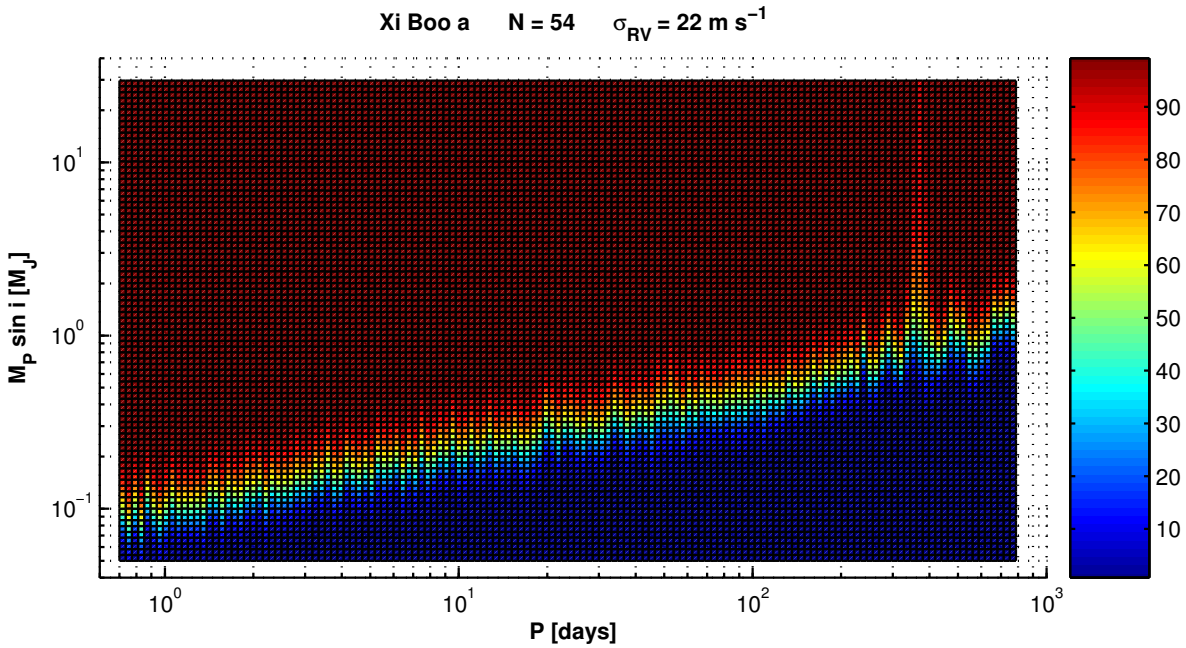
Xi Boo a N = 54 σRV = 22 m s−1
MP sin i [MJ]
P [days]
10^1
10^0
10^−1
10^0
10^1
10^2
10^3
90
80
70
60
50
40
30
20
10

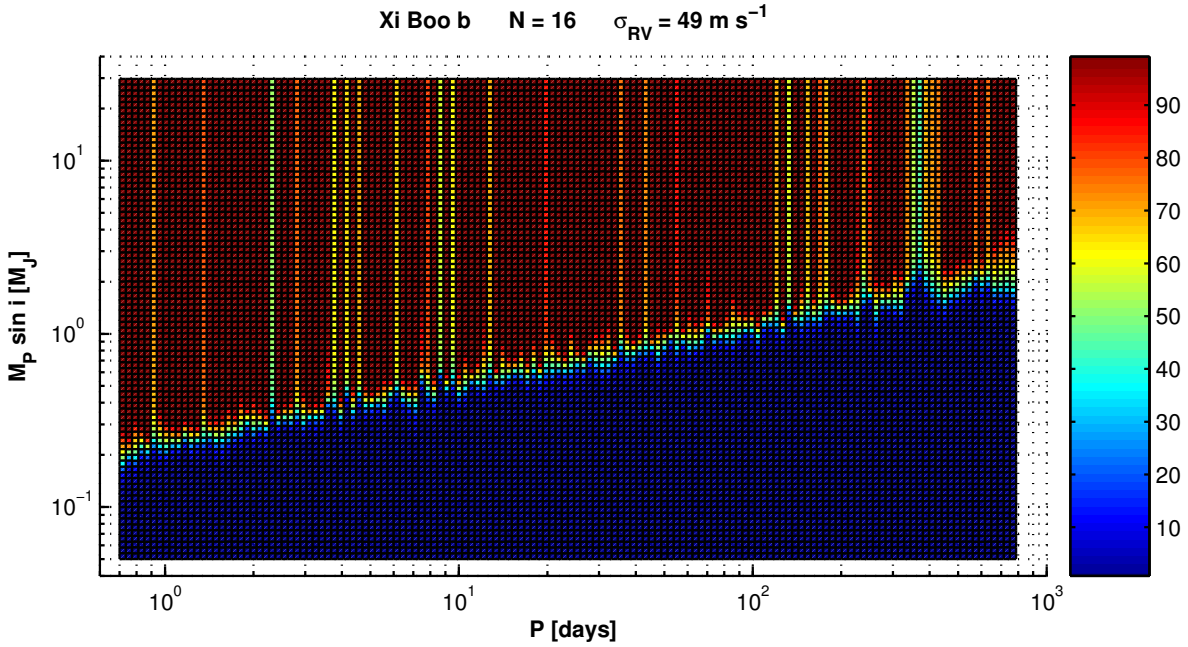
Xi Boo b N = 16 σRV = 49 m s−1
MP sin i [MJ]
P [days]
10
20
30
40
50
60
70
80
90

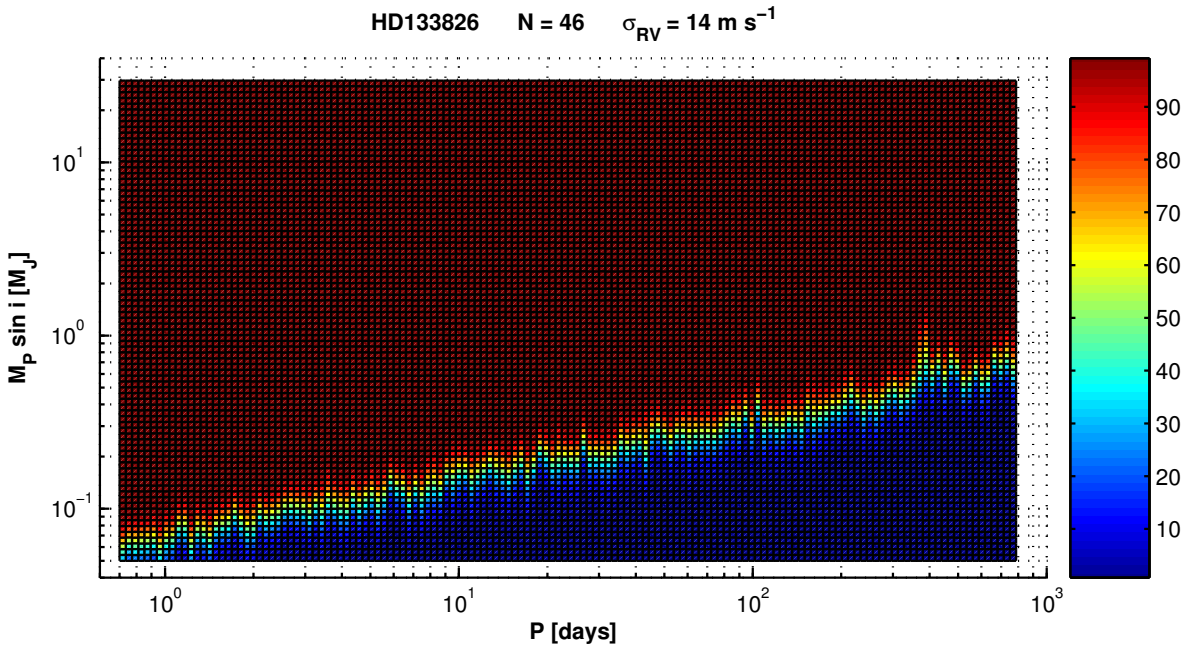
HD133826 N = 46 σRV = 14 m s−1
MP sin i [MJ]
P [days]
10
20
30
40
50
60
70
80
90

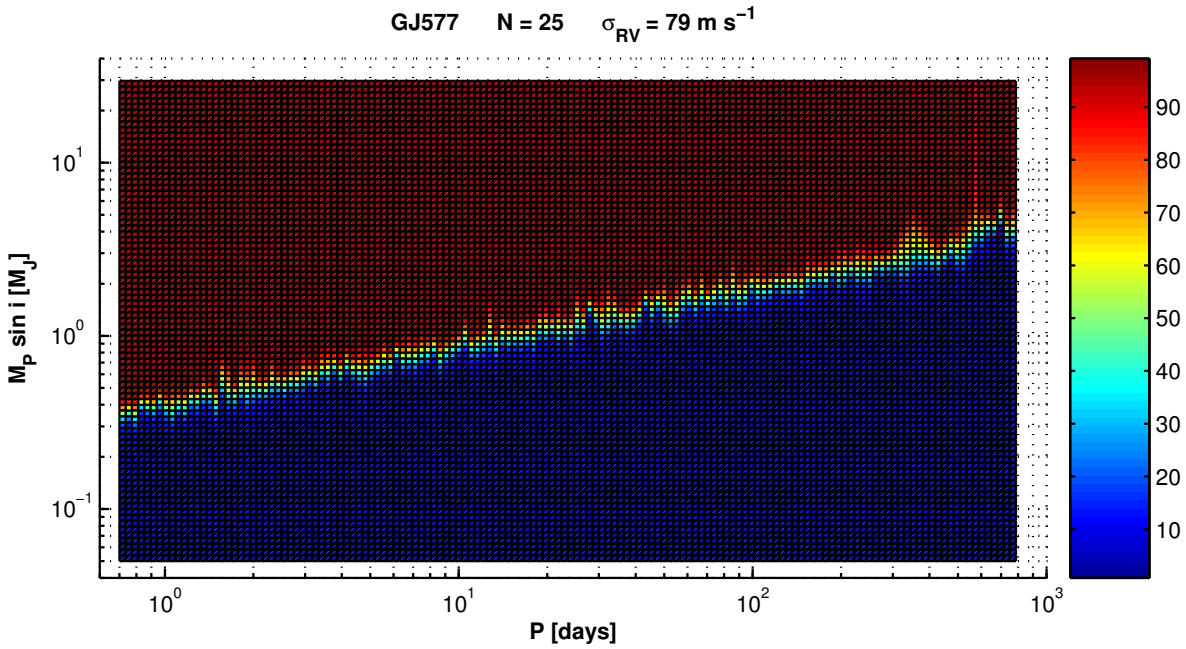
GJ577 N = 25 σRV = 79 m s−1
MP sin i [MJ]
P [days]
10^0
10^1
10^2
10^3
10^1
10^0
10^−1
90
80
70
60
50
40
30
20
10

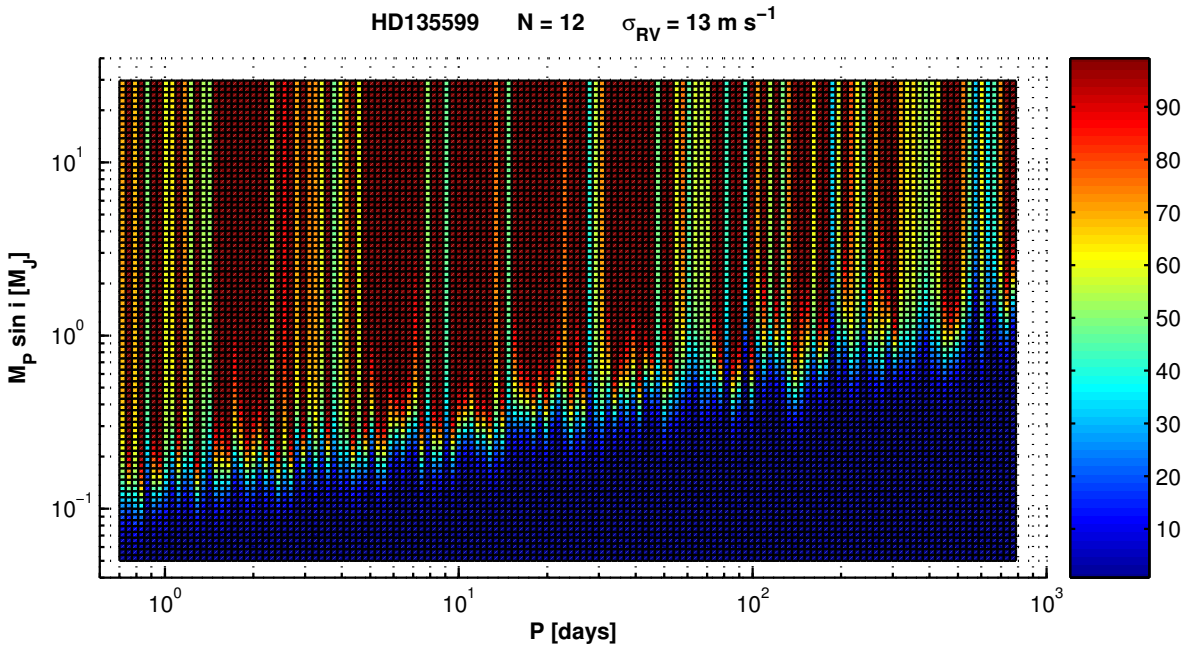
HD135599 N = 12 σRV = 13 m s−1
MP sin i [MJ]
P [days]
10^0
10^1
10^2
10^3
10^1
10^0
10^−1
90
80
70
60
50
40
30
20
10

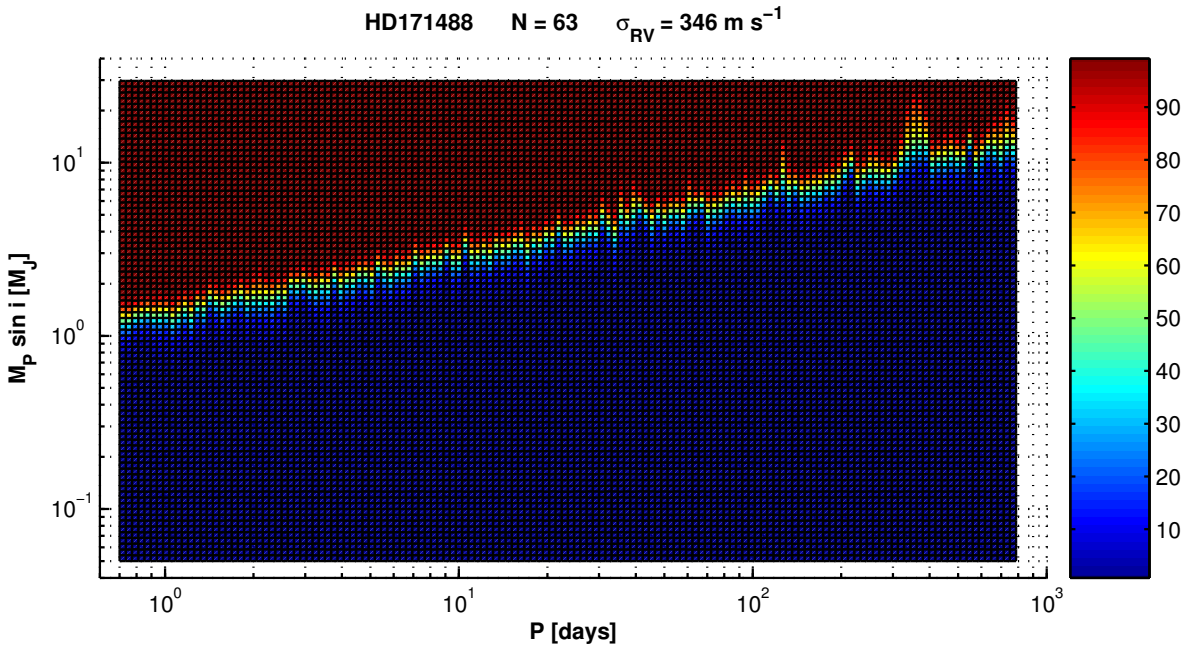
HD171488 N = 63 σRV = 346 m s−1
MP sin i [MJ]
P [days]
10
20
30
40
50
60
70
80
90

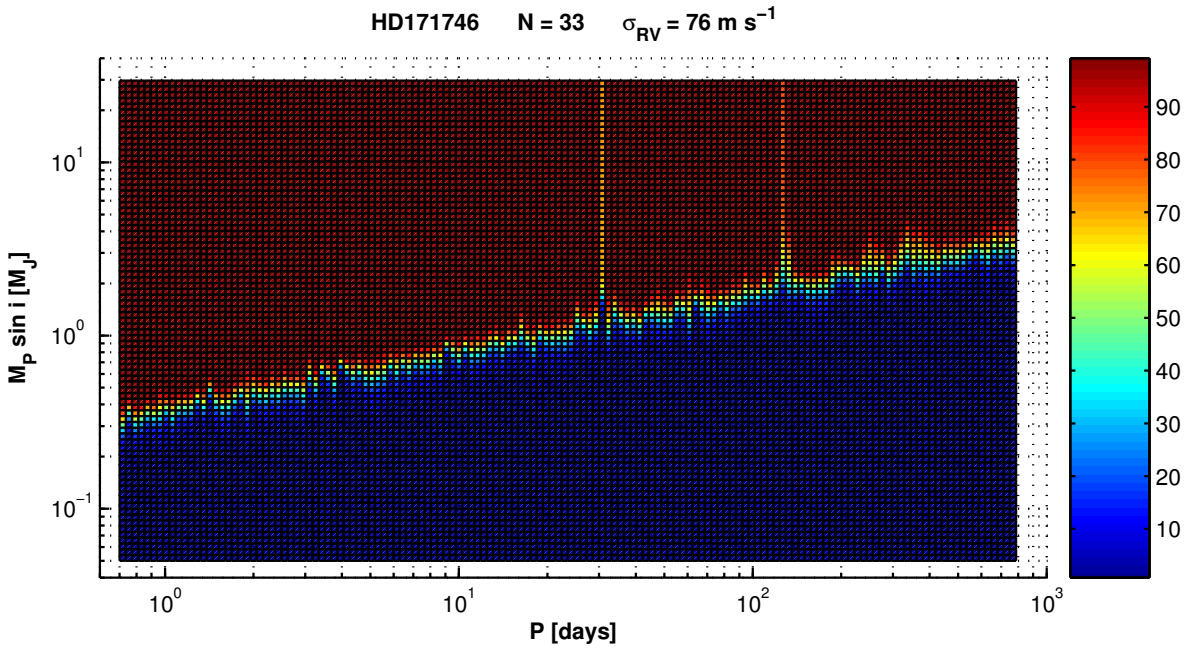
HD171746 N = 33 σRV = 76 m s−1
MP sin i [MJ]
P [days]
10
20
30
40
50
60
70
80
90

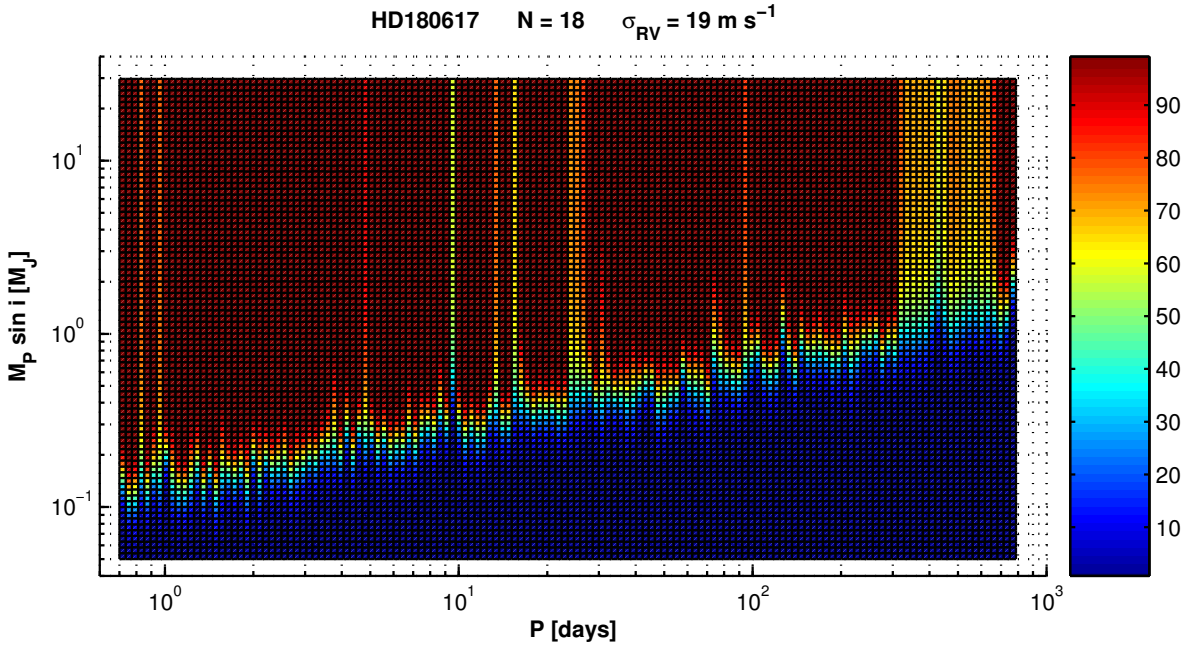
HD180617 N = 18 σRV = 19 m s−1
MP sin i [MJ]
P [days]
10^0
10^1
10^2
10^3
10^−1
10^0
10^1
90
80
70
60
50
40
30
20
10

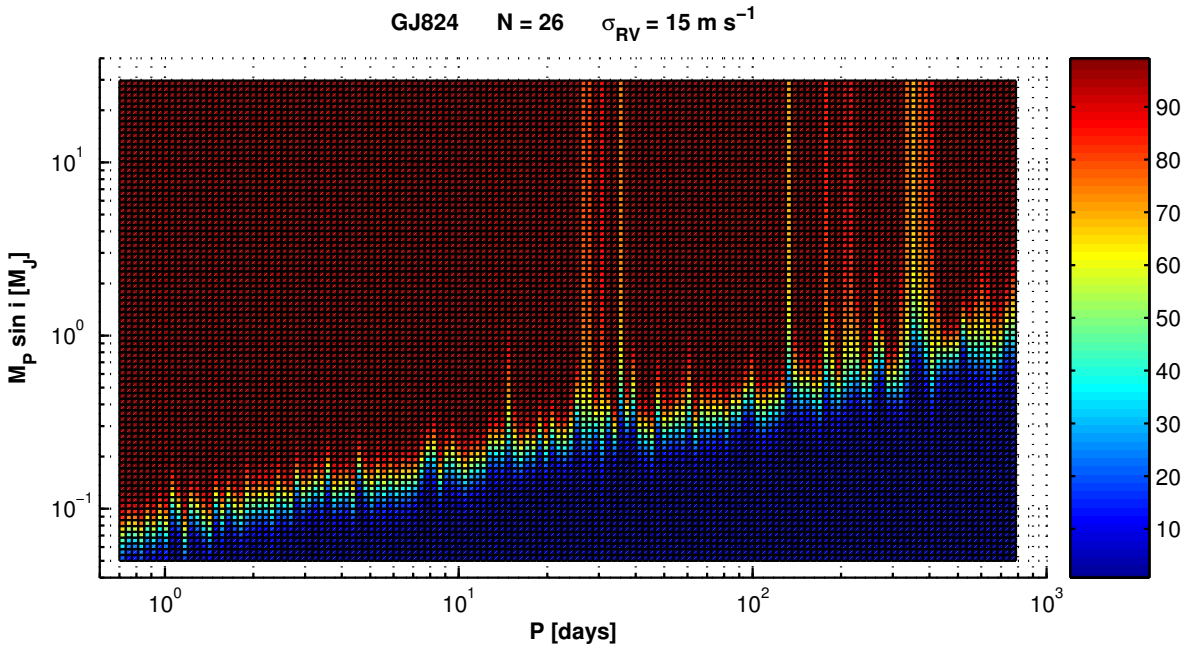
GJ824 N = 26 σRV = 15 m s−1
MP sin i [MJ]
P [days]
10^0
10^1
10^2
10^3
10^−1
10^0
10^1
90
80
70
60
50
40
30
20
10

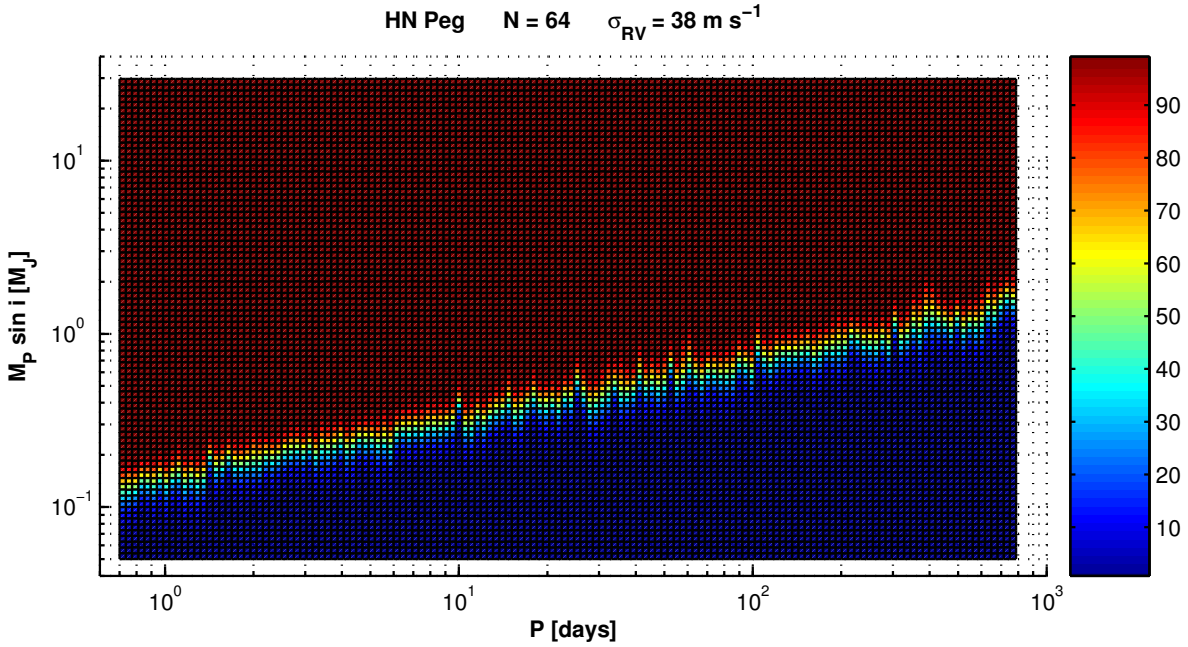
HN Peg N = 64 σRV = 38 m s−1
MP sin i [MJ]
P [days]
10^1
10^0
10^−1
10^0
10^1
10^2
10^3
90
80
70
60
50
40
30
20
10

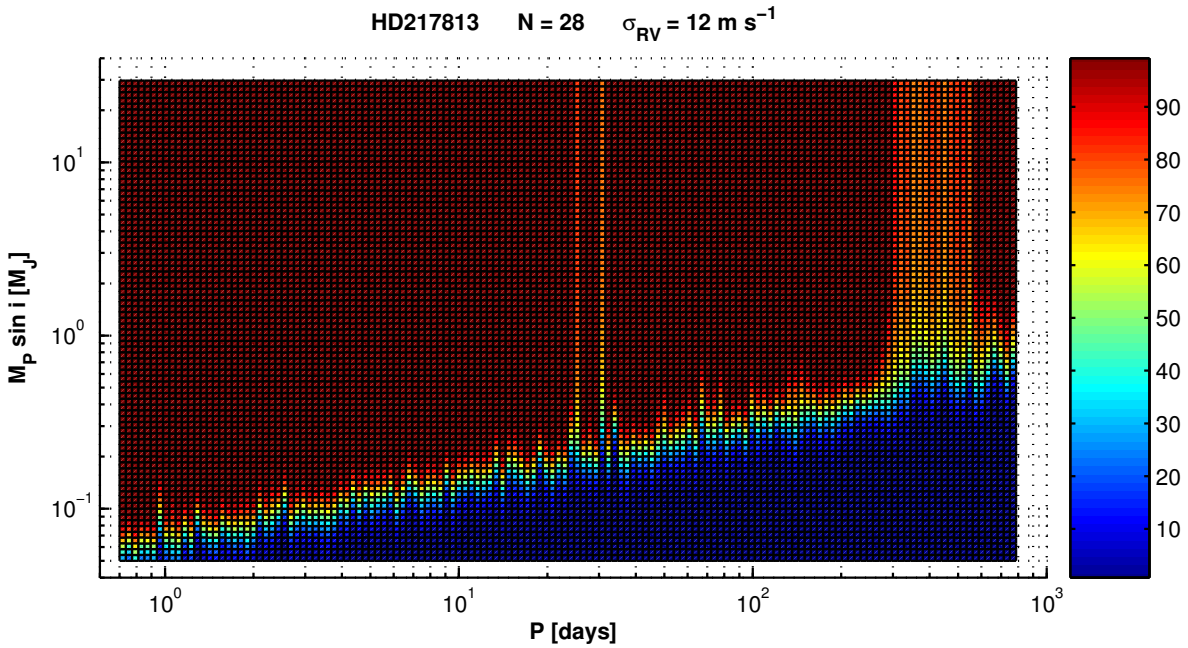
HD217813 N = 28 σRV = 12 m s−1
MP sin i [MJ]
P [days]
10^1
10^0
10^−1
10^0
10^1
10^2
10^3
90
80
70
60
50
40
30
20
10

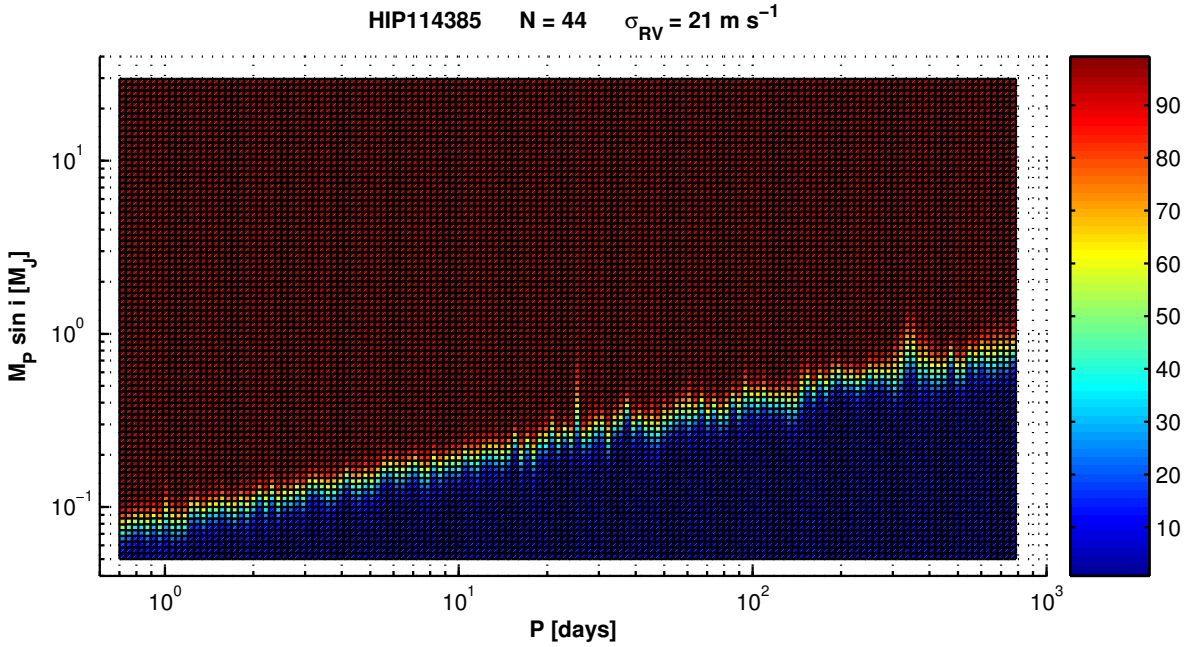
HIP114385 N = 44 σRV = 21 m s−1
MP sin i [MJ]
P [days]
10^1
10^0
10^−1
10^0
10^1
10^2
10^3
90
80
70
60
50
40
30
20
10

Acknowledgements

I want to express my gratitude to Prof. Massimo Capaccioli. He had the merit (should I say the guilt? It's up to the reader to decide it!) for introducing me to astronomy while I was an undergraduate physics student, quite indecisive about my future. I want to also thank Dr. Elvira Covino and Dr. Juan Alcalá who believed in me and helped me to get off on the right foot on my first steps as an astronomer. My genuine appreciation goes to the open-mindedness of Prof. Gaetano Scarpetta who let me free to pursue my particular interests in astronomy. I am deeply grateful to Dr. Eike Guenther. He helped me to smoothly get through all the difficulties one has to face when first he moves to a foreign country. And more important, from the very beginning to the very end of my stay in Tautenburg, he was always there to support me with useful advice and new ideas letting my project to advance.

After my arrival in Tautenburg, the observatory "italian colony" has been costantly growing. One by one, Patrizia, Alessio, Felice, Rebeca (Who would say you are Spanish in fact?) and Andrea joined up. They made working in Tautenburg much more pleasant and ... "palatable". Thank you all and good stay in Tautenburg!

A very special thank goes to "la Gnappa" (and all her declensions)! I hope I will find the way of rewarding her for all she does for me.

Finally I want to thank my parents with all my heart. Thanks to my mother who has taught me patience and humbleness. Thanks to my father who has taught me pride and tenacity. If I will ever do something good in my life, I will owe it to them.

Ehrenwörtliche Erklärung

Ich erkläre hiermit ehrenwörtlich, daß ich die vorliegende Arbeit selbständig, ohne unzulässige Hilfe Dritter und ohne Benutzung anderer als der angegebenen Hilfsmittel und Literatur angefertigt habe. Die aus anderen Quellen direkt oder indirekt übernommenen Daten und Konzepte sind unter Angabe der Quelle gekennzeichnet.

Bei der Auswahl und Auswertung folgenden Materials haben mir die nachstehend aufgeführten Personen in der jeweils beschriebenen Weise unentgeldlich geholfen:

1. Dr. Eike W. Guenther (Thüringer Landessternwarte Tautenburg): Betreeung der vorliegenden Arbeit.

2. Dr. Elvira Covino (INAF Osservatorio Astronomico di Capodimonte): Betreeung der vorliegenden Arbeit.

Weitere Personen waren an der inhaltlich-materiellen Erstellung der vorliegenden Arbeit nicht beteiligt. Insbesondere habe ich hierfür nicht die entgeltliche Hilfe von Vermittlungs bzw. Beratungsdiensten (Promotionsberater oder andere Personen) in Anspruch genommen. Niemand hat von mir unmittelbar oder mittelbar geldwerte Leistungen für Arbeiten erhalten, die in Zusammenhang mit dem Inhalt der vorgelegten Dissertation stehen.

Die Arbeit wurde bisher weder im In- noch im Ausland in gleicher oder ähnlicher Form einer anderen Prüfungsbehörde vorgelegt.

Die geltende Promotionsordnung der Physikalisch-Astronomischen Fakultät ist mir bekannt.

Ich versichere ehrenwörtlich, daß ich nach bestem Wissen die reine Wahrheit gesagt und nichts verschwiegen habe.

Tautenburg, den 27. März 2008

Massimiliano Esposito